A Study of Experimental Kagomé Antiferromagnets Based on the Jarosite Series

Andrew S. Wills

BA(Hons.) GRSC

A thesis presented for the degree of Doctor of Philosophy

The University of Edinburgh

1996

This work is dedicated to the memory of my Grandfather

Mr. C. P. Wills

A Study of Experimental Kagomé Antiferromagnets Based on the Jarosite Series

Abstract

Recent theoretical interest in Kagomé antiferromagnets arose from the prediction that they possess a new type of magnetic ground state in which there is no magnetic long-range order even at $T = 0$. Prior to this work no detailed investigations had been made of the magnetic properties of real materials that provide models for this class of magnet.

Members of the series $AB_3(SO_4)_2(OH)_6$ ($A^+ = Na^+$, K^+, Rb^+, Ag^+, NH_4^+, and H_3O^+; $B^{3+} = V^{3+}$, Cr^{3+}, and Fe^{3+}) have been studied using a combination of experimental techniques- ac and dc susceptibility, specific heat, neutron diffraction, and MuSR. The hydronium componds ($A^+ = H_3O^+$; $B^{3+} = V^{3+}$, Cr^{3+}, and Fe^{3+}) have been shown to provide the best model Kagomé antiferromagnets with $S = 1$, 3/2, and 5/2 respectively.

$(H_3O)Fe_3(SO_4)_2(OH)_6$ has been shown to possess only short-range magnetic order with a correlation length of 19 ± 2Å, below a spin-glass transition temperature, T_f ~17K. Unlike normal spin-glasses, muon spin relaxation measurements show that this magnetic phase is dynamic below T_f. $(H_3O)Fe_3(SO_4)_2(OH)_6$ is a spin-fluid: its dynamic and thermodynamic behaviour are completely unlike those seen in normal spin-glass or long-range ordered ground states; the specific heat varies as T^2 below T_f, rather than the linear T dependence observed in canonical spin-glasses. Deliberate reduction of the concentration of magnetic atoms destabilises the spin-fluid ground state and induces the formation of long-range order of the type seen in the other less magnetically concentrated members of the series. This is the first example of a system in which diamagnetic dilution causes it to order classically.

$(H_3O)Cr_3(SO_4)_2(OH)_6$ has a broad transition to a dynamic short-range ordered state at ~ 30K, similar to that seen in $(H_3O)Fe_3(SO_4)_2(OH)_6$, but with no observed spin-glass behaviour. A weak ferromagnetic transition at 2.2K is ascribed to a canting of antiferromagnetically coupled sublattices.

Specific heat and dc susceptibility measurements show that $(H_3O)V_3(SO_4)_2(OH)_6$ undergoes a sharp antiferromagnetic transition at 21K to an ordered ground state. However, neutron diffraction data taken at 4.2K reveal no evidence for long-range magnetic order. It is suggested that the magnetic ground state could be a highly correlated spin-fluid.

Acknowledgements

I would like to lay words of extreme gratitude at the feet of:

Andrew Harrison for the last four years, showing increasing patience as my stress levels rose, bringing me to Scotland, mentioning the word "*jarosite*", mentioning the word "*Mazola*", and so much more...

The inhabitants of Lab 79 (and 252), both past and present, for seemingly endless humour, and support. The cast in order of appearance are: Al (and Trish), Graeme, Gavin, Bin-bing, Debbie, Carolyn (and Phil), Gui-Hua, and Gareth. The *Twelve Days of Christma*s will never be the same again...

The supporting cast of Rm. 252. May your fish always be plentiful! (This will be completely misunderstood if anyone reads this in the future...)

Richard T. Dixon (is the T. for Tiberius??) for: my sanity, teaching me the meaning of the word "*Yesch*", the many walks up the *Alpe*, too many late night sessions of one form or another, ..., and not forgetting a great deal of computer advice to boot. What can I say at a time like this except, "*Drink a small distillery!!*"

The great many experienced people, without whose efforts the neutron and muon experiments would have been much less successful. The local contacts were: Clemens Ritter (ILL), James Lord (EMU, ISIS), Zin Tun (AECL). Additional experients and ideas were provided and performed by Sjoerd Mentink and Thom Mason.

The people that I have had the pleasure to learn from during my travels, both real and virtual. Unfortunately, I only have room to mention them; I wish my words of thanks could be greater. The list reads: Anthony Powell, Dougie Colgan, Ian Swainson, John Greedan, Steve Bramwell and Peter Holdsworth.

The Engineering and Physical Sciences Research Council, NATO, for financial support.

(This thesis was collated using a very big computer kindly "donated" by Gordon McDougall)

Courses Attended

Physical Department Colloquia

Firbush Physical Discussions

Solid State II

Crystal Structure Analysis

Aspects and Applications of NMR Spectroscopy

MaxEnt Applications

Conferences Attended

UK Neutron and Muon Users Meeting (1996)

Gordon Research Conferences: Solid State Chemistry (1996)

RSC Materials Chemistry Forum: Scottish Materials Chemistry Meeting (1996)

RSC Polar Solids Discussion Group Annual Meeting (1995)

RSC Chemical Crystallography Group Autumn Meeting (1995)

RSC Polar Solids Discussion Group Annual Meeting (1994)

RSC Chemical Crystallography Group Autumn Meeting (1994)

Ames Symposium (1994)

Table of Contents

List of Abbreviations

1-D	One-dimensional
2-D	Two-dimensional
3-D	Three-dimensional
AECL	Atomic Energy of Canada Limited, Chalk River, Ontario, Canada
χ_{ac}	Ac magnetic susceptibility
χ_{dc}	Dc magnetic susceptibility
χ_m	Molar dc magnetic susceptibility
χ_{nl}	Non-linear susceptibility
C	Specific heat
C_m	Magnetic contribution to specific heat
D-M	Dzyaloshinsky-Moriya interaction
E_f	Scattered (final) neutron energy
E_i	Incident (initial) neutron energy
esd	Estimated standard deviation
F	Free energy
fc	Field-cooled
FCC	Face-centred-cubic
FWHM	Full width at half maximum
g	Landé g-factor
γ_μ	Muon gyromagnetic ratio (81.324 kHz G^{-1})
GSAS	General Structure Analysis System
$\mathcal{H}$	Hamiltonian
η	Magnetisation
H	Modulus of magnetic field
ILL	Institut Laue-Langevin, Grenoble, France
J	Exchange coupling constant
κ	Chirality
k_B	Boltzmann's constant (1.381×10^{-23} JK^{-1})
KHAFM	Kagomé Heisenberg Antiferromagnet
KT	Kosterlitz-Thouless
L	Two-dimensional spin-spin correlation length
μ_B	Bohr Magneton (9.27408×10^{-24} JT^{-1})
μ_{eff}	Effective value of the moment
μ_{so}	Spin only value of the moment
MF	Mean (or Molecular) Field
MuSR	Muon Spin Relaxation
nn	Nearest neighbour
nnn	Next nearest neighbour
PG	Pyrolytic graphite
R	Gas constant (8.31441 J K^{-1} mol^{-1})
RAL	Rutherford Appleton Laboratory
RKKY	Ruderman Kittel Kasuya and Yosida theory
S	Spin quantum number
SGF	Strongly geometrically frustrated
SQUID	Superconducting QUantum Interference Device
T	Temperature
T_c	Critical temperature
T_f	Spin-glass freezing temperature
T_{KT}	Kosterlitz-Thouless transition temperature
TLS	Two-level system
zfc	Zero-field-cooled

1 Introduction

The understanding of magnetism and the nature of magnetic interactions has been the ambition of scientists and philosophers since the discovery of lodestone, $FeO\text{-}Fe_2O_3$. A better understanding of magnetism has implications for many other phase transitions through the principle of *universality*. This states that the common physics of many different subject areas, and the rules governing their phase transitions, can be unified [*Section 2.4*]. In this way, the understanding derived from the experimental observables of one system can be passed on to every other system in the same universality *class*, some of which it may not be possible to examine directly, e.g. Ising magnets, liquid-gas transition, and mixing in liquids.

This report continues the search for *new* types of magnetic ground state. In order to understand the types of magnetic order involved we must expand on the familiar concepts of ferromagnetism and antiferromagnetism, and begin to use the language of collective spin motion and topology.

1.1 Magnetic Interactions

It is useful to make a brief comment concerning the interaction between spins in a two-dimensional (2-D) system. In general, it is described by the Hamiltonian:

$$\mathcal{H} = \sum_{<ij>} J_{ij}\mathbf{s}_i \cdot \mathbf{s}_j + D\sum_{<i>}\left(s_{iz}\right)^2 - \mathbf{H}\cdot\sum_{<i>}\mathbf{s}_i \qquad (1.1)$$

where $<ij>$ depicts the sum over nearest-neighbours i, j; J_{ij} is the exchange interaction; D is the single ion anisotropy and $\mathbf{H}$ is an applied magnetic field. Positive values of J_{ij} correspond to an antiparallel arrangement of spins, i.e. antiferromagnetism, and negative values to a parallel arrangement, i.e. ferromagnetism. The number of spin-components or spin-dimensionality, n, can be used to classify the possible Hamiltonians into different models: Ising (n = 1) , XY (n =2), and Heisenberg or XYZ (n = 3). For the Heisenberg system with isotropic exchange we can write:

$$\mathcal{H} = J\sum_{<ij>}\mathbf{s}_i \cdot \mathbf{s}_j \qquad (1.2)$$

Later, we will need to expand on the other terms in the Hamiltonian to describe effects that may support canted spins, and the weak ferromagnetism observed in some experimental examples.

1.2 Frustration, topology and the Kagomé lattice- an overview

As a magnetic system is cooled it will tend to approach the state of lowest free energy. Competition between different terms in the Hamiltonian may prevent the formation of a simple ordered magnetic array, this is known as *frustration* [*Section 2.5*]. This frustration can result from competing exchange pathways and/or the geometry of the magnetic lattice and destabilises long-range magnetic order [*Section 2.5*]. This report is concerned with the second of these, geometric frustration and the extreme example of it- *the Kagomé lattice* [*Figure 1.1*].

The Kagomé lattice is made up of a network of triangles joined by vertex sharing. This leads to a unique topology in which neighbouring triangular plaquettes share only one moment. As a censequence we are unable to define a unique classical ground state, i.e. fixing the orientation of one moment does not define those of the rest of the lattice unambiguously, and there is a high degeneracy not present in other 2-D lattice topologies [*Section 2.8.1*]. Cooperative spin defects can exist within this degenerate manifold of spin configurations. Described by a series of *open* and *closed folds*, they interact creating energy barriers that separate the spin configurations. The rules that govern their creation and interaction are written in the language of *topology* [*Section 2.7*], an unfamiliar concept to most chemists. However, the reader should not be too discouraged at this point as these species are easy to visualise, and in doing so a simple understanding can be gained without too much difficulty.

1.3 Conclusion

The Kagomé lattice takes us beyond the conventional ideas of antiferromagnetism, to new types of magnetic order. Despite much theoretical and experimental work, this area is only now beginning to open up, and is slowly revealing its secrets. We still have a long way to go before we can claim to have any real understanding of this unique system.

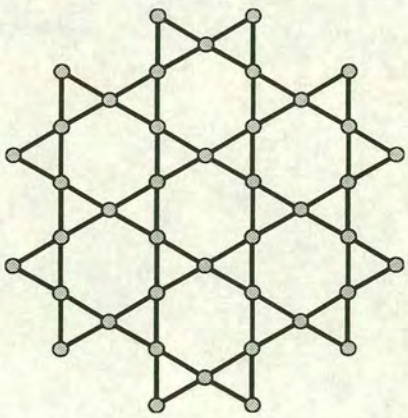

Figure 1.1. The Kagomé lattice.

2 Magnetism, frustration, and the Kagomé lattice

It is not my intention to substitute a few sparse pages of magnetic theory for the many excellent introductions to magnetism. Instead, I will concentrate on a few select areas and direct newcomers towards works such as those by Crangle,[1] Carlin,[2] and de Jongh.[3] These are very accessible, and provide a clear overview of the many varied areas of magnetism. The book by Crangle is particularly useful for those who wish to learn more about the applications of magnetic materials; this enables the reader to grasp the fact that magnetism is not just an exercise in scientific analysis, but has a direct role to play in current and future technology. The books by Carlin and de Jongh contain a wealth of experimental examples and data which will aid experimentalists who wish to learn about magnetochemistry.

This chapter will build upon the simple concepts of magnetism and describe spin-glasses in some detail, an area where magnetic theory is rapidly expanding. It leads towards the Kagomé lattice, a system where classical order does not occur: the result is a *new* type of magnetic ground state.

An informed reader may wish to skip early sections on general magnetic theory and go straight to the section on topology [*Section 2.7*] before moving onto the specifics of this particular problem.

2.1 Dimensionality and lattice thermodynamics

In insulating materials the magnetic moments are localised species that couple via short-ranged exchange interactions; this allows the simplification and broad classification into systems in which the strongest interactions, or exchange pathways, are one-dimensional (1-D) and chain-like, or in two-dimensional (2-D) sheets, or three-dimensional (3-D) magnetic lattices. The sheer complexity of magnetic interactions and exchange pathways creates a need for simplified model systems. The most elementary of such models are lattices with regular geometries, e.g. the square and triangular lattices. These systems provide a meeting ground for theorists and experimentalists: they are not so complicated that the theorists cannot solve them, while at the same time they are not so detached from reality that experimental realisations are impossible.

Whether or not a system is capable of supporting a conventional long-range ordered state at $T > 0$ depends on the lattice and spin dimensionality,[3] as shown in *Table 2.1*: 3-D systems can support long-range order no matter what the spin dimensionality, while 1-D magnets cannot have long-range order above $T = 0$ for any spin dimensionality. This is a simple consequence of the entropy created by an order-destroying defect. Consider a chain of N spins above $T = 0$: thermal fluctuations will act to create spin defects that separate the chain into spin-up and spin-down regions. If one such defect is created it may exist on any one of N sites, thus the entropy created is given by $\Delta S = k \ln N$. Above a threshold chain length this entropy gain will dominate the exchange-energy cost of creating the defect,

$\Delta U = JS^2$. Thus 1-D magnets are unstable with respect to thermal fluctuations.

	d = 1	*d = 2*	*d = 3*
Ising	○	x	x
XY	○	⊗	x
Heisenberg	○	○	x

Table 2.1. Absence (○) or presence (x) of a transition to a conventional long-range ordered state at finite temperature; (⊗) indicates a non-conventional transition.

2-D systems are intermediate between the two situations and are thus of great interest. While the 2-D Ising system orders, the 2-D Heisenberg system does not. In between lies the 2-D XY model, which holds a special fascination as it does not have a transition in the conventional sense. We cannot use an order-parameter, such as the spontaneous magnetisation to define the transition temperature, T_c. Instead the transition, known as the Kosterlitz-Thouless transition, at T_{KT} is to a topologically ordered state made up of bound half-vortex and half-anti-vortex pairs [*Section 2.6.3*]. In the language of topology [*Section 2.7*], these spin arrangements have opposite winding numbers and at the transition, they unbind and separate. Such a ground state and transition is only possible for planar spin arrangements, i.e. the 2-D Heisenberg model cannot support it.

This report is concerned with a particular 2-D antiferromagnet, the Kagomé antiferromagnet. In real materials 2-D magnetic behaviour is of course only an approximation, created as a consequence of crystal structure and exchange pathways. The quality of this approximation can be enhanced by deliberate structural changes, such as increasing the size of the non-magnetic atoms which separate the magnetic planes. This reduces the strength of the magnetic interactions between the layers and is exemplified by the family of compounds: $(C_nH_{2n+1}NH_3)_2CuCl_4$.[4] Increasing the length of the alkyl ammonium group pushes apart the magnetic Cu^{2+} layers and reduces the strength of the interplane interactions. This allows extrapolation to be made to the ideal 2-D Heisenberg $S = ½$ ferromagnet.

An important testing ground for 2-D magnetic theory (in fact it has been the subject of extensive study) is K_2NiF_4,[2,3] which is made up of $KNiF_3$ perovskite layers separated by a KF layer between the NiF_2 planes. The interaction within the layer is antiferromagnetic and the broad form of its 2-D χ_{dc} curve was explained using series expansion calculations. The transition temperature measured as the maximum in the gradient of the χ_{dc} agreed with that determined by neutron diffraction.

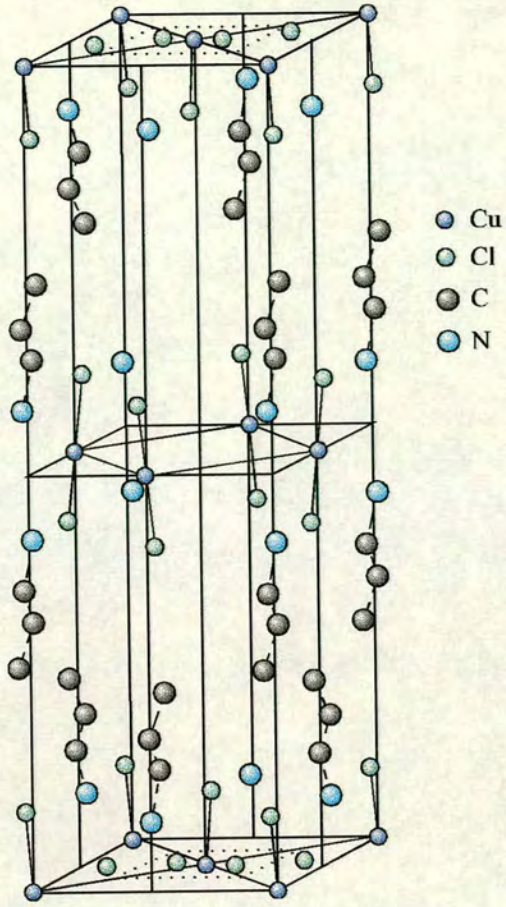

Figure 2.1. Crystal structure of $(C_3H_7NH_3)_2CuCl_4$. Part of the propylammonium groups and H atoms have been omitted for clarity.

As the temperature of a system is reduced the balance between the various different interaction energies and the thermal energy shifts. This leads to a change, or *crossover*, in the description of the system. For example, as a 2-D system is cooled it will become 3-D when the thermal energy is comparable to the interlayer interaction energy. To a first approximation we can separate the Hamiltonian of a system into different contributions, for example a 2-D Heisenberg system which cools to become a 3-D XY system will have contributions from both interplane and intraplane coupling, as well as from Ising anisotropy. The Hamiltonian may be written:

$$\mathcal{H} = J\sum_{\langle ij \rangle}^{(2d)} \mathbf{s}_i \cdot \mathbf{s}_j + J\sum_{\langle ij \rangle}^{(3d)} \mathbf{s}_i \cdot \mathbf{s}_j + A_{aniso}\sum_i s_{iz}^2 \qquad (2.1)$$

where *2d* refers to the summation being over nearest neighbours within the magnetic plane, and *3d* refers to summation over three dimensions. The anisotropy, A_{aniso}, favours ordering along the z-axis and within the XY plane, when $A_{aniso} < 0$ and $A_{aniso} > 0$ respectively.

As the system is cooled, the behaviour changes: initially anisotropy causes the spins to lose degrees of freedom, and the system settles into 2-D Ising behaviour. Further cooling causes a lattice dimensionality crossover with the system becoming 3-D. This is followed by a change in the anisotropy as the system finally corresponds to the 3-D XY model. The precise order of these events depends on the balance of the individual terms in the Hamiltonian.

To understand how the experimental quantities and responses are affected by these crossovers in the spin and lattice dimensionality we need to build up a description of the thermodynamics involved: the simplest such theory is called mean-field theory.

2.2 Mean-field theory

2.2.1 Weiss theory

The analytic description of magnetic systems is a many bodied problem that quickly becomes too complicated for workable solutions. Instead we need to resort to approximations, the simplest of which is mean-field (MF) theory.[5,6] According to the Weiss theory of ferromagnetism, the magnetic interaction of a given spin with its z nearest neighbours can be simplified by assuming that spins interact with one another through an effective molecular field proportional to the average magnetisation. In the language of the Heisenberg exchange interaction, this molecular field can be interpreted in terms of a pair-wise exchange. Thus the complex many-bodied problem can be reduced to the single-ion problem of a paramagnetic system of spins in an effective magnetic field.

If we begin with the Heisenberg Hamiltonian with a Zeeman-term:[3]

$$\mathcal{H} = \sum_{<ij>} J_{ij}\mathbf{s}_i \cdot \mathbf{s}_j - g\mu_B \mathbf{H} \cdot \sum_{<i>} \mathbf{s}_i \qquad (2.2)$$

For simplicity we now assume that the interaction is limited to the z- nearest neighbours of the reference spin. To further simplify the problem we will retain only the z-components of spins, i.e. $s_i^z = \langle s^z \rangle$. Therefore:

$$\mathcal{H}_{\mathrm{MF}} = \left\{ \sum_i J\langle s^z \rangle - g\mu_B H \right\} s_j^z \qquad (2.3)$$

Here $< s^z >$ denotes the expectation value for s^z. The interactions among the spins give rise to a magnetic field, H_{MF}, in addition to the external field H. The total effective field, H_{eff}, is given by their sum and the total Hamiltonian is of the form:

$$\mathcal{H}_{MF} = -g\mu_B H_{eff} s_j^z \tag{2.4}$$

comparison with equation (2.3) gives:

$$-g\mu_B H_{eff} = \sum_i J\langle s^z \rangle - g\mu_B H \tag{2.5}$$

$$\therefore \quad H_{eff} = -\sum_i J\langle s^z \rangle / g\mu_B + H \tag{2.6}$$

as $H_{eff} = H_{MF} + H$, the molecular field is then given by:

$$H_{MF} = -\sum_i J\langle s^z \rangle / g\mu_B = -zJ\langle s^z \rangle / g\mu_B = \lambda M_s \tag{2.7}$$

and is proportional to the spontaneous magnetisation (per spin), $M_s = g\mu_B < s^z >$, which is a function of temperature and applied field; $\lambda = -zJ/g^2\mu_B^2$ is called the molecular field parameter and is a function of the exchange integral J and so is related to the critical temperature, T_c.

An estimate of the value for H_{MF} can be obtained by equating the thermal energy at T_c to that due to the internal field:[2]

$$gS\mu_B H_{MF} = kT_c \tag{2.8}$$

g is the 'Landé g value' and may be approximated to 2 for many systems, and S is the spin. For metallic iron, $T_c \approx$ 1000K, $g \approx 2$, and $S \approx 1$, and so:

$$H_{MF} \approx 10^{-20} / (2x10^{-23}) \approx 500T \tag{2.9}$$

much larger than any magnetic field yet produced in the laboratory.

While mean-field theory gives the correct qualitative predictions for the phase diagrams of 3-D systems, it soon displays its failings for lower dimensional systems and it is important to understand its limitations. These are largely the result of the assumption that the exchange interaction of a spin is with an average of all other spins in the system. This causes mean-field theory to improve as the number of the nearest neighbours and the dimensionality increase. The assumption of an average spin configuration rather than a Boltzmann weighted interaction with all possible spin configurations means that mean-field theory is only valid when the system has settled into one spin configuration, and fluctuations are unimportant.

As the exchange interaction is with all other spins, the correlations are assumed to be over an infinite length scale, i.e. in its simplest form short-range order is not taken into account at all.

Despite all of its failings, mean-field theory does have a great strength- its simplicity. While systems

quickly become too complicated for numerical analysis as the number of nearest neighbours increases, mean-field theory is relatively easy to apply and actually becomes more accurate. It is often taken as a starting point for more sophisticated analysis.

2.2.2 Ginzberg-Landau Theory:

Ginzberg-Landau theory, or Landau theory is an alternative mean-field representation.[6] Rather than assuming the presence of an internal field, the basic assumption is that the free energy, *F*, can be expanded as a Taylor series in terms of an order parameter, such as the sublattice magnetisation, near the critical point. This is true for infinitely long-range interactions and systems with more than 4 dimensions, but otherwise fails as the thermodynamic functions are not analytic near the phase transition. However, due to its simplicity and generality it is still a good starting point for the description of the system.

As an example we will examine the transition from a ferromagnetic to a paramagnetic state in zero external field. The order parameter for this example is the magnetisation, η. Near the critical point the order parameter will be small and we can expand it as a Taylor series:[5]

$$F(T, \eta) = F_0(T) + \alpha_2(T)\eta^2 + \alpha_4(T)\eta^4 + \ldots \qquad (2.10)$$

There are no odd terms in the expansion as the free energy $F(T, \eta)$ is the same for positive and negative values of the magnetisation η. Equating $F(T, \eta)$ to be at a minimum for the system to be in equilibrium at any given temperature enables us to work through to the free energy and so to other thermodynamic functions as a function of the order parameter, η, and the expansion coefficients. This method predicts a step function in the specific heat at T_C rather than the lambda anomaly seen in experiment, an indication that the theory has problems.

However, the theory is solvable and actually works well for systems where the interactions are long-ranged, such as ferroelectrics and type I superconductors. It also clearly demonstrates that the mean-field exponents depend on the symmetry of the order parameter or the interaction.

2.2.3 Shortcomings of mean-field theory

Mean-field theory operates under the assumption that the forces involved are long- or infinitely-ranged; breakdown from this obviously causes deviation from mean-field results. For most critical phase transitions the interactions are short-ranged. The first obvious result will be the possibility of short-range order. This is completely ignored in mean-field theory where the assumption is that the interactions are infinitely ranged and each moment is under the influence of the mean-field created by all the moments in the lattice.

Short-range order becomes of increasing importance as the dimensionality of the lattice is reduced and

alternative theories must be used.

2.3 Spin wave theory

At low temperatures the magnetic properties of a system can be well described using spin wave theory. For a simple ferromagnet at $T = 0$, the magnetic moments will be in the ground state, and each moment will precess around the direction of the internal field, z. At $T = 0$ all the moments precess in phase. At $T > 0$ thermal fluctuations cause adjacent moments to have a constant difference in the phase of their precession, ka, where a is the lattice constant, $2\pi/k$ is the wavelength, and k is a quantum number called the wave number. A spin wave is propagated through a sinusoidal variation in the x, or y, components of the magnetic moments [*Figure 2.2*]. In fact these fluctuations are normal modes and have a precise analogy in lattice vibrations. The quanta of the spin waves are called *magnons* and are analogous to phonons; both obey Bose-Einstein statistics.

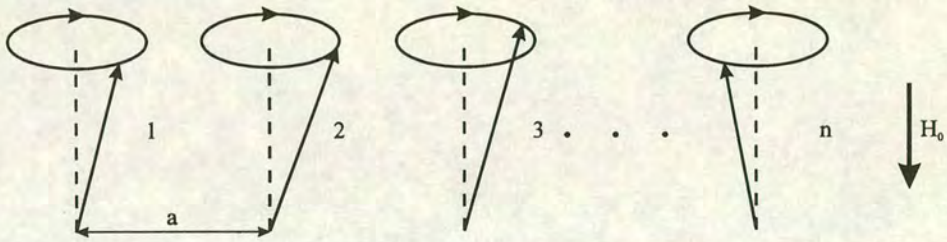

Figure 2.2. Classical picture of a spin wave in a linear ferromagnetic chain of N- spins. The arrows represent the spins precessing around the internal field.

The energy of a spin wave with wave number k is given by $h\nu$, where ν is the frequency of the spin wave. It can be shown using quantum mechanical or semiclassical arguments[7,8] that the dispersion relation for the spin waves in a ferromagnet is quadratic and is given by:

$$h\nu = Dk^2 \qquad (2.11)$$

where D is the stiffness constant. For an antiferromagnet we create a sets of spin waves for each sublattice. These sets interact via the exchange interaction and are not independent, again giving rise to normal modes but this time with a linear dispersion:

$$h\nu = Dk \qquad (2.12)$$

Using these relations and arguments similar to those used in the Debye model, the specific heat below the ordering temperature, T_c, can be derived as:[9]

$$C = AT^{d/n} \tag{2.13}$$

where A is a constant, d is the dimensionality of the lattice, and n = 1, 2 for an antiferromagnet and a ferromagnet respectively.

2.4 Critical exponents and Universality

Shortcomings in theory mean that experimental data often have to be analysed phenomenologically. It has been found that ferromagnetic susceptibility, specific heat, correlation length and the spontaneous magnetisation all obey a simple power law as they diverge at the critical point, T_c.[6] It is useful to define this power law in terms of a reduced temperature, t:

$$t = \frac{T - T_c}{T_c} \tag{2.14}$$

The critical exponent associated with a function $F(t)$ is then given by

$$\lambda = \lim_{t \to 0} \frac{\ln|F(t)|}{\ln|t|} \tag{2.15}$$

Therefore a plot of $ln\ \chi$ against $ln\ (T - T_c)$ will have a slope of λ. The indices of the power laws are known as *critical exponents* and they are defined by the asymptotic behaviour close to the critical point. As a consequence of this, their values are greatly affected by the weaker terms in the Hamiltonian and any crossovers in dimensionality. In general the form of the power law is:

$$F(t) \propto |t|^{\lambda} \tag{2.16}$$

Below some of the commonly used critical exponents used in magnetic systems are defined:

- specific heat: $C_m \propto |t|^{-\alpha}$ (2.17)
- zero field magnetisation $M_s \propto (-t)^{\beta}$ (2.18)
- zero field isothermal susceptibility $\chi \propto |t|^{-\gamma}$ (2.19)
- spin-spin correlation length $\xi \propto |t|^{-\nu}$ (2.20)

In real systems the power law is not obeyed exactly and equation (2.16) must be expanded in terms of

a power series:[6]

$$F(t) = A|t|^{\lambda}(1+bt^{\lambda_1}+...) \qquad (2.21)$$

where $\lambda_1 > 0$. The later terms become smaller close to the critical temperature.

One of the problems with this method is that T_c must be known accurately in order to define the reduced temperature. To overcome this, it is common to use T_c as a fitted parameter, adjustable so as to make the log-log plot linear, often resulting in artificially enhanced linearity. Thus, it is hard to estimate the values and to determine the error of the critical exponents accurately.

Systematic trends have been found in the values of experimental and theoretical exponents and this is usually expressed in terms of *universality*. Universality states that for a continuous phase transition the critical exponents depend on the following three properties alone:

- The dimensionality of the lattice (or more generally the system), *d*.
- The dimensionality (or more precisely the symmetry) of the order parameter, *D*.
- Whether the forces are short or long-range.

This implies that the origin of the microscopic interaction is irrelevent. We would expect this from Landau theory, as systems with a similar expansion of the free energy will share the same critical exponents. Hence mean-field theory naturally leads to groups of systems with the same critical exponents, so-called *universality classes* and these are reproduced in experimental measurements.

Theory predicts that certain relationships hold between the critical exponents within a given universality class. Two such relationships are:

$$\gamma + \alpha + 2\beta = 2 \qquad (2.22)$$

$$D\nu = 2 - \alpha \qquad (2.23)$$

where D is the spatial dimensionality of the system. Scaling relationships involving the spatial dimensionality, D, are referred to as *hyperscaling relationships*.[10]

The major importance of universality is that it offers the ability to greatly simplify the theory of continuous phase transitions. Many systems are too complicated for direct solution. Instead, we can now use the description of a simpler model system and apply its solutions to all other systems in the same universality class, e.g. Ising magnets, liquid-gas transitions, and mixing in liquids.[11] As magnetic scientists we are fortunate that the simplest such models are often magnetic, causing this to be a very active area of study.

There are four standard models:

- Ising ($D = 1$). This class is appropriate for Ising magnets, liquid-gas transitions, ordering in alloys, and mixing in liquids.
- XY ($D = 2$). The spins have 2 components and the order parameter is the vector sum of these, which is two dimensional. Applied to "easy-plane" magnets and to superfluidity in liquid ^{4}He.
- Heisenberg ($D = 3$). Isotropic magnetic materials.

This list is not exhaustive as magnetic dimensionalities greater than three are known, for example the spherical model ($D = \infty$). These models do not correspond to any physical reality, but often have the advantage that they are exactly solvable.

2.5 Frustration

Any competition between the different magnetic interactions in a system gives rise to an effect termed *frustration*, which we may define as:

Frustration: the competition between different terms in the Hamiltonian such that no spin configuration simultaneously minimises each term.

The concept is illustrated in *Figure 2.3* for the case of a triangular array of spins which are coupled antiferromagnetically and are free to rotate in the plane of the paper. Any two spins, taken in isolation, may be coupled antiferromagnetically, but the topology of the lattice prevents a third spin from coupling antiferromagnetically to this pair of spins [*Figure 2.3(a)*]; the compromise arrangement, with the lowest exchange energy, is the 120° array depicted in *Figure 2.3(b)*. This form of frustration arises in any lattice constructed from odd-numbered loops of spins. A similar result can be obtained by competing exchange pathways [*Figure 2.3(c)*].

The deviation of the Curie-Weiss law [*Section* 5.3.1], and so of $1/\chi_{dc}$ from linearity, occurs at a lower temperature than normal for frustrated systems as the frustration allows the system to be portrayed by a completely free spin in a strongly interacting environment. For VCl_2, a triangular antiferromagnet, the deviation is at $T \approx |\theta_w|/7$ rather than at $T > |2\theta_w|$ as for the Heisenberg AF-nn square lattice.[12,13] There is as yet no analytic understanding of this simple bulk behaviour.

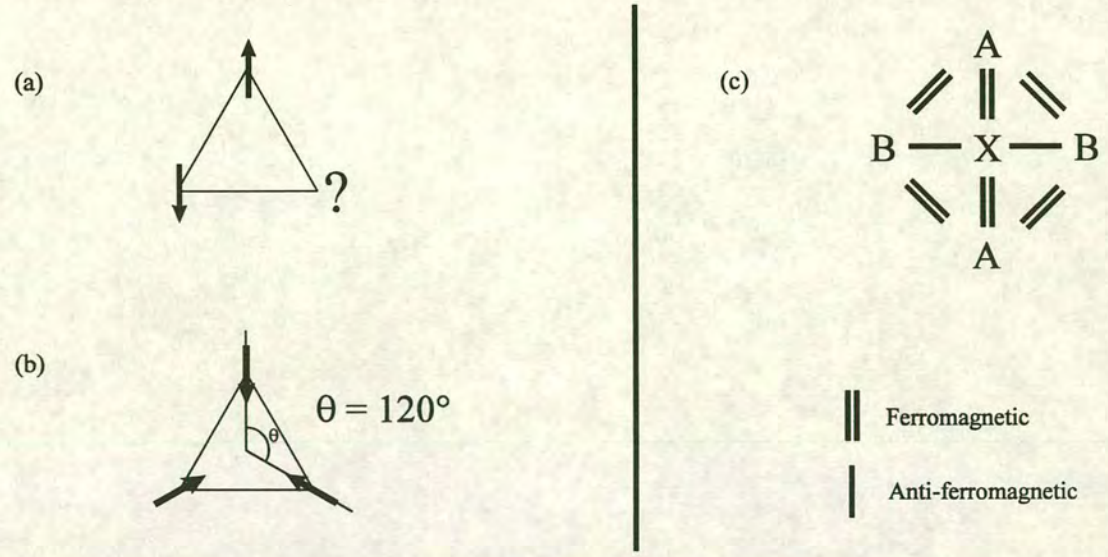

Figure 2.3. Spin configurations in: (a) a triangular lattice of antiferromagnteically coupled XY spins demonstrates the impossibility of arranging a third moment so that it is antiparallel to both its neighbours; (b) depicts the compromise spin configuration of minimum energy; (c) a frustrated system as a consequence of competing exchange pathways.

That θ_w is well defined for a frustrated system (because of the increased applicability of the Curie-Weiss law) allows the definition of an empirical measure of frustration by the quantity:

$$f = |\theta_w| / T_c \qquad (2.24)$$

In an unfrustrated 3-D system the ordering temperature T_c is identical to $|\theta_w|$ so clearly, $f > 1$ corresponds to frustration.

The face-centred-cubic (FCC) materials FeO, MnS, and MnSe are moderately frustrated with $f = 3$. Materials with $f > 10$ are for our purposes strongly geometrically frustrated (SGF) and are not describable by mean-field theory.

The most obvious similarity between the real examples of frustrated systems is that the magnetic lattices are all based on triangles. For 2-D this corresponds to triangular or to Kagomé lattices and for 3-D they are based on tetrahedra such as the pyrochlore lattice.

The entropy created by an order-destroying defect in a low dimensional system also suppresses long-range order, despite the value of θ_w. This is exemplified by the fact that of the layered lattices only the 2-D Ising model has long-range classical order. In low-dimensional systems, spin-spin correlations begin to build up well above the mean-field T_c, but below this temperature the correlations and the order parameter never develop fully. The entropy that low-dimensional systems have is as a consequence of reduction in spin density, whereas the SGF systems gain entropy by the topology of a dense spin arrangement. That being so, one expects that the ways in which these two types of system

approach the $T > 0$ ground state will be qualitatively different, and that for SGF magnets there will emerge new physics at low temperatures of a type not anticipated by MF or spin wave theory.

2.6 Spin-glasses

Spin-glasses are random magnetic systems that exist below a well defined temperature T_f, which corresponds to a co-operative freezing of spins. Below this temperature the system is highly irreversible and moves between metastable frozen states with no long-range spatial order. Experimentally a spin-glass has the properties of: a) no long-range magnetic order; b) a cusp in the ac susceptibility; c) smooth temperature dependence of the specific heat near the freezing temperature; d) time- and magnetic field history dependence of spin correlations near the transition temperature, T_f. They are characterised by a spectrum of relaxation times which range from $\tau = 10^{-13}$ to infinite.[14,15] Because a spin-glass is characterised by an evolving system of metastable states there is a great difficulty in modelling spin-glasses as equilibrium thermodynamics do not apply. The nature of the freezing transition is still a matter of conjecture as it is a co-operative transition but one with a failure to establish full thermal equilibrium. It is governed by kinetics rather than by thermodynamics.

Frustration is a necessary but not a sufficient condition for a spin-glass: there must also be significant amounts of randomness (often as site occupation); a regular triangular lattice will not exhibit the co-operative freezing transition of a spin-glass. Instead, a slow "blocking" will occur to a ground state dominated by large magnetic fluctuations. The randomness and frustration result in the failure to establish conventional ferro- or antiferromagnetic long-range order and instead the system exhibits a freezing transition to a state in which the moments are aligned in random directions.

There are many models used to describe the thermodynamic and kinetic properties of a spin-glass; it is not the place of this report to describe each in detail, only a passing note will be made.[15-17]

Much of the theory is applied to metallic, site-random, spin-glasses that are composed of magnetic impurities with a localised spin occupying random sites in a non-magnetic host metal, e.g. $Au_{1-x}Mn_x$ (*Au*Mn), $Cu_{1-x}Mn_x$ (*Cu*Mn), and $Au_{1-x}Fe_x$ (*Au*Fe). The exchange interactions in the model description are infinite and are of the RKKY type,[14,20,21] in which spins interact via polarisation of the conduction electrons. The applicability of detailed theoretical results based on these models to insulating spin-glasses which result from short-ranged interactions is a matter for debate. These insulating and semiconducting spin-glasses can similarly be made by diluting a non-magnetic sublattice with a magnetic species, e.g. $Eu_xSr_{1-x}S$ and $Fe_xMg_{1-x}Cl_2$.[15]

2.6.1 Cluster Freezing

The simplest and often most useful model used to describe the spin-glass transition is that of phenomenological cluster freezing.[15] As the temperature is lowered to T_f independent paramagnetic

spins slow down and build themselves into locally correlated units or clusters, which act and spontaneously reorientate as a whole. A distribution of cluster sizes leads to a distribution of relaxation times and so the system has a complex evolution with temperature which slows as T is reduced to T_f. These clusters are coupled and those moments not involved in clusters are independent of each other, but help to transmit the interactions between the clusters. As the system is cooled the clusters become larger and grow into diverse fractal shapes guided by the local distribution of competitive interactions.[18]

Close to T_f the spin-spin correlations are longer ranged and larger clusters develop. At T_f percolation ensues and there is an infinite cluster of spins itself made up of many smaller clusters that are rigidly frozen in random orientations. Spins inside this infinite cluster are correlated, but have their local directions governed by the random shape or anisotropy of the smaller clusters. So although the smaller clusters retain their original identity, they are no longer able to react to an external field but are instead firmly embedded within the infinite cluster. The system now becomes trapped in the metastable multidegenerate configurations that arise from the frustration. The assumption is that the clusters are the fundamental entities rather than single spins- the system is a cluster spin-glass.

One of the most important questions in the theory of spin-glasses concerns the nature of the transition at the freezing temperature- whether it is a true critical phase transition or just a gradual blocking of clusters as the system slowly settles into a frozen state. Because the system is not controlled by equilibrium thermodynamics, but by kinetics, the latter is therefore more likely.

2.6.2 Energy landscapes

Far above T_f the hypersurface which describes the free energy in the appropriate phase-space co-ordinates has a parabolic form [*Figure 2.4(a)*].[15,16] As the system is cooled towards T_f, clusters of various sizes begin to form, creating small, local minima in the energy surface. As the height of these energy barriers separating the minima is still small with respect to the thermal energy, the equilibrium thermodynamic state is an average over phase space. Just below T_f, [*Figure 2.4(b)*] co-operative freezing has raised the energy barriers creating many nearly degenerate low-lying valleys with different internal structures of sub-valleys, each one corresponding to a different microscopic configuration. The barriers are still thermally accessible and can be overcome slowly, creating a quasi-equilibrium in which the macroscopic free energy has contributions from a restricted but still significant region of phase space within the available time. Metastabilities are present as there is an increased chance of the system becoming stuck in one of the low-lying valleys

Below T_f, [*Figure 2.4(c)*] the energy barriers which separate the low-lying valleys, representing different local values of the magnetisation, will be very high compared with the thermal energy; this causes the landscape to be partitioned into mutually inaccessible valleys (that is inaccessible within any reasonable period of observation) that represent the metastable states of the frozen spin-glass. Within each of these there are many sub-valleys or smaller structures separated by small barriers. As

the system becomes trapped in a main valley it will exhibit properties specific to that valley, and so not be in true equilibrium with contributions from all the valleys in the energy surface with the appropriate thermal weights; we say that the system is *non-ergodic* or has broken ergodicity. Performing the average over the frozen-in disorder of the free-energy landscape which is required to calculate experimental observables, is a major problem as we do not know the shape of the free-energy landscape, or how it depends on the applied field as different spin configurations will have different values of the magnetisation.

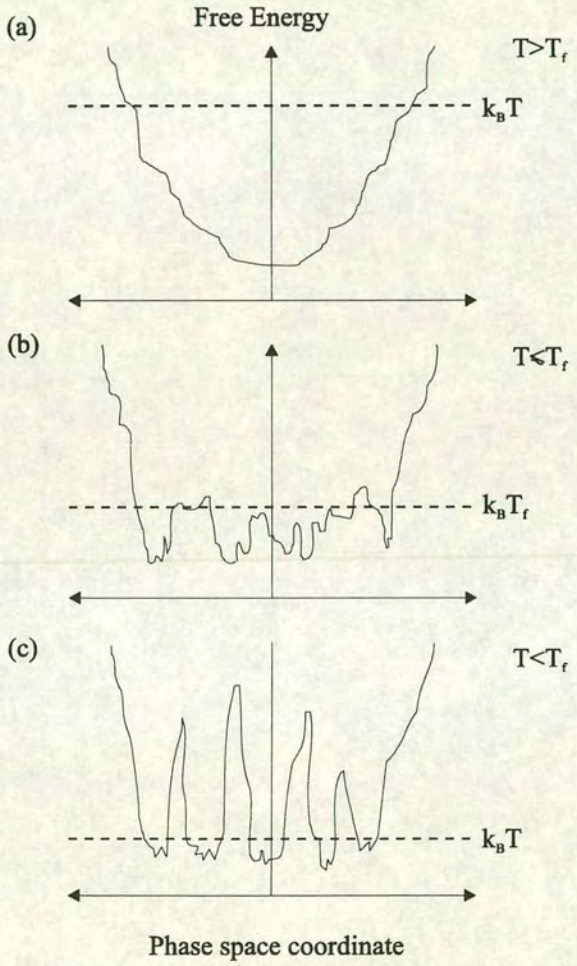

Figure 2.4. Schematic description of the multi-valley landscape as a function of temperature.

In a conventional magnetic system the broken ergodicity can be taken into account by restricting the possible values of the order parameter. In a spin-glass to fully describe all the aspects of the freezing transition, and so create an order parameter, we need to describe not only the characteristics of each individual valley, but also the correlations between all the valleys in phase space- there is no simple order parameter. So we must talk in terms of time averages appropriate to the timescale of the experiment, rather than dealing with equilibrium observables.

2.6.3 Two-level system

As we will see in the next section, many of the thermodynamic properties of spin-glasses, in particular the linear dependence of the specific heat with T, can be explained in terms of a two-level system (TLS). The exact origin of this TLS in spin-glasses is difficult to determine as it is a common result of different theoretical models.

Originally, the linear dependence of the specific heat seen in spin-glasses was proposed to have the same origin as that seen in conventional "window" glasses,[19] i.e. a statistical distribution of localised "tunnelling modes" between two local minima close in configuration space. A similar result can be obtained from cluster theory[16] where we have a system of interacting clusters with strong internal binding. Here, the rearrangements of the spin configuration can be pictured as involving thermally activated hopping over the small barriers in the rugged free energy landscape. This model reduces to single spins or clusters, having two low-lying states [*Figure 2.5*] separated by an energy ε, just as in the TLS first proposed for structural glasses, except here the barrier hopping is by thermal activation with no evidence for significant tunnelling between the two levels, in contrast to structural glasses. Numerical studies of the spectrum of excitations of a RKKY site random spin-glass have yielded a qualitatively similar result.[20,21]

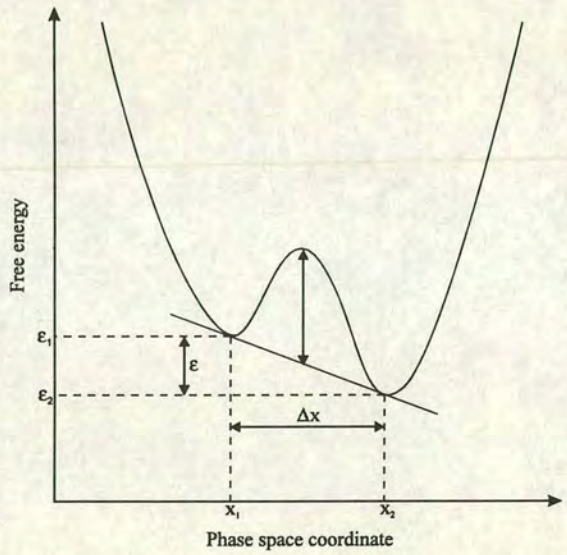

Figure 2.5. Two-level system of free energy as a function of phase space co-ordinate x.

We can understand another physical reason for the presence of a TLS by extending the concept of two-dimensional 'vortices', introduced by Kosterlitz and Thouless[22] in order to describe the excitations of a planar ferromagnet, to the ground state properties of frustrated plaquettes.[23] This time, the TLS arises from the interaction between frustrated plaquettes mediated through a 2-D sea of non-frustrated spins. Each frustrated plaquette creates a disturbance in the surrounding spin system as shown in *Figure 2.6*. If a loop is drawn around a frustrated plaquette, the direction of the spins around the loop in a clockwise sense rotates quasi-continuously through an angle ± 180°, where the sign is dependent on

the chirality of the plaquette. In a conventional vortex[22] the spins rotate through ± 360°, so this is termed a half-vortex. In the language of topology [*Section 2.7*] this corresponds to a non-integer winding number and so a defect which is not topologically stable, but here the half-vortex is present in the ground state, and is not an excitation. As two plaquettes of the same chirality would produce a complete vortex, with a winding number of ±1, the interaction between two frustrated plaquettes, i.e. two half-vortices, must be 'antiferromagnetic', i.e. the two plaquettes will have opposite chiralities. The TLS is attributed to the interactions between clusters of half-vortices and the elementary excitation in a pair of reversed chiralities of opposite signs.

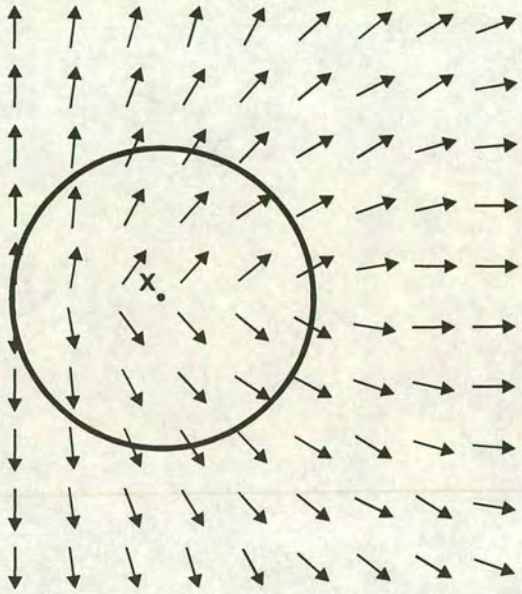

Figure 2.6. Ground state of a frustrated plaquette x in a 2-D, non-frustrated medium. The direction of the spins around the loop rotates quasi-continuously through an angle 180°.

2.6.4 Experimental characteristics

Our definition of a spin-glass is based entirely on experimental properties, so it is not difficult to extend these ideas to give a good indication of the properties of real spin-glass systems. Reiterating our previous defining characteristics that spin-glass should possess:

- no magnetic long-range order
- a cusp in the ac susceptibility
- smooth temperature dependence of the specific heat near the freezing temperature
- time- and magnetic field history dependent magnetic remanence below this temperature

At temperatures $T >> T_f$, the system is paramagnetic and we can expect it to follow the predictions of the Curie-Weiss law with deviations appearing as the system is cooled to the freezing temperature and

clusters start to develop when the spins co-operatively freeze. In agreement with the simple ideas of mean-field theory, an increase in the concentration of the magnetic ions causes a corresponding increase in the size of the mean-field and the Curie-Weiss constant, θ_w.

The primary measurement carried out on magnetic systems is that of dc susceptibility (χ_{dc}), where the irreversibility of the magnetic response creates a clear separation of the field-cooled (fc) and zero-field-cooled (zfc) measurements below T_f [*Figure 2.7*]. Both measurements have a time dependence, demonstrating the non-equilibrium nature of the spin-glass state.

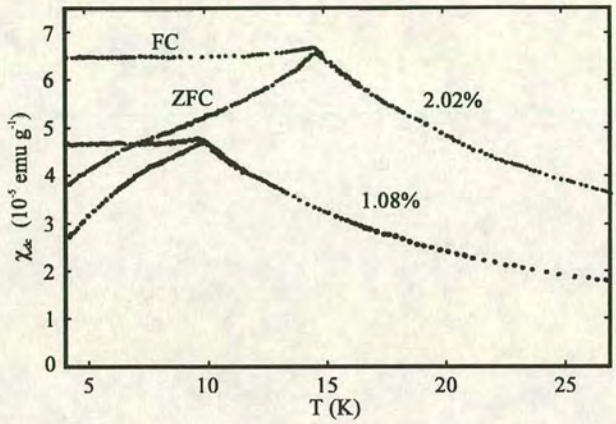

Figure 2.7. Field-cooled (FC) and zero-field-cooled (ZFC) susceptibility as a function of temperature for 2.02 and 1.08% substituted CuMn.[15]

Higher-order terms in the expansion of the equation of state[16] in terms of the magnetic field are more sensitive to spin-glass order than the zero-field susceptibility $\chi_0(T)$, e.g. the next-order term is the non-linear susceptibility, $\chi_{nl}(T)$:

$$M/H = \chi_0(T) - H^2\chi_{nl}(T) + O\left(H^4\right) \qquad (2.25)$$

Near T_f a large number of spins react co-operatively to the external field, giving rise to what appears to be a singularity in the non-linear susceptibility, χ_{nl}. In principle the critical behaviour of χ_{nl} yields information about the phase transition and is consistent with the principle of universality and a critical divergence at T_f according to the power expression:

$$\chi_{nl}(T) \propto \left[\left(T - T_f\right)/T_f\right]^{-\gamma} \qquad (2.26)$$

However, analysis of this kind is not really convincing as it is based on the assumption that there is a true phase transition at T_f and that the magnetisation is in thermal equilibrium, which is not the case for

a spin-glass.

To further examine the spin-glass state alternating current (ac), or dynamic, susceptibility, χ_{ac}, is used. In this technique the magnetisation M is measured in some small ac-driving field h and the susceptibility is taken from the derivative $\partial M/\partial h$ at some frequency ω.[15,17,24,25] χ_{ac} is an important measurement for spin-glasses because h can be made very small, ≈ 0.1Gauss, and ω can be varied over a large frequency range which allows probing of the freezing transition over a range of timescales. This allows a full determination of the real $\chi'(\omega,T)$ and imaginary (out-of-phase) $\chi''(\omega,T)$ parts, corresponding to dispersion and absorption respectively, between long and intermediate (10^{-1}-10^{-5}s) relaxation times. Whereas the dc susceptibility is irreversible below T_f, χ_{ac} remains reversible even for extremely low frequencies. The real part, $\chi'(\omega, T)$, exhibits a sharp cusp near T_f ,often with a quadratic dependence with temperature[15] below T_c and there is a shift in the position of T_f with measuring frequency [*Figure 2.8*]. This we already expected from our cluster freezing model: the freezing transition involves a gradual slowing of clusters with a range of different sizes and timescales; the higher frequency components freeze out at higher temperatures, causing T_f to be a function of measuring frequency. The peak itself is also rounded by the application of a field. In $\chi''(\omega,T)$ there is a sudden rise near T_f, corresponding to an absorption as the relaxation processes are decoupling the spins from the lattice. This is not usually found at a magnetic transition except when hysteresis arises, as in a ferromagnet. The peak in $\chi'(\omega,T)$ corresponds to the maximum slope of $\chi''(\omega,T)$.

We can get an idea of how the distribution of relaxation times changes as a function of temperature with an Argand diagram, where $\chi''(\omega)$ is plotted against $\chi'(\omega)$ at each temperature [*Figure 2.9*]. A large number of relaxation times give rise to a squashed arc which becomes more hemi-spherical as the distribution narrows. Detailed mathematical analysis of the form of the arc is complex and this is often just used as a pictorial representation to show how the relaxation time distribution moves to lower frequency as the extent of the spatial correlations increases. At T_f a very long-time tail suddenly appears and for all practical purposes the system is frozen.

A spin-glass can be modelled as a system of clusters that interact and block the reorientation of other clusters in response to an external stimulus. If there is a simple relation between the energy-barrier and thermal activation, we can estimate the activation energy, E_a, for cluster reorientation from the frequency dependence of T_f using the Arrhenius equation:

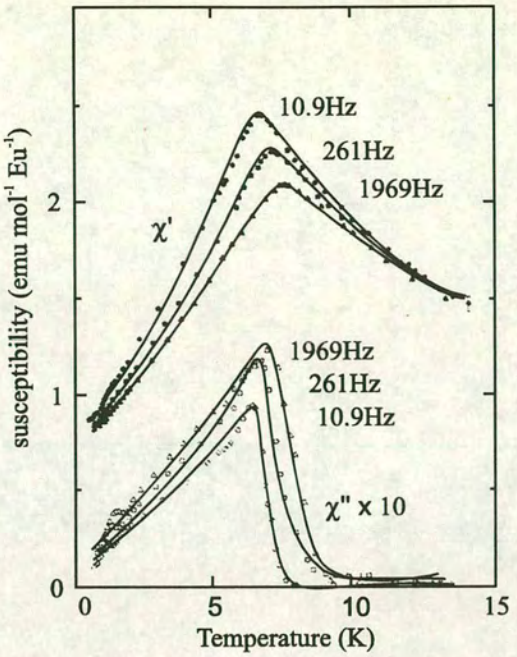

Figure 2.8. Temperature dependence of the dispersion χ' and absorption χ'' for the insulating spin-glass $Eu_{0.2}Sr_{0.8}S$.[15]

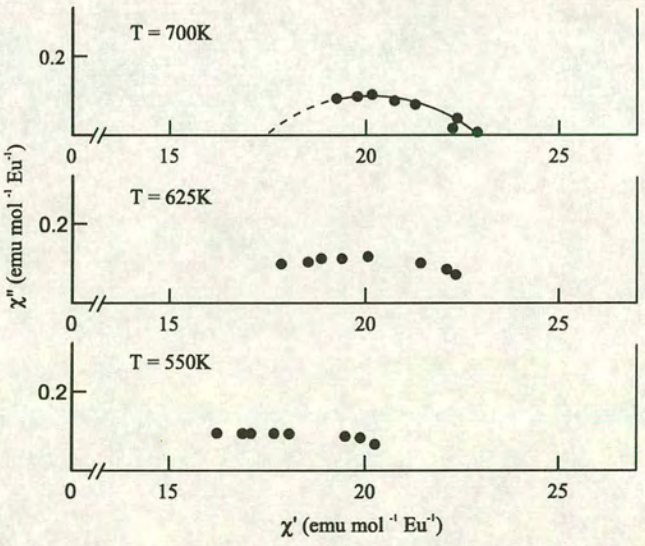

Figure 2.9. Argand diagrams at three temperatures for $Eu_{0.8}Sr_{0.2}S$.[15]

$$k = A\exp\left[-E_a/k_BT\right] \qquad (2.27)$$

where k is a rate constant, A is a pre-exponential factor and k_B is the Boltzmann constant. The T_f in ac

susceptibility measurements corresponds to the temperature at which the cluster reorientation frequency, ω, is equal to the driving frequency of the χ_{ac} measurements. Thus:

$$\omega = \omega_0 \exp\left[-E_a / k_B T_f\right] \qquad (2.28)$$

where the pre-exponential constant, ω_0, is called the frequency factor and ω is the driving frequency of the χ_{ac} measurement. This, however, leads to unphysical values for the frequency factor, ω_0 , and the activation energy, E_a, but does work for a superparamagnet, where the Arrhenius law holds.

If we extend the Arrhenius law to better take account of the interactions between clusters we obtain an empirical law used to describe the viscosity of supercooled liquids, the Vogel-Fulcher law:[15]

$$\omega = \omega_0 \exp\left[-E_a / k_B \left(T_f - T_0\right)\right] \qquad (2.29)$$

where T_0 for real glasses is called the "ideal glass" temperature and is thought to apply to the true critical temperature of an underlying phase transition. While this gives physically more reasonable values, they are still not very meaningful and are used often only as a guide, e.g. for *Cu*Mn ω_0=1.6x10^8 Hz, E_a=11.8K

Mössbauer spectroscopy can be used to study processes with a timescale of 10^{-7}s or less. Slightly higher than the cusp in χ_{ac} ($\omega \rightarrow 0$) there is a sharp splitting in the Mössbauer line indicating the formation of static or quasi-static internal fields below T_f due to frozen-in spins.[17]

The magnetic contribution to the specific heat, C_m, does not shows a singularity at T_f; instead there is a broad cusp at temperatures approximately 20% higher than T_f [*Figure 2.10*]. At temperatures $T << T_f$, C_m is approximately linear in T,[16] and this is attributed to the presence of a TLS. Detailed inspection show that the linear variation is not exact, but instead follows a quadratic dependence:

$$C_m \approx c_1 T + c_2 T^2 \qquad (2.30)$$

where c_1 and c_2 are constants. Alternatively,

$$C_m \propto T^n \qquad (2.31)$$

where n has a range of values from 1 to 3/2. The latter form is that expected for 3-D ferromagnets, and suggests the presence of large ferromagnetic clusters. Specific heat is history dependent and is largest after field cooling, although application of a magnetic field causes the specific heat to become progressively more rounded as the freezing transition is disrupted.

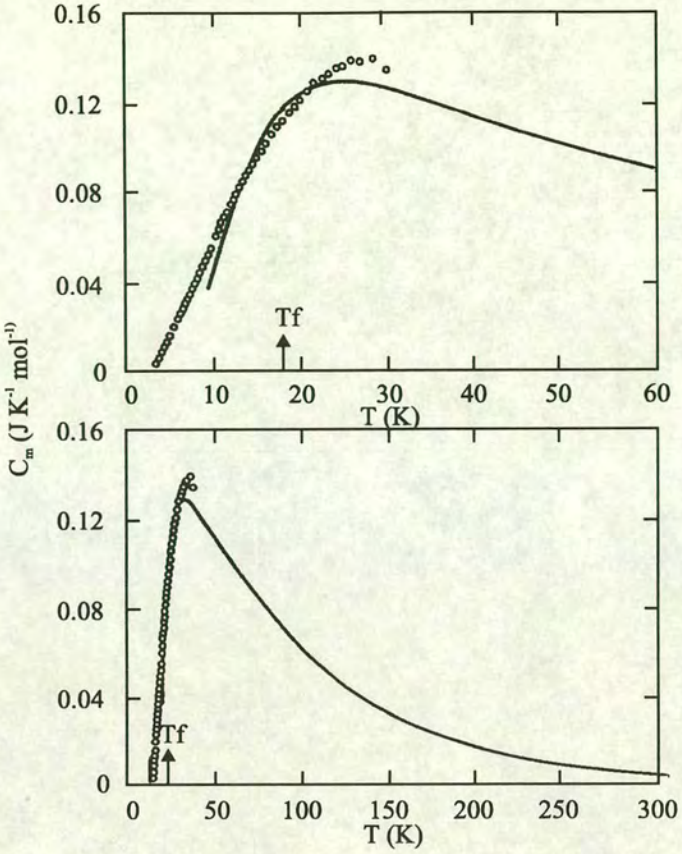

Figure 2.10. Magnetic specific heat for the metallic spin-glass CuMn over the low and high temperature regimes, demonstrating the presence of a linear region.[15]

Neutron scattering[17] [*Section 3.1.4*] can be used to yield information about the static and dynamic spin-glass. The scattering has two contributions: elastic and inelastic. The former is more accurately described as quasi-elastic as instrumental resolution causes all processes with relaxation times larger than 10^{-11}s to be considered elastic. Both contributions are temperature dependent with the broad excitation modes becoming more quasi-elastic at lower temperatures as clusters freeze out. We see that there are no Bragg peaks indicative of long-range magnetic ordering, but there is diffuse magnetic scattering indicative of static spin structures which we can characterise with some form of short-range correlation length, L, to describe the size of the clusters involved.

Muon spin relaxation[26-29] [*Section 3.1.6*] bridges the time window between neutron scattering, Mössbauer spectrometry and ac susceptibility, and is used to look at relaxation times from 10^{-4} to 10^{-11}s. For a static collection of random fields the experimentally observed longitudinal depolarisation function, $G_z(t)$, follows the Kubo-Toyabe function:

$$G_z(t) = \frac{1}{3} + \frac{2}{3}\left(1-\sigma^2 t^2\right)e^{-\frac{\sigma^2 t^2}{2}} \qquad (2.32)$$

where t is the time after implantation and σ depends on the field distribution. This is schematically shown in *Figure 2.11(a)*. The initial decay reflects the distribution of internal fields and the recovery to 1/3 is a property of a static system. Temporal fluctuations in the fields cause a decay in the 1/3 recovery and if rapid enough will reduce $G_z(t)$ to a stretched exponential decay [*Section 4.55*]:

$$G_z(t) \propto \exp\left[(-\lambda t)^{\beta}\right] \qquad (2.33)$$

β is a function of the distribution of fields and λ is the muon depolarisation rate. $\lambda \propto 1/\tau$, where τ is the moment relaxation rate.

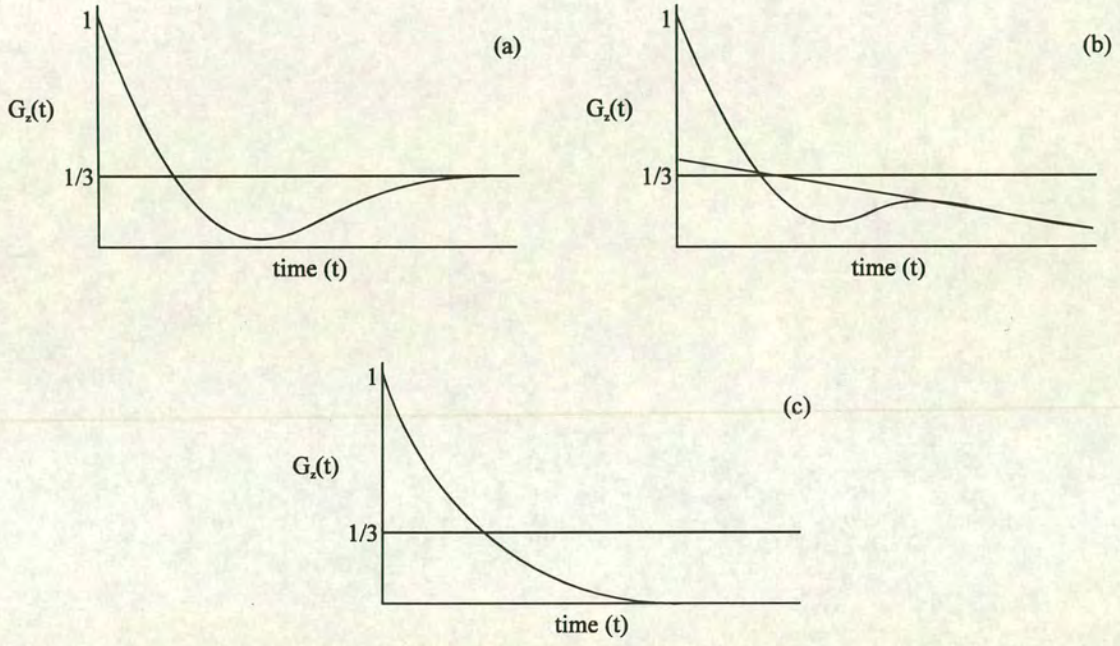

Figure 2.11. Longitudinal depolarisation function, $G_z(t)$, for (a) a Kubo-Toyabe function, (b) the onset of fluctuations reduces the $^1/_3$ recovery, (c) fast fluctuations lead to a stretched exponential decay.

2.7 Topology

It is true to say that to most solid state scientists, topology represents an area covered in the shroud of impenetrable mathematical theory. In order to explain some of the theory surrounding the Kagomé antiferromagnet, we must lift a corner of the cloth and become familiar with some of the more basic concepts. When we do this, we glimpse a new insight into the many physical systems where defects exist and interact with each other in ordered media.

Here, we use the theory of topology to classify elementary defects and to define the rules that govern their interactions.

2.7.1 Order-parameter and winding number

In order to define a defect, we must first define an uniform medium in which it exists. If the spatial dependence of the order parameter is described by the function $s(r)$, a uniform medium is simply one where $s(r)$ has a constant value, i.e. the order parameter is everywhere the same. A singularity (whether a point, line, or surface) or *defect* is thus a region where the order parameter does not vary continuously. In order to describe a defect we must look at how the values of the order parameter change around it. The possible values of the order parameter constitute a phase space known as order-parameter space, or the manifold of internal states.

If we use a 2-D XY system of spins with a singularity at point P as an example [*Figure 2.12*] and draw a circle, or contour, centred at P, and transverse its circumference in a clockwise direction, the total angle through which the vectors turn with respect to some fixed direction is $+2\pi$. Because $s(r)$ must be continuous at every point other than at P, the total angle of any defect must also be a multiple of π, i.e. $2n\pi$ where n is an integer. For an XY vector the possible values of the order-parameter map onto a circle in order-parameter space. Here the integer n simply corresponds to the number of times that the mapping of the contour (in real space) onto the circle (in order-parameter space) wraps around the circle, and is called the *winding number*.

Singularities can be made which have $n = 0$; these may be smoothed out without changing the order-parameter at some arbitrary distance from P, and are described as being topologically unstable. For non-zero n, we say that the defects are topologically stable and they cannot be removed by a simple fluctuation in the local field, only by a gross change in the order-parameter. This is not to say that a lack of topological instability results in physical instability as we have made no examination of the energy barriers involved. It is quite possible that topologically unstable defects will be metastable and their destruction involves the system passing through configurations of higher energy.

We can classify the defects according to the winding number, n. Defects with different winding numbers are in different classes; they will have a topological barrier that prevents the two configurations from being transformed into each other. Defects in the same class are said to be topologically equivalent and possess no topological barrier to their interconversion.

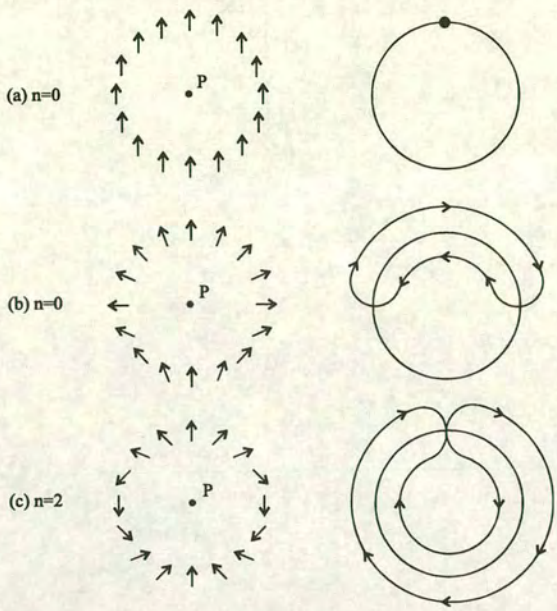

Figure 2.12. Spin configurations on circular contours drawn around a point P (left) and mapping onto order-parameter space with various winding numbers (right). In (b) the order parameter is non-uniform but the winding number is zero and the contour in order parameter space can be reduced to a point.

2.7.2 Combination of defects

If we define the product (o) of two loops *f* and *c*, *f* o *c* as the loops obtained from x and traversing *f* then *c*, we obtain an additional property describing the defect: if *f* o *c* = *c* o *f* the product commutes and the defects are said to be Abelian, if they do not commute they are non-Abelian. The simplest example of a non-Abelian defect is so-called figure-of-eight space [*Figure 2.13*] where we have a plane with two holes and two loops *f* and *c*; if we begin at point *x* we see that *f* o *c* ≠ *c* o *f*.

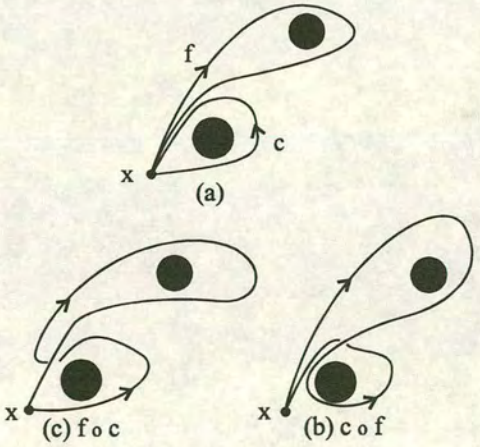

Figure 2.13. The figure-of-eight space. (a) two loops f and c; (b) loop product c o *f.; (c) loop product f* o *c.*

When we have two Abelian defects in the same region of space they become equivalent to a single defect. This means that there is no topological barrier to prevent them from fusing into a single defect with a winding number equal to that of the sum of the separate components. A special case occurs when the two defects have opposite winding numbers and their sum is equivalent to a non-singular configuration i.e. they mutually annihilate.

Non-Abelian defects have a much more complicated interaction whose details are certainly beyond the scope of all but the most theoretical of works.[30,31] Suffice it to say that when two such defects, e.g. line defects, cross they retain their individual identity and become entangled. The interaction is mediated by the creation of new defects and occurs through a series of complex deformations, giving rise to energy barriers.

2.8 Frustrated systems with no disorder

As we have already seen, any system based on a triangular plaquette is frustrated. In 2-D the simplest examples are the triangular and Kagomé lattices, the latter is a network of vertex sharing triangles. In 3-D, the building block is the tetrahedron, containing four triangular faces. When joined, again by vertex sharing the result is the pyrochlore lattice [*Figure 2.14*]. The high degree of frustration in these lattices results in the destabilisation of a simple, and possibly unique, ground state of ordered sublattices and so generates the possibility of forming new types of ground state such as the *spin nematic* or *spin-fluid* systems that will be described in detail later.

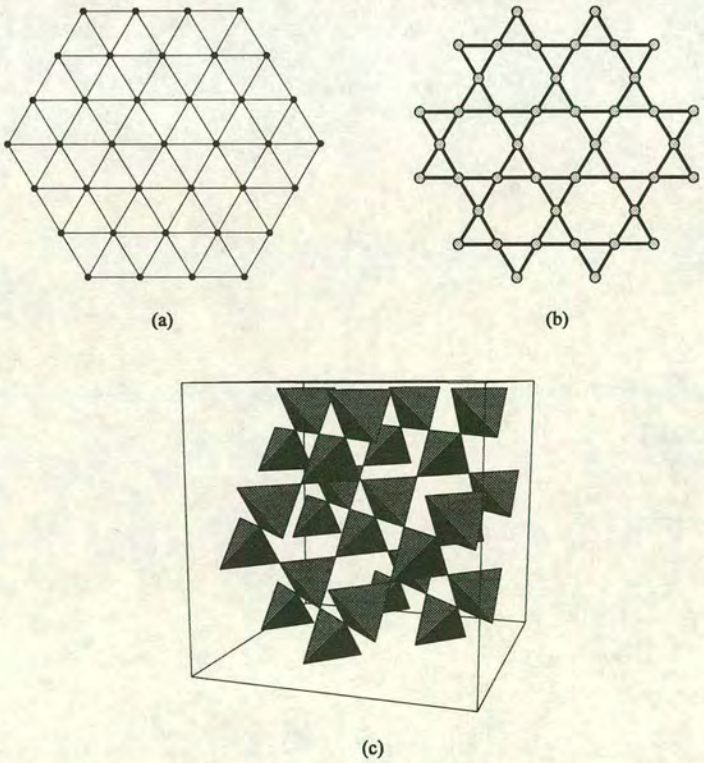

Figure 2.14. (a) The triangular, (b) Kagomé, and (c) pyrochlore lattices.

2.8.1 Chirality and degenerate ground states

To fully understand the significance of the Kagomé and pyrochlore systems we need to step beyond the simple idea of frustration. A simple consequence of frustration is an increase in the degeneracy of the ground state. This is exemplified by the square and triangular antiferromagnets: an individual square plaquette has only the trivial degeneracy associated with global rotation of the spins; the triangular plaquette, however, has an additional degeneracy that is described using the handedness, or *chirality*, of the spins around the plaquette. This is defined using the pairwise vector product of spins around the triangle:

$$\kappa = 2 / \left(3\sqrt{3}\right)\left[\mathbf{S}_1 \times \mathbf{S}_2 + \mathbf{S}_2 \times \mathbf{S}_3 + \mathbf{S}_3 \times \mathbf{S}_1\right] \qquad (2.34)$$

For the triangular plaquette we can immediately see that the chirality order parameter has two possible values, $\kappa = \pm 1$, where the positive values referring to a handedness in the clockwise sense; this degeneracy is a simple consequence of the lattice topology.

The similarity between the triangular and Kagomé lattices is obvious: both are made up of triangles and so are frustrated. But if we look at the ground state properties we see that there is a remarkable difference between the two geometries. In the triangular lattice, individual triangular plaquettes are joined by sharing an edge. A consequence of this is that if we decorate one plaquette with a 120° ground state spin structure, we also unambiguously define the spin arrangement of the neighbouring plaquettes, that is the chirality information is transferred and the fixation of the chirality of one plaquette is propagated throughout the system and as a result, the chirality of all the plaquettes is defined. Again, the only ground state degeneracy is that associated with the global rotation of spins. The topology of the Kagomé lattice removes the ability to define a unique ground state: chirality information cannot be passed on as only one spin is shared between plaquettes, giving rise to a high degeneracy not present in the other lattice topologies. Two particularly highly symmetric spin configurations of interest are known as the q = 0 and $\sqrt{3}$ x $\sqrt{3}$ states [*Figure 2.15*] because their respective magnetic lattice parameters are the same size and $\sqrt{3}$ times larger than those of the structural unit cell. The q = 0 state has 3 sublattices and corresponds to a ferromagnetic pattern of chirality, while the $\sqrt{3}$ x $\sqrt{3}$ state has 9 sublattices and an antiferromagnetic distribution of κ.

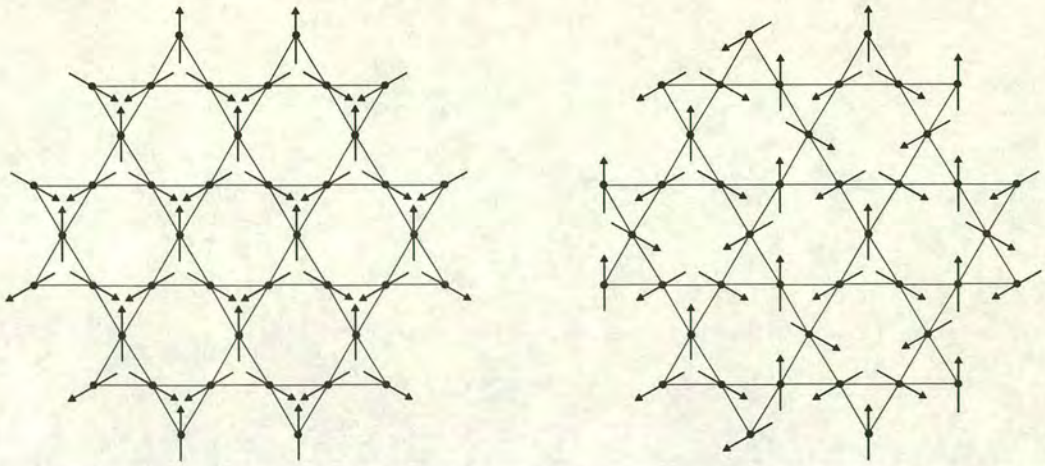

(a) (b)

Figure 2.15. The q = 0 and √3 x √3 Néel spin configurations of the Kagomé lattice.

If we go to three dimensions, the pyrochlore lattice is made up of vertex sharing tetrahedra and the consequence is the same as for the Kagomé lattice- a ground state that is non-trivially degenerate.

The interest in the Kagomé and pyrochlore systems is now apparent- their topologies, i.e. vertex sharing connectivity, increase the degeneracies of their respective ground states, and so further destabilise classical multi-sublattice order. For this reason we can immediately separate the triangular from the Kagomé and pyrochlore systems; the latter may be viewed as siblings with obvious similarities.

Because of their similarities it is useful to briefly discuss some of the experimental results for the pyrochlore antiferromagnets before beginning the discussion of the Kagomé antiferromagnet itself.

2.8.2 The pyrochlore lattice

The most studied examples of pyrochlore antiferromagnets are those based on the series of compounds $A_2B_2O_7$ (A^{3+} = Y^{3+} and Tb^{3+}; B^{4+} = Mn^{4+} and Mo^{4+}) which crystallise in the cubic space group F*d*3*m*, where the A^{3+} and B^{4+} ions form interpenetrating pyrochlore networks. Neutron and X-ray diffraction studies made on $Y_2Mo_2O_7$ [32,33] and $Tb_2Mo_2O_7$ [34] show that their spin-glass behaviour is not a consequence of structural disorder, as the conventional philosophy for a spin-glass states. Instead, it appears that the spin-glass state is the fundamental ground state of these pyrochlore antiferromagnets.

Elastic neutron scattering measurements on $Tb_2Mo_2O_7$ show strong diffuse peaks near Q=1.0 and 2.0Å^{-1}.[34,35] Such diffuse peaks are reminiscent of a liquid structure factor and short-range order; if we use the half-width as a measure of the correlation length, *L*, we arrive at a value of 5 ± 1Å for the moments with short-range order corresponding to the (111) wavevector, i.e. the correlations extend to the near-neighbours of the tetrahedra only. Their intensity is found to develop continuously below 50K. The half-width of the correlations is temperature-independent which indicates that despite the

increase in the static moment, the spatial extent of the correlations does not change with T. The inelastic scattering profile (counts *vs.* energy transfer) is dominated by a quasielastic peak that increases as temperature falls. It may be fitted to a detailed balance factor times a Lorentzian in energy; the result is then convoluted with the resolution function of the spectrometer. No anomaly is seen in the elastic scattering as T is varied through the freezing transition, suggesting that the spin-glass-like anomaly is a dynamical phase transition, and that the neutron experiments show the short-range ordered spins slowing down and becoming static on the timescale of the neutron measurement (~ $2\text{x}10^{-10}$s). As expected for a spin-glass, there is a lack of reproducibility around T_f indicating that it does not corespond to a true equilibrium phase transition.

$Y_2Mo_2O_7$ [33,34] again has no evidence for a long-range ordered phase transition. Measurements of the non-linear susceptibility, χ_{nl}, show that it follows a power-law dependence close to T_f consistent with a conventional spin-glass transition:

$$\chi_{nl} \sim \left(T - T_g\right)^{-\gamma} \qquad \gamma = 3.3 \pm 0.5 \qquad (2.35)$$

Interpretation of data collected from $A_2B_2O_7$ pyrochlores is problematic because they are not insulators but semiconductors; the magnetic description is complicated by the presence of both static and itinerant spins- the system is not a faithful realisation of the simple pyrochlore antiferromagnet described in theory. Perhaps a better model pyrochlore is $CsNiCrF_6$, also in space group F*d*3*m*, which is a true insulator.[36] Again, there is no long-range magnetic order at any temperatures above or below the spin-glass freezing temperature, T_f = 2.3K, only diffuse scattering with a correlation length essentially that of nearest neighbours. Inelastic neutron diffraction reveals that the magnetic signal develops as a strong elastic line with a broad inelastic contribution extending to higher energies. Both contributions are present and continue to develop below T_f= 1.6K, with the broad magnetic component sharpening (FWHM ≈ 0.6 meV at 8K). The broad contribution extends out to at least 7 meV; this is well beyond the energy equivalent of the spin-freezing temperature (kT_f = 0.14 meV) and is a region where normal spin-glasses possess no inelastic processes. The presence of both elastic scattering and an inelastic contribution at low temperatures suggest that while some fluctuations are being frozen out at T_f, there still exist others with energies well in excess of the spin-glass ordering energy. These dynamics are in marked contrast to those seen in conventional spin-glasses where the magnetic order is static- here the magnetic order has some significant dynamic contribution.

Their lack of structural randomness immediately indicates that the pyrochlore systems are not ordinary spin-glasses; the physical mechanism of this behaviour is still the object of much debate. One thing is certain: that it *is* a consequence of the unique geometry of the lattice, and so of its frustration and inherent degeneracy.

2.9 The Kagomé lattice: theory

It appears perverse to discuss the theoretical aspects of the Kagomé antiferromagnet as the recent flood of interest is a result of an experimental observation- the anomalous specific heat of the second layer of ^{3}He on graphite, the first experimental Kagomé system[37] [*Section 3.0*]. However, in order to make the best sense of the experimental data a firm understanding of the theory is vital. With this in mind, the experimental examples will be presented after a discussion of the theories that have been put forward to describe the ground state and its excitations.

2.9.1 The ground state of the Kagomé Heisenberg Antiferromagnet (KHAFM)- spin nematic, spin-fluid, or Néel order?

It is the consensus of theory that the Kagomé antiferromagnet with only nearest-neighbour exchange does not have a Néel ordered ground state at $T = 0$. Quantum fluctuations, enhanced by the low dimensionality, and frustration, combine with the entropy effects of an infinitely degenerate ground state manifold to cause the spin-spin correlations to decay very rapidly with distance: the spin-spin correlation at the second-neighbour is close to 15% of the nearest-neighbour value, compared to 95% for spin correlations on the triangular lattice.[38,39] The lack of long-range Néel order has been shown by variational analysis,[37,39] Monte-Carlo simulation,[40] exact diagonalisation calculations,[38,41-43] series expansion,[44,45] spin-wave theory[46] and the dependence of ground state properties with cluster size.[47] These suggest that the system is unconventional and possesses a disordered ground state. There are a number of possible ground states[46] but we will divide them broadly into two classes: spin nematic, and spin-fluid and briefly examine each one:

- Nematic order is perhaps the most general form of order.[40,48,49] There is no sublattice order and it is not characterised by an well defined ordering wavevector, but instead by tensor order parameters. The spins select a single axis in spin space and orient themselves randomly along that axis or perpendicular to it, as defined by the tensor. Within this sub-group of states there may also be an additional selection of states along a loosely defined wavevector or phase angle, as in the case of helimagnets. For example, the spin nematic state may be based upon the $\sqrt{3} \times \sqrt{3}$ state: this is a coplanar configuration and the order has a bias along the wavevector corresponding to the $\sqrt{3} \times \sqrt{3}$ state, but the spin-spin correlation length is not infinite and the order is only short-ranged. High-temperature series expansions[48] show that there is a tendency towards nematic order based on the $\sqrt{3} \times \sqrt{3}$ state and that the susceptibility corresponding to the $\sqrt{3} \times \sqrt{3}$ state appears to diverge as $T \rightarrow 0$, suggesting that the critical temperature of the KHAFM is $T = 0$ and that there is no ordered moment at this temperature. Below the nematic ordering temperature the specific heat is found to vary as $C(T) \propto T^2$, as would be expected for conventional 2-D long-range antiferromagnetic order.[50,51]

- The spin-fluid, or Resonating Valence Bond (RVB), ground state is a quantum ground state.[37,52-57] It features no long-range order and no symmetry breaking. The spins are paired in singlets and the system is a "singlet liquid", represented by contributions from all the possible singlet configurations. It is characterised by a dynamical structure factor and a broad band response in the excitation spectrum with no well identified modes.[58] Numerical analysis[39] has shown that the $q = 0$ and $\sqrt{3} \times \sqrt{3}$ states are not adequate to fully describe the ground state. However, they do represent well the low-lying excited states very close in energy to the ground state.

The introduction of spin-anisotropy, such as easy-axis anisotropy, into the spin system has been shown to cause the weak ferromagnetism usually associated with a slight canting of antiferromagnetic sublattices. In the KHAFM the situation is novel in that this arises in the absence of antiferromagnetic sublattice order even in the z- component of the spins.[59]

2.9.2 Spin-folding

We have already shown that the ground state of the KHAFM is infinitely degenerate, that is to say there are an infinite number of zero-energy modes. The form of these modes is a direct consequence of the geometry of the Kagomé lattice: within any of the possible ground states we can identify loops and lines of alternating spin orientations (ABABAB...), the spins are able to synchronously and continuously rotate through an angle ϕ about the common axis defined by their parameter spins, C, with no energy cost. These defects, or *spin-folds*,[60-62] are non-Abelian in nature, so the resulting spin configuration will depend on the order in which they are produced [*Figure 2.16*]. In this way, repeated local distortions to the spin configuration allow the system to explore its many ground states. There are two classes of spin folds:

- "Open"- where the spin-folds traverse the entire lattice. These are present in spin configurations of uniform spin chirality, e.g. the $q = 0$ configuration [*Figure 2.16(a)*].
- "Closed"- where spin-folds form closed loops. These are present in spin configurations of staggered chirality, e.g. the $\sqrt{3} \times \sqrt{3}$ configuration. The simplest example is the closed "weather-vane" mode [*Figure 2.16(b)*].

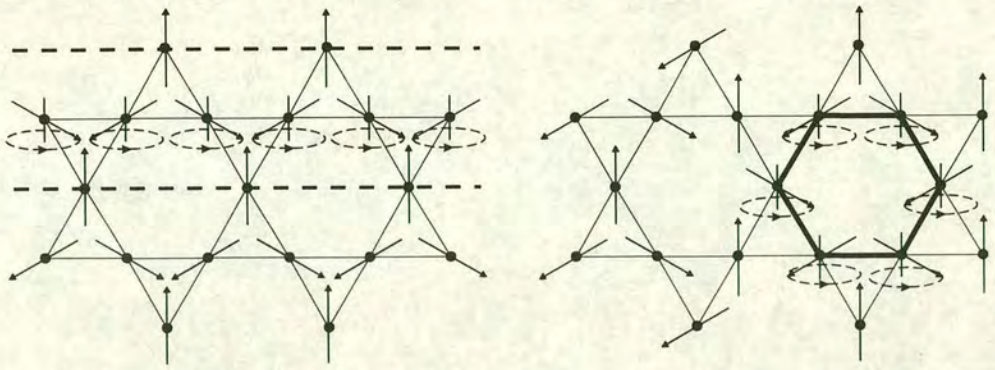

(a) (b)

Figure 2.16. (a) Open-folds traverse the entire lattice in the q = 0 configuration; (b) closed-folds form loops in the √3 x √3 configuration.

The observed spin-glass behaviour seen in experimental KHAFMs is believed to be associated with the binding of these non-Abelian defects.[61] This involves a true lattice symmetry breaking (second order) transition, a KT transition, and is thus accompanied by a specific heat divergence.

While all spin configurations, both coplanar and not, are available through these continuous spin deformations, theory and simulation have shown that coplanar configurations have lower zero-point energies than other non-coplanar configurations.[60,63,64] This creates energy barriers to this type of collective out-of-plane motion. These energy barriers will be further increased by any spin-anisotropy present in the system.

2.9.3 "Order by disorder"

That thermal fluctuations can lead to order, an effect also known as "order by disorder", is a well known idea.[40,65,66] The degeneracy of the ground state manifold can be lifted by thermal or quantum fluctuations, or trivially by the introduction of further neighbour interactions. If the selection of a subset of the large ground state manifold is restrictive enough, long-range order may result, although this is not a necessary result. The dominant classical low temperature configurations are expected to closely resemble whichever ground states have the softest fluctuations. As we have already shown, coplanar ground states (with a nematic axis perpendicular to the plane) are unique in having an entire branch of zero-energy modes. There are fewer such modes in non-coplanar configurations which leads to thermal selection of coplanar states because of their larger entropy.[64]

Spin-wave theory has shown that q = 0 and √3 x √3 Néel orderings are stabilised by second and third-neighbour exchange, the q = 0 state for $J_2 > J_3$ and that of the √3 x √3 state for $J_2 < J_3$ at $T = 0$.[46] At finite T, for the nearest-neighbour system, quantum fluctuations and entropy effects cause the √3 x √3 state to have the lower energy.[46,57,63,67]

Quantum tunnelling between different degenerate ground state configurations will compete with order by disorder selection effects and drive the system towards a superposition of degenerate states, rather than selecting a particular one. There has been found to be a qualitative difference between integer and half-integer systems: integer systems have a non-zero tunnelling amplitude while half-integer systems have zero tunnelling amplitude due to destructive interference between the two topologically distinct tunnelling paths connecting initial and final state.[68,69] These effects are expected to be of similar importance to the order from disorder selection effects and will cause systems with integer spins to have a greater tendency to be disordered.

2.9.4 Dynamical properties and excitations

In the half-integer system the continuous degeneracy of the classical ground state leads to a mode in the spin-wave excitation spectrum which has zero-excitation energy for any momentum transfer, i.e. $\omega(k) \equiv 0$. [46,70,71] There is no gap in the spin-wave spectrum for the half-integer system, while integer spin systems are expected to have a gap in the excitation spectrum.[72] This would again lead to a qualitative difference in the ground state properties of the integer and half-integer systems.

Series expansions of long-range ordered magnetic systems have shown that they are continuously deformable spin systems with no excitation gap in the spin-wave spectrum; this results in the presence of continuous excitations known as Goldstone modes.[67] The KHAFM has been shown to support Goldstone modes, which would lead to a specific heat $C(T) \propto T^2$, consistent with experimental observations.[60]

Numerical studies[73] have shown that the local magnetic field distribution remains discrete under diamagnetic dilution. The magnon distribution is largely unchanged with respect to the non-coplanar ground state except that there is an enhancement of zero-energy modes. Dilution is also found to weaken the tendency towards a nematic state. Dynamical simulations[74] have also shown that the initial relaxation rate of the spin-spin correlation function is nearly independent of the impurity concentration even for the magnetic sublattice population being below the percolation threshold, P_c. This suggests that the dynamics of the Kagomé lattice is mostly governed by local excitations. The relaxation time, τ, is found to monotonically increase with decreasing T which is again consistent with experimental observations.

2.10 The Kagomé lattice: experimental examples

Despite this theoretical interest there has been little experimental work on materials with this form of lattice owing to the lack of suitable model compounds. A transition to a partially disordered ground state was first demonstrated by the anomalous specific heat of ^{3}He adsorbed on graphite; the sharp peak at 2.5mK has only half the entropy change associated with a spin-1/2 antiferrromagnet, i.e. $0.5Rln2$.[37,75,76] Recent experiments on $RCuO_{2.66}$ delafossites,[77] $Cu_9F_2(cpa)_6.xH_3O$ [78] and the organic

radical system (*m*-N-methylpyridinium α-nitronyl nitroxide)•X^- [79] demonstrate that these materials may be example Kagomé antiferromagnets, but as yet there is little investigation of their magnetic properties. The only systems studied in any depth are $SrCr_xGa_{12-x}O_{19}$ [SCGO(x)] and relatives of the jarosite mineralogical family:

2.10.1 $SrCr_xGa_{12-x}O_{19}$ -SCGO(x)

SCGO(x) has the magnetoplumbite structure in which the S = 3/2 Cr^{3+} moments reside in Kagomé layers (12k sites) separated by Ga^{3+} triangular layers (4f and 2a sites) as shown in *Figure 2.17.*[80] The Kagomé layers are 88-95% occupied with the remaining Cr^{3+} being partially substituted into the Ga^{3+} layers complicating the magnetic structure; recent inelastic neutron scattering experiments have shown that there is no effective interaction between the 12k sites and the 4f sites, but there is between the 12k sites and the 2a sites, thus the magnetic structure is best pictured as a three-layer pyrochlore-like slabs of cation sites separated by the triangular 4f layer, rather than a simple Kagomé system.[81] As the system is based on the pyochlore structure it still has a highly degenerate ground state responsible for the low temperature properties.

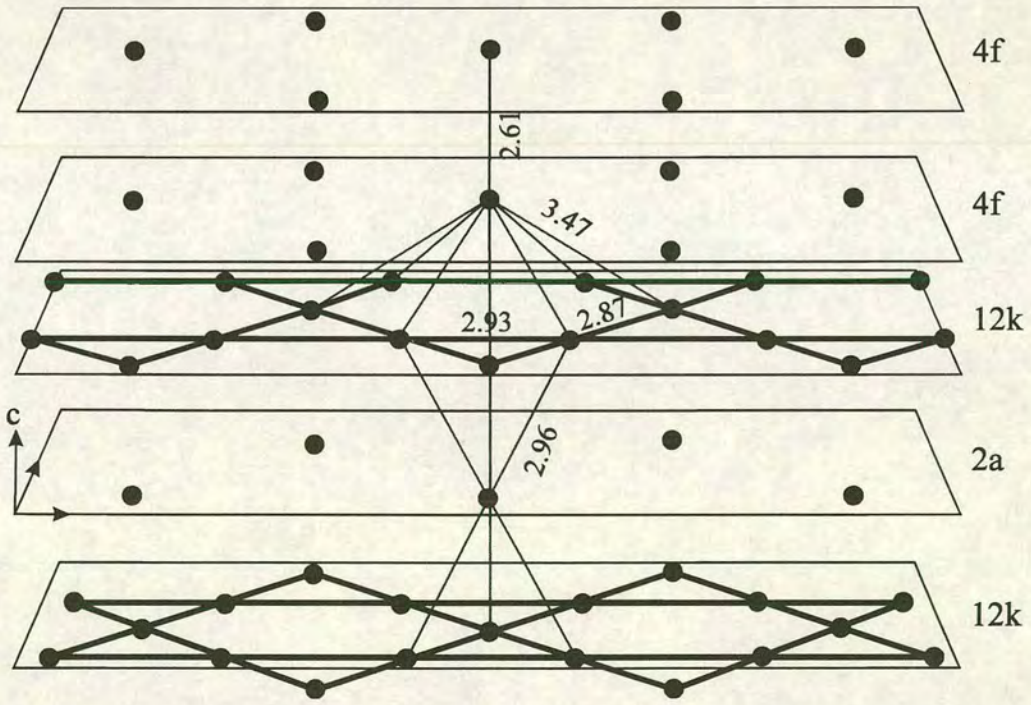

Figure 2.17. Kagomé and triangular magnetic sites in SCGO(x).

The system exhibits strong antiferromagnetic coupling (θ_w is ~ -500K) yet there is no long-range magnetic order down to at least 1.5K; instead, there is a spin-glass transition at 3.5K, and powder neutron scattering measurements reveal a broad feature indicative of short-range antiferromagnetic order, with a wavevector corresponding to the (1 0) reflection of the $\sqrt{3}$ x $\sqrt{3}$ structure (Q = 1.4Å^{-1})

and a correlation length of 7 ± 2Å.[82] The elastic signal at Q = 1.4Å^{-1} has an energy band width of ~20meV and shows a monotonic increase with cooling, this rise is found to occur more suddenly and at a lower temperature, T_f, as the energy resolution is narrowed (T_f= 15K at 0.2meV FWHM, T_f = 5K at 5μeV FWHM).[83,84] Single-crystal dc susceptibility measurements show that below T_f the out of plane components of the spins are frozen but the inplane components are still fluctuating.[85] This is compatible with muon spin relaxation studies which show that even at $T = 0.01T_f$ the system still fluctuates, with a frequency greater than 170MHz.[29,86,87] Specific heat data below T_f do not have the linear T dependence seen in conventional spin-glasses, rather C(T) is proportional to T^2 indicating the presence of long-wavelength excitations, i.e. Goldstone modes.[88,89] Diamagnetic dilution of the Cr^{3+} sites by Ga^{3+} is found to decrease T_f and sharpen the transition, while substitution of Ga^{3+} by Fe^{3+} is found to relieve the frustration and increase T_f.[90,91]

Theory has shown that the introduction of non-magnetic sites in the magnetic sublattice is found to induce non-coplanarity in the ground state. A defect will create a strong local perturbation, but because the system is soft, correlations between these defects will be weak. That is to say, dilution by a non-magnetic material cannot lead to the observed spin-glass behaviour, and the glass-like transition is an intrinsic property of the pure KHAFM.[92]

2.10.2 The jarosite family: $AFe_3(SO_4)_2(OH)_6$

The jarosite family of minerals, with general formula $AFe_3(SO_4)_2(OH)_6$ (where A=Na^+, K^+, Rb^+, Ag^+, Tl^+, NH_4^+, H_3O^+, ½Pb^{2+} or ½Hg^{2+}) appears to supply the best model Kagomé antiferromagnets. We will discuss the structure in detail later, but the essential feature for the magnetic properties is the layers of octahedrally co-ordinated Fe^{3+} ions that lie on the vertices of a Kagomé network. These planes are well separated by further layers of sulphate, hydroxide, and A cations. Synthetically, the jarosite family may be extended by the substitution of Cr^{3+}, In^{3+}, Ga^{3+} for Fe^{3+} or the replacement of the sulphate group by SeO_4^{2-}, or CrO_4^{2-}.

The potassium, ammonium, lead, and sodium iron salts have all been studied by Mössbauer spectroscopy and show a transition T_c ~ 55K.[93-96] Hydronium jarosite, however, displays a transition at ~ 17K to a phase with both static and dynamic signatures, indicated by the presence of both hyperfine-splitting and a paramagnetic doublet.[94] Neutron scattering measurements on the potassium salt show that below T_c there is long-range magnetic order with the in-plane q = 0 structure. The ordered moment is 4.3μ_B at 10K, the remaining moment possesses only short-range order and contributes to a diffuse scattering profile.[95] $KCr_3(SO_4)_2(OH)_6$ has a broad peak in the specific heat at 1.8K with an associated entropy change of 15% Rln4. Neutron diffraction again shows long- and short-range magnetic order below T_f, with an upper limit of 1μ_B on the long-range order. Inelastic neutron scattering indicates the presence of strong spin fluctuations at 0.3K.[97,98] Muon spin relaxation studies show that the spins in $KFe_3(SO_4)_2(OH)_6$ are static below 50K, while quantum fluctuations are believed to cause

$KCr_3(SO_4)_2(OH)_6$ still to fluctuate at 25mK. The application of an external magnetic field did not appreciably alter the response which suggests that the muons are coupled strongly to dynamic fields.[99] It is known that the jarosites have a tendency for the Fe^{3+} sites to be vacated while charge-balance is maintained by protonation of OH^- to form H_2O. This leads to an occupation of the Fe^{3+} sites that is generally significantly less than 100%, typically in the range 83 - 94%, i.e. these jarosites are not good example Kagomé antiferromagnets. An exception is the hydronium salt $(H_3O)Fe_3(SO_4)_2(OH)_6$ which can be prepared with an iron content of ~ 97%.[100] This thesis is primarily concerned with the magnetic properties of hydronium jarosite and its analogues, $(H_3O)Cr_3(SO_4)_2(OH)_6$ and $(H_3O)V_3(SO_4)_2(OH)_6$.

2.11 References

1. '*Solid State Magnetism*', J. Crangle (Edward Arnold, London, 1996).

2. '*Magnetochemistry*', R.L. Carlin (Springer Verlag, Berlin, 1986).

3. '*Magnetic Properties Of Layered Transition Metal Compounds*', ed. L.J. de Jongh. (Klewer, Dordrect, 1990).

4. L.J. de Jongh and A.R. Miedema, Advances in Physics **23**, 1 (1974).

5. '*Statistical Mechanics of Phase Transitions*', J.M. Yeomans (Clarendon Press, Oxford, 1992).

6. '*Magnetic Critical Scattering*', M.F. Collins (Oxford University Press, Oxford, 1989).

7. F. Keffer, H. Kaplan, and Y. Yafet, Am.J.Phys. **21**, 250 (1953).

8. J. van Kranendonk and J.H. van Vleck, Rev.Mod.Phys. **30**, 1 (1958).

9. A.P. Cracknell and A.O. Tooke, Contemp.Phys. **20**, 55 (1979).

10. '*Magnetic Systems with Competing Interactions (Frustrated Spin Systems)*', ed. H.T. Diep (World Scientific Publishing, Singapore, 1994).

11. L.P. Kadanoff, W. Götze, D. Hamblen, R. Hecht, E.A.S. Lewis, V.V. Palciouskas, M. Rayl, and J. Swift, Rev.Mod.Phys. **39**, 395 (1967).

12. K. Hirakawa, H. Ikeda, H. Kadowaki, and K. Ubukoshi, J.Phys.Soc.Jap. **52**, 2882 (1983).

13. A.P. Ramirez, Annu.Rev.Mater.Sci. **24**, 453 (1994).

14. K.H. Fischer, Phys.Stat.Sol.B **116**, 357 (1983).

15. '*Spin glasses: an experimental introduction*', J.A. Mydosh (Taylor & Francis, London, 1993).

16. K. Binder and A.P. Young, Rev.Mod.Phys. **58**, 801 (1986).

17. K.H. Fischer, Phys.Stat.Sol.B **130**, 13 (1985).

18. '*Fractals in Chemistry*', A. Harrison (Oxford University Press, Oxford, 1995).

19. P.W. Anderson, B.I. Halperin, and C.M. Varma, Philos.Mag. **25**, 1 (1972).

20. L.R. Walker and R.E. Walstedt, Phys.Rev.Lett. **38**, 514 (1977).

21. L.R. Walker and R.E. Walstedt, Phys.Rev.B Condens.Matter **22**, 3816 (1980).

22. J.M. Kosterlitz and D.J. Thouless, J. Phys. C: Solid State Phys. **6**, 1181 (1973).

23. J. Villain, J. Phys. C: Solid State Phys. **10**, 4793 (1977).

24. R.I. Bewley and R. Cywinski, *in press* (1996).

25. R. Cywinski and R.I. Bewley, *Conference Proceedings of the IOP Workshop on Magnetic Measurement Techniques* (1992).

26. S.F.J. Cox, J.Phys.C **20**, 3187 (1987).

27. I.A. Campbell, A. Amato, F.N. Gygax, D. Herlach, A. Schenck, R. Cywinski, and S.H. Kilcoyne, Phys.Rev.Lett. **72**, 1291 (1994).

28. A. Keren, P. Mendels, I.A. Campbell, and J. Lord, Phys.Rev.Lett. **77**, 1386 (1996).

29. Y.J. Uemura, A. Keren, L.P. Le, G.M. Luke, B.J. Sternlieb, and W.D. Wu, Hyperfine Interact. **85**, 133 (1994).

30. G. Toulouse and M. Kléman, J.Phys.(Paris) Lett. **37**, 149 (1976).

31. N.D. Mermin, Rev.Mod.Phys. **51**, 591 (1979).

32. M.J.P. Gingras, C.V. Stager, B.D. Gaulin, N.P. Raju, and J.E. Greedan, J.Appl.Phys. **79**, 6170 (1996).

33. J.E. Greedan, M. Sato, X. Yan, and F.S. Razavi, Solid State Commun. **59**, 895 (1986).

34. B.D. Gaulin, J.N. Reimers, T.E. Mason, J.E. Greedan, and Z. Tun, Phys.Rev.Lett. **69**, 3244 (1992).

35. B.D. Gaulin, Hyperfine Interact. **85**, 159 (1994).

36. M.J. Harris, M.P. Zinkin, and T. Zeiske, Phys.Rev.B Condens.Matter **52**, R 707 (1995).

37. V. Elser, Phys.Rev.Lett. **62**, 2405 (1989).

38. C. Zeng and V. Elser, Phys.Rev.B Condens.Matter **42**, 8436 (1990).

39. P. Sindzingre, P. Lecheminant, and C. Lhuillier, Phys.Rev.B Condens.Matter **50**, 3108 (1994).

40. J.N. Reimers, Phys.Rev.B Condens.Matter **45**, 7287 (1992).

41. P. Tomczak, A.R. Ferchmin, and J. Richter, Phys.Rev.B Condens.Matter **54**, 395 (1996).

42. D.M. Deaven and D.S. Rokhsar, Phys.Rev.B Condens.Matter **53**, 14966 (1996).

43. P.W. Leung and V. Elser, Phys.Rev.B Condens.Matter **47**, 5459 (1993).

44. R.R.P. Singh and D.A. Huse, Phys.Rev.Lett. **68**, 1766 (1992).

45. J.B. Marston and C. Zeng, J.Appl.Phys. **69**, 5962 (1991).

46. A.B. Harris, C. Kallin, and A.J. Berlinsky, Phys.Rev.B Condens.Matter **45**, 2899 (1992).

47. J.T. Chalker and J.F.G. Eastmond, Phys.Rev.B Condens.Matter **46**, 14201 (1992).

48. J.N. Reimers and A.J. Berlinsky, Phys.Rev.B Condens.Matter **48**, 9539 (1993).

49. P. Chandra and P. Coleman, Phys.Rev.Lett. **66**, 100 (1991).

50. E.F. Shender and P.C.W. Holdsworth, J.Phys.-Cond. **7**, 3295 (1995).

51. P.C.W. Holdsworth, *personal communication* (1996).

52. P.W. Anderson, Mater.Res.Bull. **8**, 153 (1973).

53. P.W. Anderson, Science **235**, 1196 (1987).

54. P.W. Anderson, G. Baskaran, Z. Zou, and T. Hsu, Phys.Rev.Lett. **58**, 2790 (1987).

55. K. Yang, L.K. Warman, and S.M. Girvin, Phys.Rev.Lett. **70**, 2641 (1993).

56. V. Elser and C. Zeng, Phys.Rev.B Condens.Matter **48**, 13647 (1993).

57. C.L. Henley and E.P. Chan, J.Magn.Magn.Mater. **140**, 1693 (1995).

58. B. Bernu, P. Lecheminant, C. Lhuillier, and L. Pierre, Phys.Scr. **T49A**, 192 (1993).

59. S.T. Bramwell and M.J.P. Gingras, *unpublished work* (1994).

60. I. Ritchey, P. Chandra, and P. Coleman, Phys.Rev.B Condens.Matter **47**, 15342 (1993).

61. P. Chandra, P. Coleman, and I. Ritchey, J.Physique **3**, 591 (1993).

62. A.J. Berlinsky and C. Kallin, Hyperfine Interact. **85**, 173 (1994).

63. A. Chubukov, Phys.Rev.Lett. **69**, 832 (1992).

64. J.T. Chalker, P.C.W. Holdsworth, and E.F. Shender, Phys.Rev.Lett. **68**, 855 (1992).

65. J. Villain, R. Bidaux, J.-P. Carton, and R. Conte, J. Physique , 1263 (1980).

66. C.L. Henley, Phys.Rev.Lett. **62**, 2056 (1989).

67. S. Sachdev, Phys.Rev.B Condens.Matter **45**, 12377 (1992).

68. J. Vondelft and C.L. Henley, Phys.Rev.Lett. **69**, 3236 (1992).

69. J. Vondelft and C.L. Henley, Phys.Rev.B Condens.Matter **48**, 965 (1993).

70. H. Asakawa and M. Suzuki, Inter.J.Mod.Phys.B **9**, 933 (1995).

71. T.C. Hsu and A.J. Schofield, J.Phys.-Cond. **3**, 8067 (1991).

72. H. Asakawa and M. Suzuki, Physica A **198**, 210 (1993).

73. D.L. Huber and W.Y. Ching, Phys.Rev.B Condens.Matter **47**, 3220 (1993).

74. A. Keren, J.Magn.Magn.Mater. **140**, 1493 (1995).

75. D.S. Greywall and P.A. Busch, Phys.Rev.Lett. **62**, 1868 (1989).

76. H. Franco, R.E. Rapp, and H. Godfrin, Phys.Rev.Lett. **57**, 1161 (1986).

77. M.D. Núñez-Regueiro, C. Lacroix, and B. Canals, Phys.Rev.B Condens.Matter **54**, R 736 (1996).

78. M. Gonzalez, F. Cervanteslee, and L.W. Terhaar, Mol.Cryst.Liq.Cryst. **233**, 317 (1993).

79. K. Awaga, T. Okuno, A. Yamaguchi, M. Hasegawa, T. Inabe, Y. Maruyama, and N. Wada, Phys.Rev.B Condens.Matter **49**, 3975 (1994).

80. X. Obradors, A. Labarta, A. Isalgué, J. Tejada, J. Rodriguez, and M. Pernet, Solid State Commun. **65**, 189 (1988).

81. S.H. Lee, C. Broholm, G. Aeppli, T.G. Perring, B. Hessen, and A. Taylor, Phys.Rev.Lett. **76**, 4424 (1996).

82. C. Broholm, G. Aeppli, G.P. Espinosa, and A.S. Cooper, Phys.Rev.Lett. **65**, 3173 (1990).

83. G. Aeppli, S. Lee, C. Broholm, T.G. Perring, M. Adams, C. Carlile, A.D. Taylor, A.P. Ramirez, and B. Hessen, Physica B **213**, 142 (1995).

84. S.H. Lee, C. Broholm, G. Aeppli, A.P. Ramirez, T.G. Perring, C.J. Carlile, M. Adams, T.J.L. Jones, and B. Hessen, Europhys.Lett. **35**, 127 (1996).

85. P. Schiffer, A.P. Ramirez, K.N. Franklin, and S.W. Cheong, Phys.Rev.Lett. **77**, 2085 (1996).

86. A. Keren, L.P. Le, G.M. Luke, W.D. Wu, Y.J. Uemura, Y. Ajiro, T. Asano, H. Kuriyama, M. Mekata, and H. Kikuchi, Hyperfine Interact. **85**, 181 (1994).

87. Y.J. Uemura, A. Keren, K. Kojima, L.P. Le, G.M. Luke, W.D. Wu, Y. Ajiro, T. Asano, Y. Kuriyama, M. Mekata, H. Kikuchi, and K. Kakurai, Phys.Rev.Lett. **73**, 3306 (1994).

88. A.P. Ramirez, G.P. Espinosa, and A.S. Cooper, Phys.Rev.Lett. **64**, 2070 (1990).

89. A.P. Ramirez, G.P. Espinosa, and A.S. Cooper, Phys.Rev.B Condens.Matter **45**, 2505 (1992).

90. B. Martinez, F. Sandiumenge, A. Rouco, A. Labarta, J. Rodriguezcarvajal, M. Tovar, M.T. Causa, S. Gali, and X. Obradors, Phys.Rev.B Condens.Matter **46**, 10786 (1992).

91. B. Martinez, A. Labarta, R. Rodriguezsola, and X. Obradors, Phys.Rev.B Condens.Matter **50**, 15779 (1994).

92. E.F. Shender, V.B. Cherepanov, P.C.W. Holdsworth, and A.J. Berlinsky, Phys.Rev.Lett. **70**, 3812 (1993).

93. M. Takano, T. Shinjo, M. Kiyama, and T. Takada, J.Phys.Soc.Jap. **25**, 902 (1968).

94. A.M. Afanasev, V.D. Gorobchenko, D.S. Kulgawczuk, and I.I. Lukashevich, Phys.Stat.Sol.A **26**, 697 (1974).

95. M.G. Townsend, G. Longworth, and E. Roudaut, Phys.Rev.B Condens.Matter **33**, 4919 (1986).

96. M. Takano, T. Shinjo, and T. Takada, J.Phys.Soc.Jap. **30**, 1049 (1971).

97. A.P. Ramirez, C. Broholm, S.H. Lee, M.F. Collins, L. Heller, C. Kloc, and E. Bucher, J.Appl.Phys. **73**, 5658 (1993).

98. C. Broholm, S.H. Lee, M.F. Collins, L. Heller, A.P. Ramirez, C. Kloc, and E. Bucher, *unpublished work* (1992).

99. A. Keren, K. Kojima, L.P. Le, G.M. Luke, W.D. Wu, Y.J. Uemura, M. Takano, H. Dabkowska, and M.J.P. Gingras, Phys.Rev.B Condens.Matter **53**, 6451 (1996).

100. J. Kubisz, Mineral.Pol. **1**, 47 (1970).

3 Experimental Techniques

3.1 Introduction

Magnetic characterisation of these materials involved the combination of a number of experimental techniques that will briefly be discussed here.

3.1.1 Dc SQUID magnetometry

The molar magnetic susceptibility, χ_m, of a sample expressed in terms of electromagnetic units (emu) per mole is given by:

$$\chi_m[\text{emu}] = \frac{m[\text{emu}]}{H[\text{G}]n[\text{mol}]} \qquad (3.1)$$

where H is the applied field, n is the number of moles of the sample, and m is the magnetisation of the sample.

One of the most sensitive methods for measuring m is to use a magnetometer based on the Superconducting QUantum Interference Device (SQUID). The SQUID itself is a superconducting circuit which is broken by two thin layers of an insulating material, these links are called Josephson junctions.[1,2] A supercurrent flowing across the SQUID divides at W, part going *via* X and part going *via* Y, and then recombines at Z [*Figure 3.1*]. Application of a magnetic field at one Josephson junction (X) alters the phase of the supercurrent wavefunction tunnelling through it. At Z the two supercurrents combine and interference results from their different phases. Application of a magnetic field varies the phase-angle across the Josephson junction and creates an interference pattern with a form that is very sensitive to the magnitude of the magnetic field at X. The SQUID amplifier then converts this pattern into an output voltage that is directly proportional to the applied magnetic field.

The dc SQUID used for these experiments was the $MPMS_2$ manufactured by Quantum Design.[3,4] Its detection coils consist of a single piece of superconducting wire wound in a second-derivative configuration: the upper and lower single turns are counterwound with respect to a two-turn centre coil. This detector configuration is used in conjunction with a Mu-metal environmental shield to reduce any disturbance from nearby magnetic sources. The detection coils form part of a superconducting loop which is wrapped around one Josephson junction of the SQUID. As the sample moves through the detection coils the electronic current induced in the loop changes. Thus, the persistent current in the detector loop varies as the sample is moved. During a scan the sample is stopped in a number of positions and the SQUID voltage sampled. The measured SQUID response then corresponds to an output voltage as a function of the sample position and is fitted to a theoretical

expression to give a very accurate value of the magnetisation. In order to measure a sample it must possess a net magnetisation; this is induced by a measuring field of up to ± 10,000G (1 Tesla). The $MPMS_2$ has an error in the field of ± 1G and a zero-field which is < 5G. The standard temperature range used in these measurements was 1.8 - 330K.

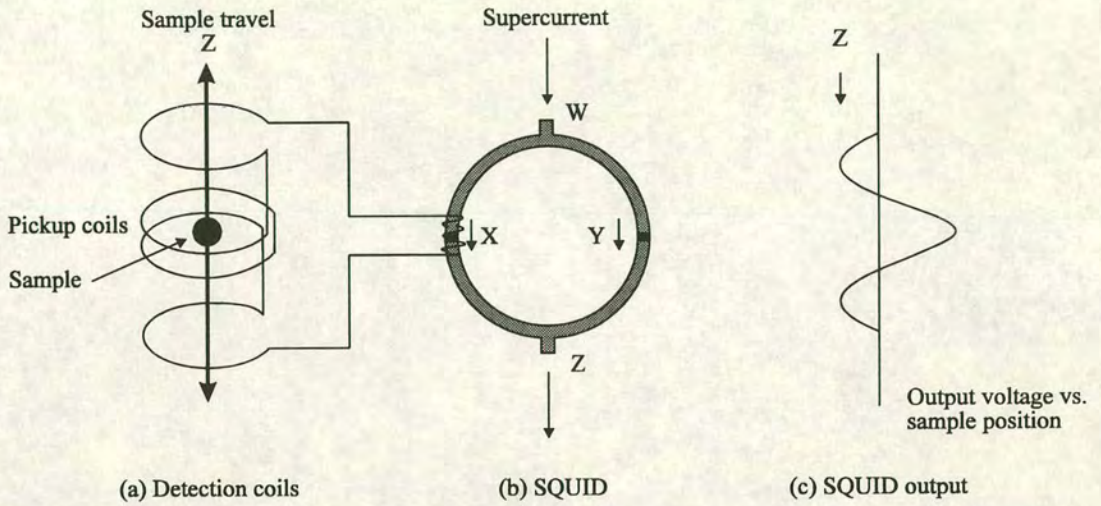

Figure 3.1. Schematic diagram of the $MPMS_2$ SQUID magnetometer showing: (a) second-derivative coil configuration; (b) the SQUID junction; (c) the SQUID response signal.

3.1.2 Ac magnetometry

Measurements of the linear susceptibility made using *Equation (3.1)* assume that the magnetisation, *m*, is directly proportional to the applied field *H*. Ac susceptibility does not require this assumption; instead one measures directly:

$$\chi_{ac} = \left(\partial m/\partial H\right)_T \qquad (3.2)$$

This technique involves the application of a small sinusoidal magnetic field (typically with a frequency ω = 10 - 20,000Hz) to the sample and measuring the modulation in the magnetisation.[5] The magnetic properties may further be examined by the application of a larger dc bias field. If the frequency of the modulation is of the same order as that of the dynamics of the magnetic system energy exchange can occur, and this will lead to an absorptive part to the susceptibility. Hence ac susceptibility is a complex quantity:

$$\chi_{ac} = \chi' + i\chi'' \qquad (3.3)$$

Measurements are made of the real (dynamic) and imaginary (absorptive) parts of χ_{ac}, i.e. χ' and χ'', as functions of field, temperature, and frequency [*Section 2.6.4*].

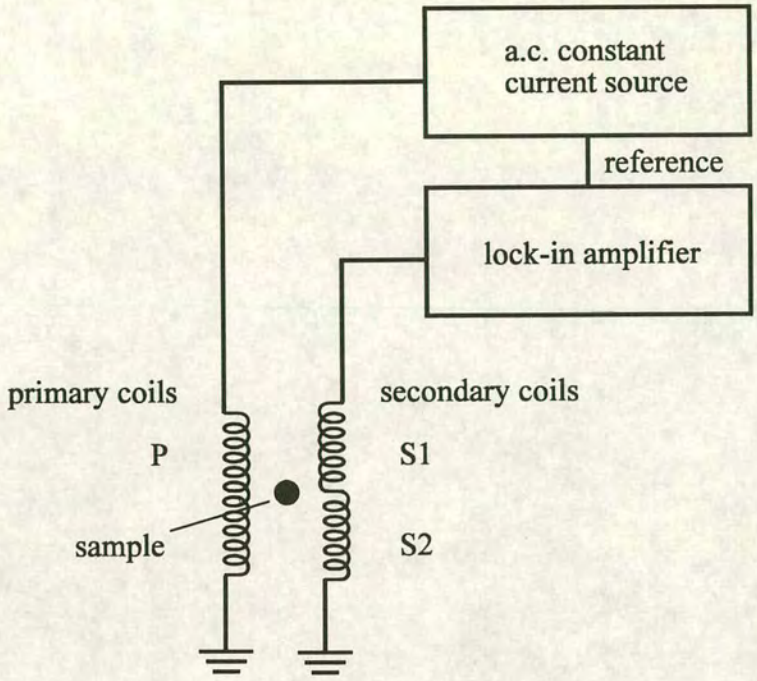

Figure 3.2. Schematic diagram of an ac magnetometer.

Actual magnetometers are based on a Hartshorn bridge with the secondary pickup coil (*S1*) and the compensation coil (*S2*) wound in opposition over a primary coil (*P*) [*Figure 3.2*]. In the absence of a sample the bridge is balanced. A sample induces an out-of-balance signal which is directly proportional to χ_{ac}. The in-phase and out-of-phase components of the out-of-balance voltage represent χ' and χ'' respectively, and are measured simultaneously with a two-phase lock-in amplifier.

The ac susceptibility measurements were performed at the University of Toronto by Dr. S.A.M. Mentink and Prof. T.E. Mason using a magnetometer with a primary coil (760 turns) and a secondary coil composed of two counterwound coils (1475 and 1495 turns). The two-phase lock-in amplifier used was a Stanford Research Systems Model SR830.

3.1.3 Specific heat

The specific heat, C_v, at constant volume is defined by:

$$C_v = \left(\frac{\partial U}{\partial T}\right)_V \qquad (3.4)$$

Where ∂T is the change in temperature brought about by the change in the internal energy ∂U. This is determined by measuring the temperature change produced by the application of a known quantity of energy, at constant volume.

The specific heat measurements were performed at the University of Toronto by Dr. S.A.M. Mentink and Prof. T.E. Mason using a vacuum calorimeter.[6]. The sample is mounted on a sapphire backing plate. The unit is then suspended by nylon fibres in a vacuum-tight brass container. Manganin leads are used to connect to the heater coil and a RuO_2 resistive temperature sensor. A pumped ^3He system (Heliox ^3He sorption refrigerator cryostat, Oxford Instruments) was used to cool the sample to 0.41K. Known quantities of heat are applied to the coil by passing known currents for definite intervals of time and the resulting temperature increase is measured.

3.1.4 Neutron diffraction

The relative merits of neutron and X-ray diffraction for structure determination are well known.[7-9] The scattering of X-rays by electrons leads to a rapid increase in scattering amplitude with atomic number, but also a decrease with increasing scattering angle, according to a form-factor defined as the Fourier transform of the density of the scattering species. Neutrons are scattered by nuclei, which act as point scatters, and so suffer no such attenuation. The complex variation of the neutron scattering length with atomic number allows different isotopes of the same element to be distinguished and light atoms to be located in the presence of heavy atoms. Neutrons have a spin of 1/2 and so have a magnetic moment that can interact with the local magnetic fields arising from the spin and orbital angular momenta of unpaired valence electrons in the sample. This also allows neutron diffraction to probe magnetic structure.

After thermalisation with a hot or a cold moderator, neutrons produced from a nuclear fission reactor have energies of 5 - 50meV (λ = 1.5 - 4Å [*Equation 3.5*]) and are ideal for the study of interatomic spatial correlations. The energy of these neutrons is comparable to the quanta of lattice vibrations (phonons) and magnetic excitations (magnons) allowing investigations of both static and dynamic phenomena.[10,11]

$$1meV \triangleq 0.24THz \triangleq 11.61K \triangleq 81.81/\lambda^2 \qquad (\lambda \text{ in Å}) \qquad (3.5)$$

Spallation sources create neutrons by accelerating high energy protons into a heavy metal target (such as tungsten or uranium) which results in a pulse of white neutrons. These sources have very high fluxes but they extend only to very short pulses. Despite this apparent limitation, spallation sources have a count rate (at a specified resolution) that is nearly 2 orders of magnitude higher than for the equivalent thermal flux at a reactor source.[12] Analysis of diffraction data is based on time-of-flight (TOF) methods.[13,14] The TOF experiments were performed using the POLARIS diffractometer at the ISIS Facility of the Rutherford Appleton Laboratory. The diffractometer has a number of counters at fixed

angles, θ, the Bragg condition for a particular d-spacing of reflection, d, will be satisfied by the time-of-flight according to:

$$2d \sin\theta = n\lambda = \frac{ht}{mL} \qquad (3.6)$$

Where t is the time of flight, m is the neutron mass, h is Planck's constant, and L is the total length of the flight path (moderator to the sample).

In a reactor-based double-axis diffraction experiment, a particular λ is selected from those emanating from the moderator by diffraction from a chosen lattice plane in a monochromator crystal. The detector is swept through 2θ and detects the reflections. This is termed a double-axis spectrometer as there are two points at which the neutrons change momentum- the monochromator and the sample [*Figure 3.3*]. Double-axis diffractometers used were: D1B and D2B at the Institut Laue-Langevin, and C2 at Chalk River Laboratories, Atomic Energy of Canada Ltd. (AECL), Ontario.

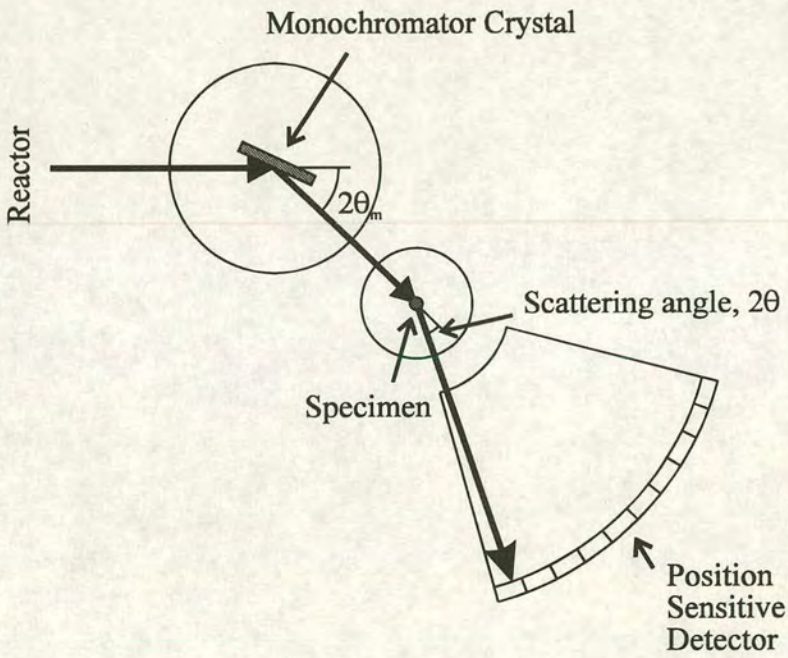

Figure 3.3. Schematic diagram of the C2 double-axis diffractometer, Chalk River Laboratories.

It is also possible to use neutron scattering to probe excitations such as magnons and phonons in a material by determining the energy of scattered neutrons relative to that of incident neutrons, and this in turn requires a third crystal called the analyser to select the wavelength of the scattered neutrons. To do this one either fixes the monochromator and the incident energy, E_i, and then moves the analyser relative to the detector to measure the different final energies, E_f, or one fixes E_f and varies E_i. This is

termed a triple-axis experiment and is displayed schematically in *Figure 3.4.* The triple-axis spectrometer used was the N5 spectrometer at Chalk River Laboratories.

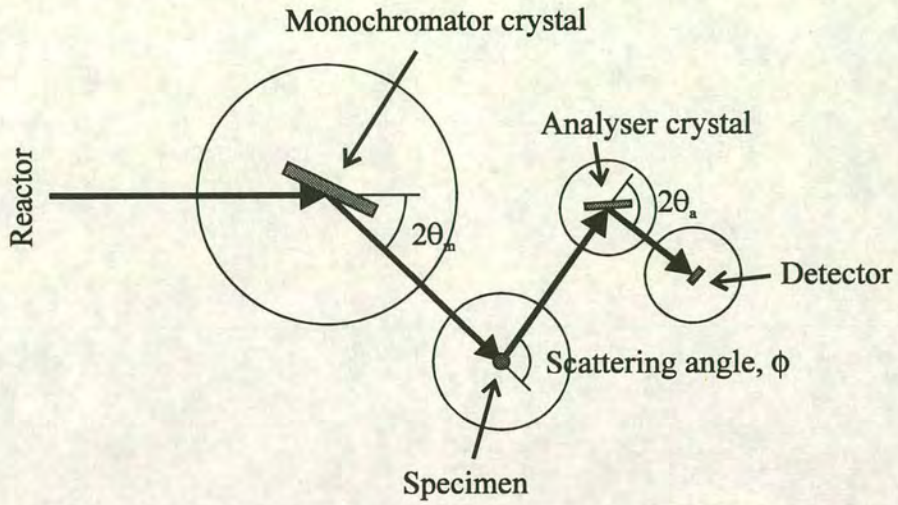

Figure 3.4. Schematic diagram of the N5 triple-axis diffractometer, Chalk River Laboratories.

3.1.5 Rietveld refinement

The overlap of reflections reduces the information contained in a powder diffraction pattern and makes harder the determination of the structure factor amplitude, F_{hkl}^2, for each reflection. In the Rietveld method, direct analysis of the profile intensities allows the maximum amount of information to be extracted from a powder diffraction pattern.[15-18] As no effort is made to resolve contributions from individual Bragg reflections a reasonably good starting model is required and Rietveld analysis is one of structure *refinement*. This model includes parameters that describe the crystal structure, background and also instrumental characteristics, such as the zero-point error. Refinement involves minimisation of the residual S_y:

$$S_y = \sum w_i \left(y_{obs}^i - y_{calc}^i \right)^2 \qquad (3.7)$$

where y_{obs}^i and y_{calc}^i are the observed and calculated intensities of each data point, w_i is the weighting parameter for each data point ($w_i \propto 1/ y_{obs}^i$), and the sum is carried out over all data points where y_{obs}^i is greater than 1% of the peak height. Because the residual function is non-linear the least-squares process is also non-linear. Thus, the refinement is an iterative procedure in which the calculated shifts are applied to the model's parameters in order to produce a improved model and the whole procedure is repeated again. If the starting model is inappropriate the non-linear least-squares procedure will not lead to a global minimum and the procedure will either diverge or lead to a false minimum. The

refinement is carried out until the best fit is obtained between the observed powder pattern and the calculated pattern. This is quantitatively determined by a number of R-factors of which the R_{wp}, 'the R-weighted pattern', is the most meaningful as the numerator of the residual is minimised with respect to the observed intensity. A 'goodness of fit' parameter χ^2 is also useful for watching the refinement progress. These functions are defined as:

$$R_{wp} = \sqrt{\frac{\sum w_i \left(y_{obs}^i - y_{calc}^i\right)}{\sum w_i \left(y_{obs}^i\right)^2}} \qquad (3.8)$$

$$\chi^2 = \frac{\sum w_i \left(y_{obs}^i - y_{calc}^i\right)^2}{N_{obs} - N_{\text{var}}} \qquad (3.9)$$

where N_{obs} is the number of observables and N_{var} is the number of variables to be fitted. While these numerical criteria are important, the refined model should always make chemical sense and attention should always be paid to what the fit is graphically like: a difference plot will show whether an inflated R_{wp} is a result of a poor structural model or a failure to describe other experimental factors. It should be noted that the estimated standard deviations (esd) values are not experimental errors in the traditional sense; they represent the minimum probable error arising solely from random errors in the refinement.

Rietveld method for this work was carried out using version 6 of the PC translation of the General Structure Analysis System (GSAS).[19] This package can simultaneously refine multiple phases (both crystal and magnetic) and multiple data sets collected from X-ray and/or neutron diffraction. An excellent introduction to Rietveld analysis is given in the book by Young[15], and the details of the sequence in which refined parameters are introduced will not be described unless it is instructive to do so.

3.1.6 Muon Spin Relaxation (MuSR)

The positive muon (μ^+) behaves as a light proton (its mass is ~ 0.11 that of a proton); it has a lifetime of 2.2μs after which it decays according to the scheme:

$$\mu^+ \rightarrow e^+ + \bar{\nu}_e + \nu_\mu \qquad (3.10)$$

where e^+ is a positron, and $\bar{\nu}_e$ and ν_μ are the neutrinos associated with the electron and the muon respectively.[20] Muons are polarised either parallel or antiparallel to their direction of propagation.[21] The positrons will be preferentially emitted along the muon spin axis with the probability of positron emission, $w(\theta)$, at an angle θ between the muon spin and the positron trajectory given by:

$$w(\theta) = 1 + a_0 \cos\theta \qquad (3.11)$$

The anisotropy a_0 depends on the energy selection of the positrons. If only positrons with the maximum possible energy are recorded the anisotropy is at a maximum, a_0 = 1. If positrons of all energies are accepted a_0 = 1/3. The positrons possess sufficient energy to be able to leave the sample and are detected using scintillation counters.

The acronym MuSR is used to refer to a number of different muon experiments: muon spin resonance, muon spin relaxation and muon spin rotation. In this work it will be used to describe only muon spin *relaxation*.[21-23] In a MuSR experiment polarised muons are directed towards and implanted in a sample. Due to its positive charge the muon will normally come to rest at an interstitial site, generally similar to that for localisation of a proton. If the implanted muons experience any static magnetic field ,B_μ, that is not parallel to their polarisation they will begin to precess around it with the corresponding Larmor frequency ω_μ:

$$\omega_\mu = \gamma_\mu B_\mu \qquad (3.12)$$

where γ_μ is the muon gyromagnetic ratio ($\gamma_\mu/2\pi$ = 13.554 kHz G^{-1}).

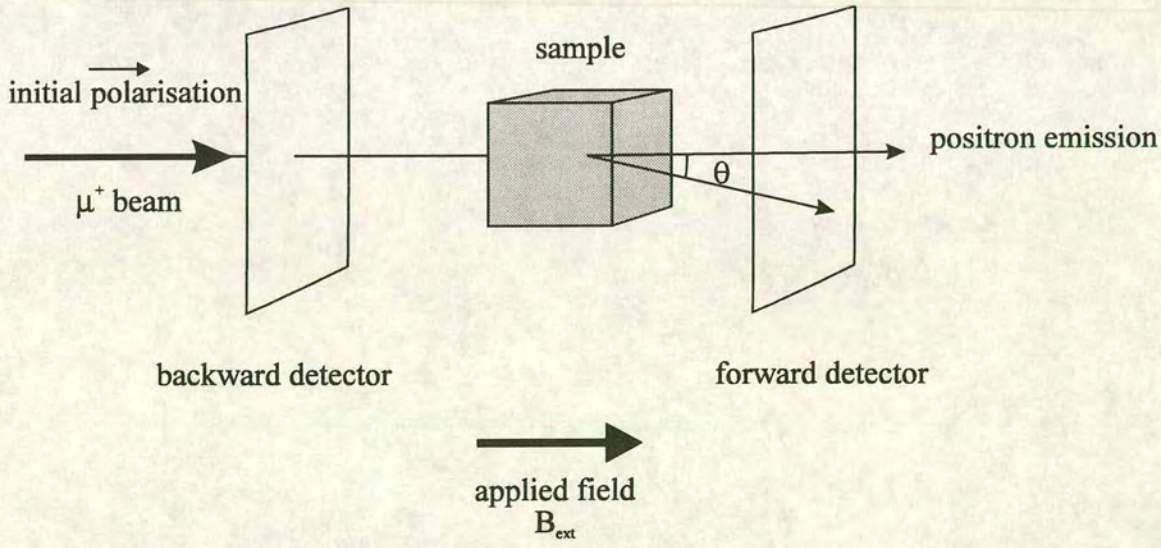

Figure 3.5. Schematic experimental set-up for muon spin relaxation in the longitudinal field geometry.

In a MuSR experiment, muons are polarised in the direction of the muon beam (now taken as the z-axis) and one measures the longitudinal relaxation (or depolarisation) function $G_z(t)$. $G_z(t)$ is obtained

by measuring the numbers of positrons emitted in the forward and backward directions (with respect to the muon spin-direction [*Figure 3.5*]):

$$G_z(t) \propto \frac{F(t) - \alpha B(t)}{F(t) + \alpha B(t)} \qquad (3.13)$$

where α is an experimental calibration factor which accounts for the different characteristics of forward and backward detectors, and t is the time elapsed after muon implantation. If the muons adopt equivalent sites within the lattice and experience identical local fields, the spin ensemble will precess in-phase with a unique angular frequency. However, a distribution of local fields will cause a range of precession frequencies and a depolarisation (dephasing) of muon spins as they precess. This is seen as a loss of amplitude of $G_z(t)$ with time. The larger the frequency distribution of muons, the more rapid the depolarisation. A slow relaxation of magnetic moments within the sample will again lead to a depolarisation. Thus, $G_z(t)$ describes the time dependence of the muon spin-depolarisation and the particular physical parameters which cause the depolarisation. Some of the relaxation functions that are used to describe $G_z(t)$ and characterise the spatial and temporal variations of these local fields are described in *Sections 2.6.4* and *4.5.5*.

The MuSR experiments were performed using the EMU spectrometer at the Rutherford Appleton Laboratory.

3.2 References

1. '*Solid State Magnetism*', J. Crangle (Edward Arnold, London, 1996).

2. J. Clarke, Scientific American, August, 36 (1994).

3. '*MPMS2 User Manual*', Quantum Design (Quantum Design, San Diego, 1991).

4. '*Fundamantals of Magnetism and Magnetic Measurements Featuring Quantum Design's Magnetic Property Measurement System*', M. McElfresh (Quantum Design, San Diego, 1994).

5. R. Cywinski and R.I. Bewley, *Conference Proceedings of the IOP Workshop on Magnetic Measurement Techniques* (1992).

6. '*Specific Heats at Low Temperatures*', E.S.R. Gopal (Heywood Books, London, 1966).

7. '*Neutron Diffraction*', G.E. Bacon (Clarendon Press, Oxford, 1975).

8. '*Neutron Diffraction*', ed. H. Dachs. (Springer Verlag, Berlin, 1978).

9. '*Introduction to the Theory of Thermal Neutron Scattering*', G.L. Squires (Cambridge University Press, Cambridge, 1978).

10. '*Theory of Neutron Scattering from Condensed Matter, Volume I*', S.W. Lovesey (Clarendon Press, Oxford, 1986).

11. '*Theory of Neutron Scattering from Condensed Matter, Volume II*', S.W. Lovesey (Clarendon Press, Oxford, 1986).

12. C.G. Windsor, *AIP Conference on Neutron Scattering- 1981* (1982).

13. '*Chemical Crystallography with Pulsed Neutrons and Synchrotron Radiation*', H. Fuess (NATO Advanced Study Institute, 1987).

14. C.G. Windsor, Methods Exp.Phys. **23**, 197 (1986).

15. '*The Rietveld Method*', ed. R.A. Young (Oxford University Press, Oxford, 1995).

16. A.K. Cheetham and J.C. Taylor, J.Solid State Chem. **21**, 253 (1977).

17. H.M. Rietveld, J.Appl.Cryst. **2**, 65 (1969).

18. H.M. Rietveld, Acta Cryst. **22**, 151 (1967).

19. '*GSAS General Structure Analysis System*', A.C. Larson and R.B. von Dreele (LANSCE, Los Alamos National Laboratory, Los Alamos, 1994).

20. '*The Forces of Nature*', P.C.W. Davies (Cambridge University Press, Cambridge, 1988).

21. '*Muons and Pions in Materials Research*', ed. J. Chappert and R.I. Grynszpan (Elsevier Science Publishers, Amsterdam, 1984).

22. S.F.J. Cox, J.Phys.C **20**, 3187 (1987).

23. '*The Muon Data Analysis Program RUMDA*', S.H. Kilcoyne (Daresbury and Rutherford Appleton Laboratory, Didcot, 1994).

4 Experimental Kagomé Antiferromagnets: $S = 5/2$

4.1 Introduction

The members of the jarosite mineral family are of great interest to mineralogists as common minerals found in diverse environments ranging from the Antarctic[1] and Scandinavia,[2] to the locality that they are named after- the Jaroso ravine in Sierra Almagrera, Spain.[3] Considerable synthetic effort has been devoted to reproducing the conditions for jarosite formation [*Table 4.1.*] and in the study of the incorporation of impurity ions. Interest is further fuelled by their importance as metal ores, particularly of silver,[4,5] and in metallurgical industries where their formation provides a highly efficient method for the precipitation of iron from hydrometallurgical processing solutions with minimal loss of valuable commercial ions such as Cu^{2+} or Zn^{2+}.[6]

The jarosites are members of a more general mineralogical family called the alunites; alunite itself has the formula $KAl_3(SO_4)_2(OH)_6$. The alunite crystal structure is able to accommodate a variety of ions with a large range of ionic radii. This results in the natural materials occurring as a solid-solution of the different family members. Synthetically, the jarosite family can be extended to include rubidium, thallium, and mercury salts;[7] the sulfate group can be replaced by SeO_4^{2-} or CrO_4^{2-}; or other trivalent cations can be substituted for the Fe^{3+} ions, e.g. Ga^{3+} , In^{3+}, and Cr^{3+}.[6] This work includes the synthesis of $(H_3O)V_3(SO_4)_2(OH)_6$ [*Section 6.2*], and so further increases the range of materials available by substitution of these ions into the jarosite relatives. Materials based on the alunite structure not only provide examples of $S = 5/2$, 3/2, and 1 Kagomé systems, but the selection of the other ions in the structure allows us to deliberately tune the strength of the interactions between magnetic layers, and so further examine the properties of the Kagomé antiferromagnet.

Formula	*Chemical Name*	*Mineral Name*
$(H_3O)Fe_3(SO_4)_2(OH)_6$	hydronium jarosite[8-10]	hydronium jarosite (formally known as carphosiderite)
$NaFe_3(SO_4)_2(OH)_6$	sodium jarosite[8,9]	natrojarosite
$KFe_3(SO_4)_2(OH)_6$	potassium jarosite[8,9,11-14]	jarosite
$RbFe_3(SO_4)_2(OH)_6$	rubidium jarosite[7,11]	no mineral equivalent
$AgFe_3(SO_4)_2(OH)_6$	silver jarosite[8,11]	argentojarosite
$(NH_4)Fe_3(SO_4)_2(OH)_6$	ammonium jarosite[8]	ammoniojarosite
$Tl_{0.5}Fe_3(SO_4)_2(OH)_6$	thallium jarosite[7]	no mineral equivalent
$Pb_{0.5}Fe_3(SO_4)_2(OH)_6$	lead jarosite[8,11]	plumbojarosite
$Hg_{0.5}Fe_3(SO_4)_2(OH)_6$	mercury jarosite[7,8]	no mineral equivalent

Table 4.1. Chemical and mineral names of the jarosites. References are to synthetic procedures.

4.2 The alunite structure

Before a discussion of the synthetic details, it is useful to briefly discuss the major points of the alunite crystal structure. A much more detailed discussion of the structure of hydronium jarosite will be left until *Section 4.6*. Alunite belongs to the rhombohedral space group $R\bar{3}m$ and the crystal structure determined from single-crystal X-ray diffraction from a natural sample is displayed in *Figure 4.1*.[15] This structure is adopted by all the jarosites except plumbojarosite, in which segregation of the Pb^{2+} ions into alternately vacant and filled sites (actual occupancies are 0.04 and 0.96 respectively) causes the c-axis to be doubled; the remainder of the structure has no gross distortions away from the alunite structure.[16]

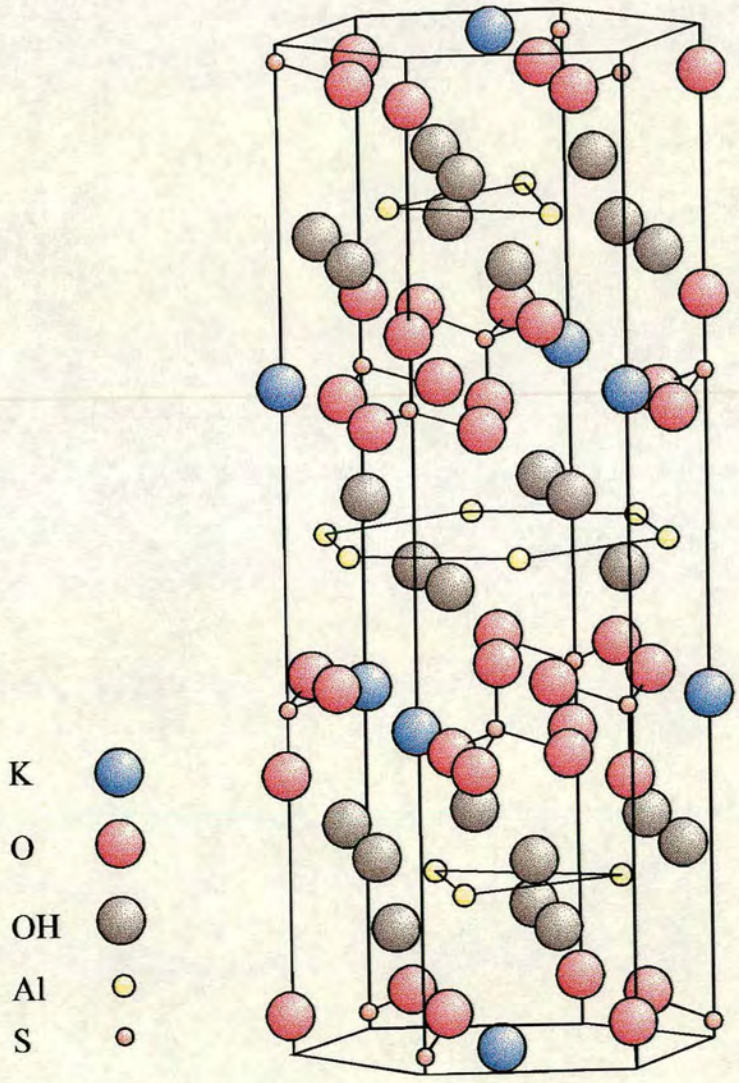

Figure 4.1. The crystal structure of alunite- $KAl_3(SO_4)_2(OH)_6$

In the alunite structure, the Al^{3+} ions are co-ordinated by a distorted octahedron of four hydroxy and two sulfate oxygen atoms. These octahedra are joined by corner sharing to form the Kagomé net [*Section 4.5.4*]. The K^+ ions occupy 12-co-ordinate sites within sulfate layers.[15,17]

It is well known that the jarosites are prone to non-stoichiometry with up to 80% of the A cations being replaced by H_3O^+. The low relative concentration of ferric ions in the reaction solution results in a deficiency of Fe^{3+}; charge balance is maintained by protonation of the hydroxy groups to form H_2O.[9] This leads to an occupation of Fe^{3+} sites that is generally less than 100%, and typically in the range 83 - 93%. An exception is the hydronium salt which can be prepared with an iron content of ~ 97%.[8,9]

4.3 The mechanism of jarosite formation

Jarosite precipitates are the result of the hydrolysis of strongly acidic (pH 0.5 - 2)[8,18] solutions of Fe^{3+}, sulfate and the relevant A cation. The yield and stoichiometry of this low-temperature hydrothermal reaction depends markedly on the reaction temperature; equilibration times range from several months at room temperature,[13] to several hours at higher temperatures.[8,9] If the reaction temperature is above 180°C, or the solution too basic, the reaction results in the formation of an amorphous iron hydroxysulfate identified as $Fe_4(OH)_{10}SO_4$.[19,20]

The microscopic mechanism for hydronium, and potassium jarosite precipitation has been studied by spectrophotometry and potentiometric titrations to give the equilibrium constants of various complex species present in solution.[21] At low temperatures, the dominant reaction species were found to be $FeSO_4^+$ and $FeOH^{2+}$. With increasing temperature the hydrolysis equilibrium moves towards the hydroxy products and the relative concentration of $Fe(OH)_2^+$ rises; at 80°C this species exceeds the concentration of the primary hydrolysis product $FeOH^+$ which suggests that the dominant reaction species under our reaction conditions are $Fe(OH)_2^+$ and $FeSO_4^+$. Further work[20,22] indicates that the primary building block in these reactions is $Fe(OH)_2^+$ and that the chemical formula of the hydronium jarosite product is best described as $H_3O[Fe(OH)_2]_3(SO_4)_2$. Protons are released in these hydrolysis reactions and cause the pH of the solution to fall, thus retarding the formation of further product. The sulfate concentration also influences the hydrolysis reactions of the Fe^{3+} ion, and so the concentration of $Fe(OH)_2^+$, again affecting the rate of precipitation. One consequence of this reaction pathway is that the product crystallites are commonly small, ~ 10μm.[14]

4.4 Synthesis

The preparations for this work were based on established thermodynamic routes, but in order to maximise the reproducibility of these low pH solutions no pH adjustment was made to the reactant solution in any of these preparations. Instead the pH was controlled using the hydrolysis reactions and thus the concentration of Fe^{3+} in solution.

Preliminary syntheses of jarosites, for characterisation by X-ray diffraction and SQUID magnetometry, were carried out in sealed Pyrex ampoules with an outside diameter of 17mm. This size provided a convenient reaction volume, 15ml, and ampoules that were still easy to seal. The larger samples required for neutron diffraction experiments were prepared in a PTFE-lined stainless-steel bomb manufactured at the Departmental mechanical workshop with a reaction volume of 300ml. The reaction-vessels were heated in a precision furnace (Pekin Elmer) with a temperature stability of ± 0.5°C. All of the experimental data that follow were collected from the appropriate neutron samples.

S and H (or D) contents were determined by elemental combustion analysis, while the metal content was determined by using an Atomscan atomic absorption spectrometer (Thermoelectron) equipped with an argon plasma torch, and solutions prepared by boiling the sample in concentrated HCl to which a small amount of concentrated HNO_3 had been added. The O content was then deduced by subtraction, and the overall stoichiometry determined with the assumption that the S content is stoichiometric.[16] The principal error arises from the metal analysis ± 1.0 wt.% and these are worked through to give the error in the coverage of the Fe sites.

The elemental compositions and stoichiometries of the jarosites used for neutron diffraction are displayed in *Table 4.2*. Any compositional data available from neutron diffraction has also been included.

Idealised formula	*Elemental composition/ wt.%*	*Stoichiometric formula*	*Magnetic occupation of Kagomé Lattice*
$(H_3O)Fe_3(SO_4)_2(OH)_6$	2.1 H, 34.2 Fe, 13.7 S, 50.0 O	$Fe_{2.84}H_{9.77}S_{2.00}O_{14.56}$	95 ± 4%, 97.3 (6)%*
$(D_3O)Fe_3(SO_4)_2(OD)_6$	1.7 D, 36.5 Fe, 13.8 S, 48.0 O	$Fe_{3.03}D_{3.87}S_{2.00}O_{13.92}$	101 ± 4, 94.8 (9)%*
$(D_3O)Fe_{3-x}Al_x(SO_4)_2(OD)_6$	3.8 D, 30.7 Fe, < 0.9 Al, 13.2 S, 51.4 O	$Fe_{2.67}Al_{0.15}D_{9.2}S_{2.00}O_{15.58}$	89 ± 3%
$NaFe_3(SO_4)_2(OD)_6$	3.5 D, 32.9 Fe, 13.2 S, 2.8 Na, 47.6 O	$Fe_{2.86}Na_{0.59}D_{8.50}S_{2.00}O_{14.5}$	95 ± 4%
$(ND_4)Fe_3(SO_4)_2(OD)_6$	4.4 D, 32.9 Fe, 13.8 S, 2.0 N, 46.9 O	$Fe_{2.74}N_{0.66}D_{10.23}S_{2.00}O_{13.63}$	91 ± 3%
$AgFe_3(SO_4)_2(OD)_6$	2.6 D, 27.2 Fe, 11.6 S, 6.0 Ag, 52.6 O	$Fe_{2.68}Ag_{0.31}D_{14.44}S_{2.00}O_{18.12}$	89 ± 3%
$RbFe_3(SO_4)_2(OD)_6$	3.1 D, 28.3 Fe, 12.4 S, 9.4 Rb, 46.8 O	$Fe_{2.62}Rb_{0.57}D_{8.02}S_{2.00}O_{15.13}$	87 ± 3%

*Table 4.2. Elemental compositions of neutron samples; * refers to values determined by neutron diffraction with estimated standard deviations shown in brackets.*

X-ray diffraction of the synthesised materials showed no evidence of any crystalline impurity phases or unreacted starting materials. There was also no evidence of red amorphous iron hydroxy sulfate contaminant and the precipitates all had the characteristic rapid settling time of the jarosites.[6]

4.4.1 Synthesis of $(H_3O)Fe_3(SO_4)_2(OH)_6$

The synthesis of $(H_3O)Fe_3(SO_4)_2(OH)_6$ used was based on an established route,[9] but no pH adjustment was made of the reactant solution. 40.000g of $Fe_2(SO_4)_2.nH_2O$ (Aldrich 97%) were dissolved in

deionised water and made up to 300ml. The reaction solution was heated in a PTFE-lined stainless-steel bomb at 140°C for 4 hours. The jarosite precipitate was washed three times with deionised water and dried well at 120°C for 2 hours. The resulting ochre powder was finely ground and the mass of the final product was 1.83g.

4.4.2 Synthesis of $(D_3O)Fe_3(SO_4)_2(OD)_6$

Partially deuterated hydronium jarosite was prepared by dissolving 40.000g of $Fe_2(SO_4)_2.nH_2O$ in D_2O (CDN Isotopes 99.9 atom % D) and the solution was made up to 300ml. The hydrolysis reactions were found to be subject to a kinetic isotope effect so the reaction was carried out in a PTFE-lined stainless-steel bomb at the elevated temperature of 155°C, for 4 hours. The jarosite precipitate was washed three times with D_2O and dried well at 120°C for 2 hours. The resulting ochre powder was finely ground and the mass of the final product was 2.61g. The low measured deuterium content in the product is most likely a consequence of isotopic exchange with the atmosphere.

4.4.3 Synthesis of $(D_3O)Fe_{3-x}Al_x(SO_4)_2(OD)_6$

Most jarosites suffer from an occupation of magnetic sites that is significantly less than 100%. Hydronium jarosite presents an ideal opportunity to examine the effects of deliberately reducing the magnetic coverage. Previous work has shown that reducing the reaction temperature has an effect on the iron content of the jarosite. For this reason the synthesis was carried out at a reduced temperature, 110°C. $Al_2(SO_4)_3.18H_2O$ was also introduced to reduce the partial iron concentration. Chemical analysis of the product did indeed show a reduced iron content (~ 89% occupation). The trace amount of aluminium incorporated into the structure indicates a large degree of preferential incorporation of iron under these conditions. The iron vacancies are thus charge balanced by protonation of hydroxy groups.

The partially deuterated $(D_3O)Fe_{3-x}Al_x(SO_4)_2(OD)_6$ was prepared by dissolving 20.000g of $Fe_2(SO_4)_2.nH_2O$ and 31.500g $Al_2(SO_4)_3.18H_2O$ (Fisons 98%) in 50ml D_2O with gentle heating and then most of the water was removed by rotary evaporation; the viscous fluid that remained was made up to 300ml in D_2O and heated in a PTFE-lined stainless-steel bomb at 110°C for 24 hours. The precipitated product was washed three times in D_2O and dried well at 120°C for 2 hours to produce an ochre coloured material, lighter in colour than the pure iron compound. The powder was finely ground and the mass of the final product was 0.12g.

4.4.4 Synthesis of $NaFe_3(SO_4)_2(OD)_6$

Again, for the preparation of $NaFe_3(SO_4)_2(OD)_6$ an established synthetic procedure[9] was modified to exclude pH adjustment. The partially deuterated sample was prepared by dissolving 51.600g of

a PTFE-lined stainless-steel bomb at 155°C for 4 hours. The jarosite precipitate was washed four times with D_2O and dried well at 120°C for 3 hours. The resulting ochre powder was finely ground and the mass of the final product was 12.48g.

4.4.5 Synthesis of $(ND_4)Fe_3(SO_4)_2(OD)_6$

The literature synthesis[8] failed to yield an ammonium jarosite precipitate; the product was an amorphous species. A synthesis was designed using conditions derived from the preparation of $NaFe_3(SO_4)_2(OD)_6$. The partially deuterated sample was prepared by dissolving 51.600g of $Fe_2(SO_4)_2.nH_2O$ and 80.000g $(NH_4)_2(SO_4)_3$ (Prolabo 99%) in 50ml D_2O with gentle heating and reducing the reactant solution by rotary evaporation. The reactant was then made up to 300ml with D_2O. The reaction solution was heated in a PTFE lined stainless-steel bomb at 155°C for 4 hours. The jarosite precipitate was washed three times with D_2O and dried well at 120°C for 4 hours. The resulting ochre powder was finely ground and the mass of the final product was 14.13g

4.4.6 Synthesis of $AgFe_3(SO_4)_2(OD)_6$

The partially deuterated sample of $AgFe_3(SO_4)_2(OD)_6$ was prepared by mixing 6.000g of $Fe_2(SO_4)_2.nH_2O$ and 6.000g Ag_2SO_4 (Aldrich 99.999%) in 50ml D_2O with gentle heating (note that this amount of Ag_2SO_4 exceeds the solubility and so the Ag_2SO_4 will not completely dissolve). [8] The reactant solution was reduced by rotary evaporation before being made up to 200ml with D_2O. 7.500g D_2SO_4 (99.8 atom %, CDN Isotopes 96%) was added before the mixture was finally made up to 300ml with D_2O. The reaction solution was heated in a PTFE lined stainless-steel bomb at 155°C for 4 hours. The jarosite precipitate was washed three times with D_2O and dried well at 120°C for 3 hours. The resulting bright yellow powder was finely ground and X-ray diffraction revealed no evidence of unreacted materials and the mass of the final product was 1.29g. To minimise photodecomposition all silver-containing reagents, reaction solutions and products were handled under dull light conditions and their containers stored wrapped in aluminium foil.

4.4.7 Synthesis of $RbFe_3(SO_4)_2(OD)_6$

The partially deuterated sample of $RbFe_3(SO_4)_2(OD)_6$ was prepared using a literature synthesis.[7] 46.500g of $Fe_2(SO_4)_2.nH_2O$ and 7.500g Rb_2SO_4 (Fluka 98%) were dissolved in 50ml D_2O with gentle heating and reducing the reactant solution by rotary evaporation. The reactant was then made up to 200ml with D_2O and 4 drops of D_2SO_4 were added before the mixture was made up to 300ml with D_2O. The reaction solution was heated in a PTFE-lined stainless-steel bomb at 111°C for 4 hours. The jarosite precipitate was washed three times with D_2O and dried well at 120°C for 4 hours. The resulting ochre powder was finely ground and the mass of the final product was 2.84g

4.4.8 Synthesis of $(H_3O)Ga_3(SO_4)_2(OH)_6$

The preparation was based on conditions derived from the synthesis of $(H_3O)Fe_3(SO_4)_2(OH)_6$ but with a reduced reaction volume. 2.000g of $Ga_2(SO_4)_2$ (Aldrich 99.999%) was dissolved in deionised water and made up to 5ml. The reaction solution was heated in a Pyrex ampoule at 140°C for 17 hours. The resulting precipitate was washed three times with deionised water and dried well at 120°C for 2 hours. The resulting white powder was finely ground and the mass of the final product was 0.21g.

4.5 $(H_3O)Fe_3(SO_4)_2(OH)_6$

4.5.1 Dc susceptibility

A SQUID sample was weighed out in a gelatine capsule (Quantum Design) and lodged in the centre of a polythene drinking straw using Kapton tape (R.W. Greef). The straw was mounted on the end of a nonmagnetic rod and lowered into the SQUID magnetometer. Centring scans were performed with an applied field of 10G at 300K before the sample was cooled to 1.8K in zero applied field. Once at base temperature, the sample was allowed to equilibrate for 600s before a measuring field of 10G was applied and data collection began.

Dc susceptibility data are summarised in *Figure 4.2*. The dependence of the molar dc susceptibility, χ_m, for a conventional 2-D antiferromagnet reflects the effect of strong in-plane correlations at high temperatures which is manifested by a broad maximum. Real, layered antiferromagnets show 3-D long-range magnetic order on cooling further owing to the influence of additional terms in the Hamiltonian, e.g. interplane interactions and single-ion anisotropy. The susceptibility curve depicted in *Figure 4.2(a)* shows a broad inflection centred at ~ 250K, which reflects in-plane correlations, and it is likely that deviations will extend beyond this temperature. The inverse molar susceptibility, $1/\chi_m$, as a function of temperature [*Figure 4.2(b)*], confirms this, showing some curvature even at 300K. In the absence of susceptibility data taken at higher temperature we can only determine a very approximate value of the Curie-Weiss constant, θ_w. Extrapolation of $1/\chi_m$ against temperature to $T = 0$ will underestimate $|\theta_w|$ for T above the inflection, while data taken just below the inflection will overestimate $|\theta_w|$. The range of values deduced from these extreme cases provides an estimate of θ_w of -1200 ± 200K. The effective magnetic moment was found to be ~ $3.7\mu_B$ at 300K. As the ground term for S = 5/2 Fe^{3+} is $^6A_{1g}$, it is expected to be well described by the spin-only moment of $5.92\mu_B$. Reduction from this indicates that there is a large degree of antiferromagnetic correlations at these temperatures.

At lower temperatures, there is a clear divergence between field-cooled (fc) and zero-field-cooled (zfc) measurements at 17.2K, indicating some form of spin-glass-like transition. This is consistent with

previous reports of spin-freezing in hydronium jarosite at 17.5K determined by Mössbauer spectroscopy.[23] No other features are observed down to 1.8K, apart from anomalies at 4.2 and 2.2K which we believe arise from instabilities in the temperature of the sample near the boiling point and the lambda point of helium, respectively. When the sample is warmed from 1.8K, it overshoots at these temperatures then equilibrates, and the attendant irreversibility in the magnetic response of the sample is consistent with spin-glass behaviour below $T_f = 17.2$K.

4.5.2 Neutron scattering

The large degree of H-bonding in the jarosite structure could lead to significant differences between the structures of protonated and of deuterated materials. As this would reduce the relevance towards our understanding of natural mineral and its geological role, the unusual step was taken of performing neutron diffraction on a purely protonated sample, despite the large contribution from incoherent scattering.

Neutron powder diffraction patterns were taken at 1.5, 4.5, 20, 300, and 300K using an 'Orange' cryostat on the POLARIS diffractometer at the ISIS Facility of the CLRC Rutherford Appleton Laboratory, UK.

As expected for a spin-glass, there was no indication of long-range magnetic order in any of the powder neutron diffraction patterns: no new Bragg peaks appeared at any temperature even after careful scrutiny at the positions where magnetic Bragg scattering is observed in the other jarosites. Although the KHAFM with nearest-neighbour exchange does not possess long-range order, we expect the q = 0 and the $\sqrt{3}$ x $\sqrt{3}$ in-plane structures to be stabilised by further-neighbour interactions; this is not seen in this sample. The diffuse scattering background rose as the sample temperature was lowered from 330 to 1.5K, but its form cannot be analysed from this data due to the poor signal to noise ratio: the background for this highly hydrogenated sample is high, and the flux distribution of POLARIS is not ideal for the study of such effects.

The data collected at 1.5K were used to refine the structure of hydronium jarosite and locate the hydrogen atoms of the hydroxy and hydronium groups. Data collection from ~ 1.8g of sample held in a vanadium sample can with helium exchange gas took 3 hours (549μA). This work is summarised in Wills and Harrison.[24]

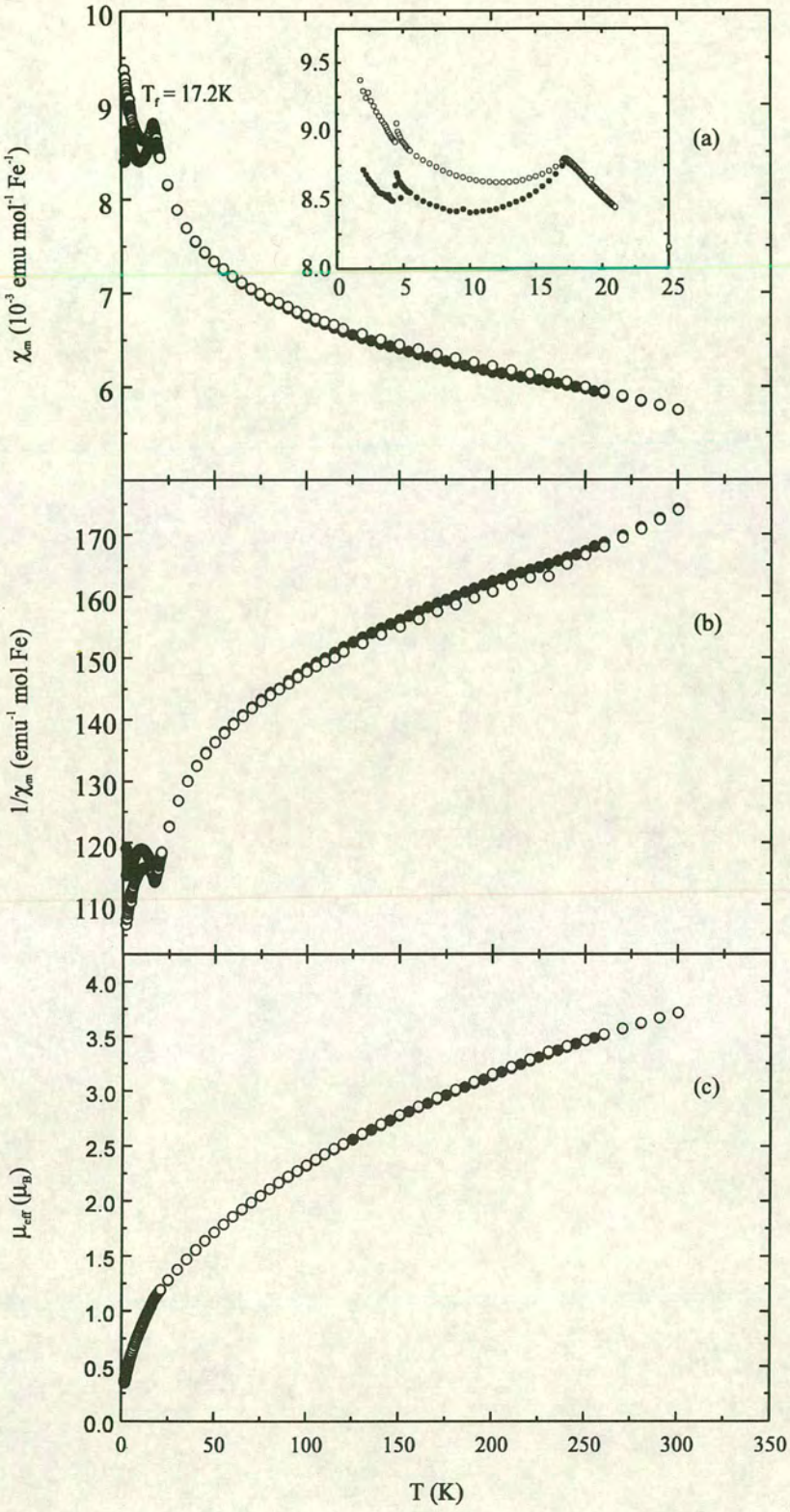

Figure 4.2. (●) Zero-field-cooled and (○) field-cooled dc susceptibility measurements as a function of temperature for $(H_3O)Fe_3(SO_4)_2(OH)_6$: (a) susceptibility, χ_m, inset shows spin-glass-like separation at T_f = 17.2K; (b) inverse susceptibility, $1/\chi_m$; (c) effective moment, μ_{eff}.

4.5.3 Rietveld refinement

Simultaneous refinement was performed on data collected from the low angle (A) and backscattering (C) banks for which the range of d-spacing is 0.5 - 8.15Å and 0.2 - 3.2Å, respectively. Refinement of the crystal structure was carried out using version 6 of the PC translation of GSAS. Due to the poor statistics, data in the region 17.5 - 20ms were excluded from refinement of the C bank pattern. As these reflections also appear in the A bank d-spacing range there was little loss of crystallographic information. The weak peak at d = 2.13 Å due to the (0 1 1) reflection of the vanadium sample can was not excluded from the final interactions of the refinement as it did not contribute significantly to the values of χ^2 or R_{wp}.

The peak profile was best described by a Gaussian function convoluted with a Lorentzian component with an angularly dependent width, a pseudo Voigt function. The background scattering for each histogram was fitted to a power series of two variables. This best accounted for an increase in the background intensity at both low and high d-spacing; the latter was a result of the large incoherent scattering contribution from the protons. The high degree of protonation also caused an important absorption term[25] and coefficients were independently refined for each bank.

The jarosite and parent alunite mineral families belong to the rhombohedral space group $R\bar{3}m$. The crystal structure of potassium jarosite, including approximate configurations of the hydrogen atoms of the hydroxy groups, has already been determined by single-crystal X-ray diffraction from a natural sample.[15,17] This was used as the starting point for our refinement, with H_3O^+ substituted for K^+ and the oxygen atom O(4) moved to the more general position (6c) (0 0 *z*). The atoms of the H_3O^+ ion were given a 50% fractional occupation at each of the six symmetry-generated sites to represent statistical disorder.

Data taken at 1.5K were first refined with the H_3O^+ molecular unit entirely free to be distorted, resulting in a profile fit that appeared to be excellent and yielded weighted pattern *R* values, R_{wp}, of 0.97%, 0.86% and 0.89% for the A bank data, and C bank data and combined data set, respectively, and a value for χ^2 of 2.05. These unusually low values of R_{wp} reflect the high incoherent background contribution to the scattering. This refinement resulted in an O—H bond length of 0.846 (10)Å and an H—O—H bond angle of 95.0 (8)°, which is clearly at odds with values determined for these parameters in the few materials containing H_3O^+ that have been studied to date; more typical values are 0.96 ± 0.08Å for the O—H bond length and 111 - 120° for the H—O—H angle.[26-30] In this co-ordination geometry, hydrogen bonding is expected to cause a decrease in the H—O—H bond angle and also an increase in the O—H bond length. For this reason, the H_3O^+ unit was arbitrarily defined as a rigid body with a 112° bond angle and a 0.96Å bond length [*Table 4.3*], based on the hydronium structure in hydronium perchlorate. Some deviation from this idealised geometry is expected but it does, however, give a physically more reasonable structure than that resulting from free refinement.

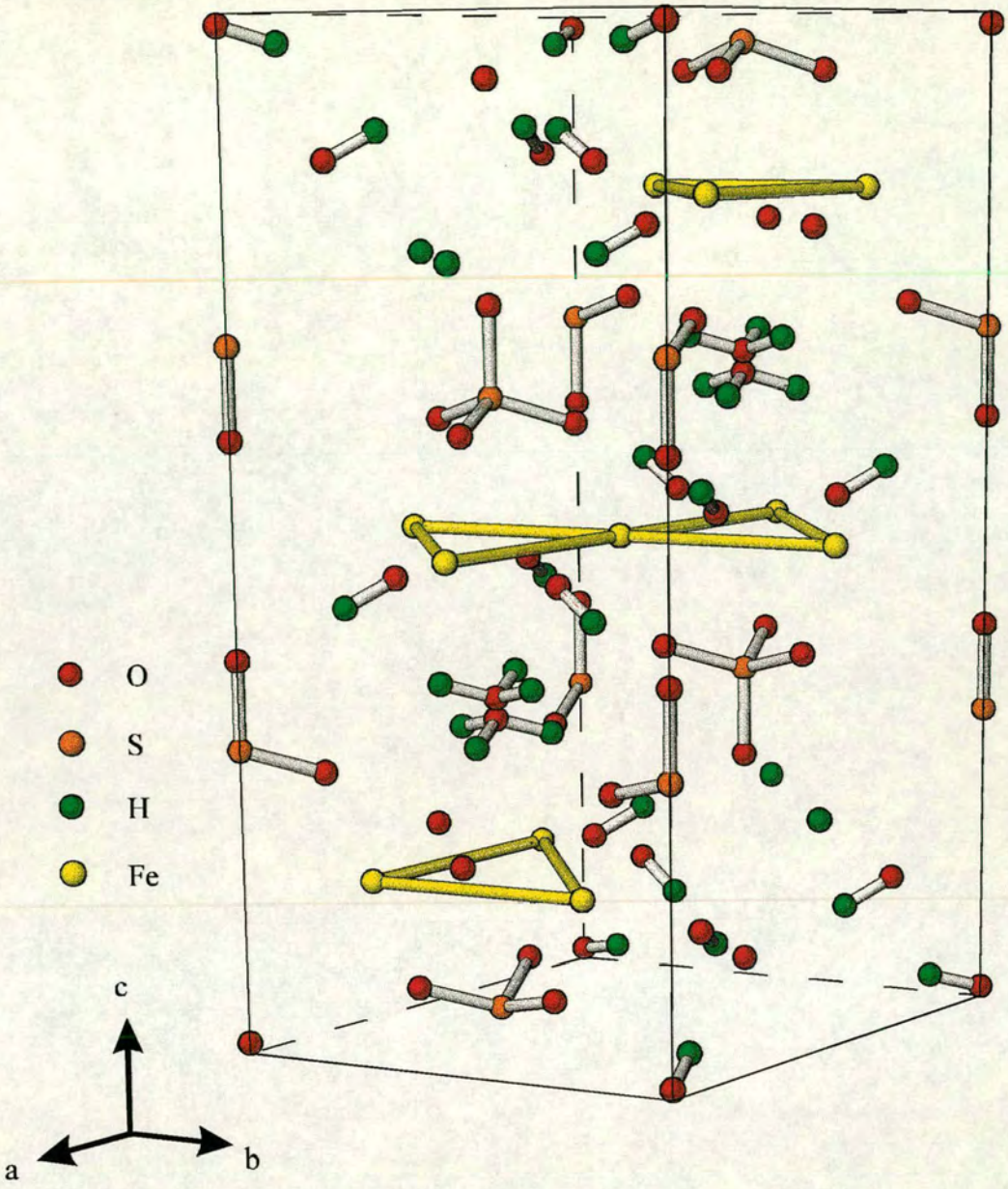

Figure 4.3. Unit cell of hydronium jarosite in a hexagonal setting.

	x	*y*	*z*
O	0	0	0
H	0	-0.957290	-0.289129
H	0.829037	0.478645	-0.289129
H	-0.829037	0.478645	-0.289129

Table 4.3. Unit vectors used to define the H_3O^+ rigid body with a bond angle of 112°.

Two orientations of the H_3O^+ unit were examined: the first involved the O(4)—H(1) bond pointing towards the basal oxygen atoms O(2) of the sulfate group. The second was derived from this by rotating the H_3O^+ unit by 60° so that the O(4)—H(1) bond points between the oxygen atoms O(2) of the sulfate group and towards the hydroxy oxygen atoms O(3). We were unable to obtain a stable refinement with the first orientation of H_3O^+ while the second gave values of R_{wp} for the A and C bank refinements and also of the combined data of 1.29%, 0.89%, and 1.02%, respectively and $\chi^2 = 2.67$, an increase relative to the values obtained when H_3O^+ was free to be distorted. The atomic co-ordinates of the other atoms in the unit cell and the fractional occupancy of the Fe sites did not change significantly.

Free variation of the isotropic thermal parameters of O(1), O(2), and O(3) lead to an unstable refinement. For this reason they were constrained to all have the same value. The final fitted profiles are displayed in *Figures 4.4(a)* and *(b)* for the A and C bank data respectively and the crystal structure is displayed in a hexagonal setting of this space group in *Figure 4.3* with a ≈ 7.32Å and c ≈ 16.92Å. The refined positions of the atoms and their thermal parameters, together with cell constants, are given in *Table 4.4*. The isotropic temperature factor, U_{iso}, is proportional to the mean square of the displacement of the atom from its equilibrium position.

atom (Wyckoff site)	*x*	*y*	*z*	U_{iso}/Å^2	*site symmetry*	*fractional occupancy*
Fe (9d)	0.16667	-0.16667	-0.16667	0.0105 (6)	2/M(110)	0.973 (6)
S (6c)	0.00000	0.00000	0.30555 (34)	0.091 (12)	3M(100)	1.000
O1 (6c)	0.00000	0.00000	0.39374 (20)	0.0162 (5)	3M(100)	1.000
O2 (18h)	0.22471 (12)	-0.22471 (12)	-0.05437 (11)	0.0162 (5)	M(110)	1.000
O3 (18h)	0.12789 (15)	-0.12789 (15)	0.13452 (11)	0.0162 (5)	M(110)	1.000
O4 (6c)	0.00000	0.00000	-0.01076 (46)	0.0047 (14)	3M(100)	0.500
H1 (18h)	-0.07244 (*)	0.07244 (*)	-0.02716 (46)	0.1691 (75)	M(110)	0.500
H4 (18h)	0.19342 (27)	-0.19342 (27)	0.10751 (18)	0.0322 (9)	M(110)	1.000

Table 4.4. Structural parameters for $(H_3O)Fe_3(SO_4)_2(OH)_6$ at 1.5K in the space group $R\bar{3}m$ with Z = 3. Figures with asterisks are reported without errors because they were subject to rigid body constraints in the refinement that did not allow variation in that parameter. Cell parameters: a = 7.32457 (12)Å and c = 16.9153 (4)Å. χ^2 = 2.67%. R_{wp} = 1.29% (A bank), 0.89% (C bank), and 1.20% (combined data set).

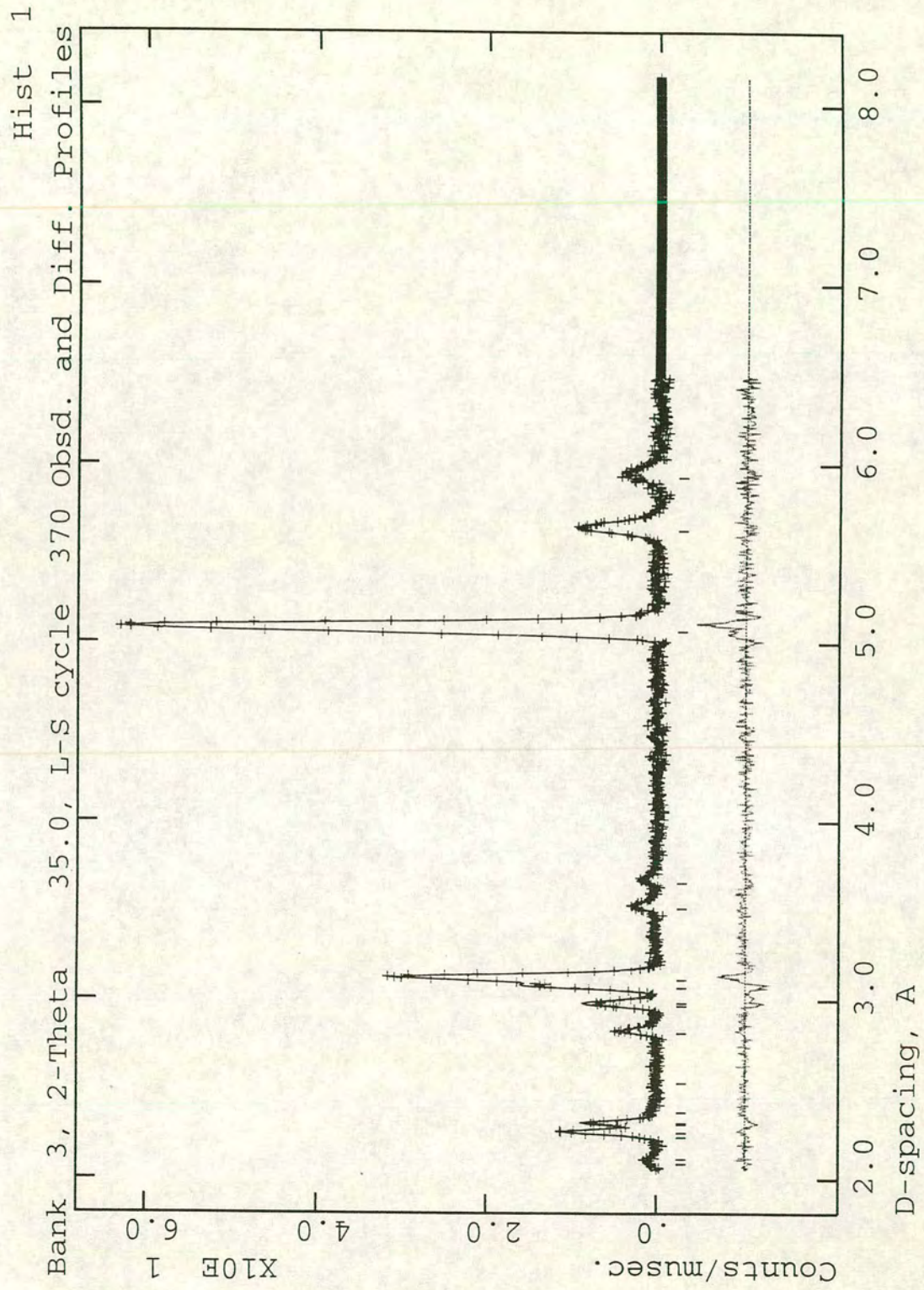

Figure 4.4(a). Fit of refined profile to A bank neutron scattering data for $(H_3O)Fe_3(SO_4)_2(OH)_6$ using the $R\bar{3}m$ space group.

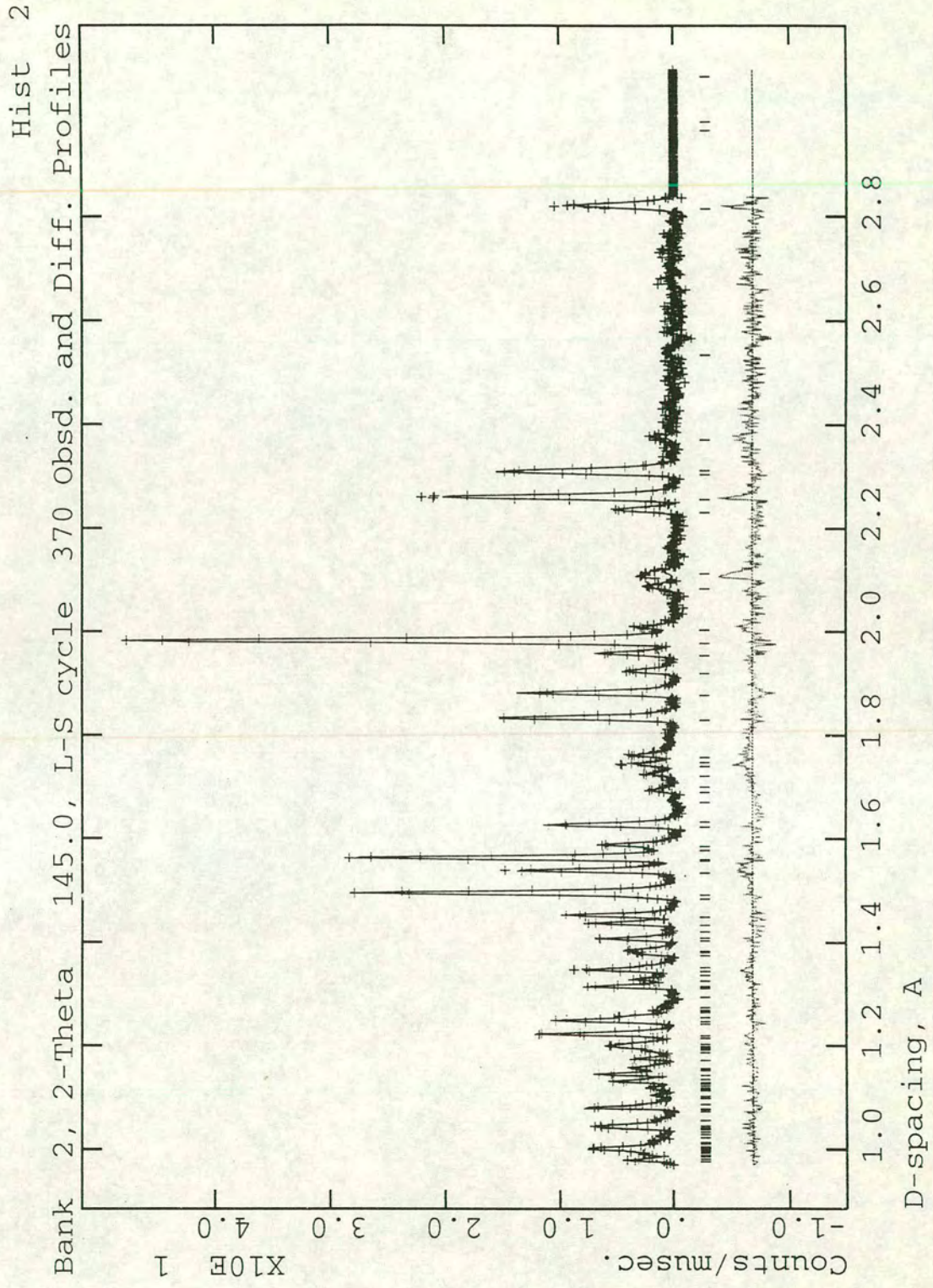

Figure 4.4(b). Fit of refined profile to C bank neutron scattering data for $(H_3O)Fe_3(SO_4)_2(OH)_6$ using the $R\bar{3}m$ space group.

Although we have located all the hydrogen atoms in the structure, there is still uncertainty about the geometry of the H_3O^+ ion. This may be clarified by theoretical work on the expected structure of H_3O^+ in this environment. It is probable that we would also be able to refine the structure to a more precise set of parameters with sufficiently high resolution data taken from a fully deuterated sample, a process that will greatly reduce the incoherent neutron scattering background.

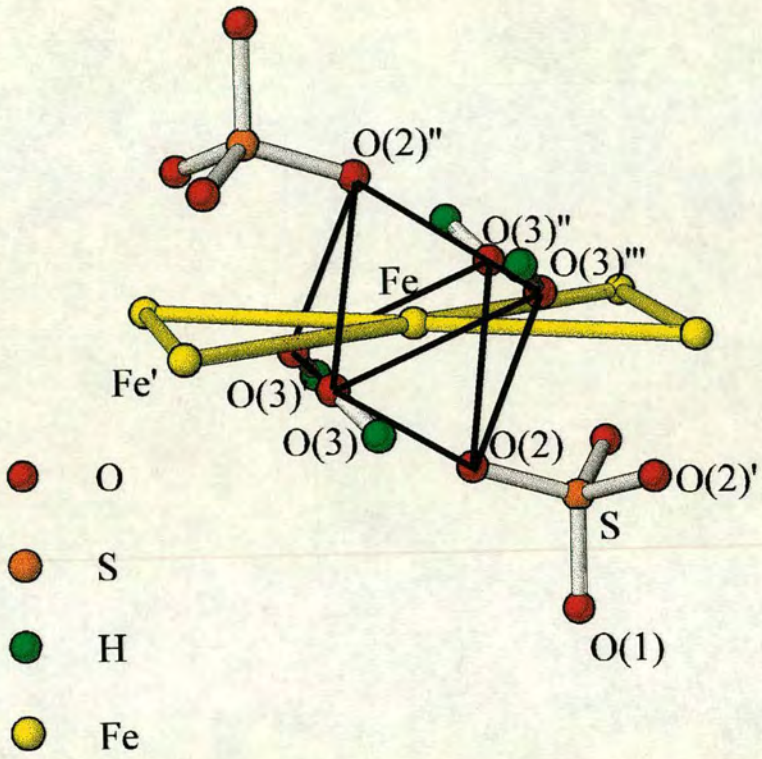

Figure 4.5. Local co-ordination of Fe^{3+} ions in hydronium jarosite showing the distorted octahedral co-ordination by OH and SO_4^{2-} and defining the atom labels used in Table 4.5.

4.5.4 Structure: discussion

Our neutron refinement defined the character and dispositions of a number of molecular units in the structure. Selected bond lengths and angles are given in *Table 4.5*. The Fe^{3+} ions have a distorted octahedral co-ordination, lying at the centre of a distorted square plane of four hydroxy O(3) atoms, [Fe—O(3)] is 1.992Å], with two basal sulfate (O2) atoms above and below [Fe—O(2) is 2.037Å] [*Figure 4.5*]. These octahedra are linked by their corners to form the Kagomé lattice [*Figure 4.6*]. The distance between nearest neighbours within the Kagomé planes is 3.662Å and the distance between Kagomé planes is 5.639Å.

The sulfate tetrahedra may be divided into two types, alternatively pointing up and down, while the H_3O^+ molecules reside in spaces between the sulfate bilayers. In potassium jarosite the K atom at (0 0 0) is 12-co-ordinate, with six sulfate oxygen atoms at 2.913Å and six hydroxy oxygens atoms at 2.816Å.[17] In hydronium jarosite each proton of the H_3O^+ unit is hydrogen bonded to two sulfate oxygen atoms [H(1)—O(2) is 2.562Å], and to one hydroxy oxygen atom [H(1)—O(3) is 1.948Å]. As the shortest hydrogen bonds are to the oxygen atoms of the hydroxy group we conclude that this must be the dominant interaction and that defines the H_3O^+ orientation. The apical sulfate oxygen atoms are hydrogen bonded to three hydroxy hydrogen atoms, with an H(2)—O(1) separation of 1.946Å, The inequivalence of the bonding of apical and basal oxygen atoms leads to a slight distortion of the sulfate tetrahedra. The three equivalent bonds from sulfur to the three basal oxygen atoms, S—O(2), have a length of 1.450Å, while the bond length of the sulfur atom and the apical oxygen atom, S—O(1), is 1.492Å. The mean S—O bond length 1.461Å.

S—O(1)	1.492 (5)	O(2)—S—O(2′)	110.83 (23)
S—O(2)	1.4495 (26)	O(2)—S—O(1)	108.08 (24)
O(1)—O(2)	2.381 (4)		
O(2)—O(2′)	2.3868 (27)		
		S—O(2)—Fe	129.265 (8)
Fe—Fe	3.66228 (6)	Fe—O(3)—Fe′	133.625 (12)
Fe—O(2)	2.0374 (19)	O(2)—Fe—O(3)	88.968 (13)
Fe—O(3)	1.9921 (8)	O(2″)—Fe—O(3)	91.035 (15)
O(2)—O(3)	2.8236 (15)	O(3)—Fe—O(3′)	89.721 (13)
O(2″)—O(3)	2.8750 (27)	O(3′)—Fe—O(3″)	90.279 (19)
O(3)—O(3′)	2.8103 (33)		
O(3′)—O(3″)	2.8240 (20)		

Table 4.5. Selected bond lengths (Å) and angles (degrees) in hydronium jarosite with estimated standard deviations in brackets.

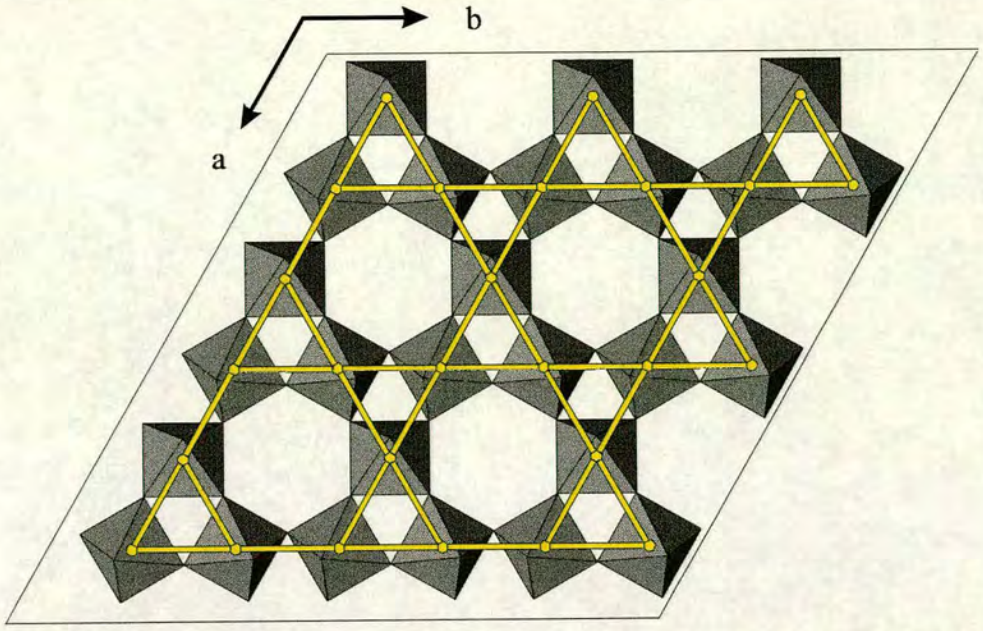

Figure 4.6. Network of interlinked Fe-O octahedra that form a Kagomé network of Fe^{3+} ions in hydronium jarosite.

4.5.5 MuSR results

Approximately 1.8g of $(H_3O)Fe_3(SO_4)_2(OH)_6$ were pressed into a 30mm diameter circular depression in an aluminium plate. The sample was covered with a mylar sheet and the surrounding aluminium plate shielded from the muon beam by a silver mask which absorbs muons. The sample mount was then loaded into an Oxford 'Blue' helium cryostat which has an approximate temperature range of 1.5 - 300K.

The calibration constant (α = 1.05) [*Equation 3.13*] was determined at 200K for the forward and backward detectors using a 20G transverse field. After this, the transverse field was removed and the sample cooled to 60K in the absence of any applied field. An observed precession signal due to coupling of the muon to the proton nuclear fields was decoupled using a 50G longitudinal field. Measurements were then taken between 5 and 70K with an equilibration time of ~ 15 minutes and a counting time of ~2 hours (1E7 events) at each temperature. Initial data were taken with the 50G longitudinal field removed between temperature changes. Later experiments showed that cooling the sample in a field had no effect and the 50G longitudinal field was constantly applied.

At high temperatures, dense magnetic systems have a Gaussian distribution of local fluctuating fields that act to depolarise the muon spins. If there is only a unique value of the muon depolarisation rate, λ, the longitudinal relaxation function $G_z(t)$ will have the form:[31]

$$G_z(t) \propto \exp(-\lambda t) \tag{4.1}$$

where t is the time elapsed after muon implantation. As the system is cooled, the distribution of local fields broadens and experiments show $G_z(t)$ to have the more general form of a stretched exponential:[32,33]

$$G_z(t) = A + B\exp\left[(-\lambda t)^{\beta}\right] \tag{4.2}$$

where A reflects a small time-independent signal from aluminium that is exposed to the muon beam, B is a proportionality constant, and β is a function of the distribution of local fields. In the high temperature limit, $T >> 4T_f$, β is found to approach unity, the value expected for a single muon depolarisation rate. As the system is cooled the spin fluctuations slow down and the distribution of local fields becomes progressively wider. This causes the value of β to fall and λ to increase which in turn changes the shape of $G_z(t)$ [*Figure 4.7*]. Close to T_f the muon depolarisation rate, λ , diverges and at T_f, the longitudinal relaxation rate takes a form that appears to be universal for spin-glasses, with $\beta = 1/3$. [32,33]

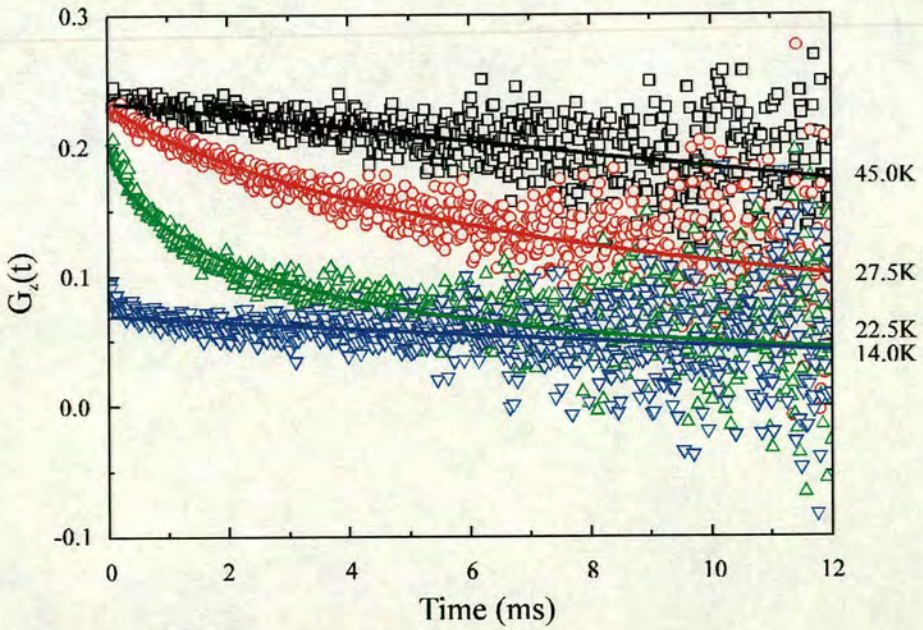

Figure 4.7. The muon spin relaxation function $G_z(t)$ for $(H_3O)Fe_3(SO_4)_2(OH)_6$ and fits to the stretched exponential decay at (-)14.0, (-)22.5, (-) 27.5, and (-) 45K. The poor fit to the initial decay at 14.0 K, and hence unreliable value of λ and β, is a consequence of the very rapid decay of λ at this temperature, and instrumental limitations.

The $G_z(t)$ decay spectra at $T > T_f$ were fitted to the stretched exponential *Equation 4.2*. On cooling from ~ 50K the muon depolarisation rate, λ, increases gradually with decreasing temperature as the Fe spin fluctuations slow down [*Figure 4.8*]. This temperature range is much larger than that of a normal spin-glass where the spin fluctuations slow over the temperature region $T_f \leq T \leq 2T_f$. As the temperature is reduced towards T_f the value of β falls from 1 and approaches ~ 1/3, as seen in other spin-glasses. Unfortunately the instrumental limitations of EMU prevent reliable fitting of λ to values above $10\mu s^{-1}$ as there are insufficient data to characterise the form of the curve [*Figure 4.7*], so no quantitative analysis can be made on data below ~ 20K.

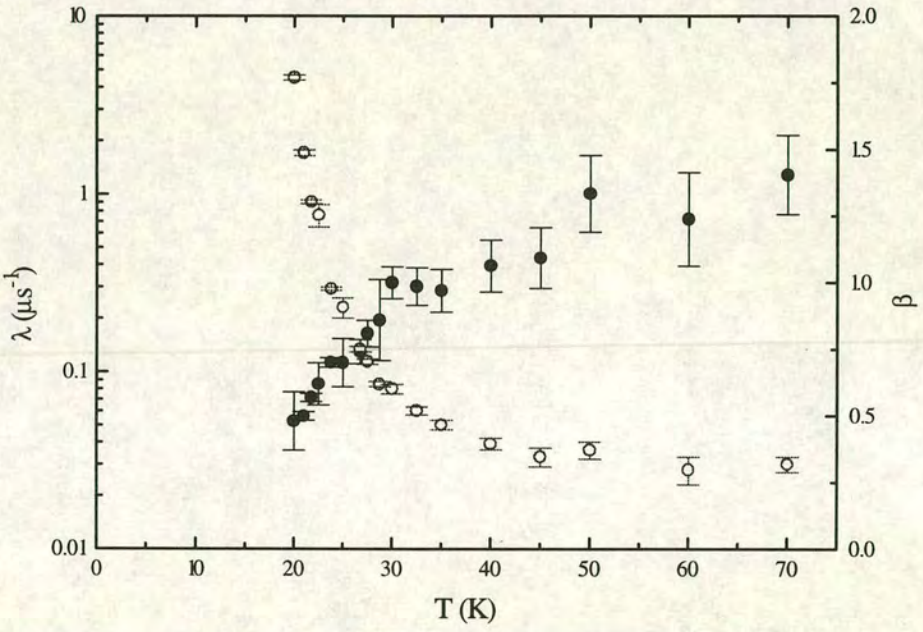

Figure 4.8. (○) Muon depolarisation rate, λ, and exponent (●) β as a function of temperature for $(H_3O)Fe_3(SO_4)_2(OH)_6$.

Below T_f $G_z(t)$ does not show precession and the recovery to 1/3 that are the signatures of a static field, as would be the case for a conventional spin-glass;[32] instead dynamic fluctuations persist at 5K. Due to the rapid decay of the muon polarisation the form of the initial decay cannot be analysed from this data. Application of a longitudinal field up to 4,000G caused no significant change to $G_z(t)$, i.e. $G_z(t)$ is essentially independent of the applied field. This inability to decouple the muons from their local fields suggests that the muon is coupling to a very strong local field and the applied field is very weak in

comparison. While it has been suggested that these large local fields could be created by the sporadic creation of unpaired spins in a singlet spin-fluid,[34] they could simply be the result of spontaneous excitation in which the vector sum of the three spins on an individual triangular plaquette is nonzero. This would give rise to a local field in the vicinity of the excitation. If the lifetime of such an excitation was an appreciable fraction of that of the muon it would result in both dynamic and static components. Such an undecouplable Gaussian decay has only been observed in SCGO(x)[31,34] and $KCr_3(SO4)_2(OH)_6$,[35] and may be unique to these highly frustrated systems. The difference between these materials and the magnetically dilute $KFe_3(SO_4)_2(OH)_6$ is highlighted by the observation of a precession signal in the latter below T_c.[35]Whether this is an effect of lower iron coverage and/or increased interlayer exchange is a matter for debate.

4.6 $(H_3O)Ga_3(SO_4)_2(OH)_6$

4.6.1 Rietveld refinement

$(H_3O)Ga_3(SO_4)_2(OH)_6$ was prepared as a diamagnetic analogue for subtraction of the phonon contribution from the specific heat measurements. X-ray powder diffraction was done using a Rigaku "Geigerflex" diffractometer with CuKα radiation by Dr. S.A.M. Mentink at the Department of Physics, The University of Toronto. Crystallographic parameters refined by the Rietveld method are displayed in *Table 4.6*; the experimental and calculated diffraction patterns are shown in *Figure 4.9*. The refined structure of hydronium jarosite was used as a starting model and the parameters described as before, except for the absorption correction which is insignificant and not refined. Protons were not included in the final structure as their presence did not improve the refinement.

atom (Wyckoff site)	*x*	*y*	*z*	U_{iso}/Å^2	*site symmetry*	*fractional occupancy*
Ga(9d)	0.16667	-0.16667	-0.16667	0.0236(4)	2/M(110)	0.987(4)
S(6c)	0.00000	0.00000	0.30731(16)	0.0282(10)	3M(100)	1.000
O1(6c)	0.00000	0.00000	0.39413(34)	0.0276(22)	3M(100)	1.000
O2(18h)	0.21771(26)	-0.21771(26)	-0.05528(20)	0.0314(15)	M(110)	1.000
O3(18h)	0.12843(21)	-0.12843(21)	0.13373(17)	0.0265(13)	M(110)	1.000
O4(3a)	0.00000	0.00000	0.00000	0.0128(25)	-3M(100)	1.000

Table 4.6. Structural parameters for $(H_3O)Ga_3(SO_4)_2(OH)_6$ at room temperature in the space group $R\bar{3}m$ with Z = 3. Cell parameters: a = 7.17540 (23) Å and c = 17.1635 (6) Å. χ^2 = 2.09 and R_{wp} = 10.13%.

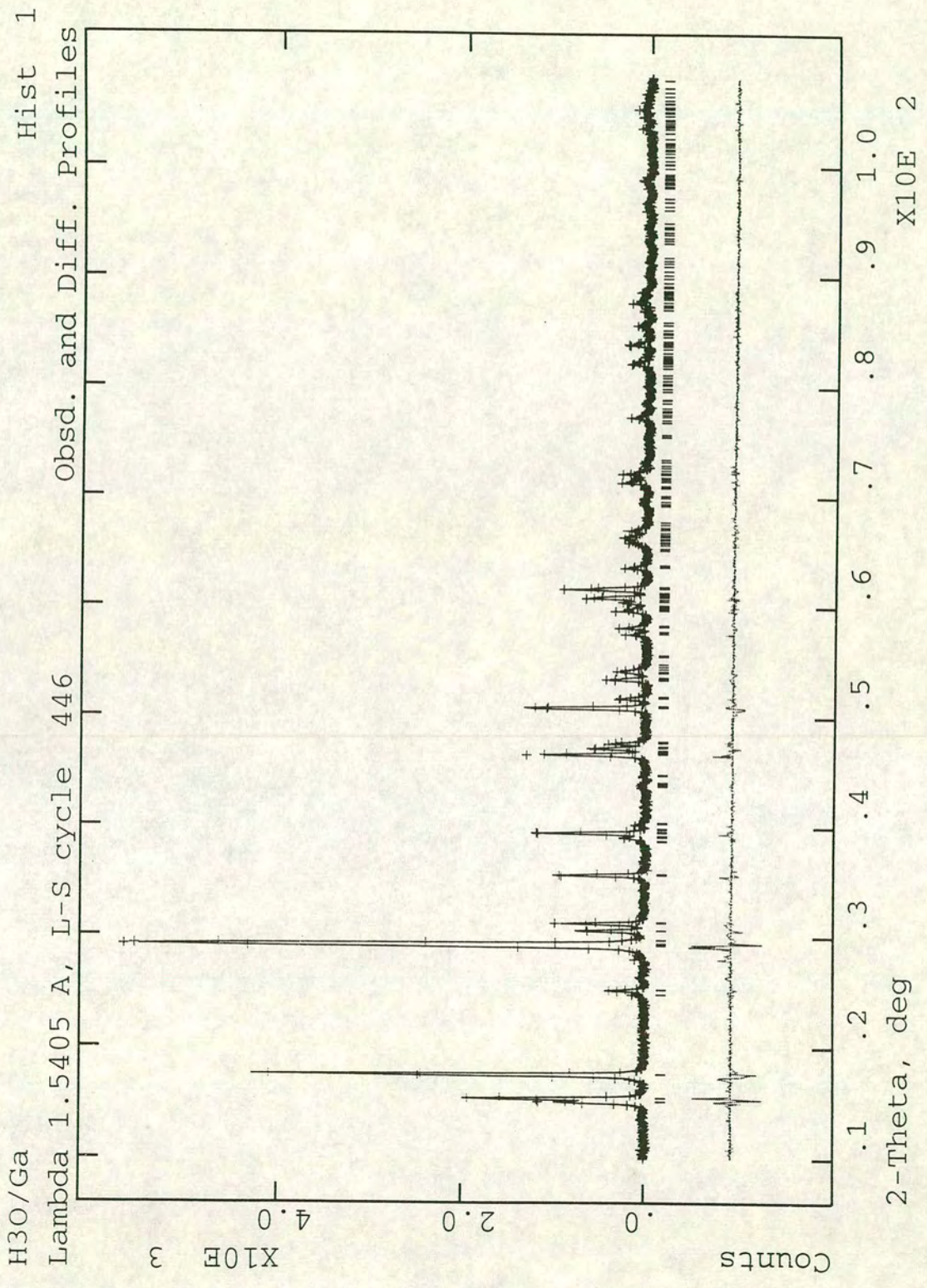

Figure 4.9. Fit of refined profile to X-ray diffraction data for $(H_3O)Ga_3(SO_4)_2(OH)_6$ using the $R\bar{3}m$ space group.

4.6.2 Specific heat measurements

Debye calculated the specific heat due to lattice vibrations in a 3-D solid system by approximating the system to a series of harmonic oscillators with a distribution of frequencies. Each oscillator has two degrees of freedom along the three Cartesian axes. According to this model, the specific heat close to $T = 0$ is proportional to T^3:

$$C_v = \frac{12\pi^4}{5} nk_B \left(\frac{T}{\Theta_D}\right)^3 \qquad (4.3)$$

where Θ_D is the Debye temperature and C_v is the molar constant volume specific heat of the material, the molecules of which contain n atoms. The failure of the Debye T^3 law to accurately describe the phonon contribution at intermediate temperatures is well known.[36,37]To improve the approximation a higher order T^5 term may be added to take into account anharmonic contributions. A further correction to allow for an electronic contribution can be equated to a linear T term. Thus, the specific heat data taken between 10 and 40 K for $(H_3O)Ga_3(SO_4)_2(OH)_6$ were fitted to a phonon contribution described by the polynomial:

$$C_v = \alpha T + \beta T^3 + \delta T^5 \qquad (4.4)$$

where α = 2.11E-3, β = 4.67E-5, δ = 5.50E-9. This fitted expression was used to model the phonon background in later experiments. The poor statistics of the data for $(H_3O)Ga_3(SO_4)_2(OH)_6$ will not limit later analyses as the phonon contribution is generally much smaller than the magnetic component.

4.7 $(D_3O)Fe_3(SO_4)_2(OD)_6$

In order to examine further the nature of the magnetic correlations in hydronium jarosite, a partially deuterated sample was prepared. Analysis of its structure and magnetic properties were carried out using a range of experimental techniques: dc and ac susceptibility, specific heat and neutron diffraction. This work is summarised in a letter by Wills et al.[38]

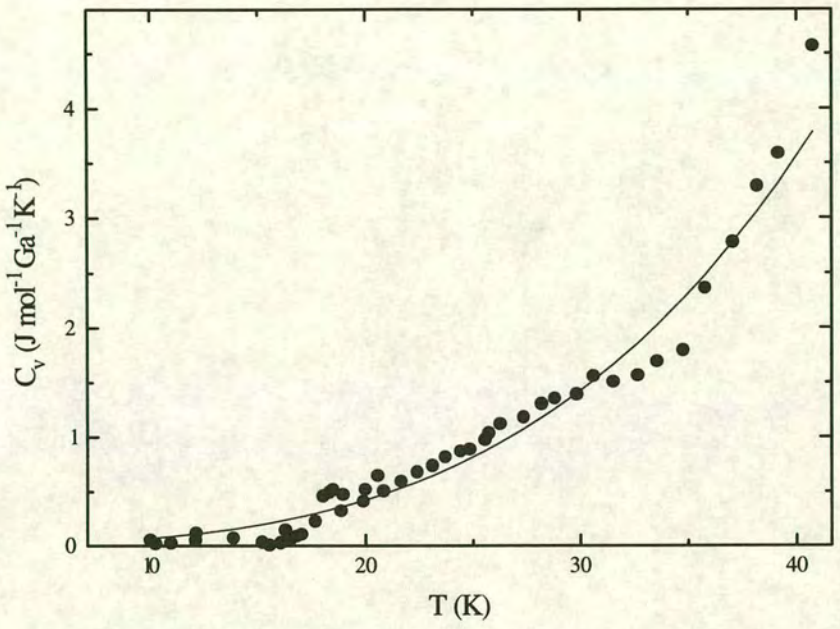

Figure 4.10. Specific heat, C_v, for $(H_3O)Ga_3(SO_4)_2(OH)_6$. The line represents the curve fit to C_v = (2.11E-3) T + (4.67E-5)T^3 + (5.50E-9)T^5.

4.7.1 Dc susceptibility

The onset of spin-glass-like behaviour at T_f = 13.8K is clearly shown in *Figure 4.11(a)* as a divergence between zfc and fc measurements, where the cooling and the applied field are both 100G. The anomaly at 4.5K is believed to be an artefact of the temperature control; it is not seen in the measurements of χ_{ac} or specific heat which show no anomalies other than at T_f down to 80mK. At higher temperatures the susceptibility conforms approximately to the Curie-Weiss law, with some curvature in the dependence of $1/\chi_m$ on temperature between 150 and 300K as a result of short-range 2-D correlations. Extrapolation of this curve to $1/\chi_m = 0$ provides an estimate for θ_w of -1500 ± 300K. The relative values of T_f and θ_w are broadly consistent with theoretical predictions: Monte-Carlo simulations on the KHAFM with a small XY exchange anisotropy ($J_x = J_y > J_z$) indicate that the weathervane modes [*Section 2.9.2*] freeze out at $\approx \theta_w/96$ ($\approx$ 15K for deuterated hydronium jarosite). When an Ising anisotropy is present, freezing is expected at $T = 0.058J$ ($\approx$ 4K for deuterated hydronium jarosite) accompanied by a parasitic ferromagnetic moment.

4.7.2 Ac susceptibility

The in-phase and out-of-phase components of the χ_{ac} were measured over the temperature range 5 - 25K at frequencies of 1.157 - 1157 Hz and the data are presented in *Figure 4.12*. The fall of T_f with measuring frequency ω is in a manner typical of an 'ideal' spin-glass.[39] These data were fitted to the empirical Vogel-Fulcher law [*Equation 2.29*] with the activation energy E_a = 64K, the ideal glass temperature T_0 = 15.6K and $\tau_0 = 1/\omega_0 = 1.6 \times 10^{-12}$s.

4.7.3 Specific heat

Specific heat data taken for $(D_3O)Fe_3(SO_4)_2(OD)_6$ over the temperature range 0.4 - 40K were corrected for the phonon background measured with the gallium compound [*Section 4.6.2*] (which contributes about 10% of the signal at these temperatures) to give the magnetic contribution C_m. The linear dependence of $C_m(T)/T$ against T [*Figure 4.13(c)*] highlights the T^2 dependence below T_f. This contrasts with conventional spin-glasses where localised modes with an energy-independent density of states dominate at low temperatures, giving a linear dependence of $C_m(T)$ on T. A similar T^2 dependence is observed in SCGO(x)[40] and suggests the presence of a gapless excitation spectrum, either the result of propagating spin-waves based on long-range magnetic order as in a conventional 2-D antiferromagnet, or a 2-D spin nematic phase.[41,42]

The magnetic specific heat, C_m, was fitted to a polynomial equation and C_m/T integrated to give the magnetic entropy. Here also, deuterated hydronium jarosite resembles SCGO(x) in that only a small fraction of the magnetic entropy is released at T_f, 6.2% of the full value of $Rln(2S+1)$ for free spins S compared with approximately 7% at T_f for SCGO(x).[45] However, in contrast to SCGO(x) and also to 'ideal' glasses, the high temperature of the transition and the large temperature range over which the spins freeze causes there to be no peak is observed in $C_m(T)/T$; instead, $C_m(T)/T$ changes monotonically with T over a wide range of temperatures.

4.7.4 Neutron scattering:

Neutron powder diffraction measurements were performed on deuterated hydronium jarosite to probe the magnetic pair correlation function more incisively. Diffraction patterns were taken on the multidetector diffractometer C2 at the NRU Reactor, Chalk River. C2 has a angular range of 2θ = 5 - 117° (step size 0.1°) and a Si (5 3 1) monochromator was used to provide neutrons with a wavelength of 1.5041Å. ~ 2g of sample was loaded in a vanadium can with helium exchange gas. Powder diffraction patterns were taken at 2, 4, 25, and 250K. As with the protonated sample, there was no evidence of magnetic Bragg peaks at any temperatures. No significant coherent scattering was observed from the vanadium sample can.

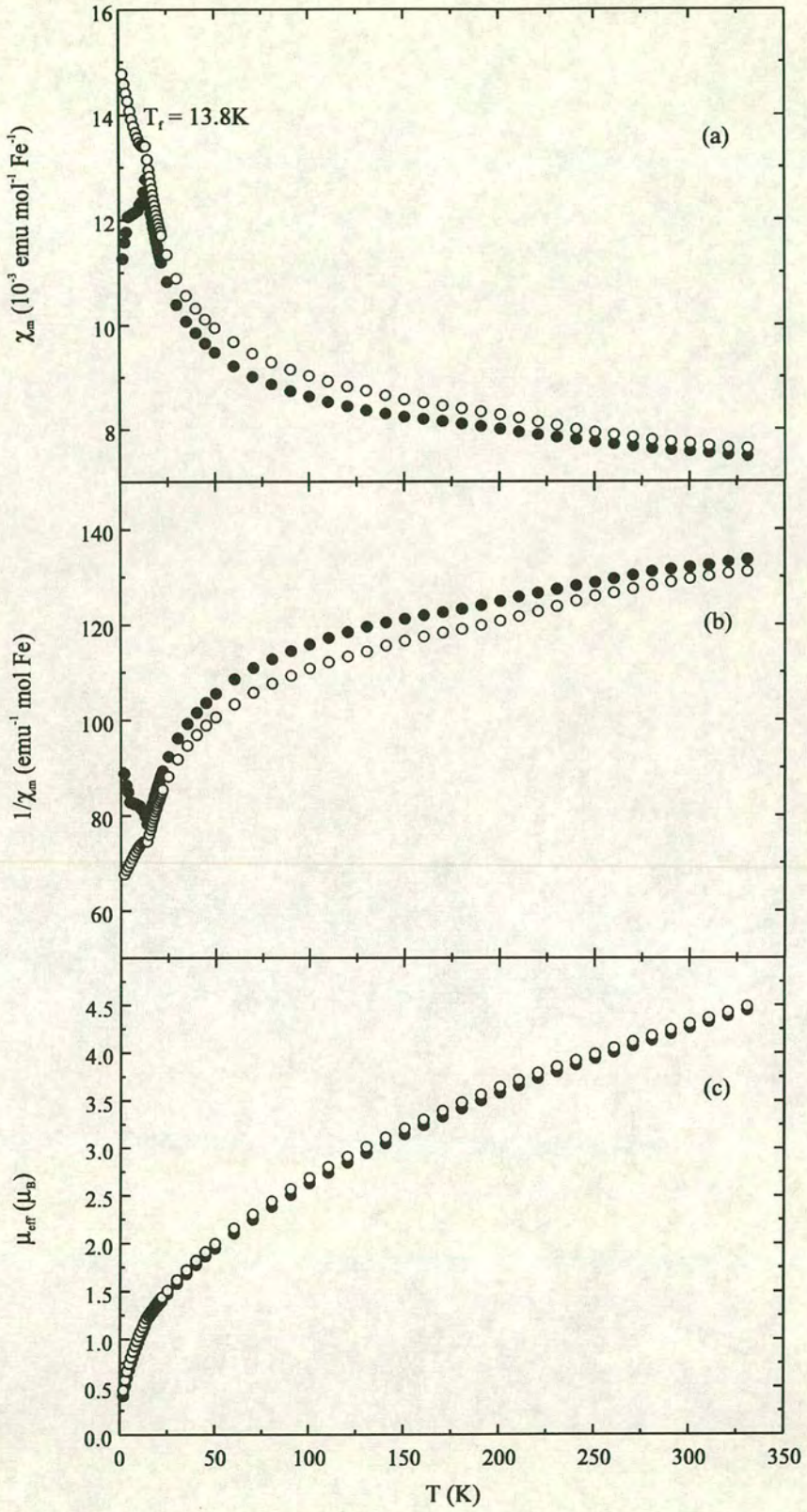

Figure 4.11. (●) Zero-field-cooled and (○) field-cooled dc susceptibility measurements as a function of temperature for $(D_3O)Fe_3(SO_4)_2(OD)_6$: (a) susceptibility, χ_m; (b) inverse susceptibility, $1/\chi_m$; (c) effective moment, μ_{eff}.

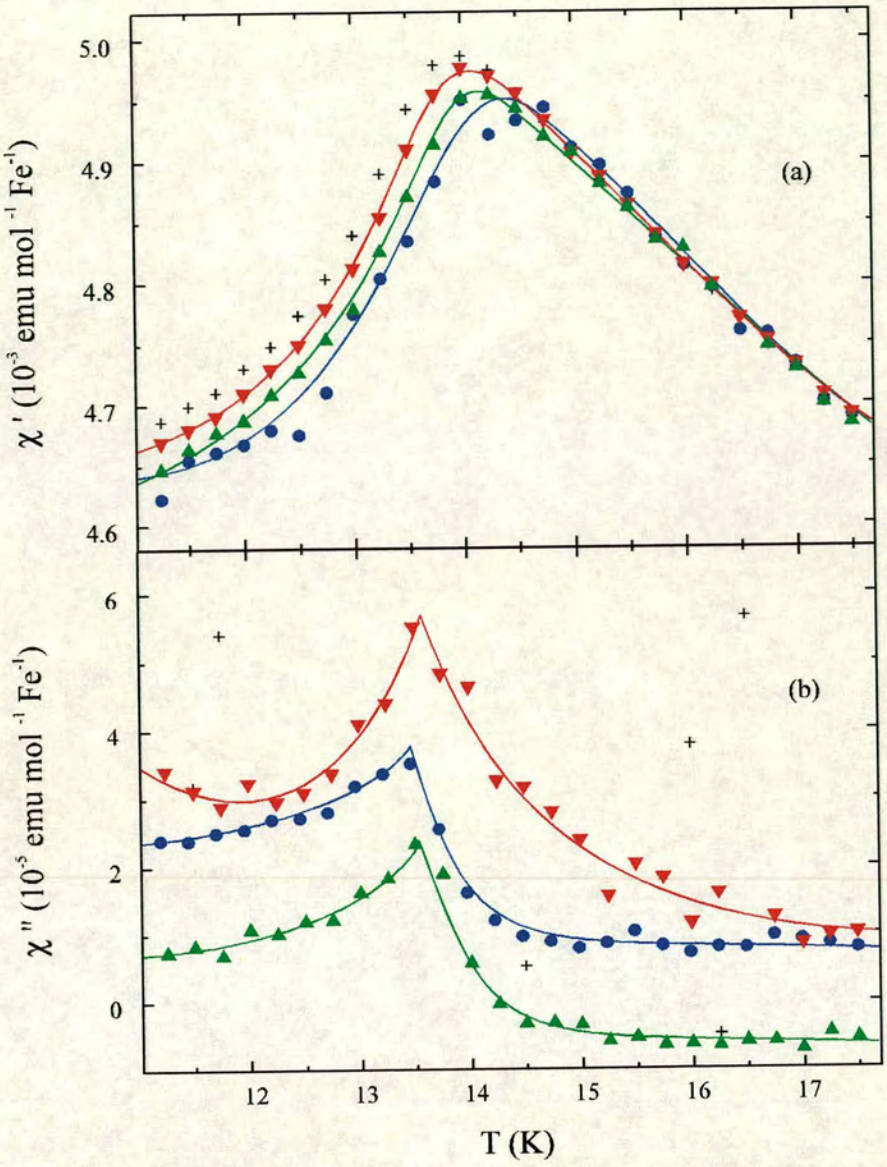

Figure 4.12. Real and imaginary parts of the complex susceptibility as a function of temperature and the measuring frequency: ● *1.157 Hz,* ▲ *11.57 Hz,* ▼ *115.7 Hz,* + *1157 Hz; the lines drawn are guides to the eye.*

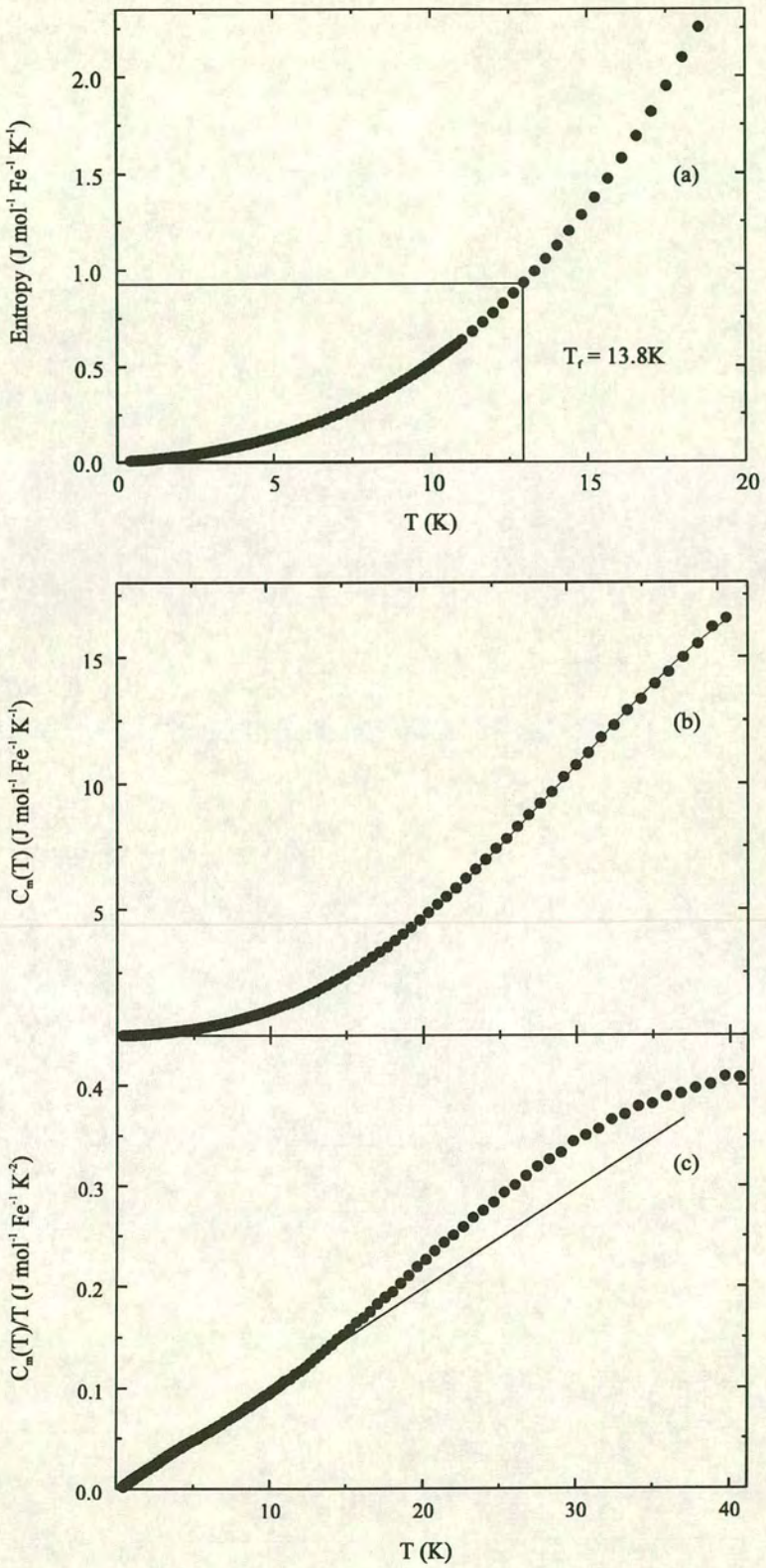

Figure 4.13. Specific heat data for $(D_3O)Fe_{3-x}Al_x(SO_4)_2(OD)_6$: (a) Entropy; (b) C_m, magnetic contribution to the specific heat; (c) C_m/T, the straight line through the low-temperature data represents a T^2 dependence.

The dynamic character of the short-range magnetic correlations was studied in further detail with the triple axis diffractometer N5 at the NRU Reactor, configured both as a two-axis instrument without energy analysis, and later as a triple-axis instrument with energy analysis. Incident energies of 3 and 5THz (λ = 2.568 and 1.989Å respectively) were used in conjunction with a Si (1 1 1) monochromator and a pyrolytic graphite (0 0 2) analyser crystal. The angular divergence of the neutron optics was as follows: monochromator to sample 1.2°, sample to analyser 1.0°, and analyser to detector 2.1°.

4.7.5 $(D_3O)Fe_3(SO_4)_2(OD)_6$: Rietveld refinement

The data collected at 2K over 3 hours (6.5E6 events) were refined using the $R\bar{3}m$ structure of $(H_3O)Fe_3(SO_4)_2(OH)_6$ as a starting point with the background and peak profile described as before. Due to some isotopic substitution, the absorption correction and the deuterium scattering length were refined, the latter with the assumption that D(4) was stoichiometric. Unfortunately, the quality of the data was insufficient to allow free refinement of the D_3O^+ geometry and the unit was entered as a rigid body with the same geometry used in refinement of the protonated salt. The thermal parameters of the sulfate oxygen atoms were again constrained to have the same values. Even with these constraints the negative value of the S thermal parameter indicates that there are still problems with refining this model from this dataset. The refined structural parameters are displayed in *Table 4.7* and the refinement profile in *Figure 4.14*. Changing the orientation of the D_3O^+ unit so that the O(4)—D(1) bonds point towards the sulfate oxygen atoms resulted in a worse refinement, R_{wp} = 5.2%, χ^2 = 7.65. This is in agreement with the observation that the H_3O^+ orientation in $(H_3O)Fe_3(SO_4)_2(OH)_6$ is defined by hydrogen bonding to the hydroxy groups and not to the sulfate oxygen atoms.

While it is expected that the structures of the H_3O^+ and D_3O^+ ions will be different, there is little structural information for the D_3O^+ unit in the literature. Higher resolution diffraction studies and/or *ab initio* calculations are required to define the geometries of these ions in the jarosite structure.

atom (Wyckoff site)	*x*	*y*	*z*	U_{iso}/Å^2	*site symmetry*	*fractional occupancy*
Fe (9d)	0.16667	-0.16667	-0.16667	0.005 (7)	2/M(110)	0.948 (9)
S (6c)	0.00000	0.00000	0.3084 (8)	-0.08 (8)	3M(100)	1.000
O1 (6c)	0.00000	0.00000	0.39560 (46)	0.013 (7)	3M(100)	1.000
O2 (18h)	0.22343 (29)	-0.22343 (29)	-0.05552 (22)	0.013 (7)	M(110)	1.000
O3 (18h)	0.12840 (33)	-0.12840 (33)	0.13631 (27)	0.013 (7)	M(110)	1.000
O4 (6c)	0.00000	0.00000	-0.02216 (90)	0.0076 (10)	3M(100)	0.500
D1 (18h)	-0.07224 (*)	0.07224 (*)	-0.03859 (90)	0.284 (21)	M(110)	0.500
D4 (18h)	0.1955 (4)	-0.1955 (4)	0.10671 (4)	0.037 (7)	M(110)	1.000

Table 4.7. Structural parameters for $(D_3O)Fe_3(SO_4)_2(OD)_6$ at 2K in the space group $R\bar{3}m$ with Z = 3. Figures with asterisks are reported without errors because they were subject to rigid body constraints in the refinement that did not allow variation in that parameter. Cell parameters: a = 7.3444 (8)Å and c = 16.9034 (18)Å. R_{wp} = 4.6% and χ^2 = 6.1.

4.7.6 $(D_3O)Fe_3(SO_4)_2(OD)_6$: Warren-lineshape

No additional Bragg peaks were seen at the lowest temperature; instead we observed a broad asymmetric peak centred at $Q \approx 1.05\text{Å}^{-1}$ (where $Q = 2\pi/d$) indicative of short-range magnetic correlations [*Figure 4.15*]. Nuclear Bragg peaks were excluded from the diffuse scattering, and the data that remained were fitted to a Warren function[44,45] which describes the static structure factor, $P_{2\theta}$, for scattering from 2-D moments with a propagation vector $\boldsymbol{Q}$ and a spin-spin correlation length L:

$$P_{2\theta} = Km\frac{F_{hk}^2\left(1+\cos^2 2\theta\right)}{2\left(\sin\theta\right)^{3/2}}\left(\frac{L}{\lambda\sqrt{\pi}}\right)^{1/2} \qquad (4.5)$$

where $a = \left(2\sqrt{\pi}\,L/\lambda\right)\left(\sin\theta - \sin\theta_0\right)$, K is a scaling constant, m is the multiplicity of the reflection, F_{hk} is the two-dimensional structure factor, λ is the wavelength, θ_0 is the peak position, and the function $F(a)$, which is proportional to an integral of the scattering strength over different sizes and orientations of correlated moments, is calculated self-consistently from L and the scattering geometry. This yielded a correlation length of $L = 19 \pm 2$Å, the approximate point to point distance across an individual Kagomé star. The fitted peak is centred at $Q = 1.05\text{Å}^{-1}$, close to the position of the (2 1) peak of the $\sqrt{3}$ x $\sqrt{3}$ spin-structure (1.09Å^{-1}) which indicates that the spin-fluid ground state is based on this configuration. Comparison with the pattern obtained at 25K revealed no significant change, indicating that short-range ordering is largely established before the 13.8K transition in χ_m.

4.7.7 $(D_3O)Fe_3(SO_4)_2(OD)_6$: triple-axis measurements

The diffractometer was initially configured as a two-axis instrument, i.e. without energy analysis, with an incident energy of 5THz (λ = 1.989Å); data were collected for 1E7 counts after 5E6 counts equilibration at each point. $S(Q)$ measured at $Q = 1.4\text{Å}^{-1}$, which is in the region of the strong diffuse scattering but avoids the nearby Bragg peak, is found to rise steadily as the sample is cooled from approximately $4T_f$ [*Figure 4.16*]. The development of short-range magnetic correlations was more marked when the incident neutron energy was reduced to 3THz (λ = 2.568Å) and the instrument was reconfigured as a triple axis spectrometer with an energy resolution of $\Delta\omega \leq 0.22$THz. After normalisation to the intensity of the (0 0 3) reflection, the scattering intensity at this wavevector was found to be reduced by a factor of 4 by the change in spectrometer configuration. Thus, 75% of the neutrons scattered at 2K are from fluctuations faster than 0.22THz and are rejected by the analyser. The observation that these correlations set in at temperatures higher than the freezing temperatures observed with dc and ac susceptibility is consistent with the much higher frequency probed in these relatively low resolution measurements. The gradual slowing of the short-range magnetic fluctuations

based on the $\sqrt{3}$ x $\sqrt{3}$ structure also leads to a reduction, with improving energy resolution, of the temperature at which the correlations set in.

4.8 $(D_3O)Fe_{3-x}Al_x(SO_4)_2(OD)_6$

Deliberate dilution of the magnetic Fe^{3+} sites by diamagnetic Al^{3+} allows investigation of the competition between the different ground states in this Kagomé system, and to probe the spin-fluid itself. In order to examine the possibility that the spin-fluid ground state in $(H_3O)Fe_3(SO_4)_2(OH)_6$ is a consequence of an exchange pathway that operates through the H_3O^+ cations, other members of the jarosite series ($A^+ = Na^+$, ND_4^+, Ag^+, and Rb^+) which have lower occupations of magnetic sites were also studied.

4.8.1 Dc susceptibility

Dc magnetic susceptibility data were taken between 1.8 and 330K in an applied magnetic field of 100G. *Figure 4.17* shows clearly a divergence of the fc and zfc data at high temperatures, above a broad cusp that corresponds to in-plane antiferromagnetic correlations. A second, sharper cusp is observed at 25.5K, accompanied by a second divergence of the zfc and fc susceptibility. This behaviour contrasts with that of the undiluted deuterated hydronium jarosite, in which there is far less divergence in χ_m at higher temperature, and the sharper cusp at lower temperatures is seen at 13.8K. The inability of current KHAFM theory to explain such an increased divergence at higher temperatures in a diluted Kagomé antiferromagnet suggests that this response is not from the diluted Kagomé system, but is instead due to some ferromagnetic impurity species. This view is supported by the absence of similar divergence in *all* the other members of the jarosite series studied. Dc suceptibility measurements have shown that these less magnetically concentrated materials have similar critical temperatures, ~ 50K, which indicates that their magnetic structures are very similar.

That, for example, $(ND_4)Fe_3(SO_4)_2(OD)_6$ [*Section 4.10*] shows no significant fc/zfc separation above T_c while $AgFe_3(SO_4)_2(OD)_6$ [*Section 4.11*] does, is most simply explained by the presence of a small amount of ferromagnetic impurity in the argentojarosite phase that is not seen in the X-ray or neutron diffraction patterns. Whether or not this impurity is present depends on the synthesis conditions.

The discontinuity seen at 4.5K in the dilute sample is an artefact of the SQUID temperature control.

To a first approximation, the high temperature value of θ_w is related to the strength of nearest-neighbour exchange according to the relation:[46]

$$|\theta_w| = \frac{2}{3} zS(S+1)k_B|J| \qquad (4.6)$$

where z is the number of nearest neighbours.

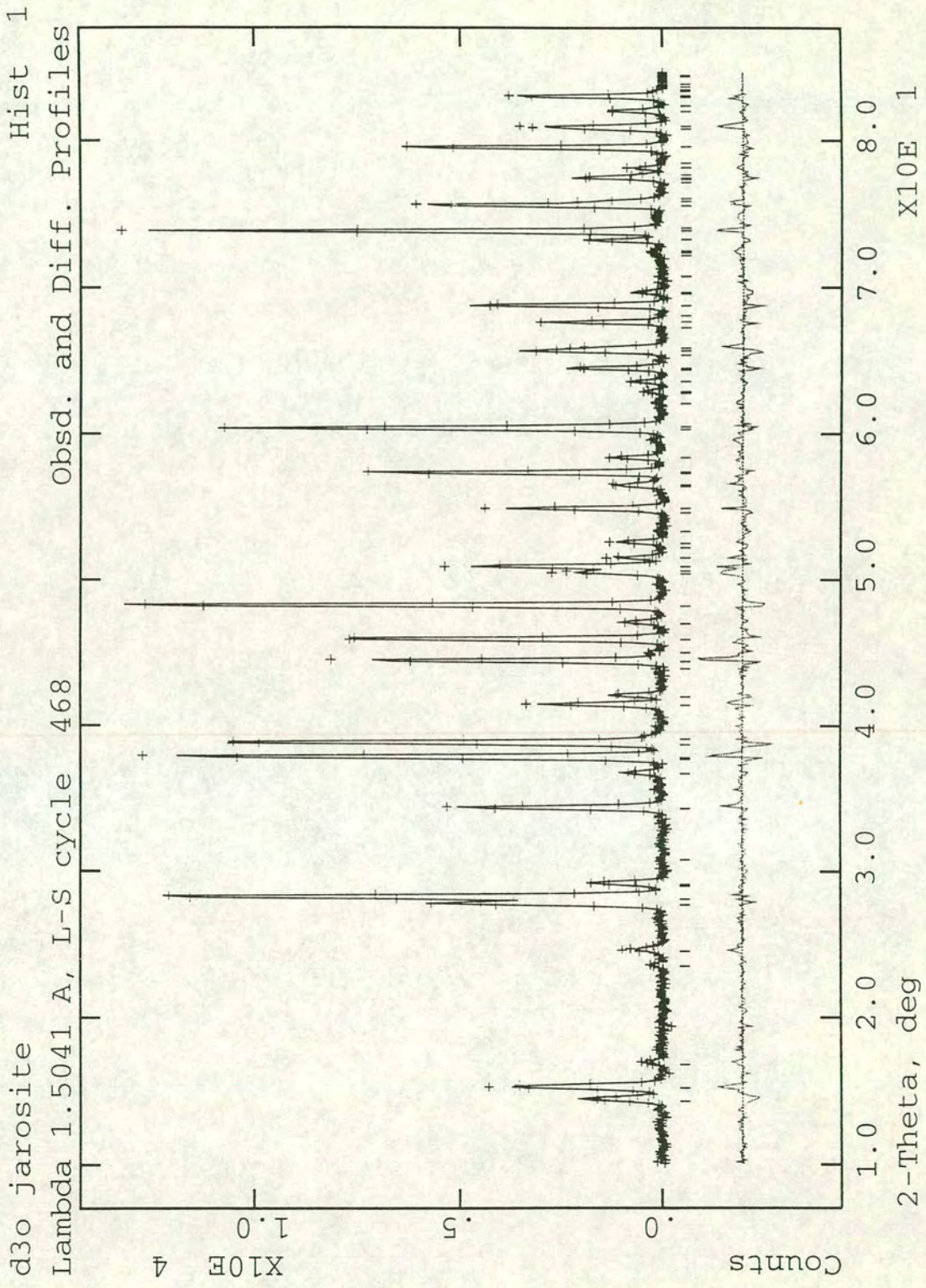

Figure 4.14. Fit of refined profile to neutron diffraction data for $(D_3O)Fe_3(SO_4)_2(OD)_6$ using the $R\bar{3}m$ space group.

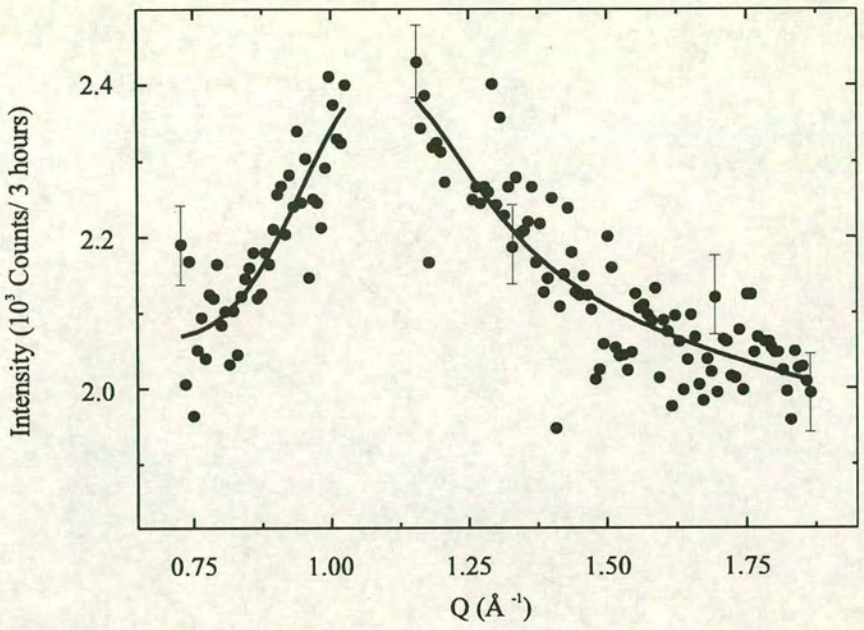

Figure 4.15. Diffuse scattering profile from deuterated hydronium jarosite at 2K with a fit to the Warren lineshape function centred near the (2 1) reflection of the √3 x √3 spin structure. Breaks in the data and fit indicate regions where nuclear Bragg peaks have been subtracted.

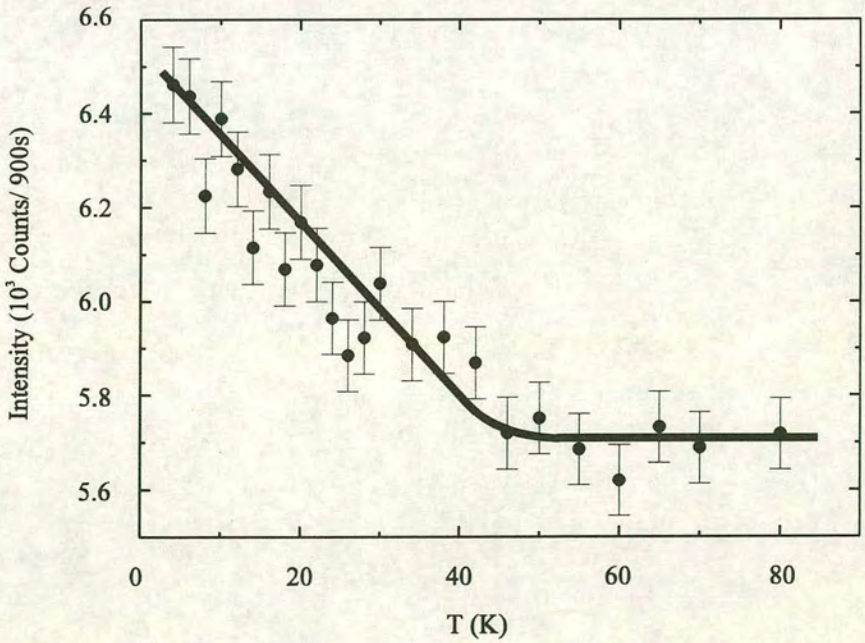

Figure 4.16. Temperature dependence of the diffuse scattering from deuterated jarosite at Q = 1.4Å and $\Delta\omega \leq 0.22$THz. The line through the data provides a guide to the eye.

The reduction of θ_w to -900 ± 250K [compared with -1500 ± 300K in $(D_3O)Fe_3(SO_4)_2(OD)_6$] is an expected consequence of diamagnetic dilution reducing the mean-field experienced by any Fe moment, and so the effective value of J. The increase in the temperature of the cusp in χ_m is compatible with both a release of frustration at lower temperatures, and the system becoming more 3-D as a result of a relative increase in smaller terms in the exchange energy Hamiltonian, i.e. increased interlayer exchange. The crossover to 3-D behaviour stabilises the formation of a long-range magnetic order [*Section 2.1*] and will therefore act to increase T_c as the interlayer interactions become stronger.

4.8.2 Neutron diffraction

Neutron diffraction was performed on the deuterated sample of $(D_3O)Fe_{3-x}Al_x(SO_4)_2(OD)_6$ using the D1B diffractometer at ILL using a pyrolytic graphite (0 0 2) monochromator at a wavelength of 2.52Å. The detectors of D1B have an angular range of $2\theta = 80°$ and may be moved so as to cover angles within the range $-60° < 2\theta < 144°$. Diffraction patterns were taken at 1.4K and 30.8K from ~ 0.1g of sample, and the structure refined using the $R\bar{3}m$ spacegroup. No Bragg peaks were observed from the vanadium sample can. Data collection took 5 hours (18.8E6 events) and 2 hours (7.5E6 events) respectively. At higher temperature the diffraction pattern shows no evidence of long-range magnetic order, only a broad, asymmetric peak centred at $Q = 1.06Å^{-1}$ which corresponds to the (2 1) reflection of the $\sqrt{3}$ x $\sqrt{3}$ structure. This peak was corrected for nuclear Bragg scattering and least-squares fitted to a Warren function to yield a spin-spin correlation length $L = 16.2 \pm 2.5Å$. On cooling there is a reduction in diffuse intensity and additional Bragg scattering is observed which may be attributed to long-range magnetic order. These additional reflections were indexed with a unit cell with the same dimensions as the nuclear cell in the *ab* plane but doubled in the *c* axis; similar magnetic scattering has been observed in $KFe_3(SO_4)_2(OD)_6$.[47]

4.8.3 Rietveld refinement

The restricted two-theta range of D1B prevents unambiguous refinement of the crystal structure parameters, so they were allowed to vary freely and attain unphysical values that will not be discussed here. The structural contribution was thus used as a background for modelling the magnetic peaks which could be properly refined in such a short data set. With this in mind, the refined values R_{wp} = 1.2 and χ^2 = 9.099 have little meaning. Previous work suggested a model for the magnetic order in which the directions of moments in the second-half of the magnetic unit cell are reversed[47,48] and the magnetic layers have the sequence order ...ABC-A-B-C..., this then doubles the magnetic c-lattice parameter. We assigned this magnetic structure to the $P\bar{3}$ space group and modelled the spin structure by the introduction of a second, purely magnetic, phase in the space group $P\bar{3}$ with magnetic vectors located at each of the iron atoms and having the in-plane q = 0 structure. The background and profile parameters were refined and modelled as for hydronium jarosite. The refined profile is displayed in *Figure 4.18*. Assuming an iron occupancy given by the chemical analysis, the refined ordered

sublattice moment of 1.02 (10)μ_B, suggests that ~83% of the moment of Fe^{3+} (spin-only value for $3d^5$ is 5.92μ_B) does not contribute to the magnetic Bragg peaks and so are still contributing to short-range static order and rapid fluctuations. A projection of this spin structure along the *c* axis is shown in *Figure 4.19* and magnetic vectors in the space group $P\bar{3}$ are listed in *Table 4.8.*

atom	*x*	*y*	*z*	m_x	m_y	m_z
Fe (1)	0.5	0.5	0.75	-0.8667	0.5000	0.0000
Fe (2)	0.6667	0.8333	0.4167	0.8667	0.5000	0.0000
Fe (3)	0.8333	0.6667	0.0833	0.0000	-1.0000	0.0000

Table 4.8. Positional parameters of iron atoms and refined magnetic unit vectors in $(D_3O)Fe_{3-x}Al_x(SO_4)_2(OD)_6$. *Magnetic cell parameters: a = 7.3453(30)Å and c = 33.997(31)Å in space group* $P\bar{3}$ *with Z = 3. The vectors are defined in Cartesian geometry with the x-axis parallel to the crystallographic a-axis, and the z-axis parallel to the crystallographic c-axis.*

4.8.4 Discussion of exchange pathways

These experiments have shown that dilution of the magnetic sites in the jarosite structure stabilises the creation of long-range magnetic order. Previous work describing the magnetic exchange has been in terms of a ferromagnetic or antiferromagnetic interaction between a magnetic atom and its two further neighbours, either in the plane above or below it.[46] Such a picture ignores the actual magnetic exchange structure and in order to explain this effect we must instead examine the individual exchange pathways between Fe atoms. The simplest intralayer and interlayer exchange pathways are mediated through a system of hydroxy[49] and sulfate[50] groups, and are shown in *Figure 4.20.*

The compromise spin configuration of the isolated triangular plaquette contains three spins at 120° to each other. The vector sum of these spins is zero so the net mean-field experienced by a spin interacting equally with all three spins must also be zero. As interplanar exchange acts symmetrically through the three basal oxygen atoms of the sulfate group, the spins of neighbouring planes must necessarily interact with a triangle of three 120° spins and so there is no net interaction. Dilution of the Kagomé sites will disrupt this balance and leads to a net exchange between layers which stabilises certain long-range ordered spin configurations. Thus, in the jarosite crystal structure we have the remarkable situation of there being no net interaction between perfectly occupied magnetic lattices;

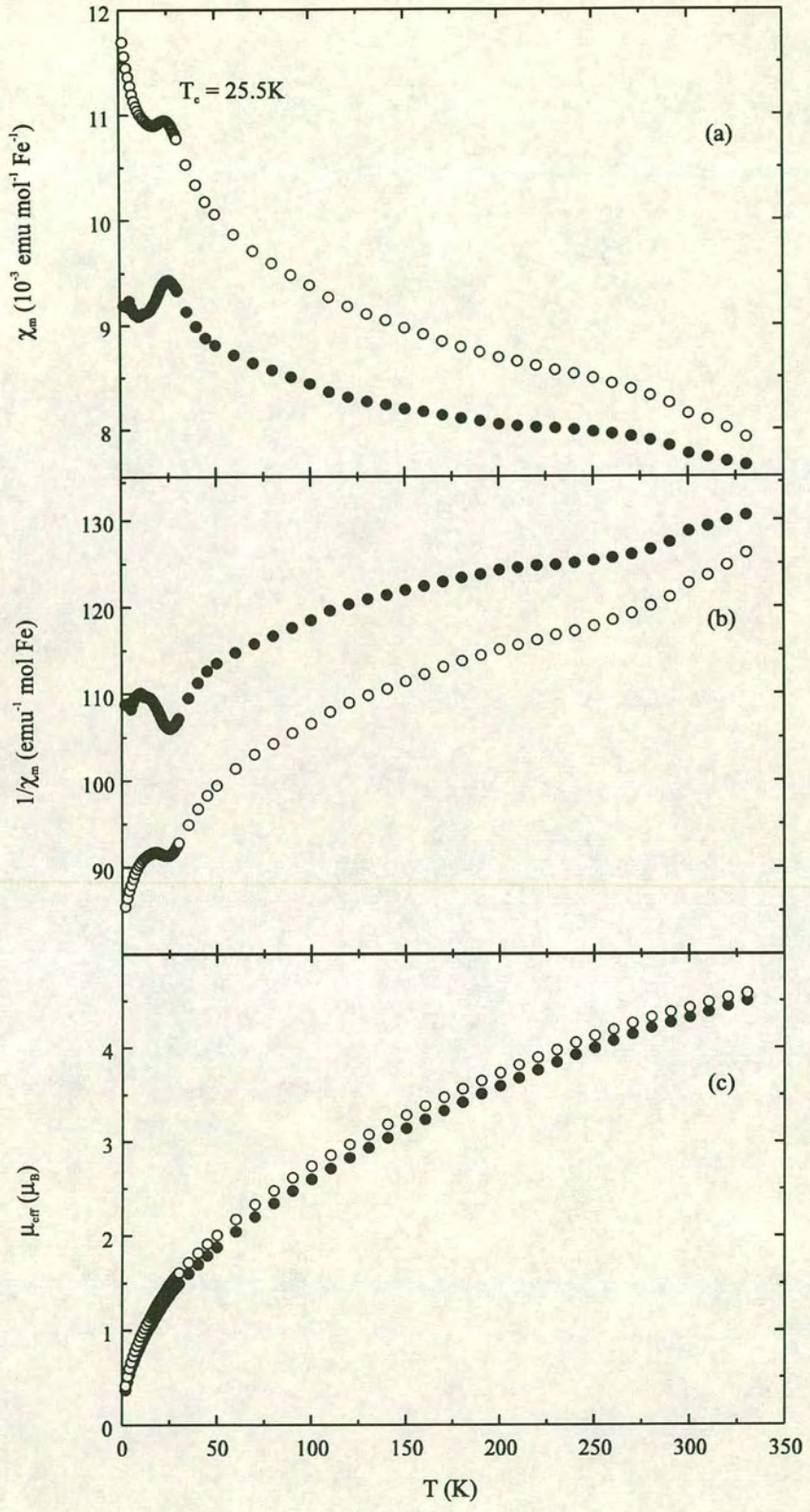

Figure 4.17. (●) Zero-field-cooled and (○) field-cooled dc susceptibility measurements as a function of temperature for $(D_3O)Fe_{3-x}Al_x(SO_4)_2(OD)_6$: (a) molar susceptibility, χ_m; (b) inverse susceptibility, $1/\chi_m$; (c) effective moment, μ_{eff}.

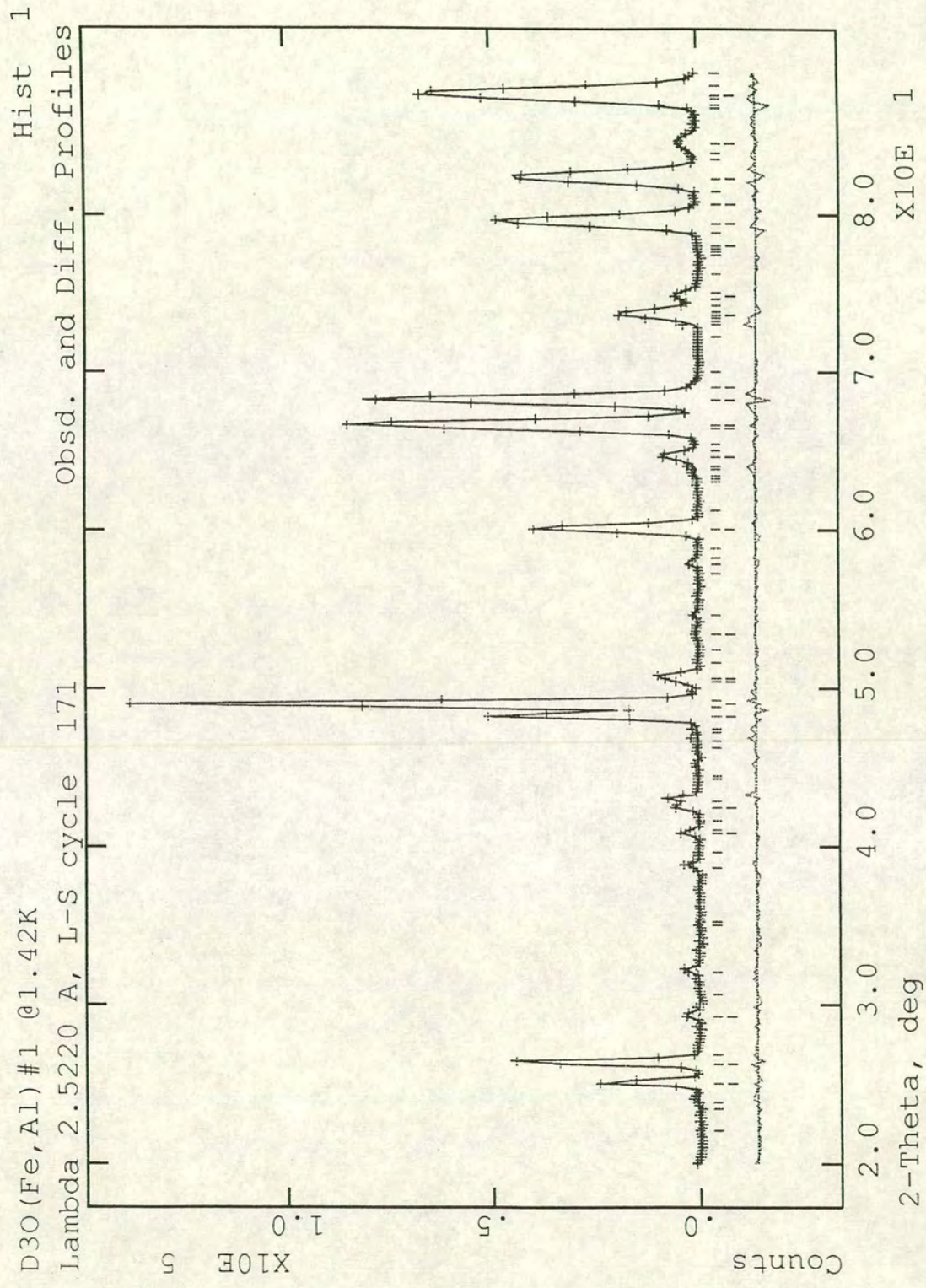

Figure 4.18. Fit of refined profile to neutron diffraction data for $(D_3O)Fe_{3-x}Al_x(SO_4)_2(OD)_6$ using the $R\bar{3}m$ nuclear and $P\bar{3}$ magnetic unit cells.

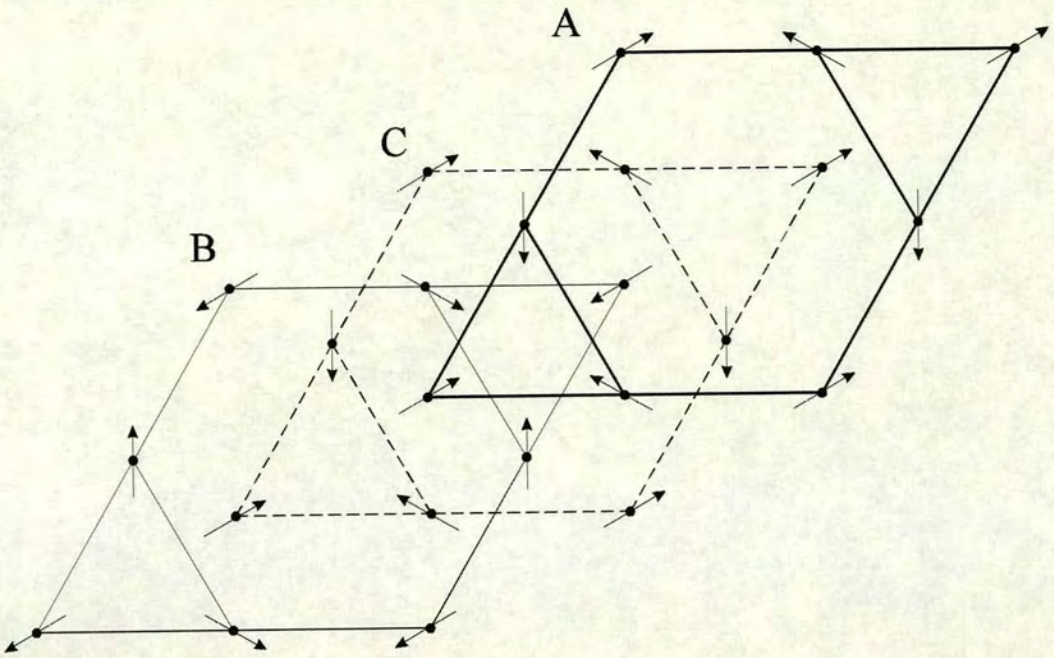

Figure 4.19.Spin directions at iron atoms of the three Kagomé planes (ABC) of the hexagonal unit cell of $(D_3O)Fe_{3-x}Al_x(SO_4)_2(OD)_6$. *The magnetic cell is doubled: reversed spin directions in the second half of the magnetic cell are not shown. In-plane order corresponds to the q = 0 configuration .*

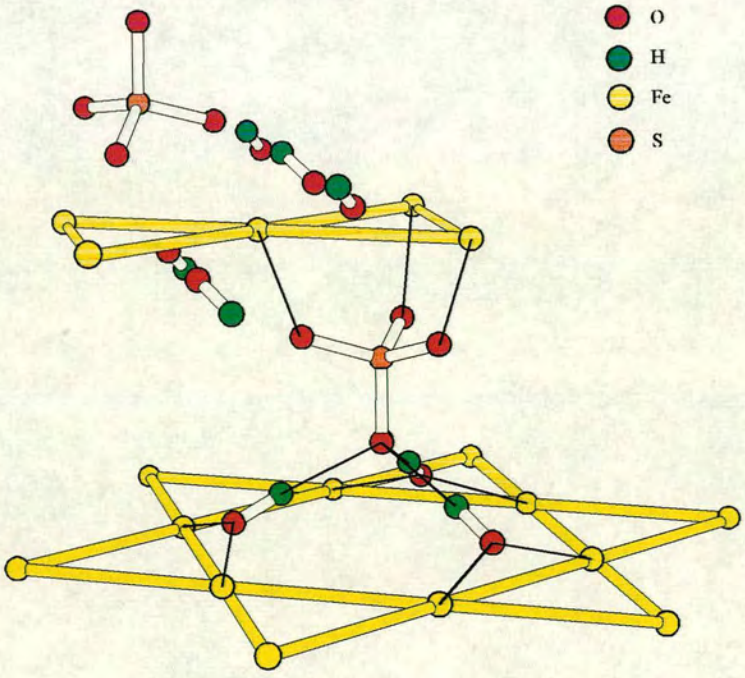

Figure 4.20. Intraplane and interplane exchange pathways in the jarosite structure mediated through hydroxy and sulfate groups. The lines drawn indicate the closest through space interactions.

dilution causes an increase in the mean-field experienced by the moments at low temperatures and this increased exchange conectivity releases the frustration associated with the Kagomé lattice. This leads to the observed increase in the temperature of the cusp in the dc susceptibility. Hydronium jarosite presents the first example of a magnetic system where diamagnetic dilution causes the system to have long-range order. As the disruption in the exchange field around such a defect decays rapidly with distance, a non-uniform distribution would stabilise long-range order in regions where they have a high concentration; areas with relatively few such defects would still have only short-range order. The strength of further-neighbour intraplane interactions will similarly be affected by dilution of the magnetic atoms. The relative strengths of these additional intraplane and interplane interactions, and how they change with the degree of dilution, is not immediately obvious and little more can be said without detailed calculations.

4.9 $NaFe_3(SO_4)_2(OD)_6$

Sodium jarosite has a magnetic occupancy of 95 ± 4%, and so is an example of a diluted Kagomé antiferromagnet. Neutron diffraction [*Section 4.9.1*] has shown it to possess the same long-range spin configuration as $(D_3O)Fe_{3-x}Al_x(SO_4)_2(OD)_6$. This supports the conclusion that the spin-fluid ground state in $(H_3O)Fe_3(SO_4)_2(OH)_6$ is indeed a consequence of its high magnetic coverage, and not of any changes to the exchange pathway which result from substitution of the A^+ cation.

Dc susceptibility measurements taken in an applied magnetic field of 100G show clear spin-glass-like separation [*Figure 4.21*] above and below a sharp cusp at T_c = 51K (θ_w = -1050 ± 100K). Comparison of the fc/zfc separation above T_c with that of $(D_3O)Fe_{3-x}Al_x(SO_4)_2(OD)_6$ suggests the presence of a small amount of ferromagnetic impurity. As no other magnetic transitions are observed the spin-glass-like separation below T_c is intrinsic to $NaFe_3(SO_4)_2(OD)_6$. The presence or not of long-range magnetic order in this material was examined by powder neutron diffraction using the POLARIS diffractometer. The weak Bragg peak at d = 2.13Å attributed to the vanadium sample can was not excluded from the refinement. Neutron powder patterns were taken from ~ 8g of sample at 40, 50, and 300K. At 50K there was no evidence of long-range magnetic order; only a diffuse scattering of the form observed in the hydronium jarosite experiment was present. Again the lineshape of this scattering could not be analysed. The 40K pattern did show magnetic Bragg peaks and these were indexed to the q = 0 in-plane spin structure with a doubled c-axis. The nuclear and magnetic structure were refined from the 40K data collected over 11 hours (1800μA).

4.9.1 Rietveld refinement

Simultaneous refinement of the A and C bank data was performed using the $R\bar{3}m$ spacegroup and the structure of hydronium jarosite as a starting point. There was no evidence of crystalline impurity phases, which indicates that the ferromagnetic impurity could either be amorphous or only present in very small quantities, ≤ 2%. The magnetic contribution was modelled as a separate phase in the $P\bar{3}$

space group and the value of the sublattice magnetisation refined to 1.534 (27)μ_B. Absorption coefficients, deuterium scattering length, the background, profile parameters, and the sulfate oxygen atoms' thermal parameters were refined and modelled as for hydronium jarosite.

The 12-co-ordinate cavity in the sulfate layers is occupied by both Na and D_3O. A statistical distribution of these ions is assumed with the rigid D_3O unit in the same configuration as the hydronium salt. Free variance of fractional occupancy or thermal parameters of these species caused the refinement to diverge. For this reason, the thermal parameters of the D_3O unit were fixed at the values refined in $(D_3O)Fe_3(SO_4)_2(OD)_6$ and the Na and D_3O fractional occupancies were fixed at those obtained from chemical analysis. The refinement was now stable enough to allow the thermal parameter of the Na atom to vary. We were unable to separately refine the Fe occupancy and the thermal parameters freely so fractional occupation was also set at the chemically analysed value. The thermal parameters of the magnetic Fe atoms were constrained to be the same as the nuclear Fe atoms.

The GSAS package failed to predict magnetic reflections in the C bank data. This will not affect the magnetic refinement greatly as the form-factor dependence of the magnetic scatting intensity causes most of the magnetic scattering to be in the A bank d-spacing range. These peaks were not excluded from the refinement so that they could be displayed in the refinement profile, but will inflate the values of R_{wp} and χ^2. The refined profiles are displayed in *Figure 4.22* and the refined structural parameters for $NaFe_3(SO_4)_2(OD)_6$ are displayed in *Table 4.9*.

To further define the geometries of the species in the Na^+/D_3O^+ cavity higher resolution diffraction studies need to be done.

atom (Wyckoff site)	*x*	*y*	*z*	U_{iso}/Å^2	*site symmetry*	*fractional occupancy*
Fe (9d)	0.16667	-0.16667	-0.16667	0.0106 (4)	2/M(110)	0.95 (*)
S (6c)	0.00000	0.00000	0.30681 (26)	0.0110 (9)	3M(100)	1.000
O1 (6c)	0.00000	0.00000	0.39724 (15)	0.0153 (4)	3M(100)	1.000
O2 (18h)	0.22366 (9)	-0.22366 (9)	-0.05257 (7)	0.0153 (4)	M(110)	1.000
O3 (18h)	0.12625 (12)	-0.12625 (12)	0.13363 (8)	0.0153 (5)	M(110)	1.000
Na (3a)	0.00000	0.00000	0.00000	0.045 (4)	-3M(100)	0.585 (*)
O4 (6c)	0.00000	0.00000	-0.02740 (65)	0.0076 (*)	3M(100)	0.208 (*)
D1 (18h)	-0.07243 (*)	0.07243 (*)	-0.04412 (65)	0.2840 (*)	M(110)	0.208 (*)
D4 (18h)	0.19569 (12)	-0.19569 (12)	0.10791 (10)	0.0326 (6)	M(110)	1.000

Table 4.9. Structural parameters for $NaFe_3(SO_4)_2(OD)_6$ at 40K in the space group $R\bar{3}m$ with Z = 3. Figures with asterisks are reported without errors because they were subject to rigid body constraints or their values fixed. Nuclear cell parameters: a = 7.32581 (6) c = 16.59525 (20). χ^2 = 40.66. R_{wp} = 1.83% (A bank), 2.74% (C bank), 2.51% (combined data set). Sublattice moment: 1.534 (27)μ_B.

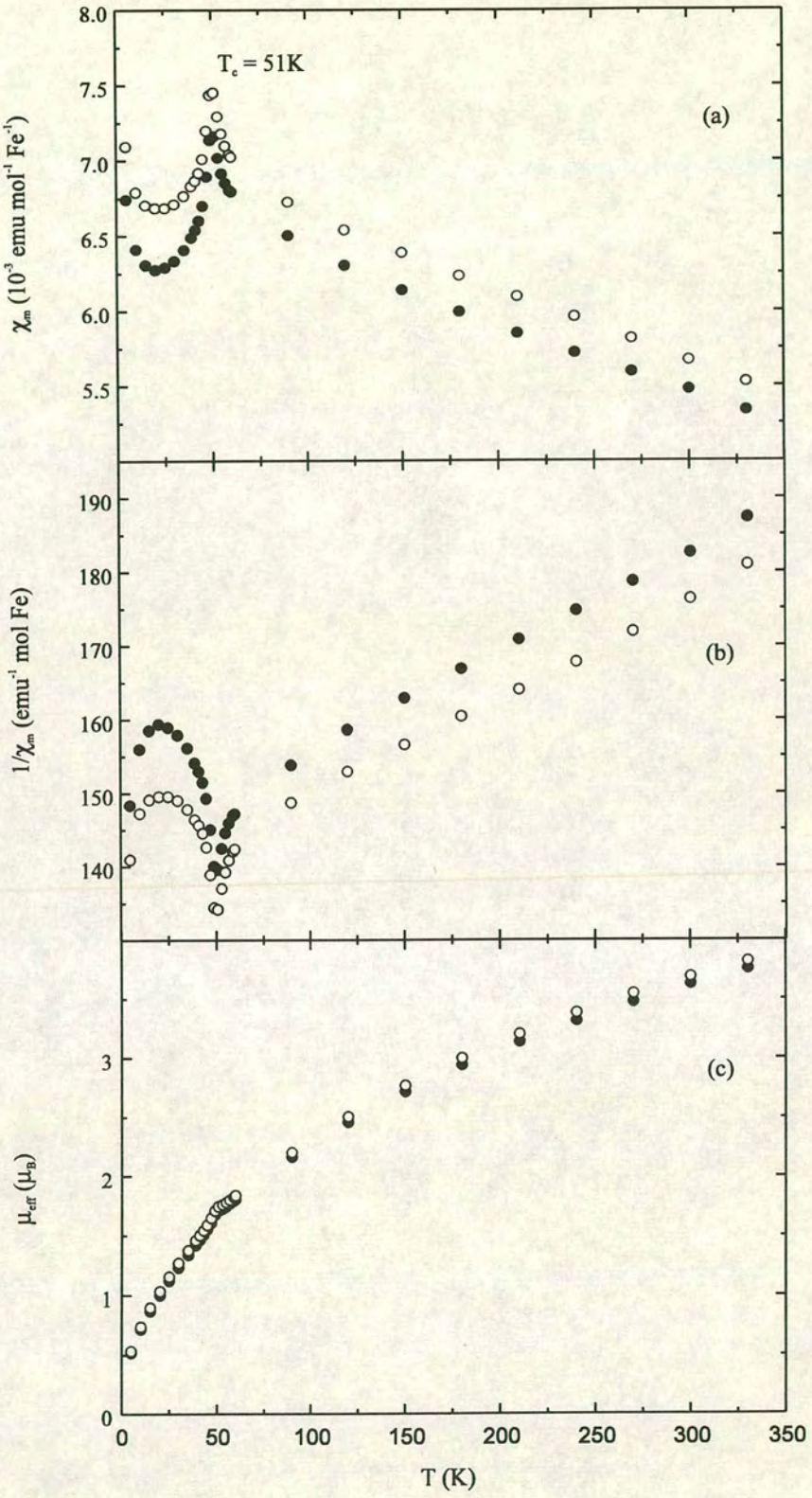

Figure 4.21. (●) Zero-field-cooled and (○) field-cooled dc susceptibility measurements as a function of temperature for $NaFe_3(SO_4)_2(OD)_6$: (a) molar susceptibility, χ_m, shows spin-glass-like separation at $T_f = 51K$; (b) inverse susceptibility, $1/\chi_m$; (c) effective moment, μ_{eff}.

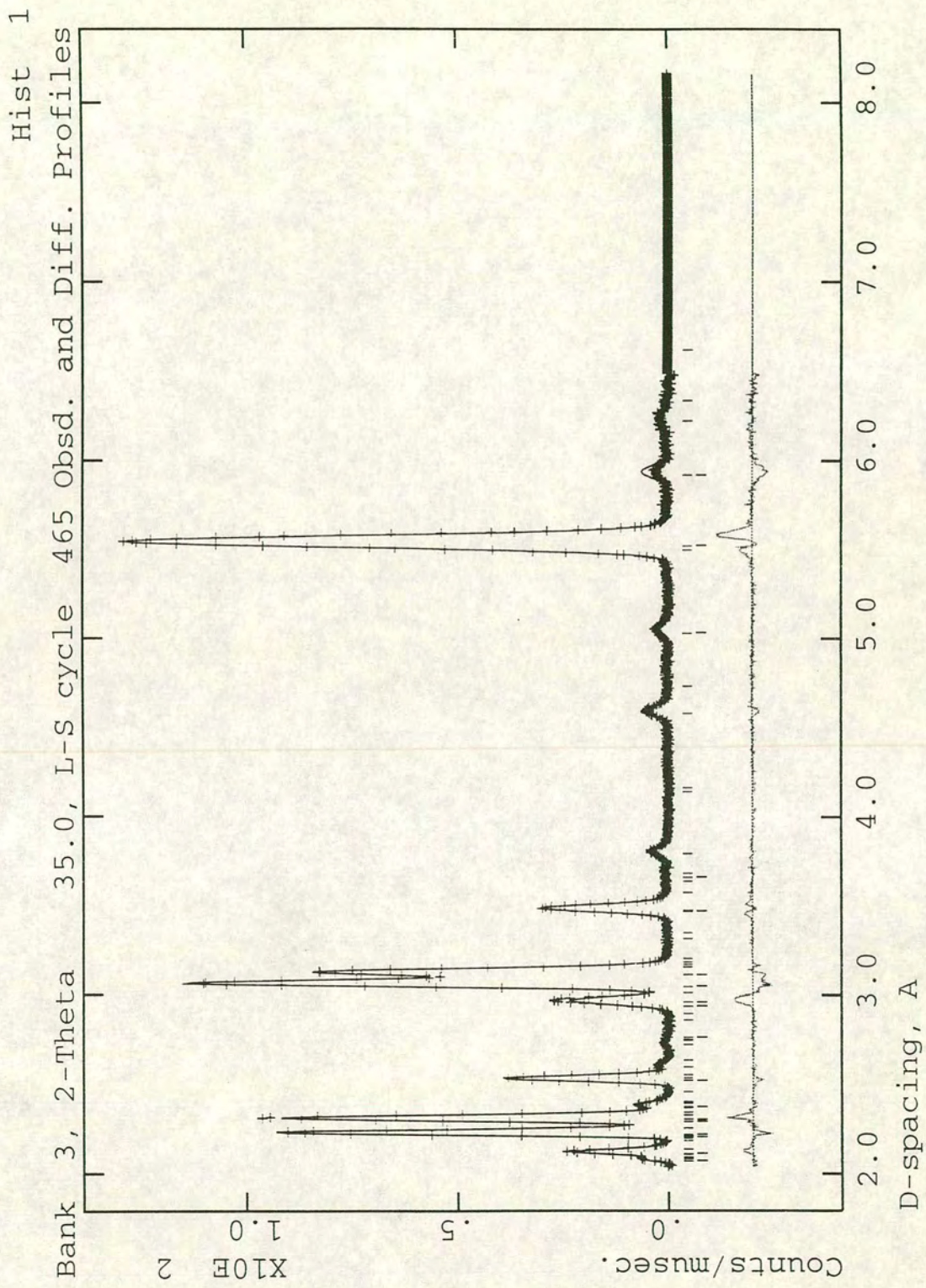

Figure 4.22(a). Fit of refined profile to A bank neutron scattering data for $NaFe_3(SO_4)_2(OD)_6$ using the $R\bar{3}m$ nuclear and $P\bar{3}$ magnetic unit cells.

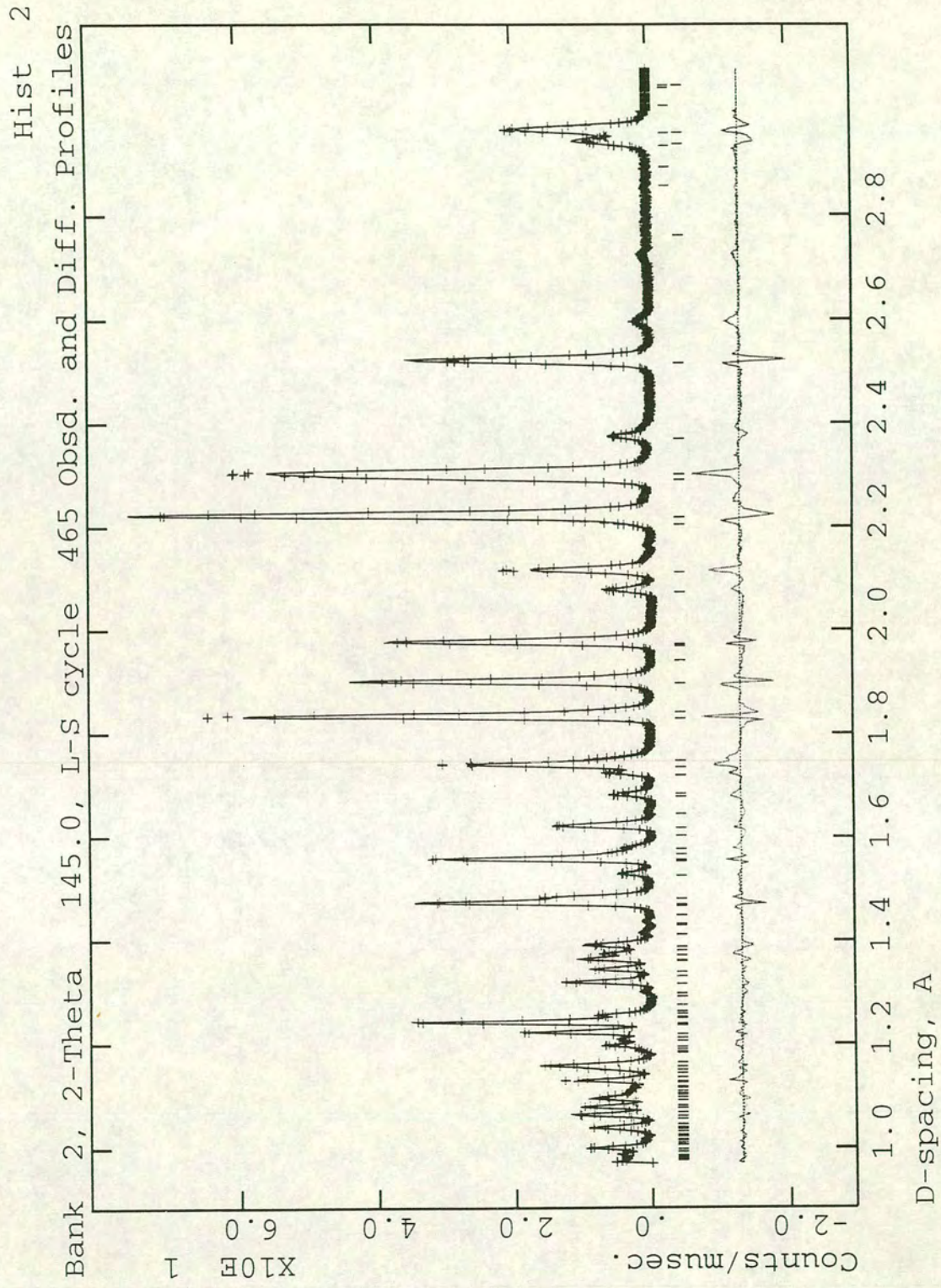

Figure 4.22(b). Fit of refined profile to C bank neutron scattering data for $NaFe_3(SO_4)_2(OD)_6$ using the $R\bar{3}m$ nuclear and $P\bar{3}$ magnetic unit cells.

4.10 $(ND_4)Fe_3(SO_4)_2(OD)_6$

Dc susceptibility measurements taken with a measuring field of 100G show clear spin-glass-like separation [*Figure 4.23*] above and below a sharp cusp at T_c = 47K (θ_w = -850 ± 100K). Powder neutron diffraction patterns were taken using the D2B diffractometer at the Institut Laue-Langevin. D2B has a angular range of 2θ= 5 - 165° (step size 0.1°) and a Ge (1 1 5) monochromator was used to provide neutrons with a wavelength of 1.5943Å. Neutron powder patterns from ~ 14g of sample were taken over 6 hours (5.2E5 events) at 1.5 and 60K. At 60K there was no evidence of long-range magnetic order; only diffuse scattering that was fitted to a Warren function centred at Q = 1.02Å with a spin-spin correlation length of 19.1 ± 0.1Å. As well as diffuse scattering with L = 15 ± 4Å, the 1.5K pattern did show magnetic Bragg peaks and these were indexed to the q = 0 in-plane spin structure with a doubled c-axis. The nuclear and magnetic structure were refined from the 1.5K data. There were no additional Bragg peaks from the vanadium can.

4.10.1Rietveld refinement

Refinement was performed using the $R\bar{3}m$ spacegroup and the structure of hydronium jarosite as a starting point. The magnetic contribution was modelled as a separate phase in the $P\bar{3}$ space group and the value of the sublattice magnetisation refined to 3.38 (7)μ_B. Absorption coefficients, deuterium scattering length, the background, profile parameters, and the sulfate oxygen atoms' thermal parameters were refined and modelled as for hydronium jarosite. Additional constraints used were that the ND_4^+ deuterium thermal parameters are equal and the unit is a rigid body as defined in *Table 4.10.* A statistical distribution of ND_4^+ and D_3O^+ ions is assumed. Stable refinements resulted only with the rigid D_3O^+ and ND_4^+ units in the same configuration and pointed towards the hydroxy oxygen atoms. Free refinement of fractional occupancy or thermal parameters of these species caused the refinement to diverge. For this reason, the thermal parameters of the D_3O^+ unit were fixed at the values refined in $(D_3O)Fe_3(SO_4)_2(OD)_6$ and the ND_4^+ and D_3O^+ fractional occupancies were fixed at those obtained from chemical analysis. The refinement was now stable enough to allow the thermal parameter on the ND_4^+ to vary. We were unable to separately refine the Fe occupancy and the thermal parameters freely so fractional occupation was also set at the value determined by chemical analysis. The thermal parameters of the magnetic Fe atoms were constrained to be the same as the nuclear Fe atoms.

The poor values of R_{wp} and χ^2, and the unstable thermal parameters [*Table 4.11*], reflect the inability of the refinement to describe the profile function [*Figure 4.24*]. The physical origin of this could be a slight structural distortion away from the $R\bar{3}m$ space group or the presence of some structurally similar impurity phase. Possible lower symmetry structures will be discussed in more detail in *Section 5.4.*

	x	*y*	*z*
N	0	0	0
D	0	-0.942809	-0.333334
D	-0.816496	0.471405	-0. 333334
D	0.816496	0.471405	-0. 333334
D	0	0	1

Table 4.10. Unit vectorsused to define the ND_4^+ rigid body.

atom (Wyckoff site)	*x*	*y*	*z*	U_{iso}/Å^2	*site symmetry*	*fractional occupancy*
Fe (9d)	0.16667	-0.16667	-0.16667	0.0002 (6)	2/M(110)	0.910
S (6c)	0.00000	0.00000	0.3056 (13)	0.036 (5)	3M(100)	1.000
O1 (6c)	0.00000	0.00000	0.38934 (40)	0.009 (9)	3M(100)	1.000
O2 (18h)	0.22362 (28)	-0.22362 (28)	-0.05663 (20)	0.009 (9)	M(110)	1.000
O3 (18h)	0.12983 (27)	-0.12983 (27)	0.13658 (25)	0.009 (9)	M(110)	1.000
O4 (6c)	0.00000	0.00000	-0.00665 (73)	0.0076(*)	3M(100)	0.170
D1 (18h)	-0.072403 (*)	0.072403 (*)	-0.02269 (90)	0.2840(*)	M(110)	0.170
N (6c)	0.00000	0.00000	-0.0107 (7)	0.0163 (35)	3M(100)	0.330
D (18h)	-0.07428 (*)	0.07428 (*)	-0.02996 (73)	0.1529 (171)	M(110)	0.330
D (6c)	0.00000	0.00000	0.04711 (73)	0.1529 (171)	3M(100)	0.330
D4 (18h)	0.19564 (29)	-0.19564 (29)	0.10762 (21)	0.018 (10)	M(110)	1.000

Table 4.11. Structural parameters for $(ND_4)Fe_3(SO_4)_2(OD)_6$ at 1.5K in the space group $R\bar{3}m$ with Z = 3. Figures with asterisks are reported without errors because they were subject to rigid body constraints or their values fixed. Nuclear cell parameters: a = 7.32816 (23)Å and c = 17.3004 (8)Å. χ^2 = 68.9%. R_{wp} = 10.4%. Sublattice moment = 3.38 (7)μ_B.

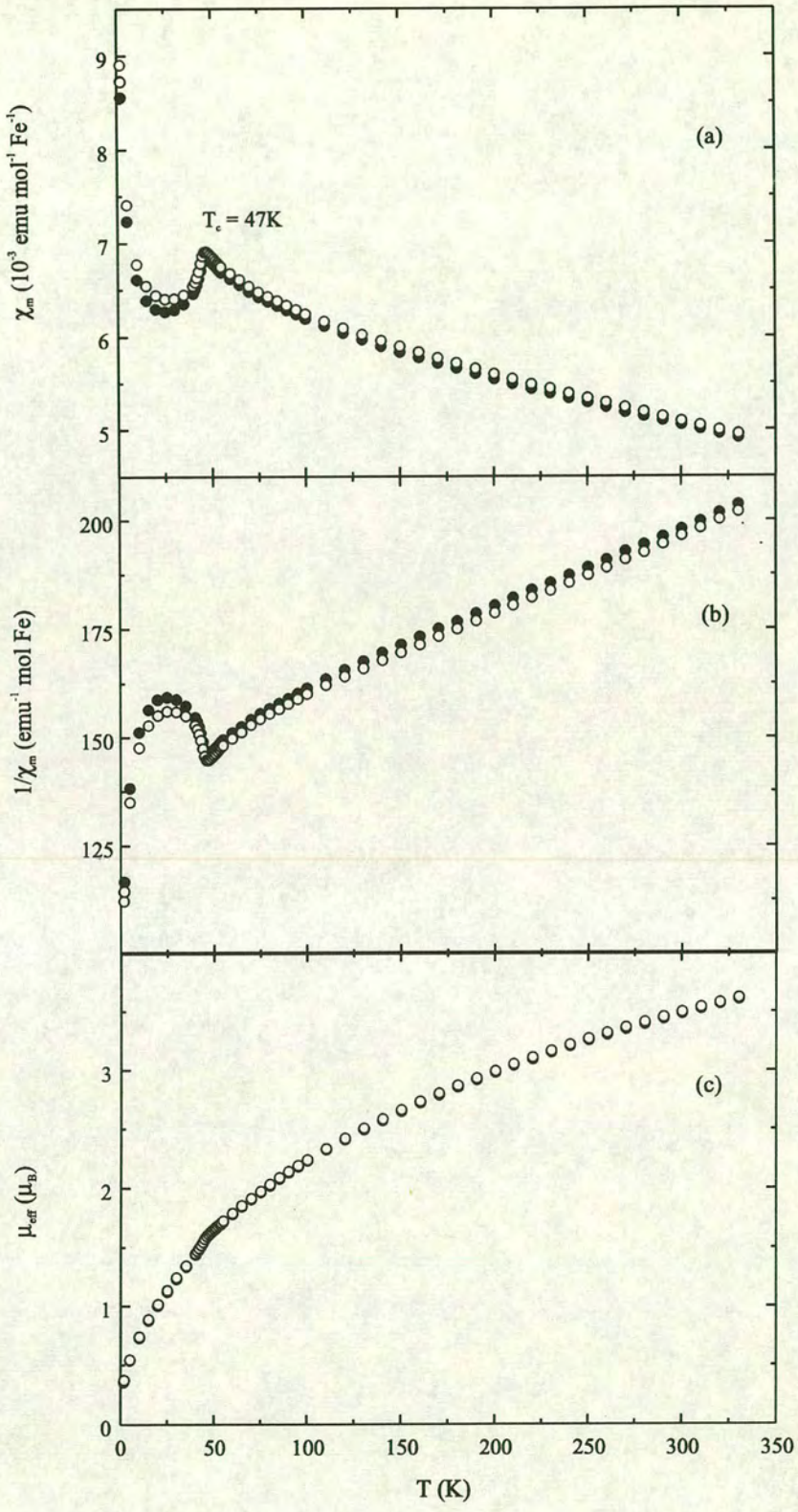

Figure 4.23. (●) Zero-field-cooled and (○) field-cooled dc susceptibility measurements as a function of temperature for $ND_4Fe_3(SO_4)_2(OD)_6$: (a) molar susceptibility, χ_m, shows spin-glass-like separation at T_f =47K; (b) inverse susceptibility, $1/\chi_m$; (c) effective moment, μ_{eff}.

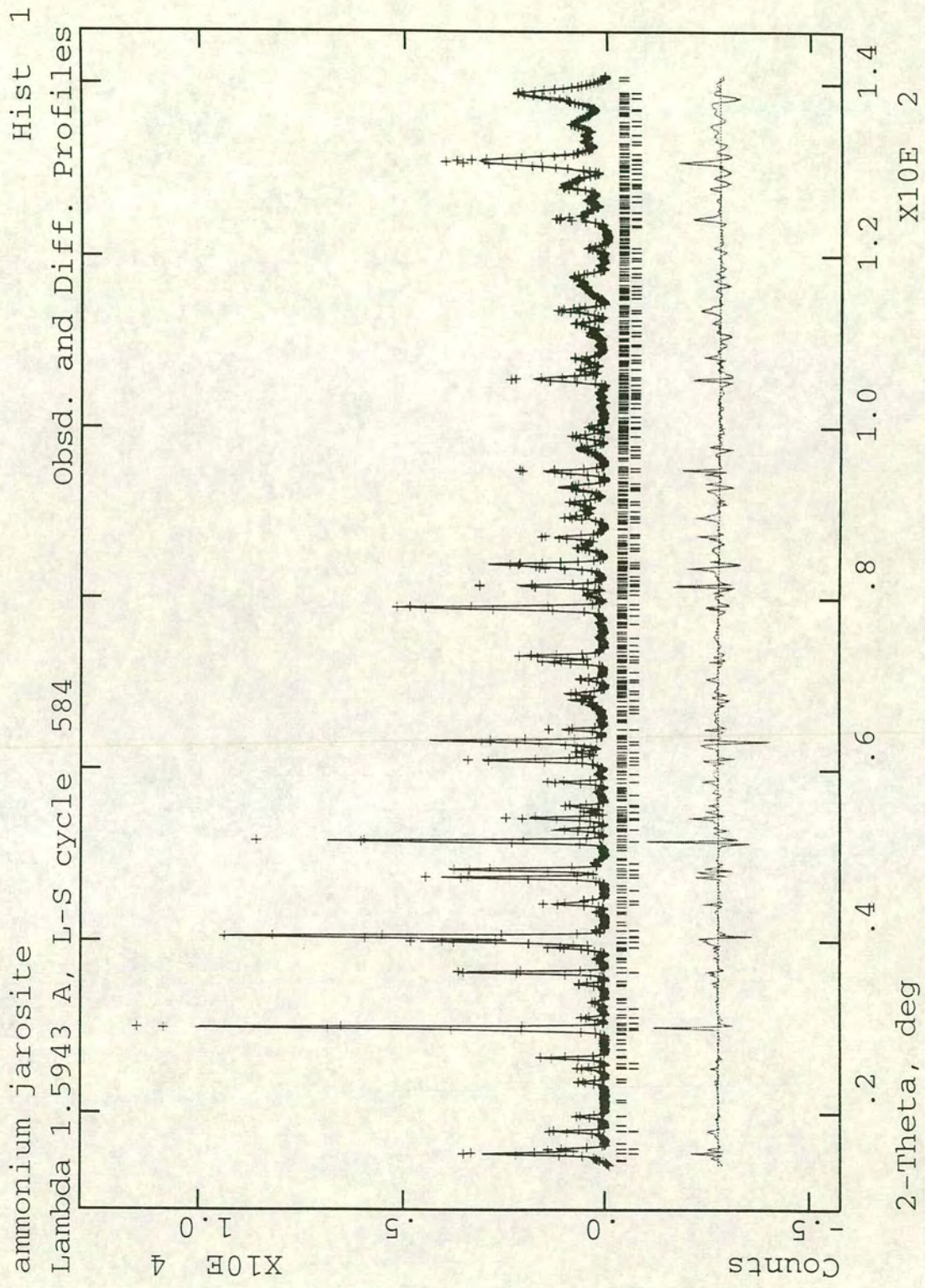

Figure 4.24. Fit of refined profile to neutron scattering data for $(ND_4)Fe_3(SO_4)_2(OD)_6$ *using the* $R\bar{3}m$ *nuclear and* $P\bar{3}$ *magnetic unit cells.*

4.11 $AgFe_3(SO_4)_2(OD)_6$

Dc susceptibility measurements taken with a measuring field of 100G show clear spin-glass-like separation [*Figure 4.26*] above and below a sharp cusp at T_c = 51K (θ_w = -2000 ± 250K). The large fc/zfc separation above and at T_c suggests a ferromagnetic impurity is again present. No Bragg peaks from additional phases are observed. Neutron diffraction was performed on the deuterated sample on the D1B diffractometer at ILL using a wavelength of 2.52Å. Patterns were taken at 1.5K and 65.0K and the structure refined using the $R\bar{3}m$ spacegroup. No significant coherent scattering was observed from the vanadium sample can. Data collection from ~ 1.2g of sample took 1 hour (5.7E6 events) and 1.25 hours (7.1E6 events) respectively. At higher temperature the Warren peak centred, at Q = 1.05Å^{-1}, was fitted L = 18.5 ± 0.8Å. At 1.5K the correlation length of the short-range order was fitted with L = 18.7 ± 2.2Å. The additional magnetic Bragg scattering was indexed to the q = 0 in-plane spin structure with a doubled c-axis.

4.11.1 Rietveld refinement

Refinement was performed using the $R\bar{3}m$ spacegroup and the structure of hydronium jarosite as a starting point. The magnetic contribution was modelled as a separate phase in the $P\bar{3}$ space group with the value of the sublattice moment refined to 2.42 (4)μ_B; magnetic lattice parameters a = 7.35796 (81) and c = 33.0506 (39). The background and profile parameters were refined and modelled as for hydronium jarosite. The Fe fractional occupancy was fixed at that obtained from chemical analysis and the D_3O^+/Ag^+ scattering was best described by only a rigid D_3O^+ unit with refined thermal parameters. Crystallographic structural parameters were allowed to vary freely and attain unphysical values, and so will not be discussed further. Again, the refined values R_{wp} = 2.3 and χ^2 = 18.4 have little meaning. The refined profile is displayed in *Figure 4.26*.

4.12 $RbFe_3(SO_4)_2(OD)_6$

Dc susceptibility measurements taken with a measuring field of 100G show clear spin-glass-like separation [*Figure 4.28*] below a sharp cusp at T_c = 45K (θ_w = -1000 ± 200K). Neutron diffraction was performed on the deuterated sample on the D1B diffractometer at ILL using a wavelength of 2.52Å. A pattern was collected from ~ 2.8g of sample held in a vanadium sample can at 1.5K over 1 hour (5.7E6 events) and the crystal and magnetic structures refined using the $R\bar{3}m$ and $P\bar{3}$ spacegroups respectively. No significant coherent scattering was observed from the sample can. The Warren peak was centred at Q = 1.01Å^{-1} and had a correlation length of L = 22.5 ± 4Å. The Fe

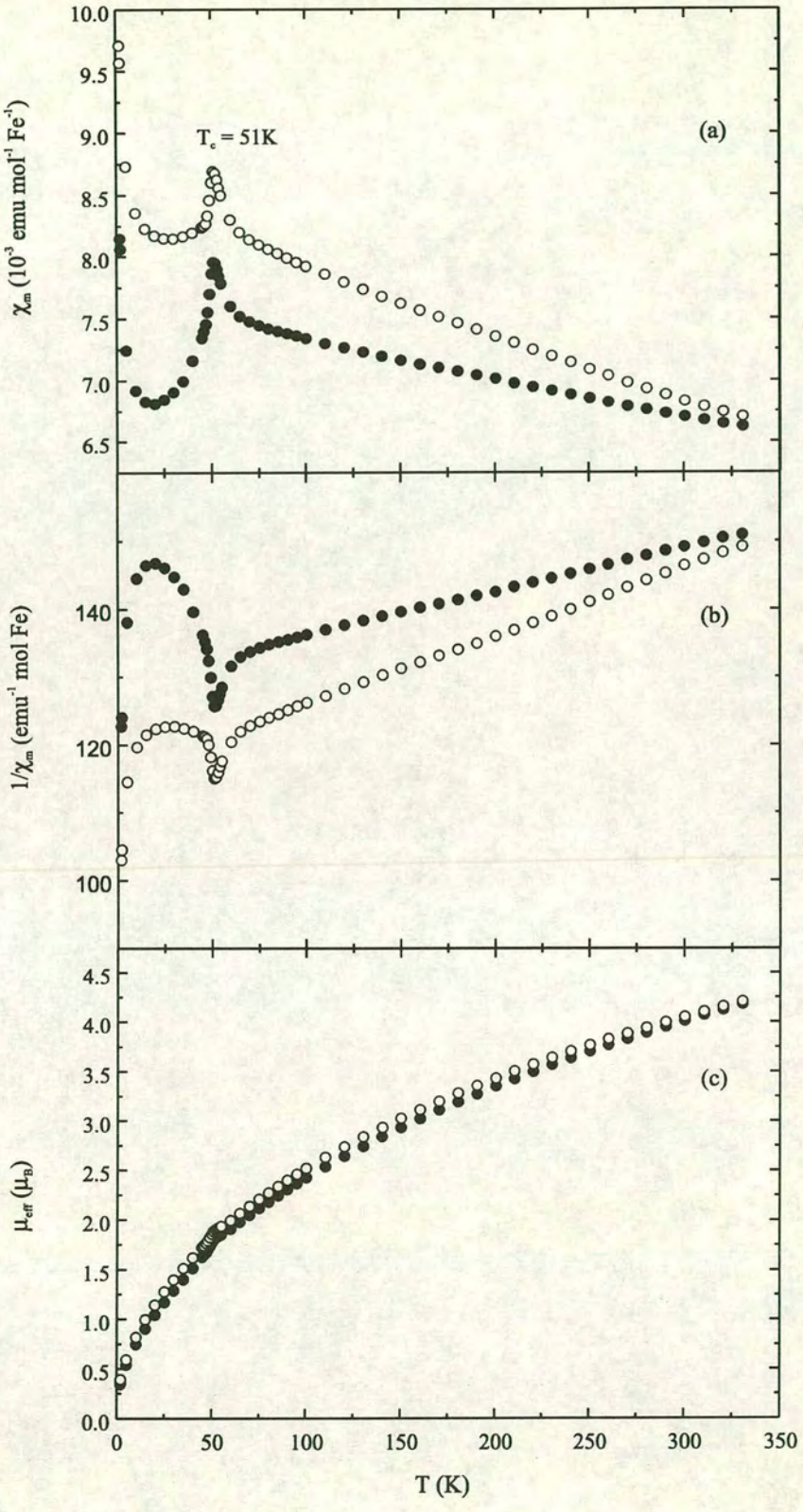

Figure 4.25. (●) Zero-field-cooled and (○) field-cooled dc susceptibility measurements as a function of temperature for $AgFe_3(SO_4)_2(OD)_6$: (a) molar susceptibility, χ_m, shows spin-glass-like separation at T_f =51K; (b) inverse susceptibility, $1/\chi_m$; (c) effective moment, μ_{eff}.

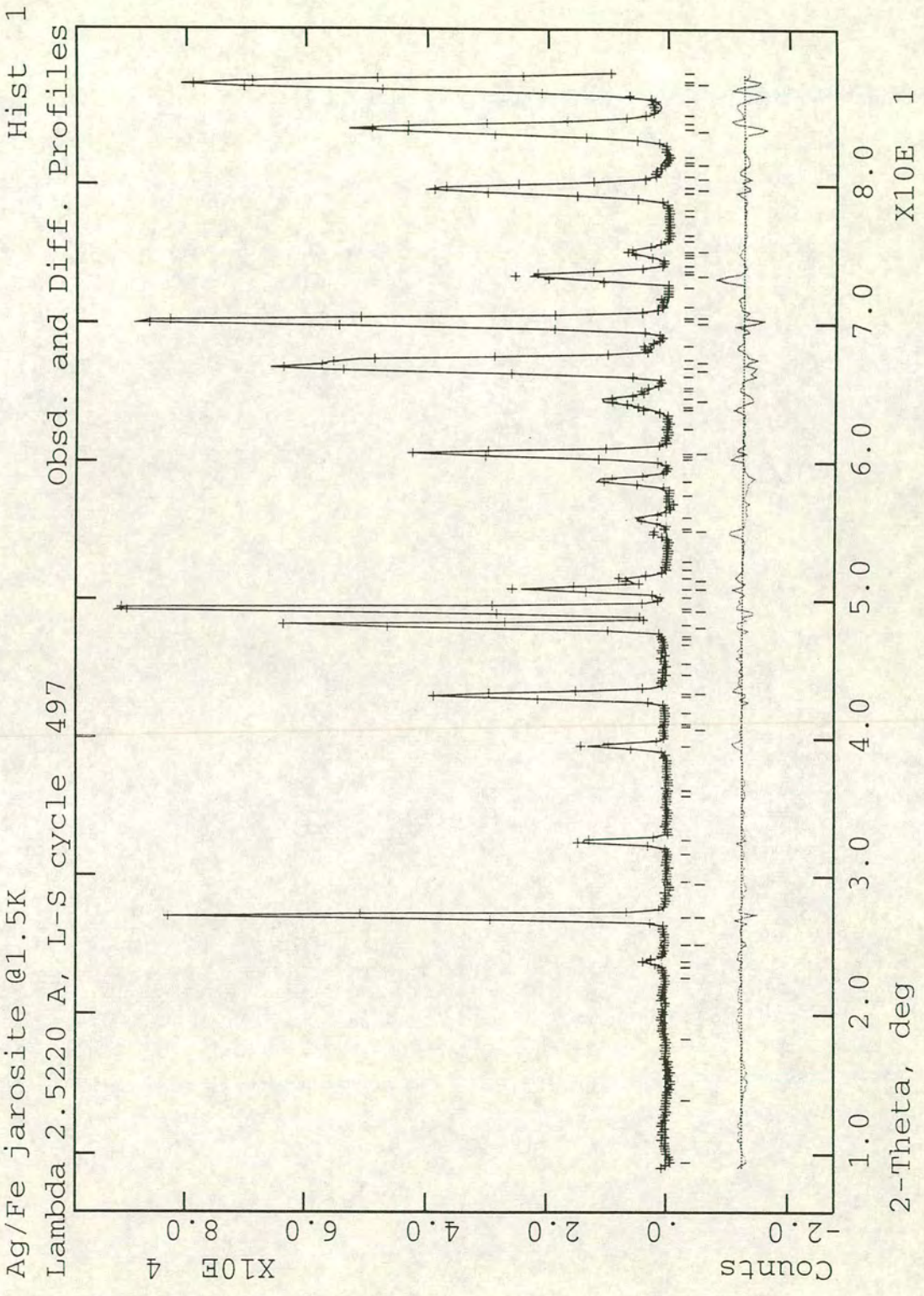

Figure 4.26. Fit of refined profile to neutron scattering data for $AgFe_3(SO_4)_2(OD)_6$ using the $R\bar{3}m$ nuclear and $P\bar{3}$ magnetic unit cells.

fractional occupancy was fixed at that obtained from chemical analysis and the scattering from D_3O^+ and Rb^+ units was best described with the fractional occupancy of the Rb set to unity and only the deuterium atoms of the rigid body D_3O^+ group present; their fractional occupancy and thermal parameters allowed to vary. Crystallographic structural parameters were allowed to vary freely and attain unphysical values, and so will not be discussed here. Again, the refined values $\chi^2 = 72.5$ $R_{wp} =$ 3.35% have little meaning. The refined sublattice moment was 2.23 (6)μ_B and the magnetic lattice parameters: a = 7.3342 (9) and c = 34.777 (60). The experimental and calculated diffraction profiles of $RbFe_3(SO_4)_2(OD)_6$ are displayed in *Figure 4.28*.

4.13 Conclusion

A combination of techniques- ac and dc magnetometry, specific heat, neutron diffraction, and MuSR- were used to study the magnetic properties and crystal structures of the jarosite series. Particular attention was paid to hydronium jarosite, which this work has shown to be the best model $S = 5/2$ Kagomé antiferromagnet studied to date. Neutron diffraction indicates the presence of only 2-D short-range order below the spin-glass-like transition, $T_f \sim$ 17K. MuSR and neutron scattering showed this short range order to be largely dynamic: in contrast with conventional spin-glass behaviour. The T^2 dependence of the specific heat observed below T_f is consistent with the presence of a gapless excitation spectrum either of the type seen in long-range ordered 2-D antiferromagnets, or a 2-D spin nematic phase. The large local fields observed in MuSR cannot be the result of zero-energy spin fold-type spin defects. Instead, an excitation that gives rise to net spin on an individual triangular plaquette is required. These excitations and zero-energy defects exist in, or give rise to, the short-range spin structure based on the $\sqrt{3}$ x $\sqrt{3}$ configuration observed by neutron diffraction. These properties are very similar to those observed in the highly frustrated SCGO(x). However, a clear contrast is seen in the effects of dilution of magnetic sites; in SCGO(x) this does not lead to a marked change in behaviour, only to a depression of T_f. Quite different behaviour is observed in hydronium jarosite where in addition to the short-range order, dilution of the magnetic sites has the unusual effect of increasing the exchange field experienced by the moments and so stabilises long-range antiferromagnetic order with the in-plane q = 0 spin configuration; in the remaining, and less magnetically concentrated members of the jarosite family, neutron scattering shows that the magnetic moments contribute to both a long-range ordered phase and a short-range ordered phase below T_c, of the types observed in hydronium jarosite. This is compatible with a non-uniform distribution of defects stabilising long-range order only in some areas of the magnetic lattice; areas with relatively few such defects will possess only short-range order.

Further synthetic work needs to be done to reduce and identify the ferromagnetic impurity that appears to be present in some jarosite samples. While it is likely to be $Fe_4(OH)_{10}SO_4$, this cannot be proven without magnetic characterisation of the pure material.

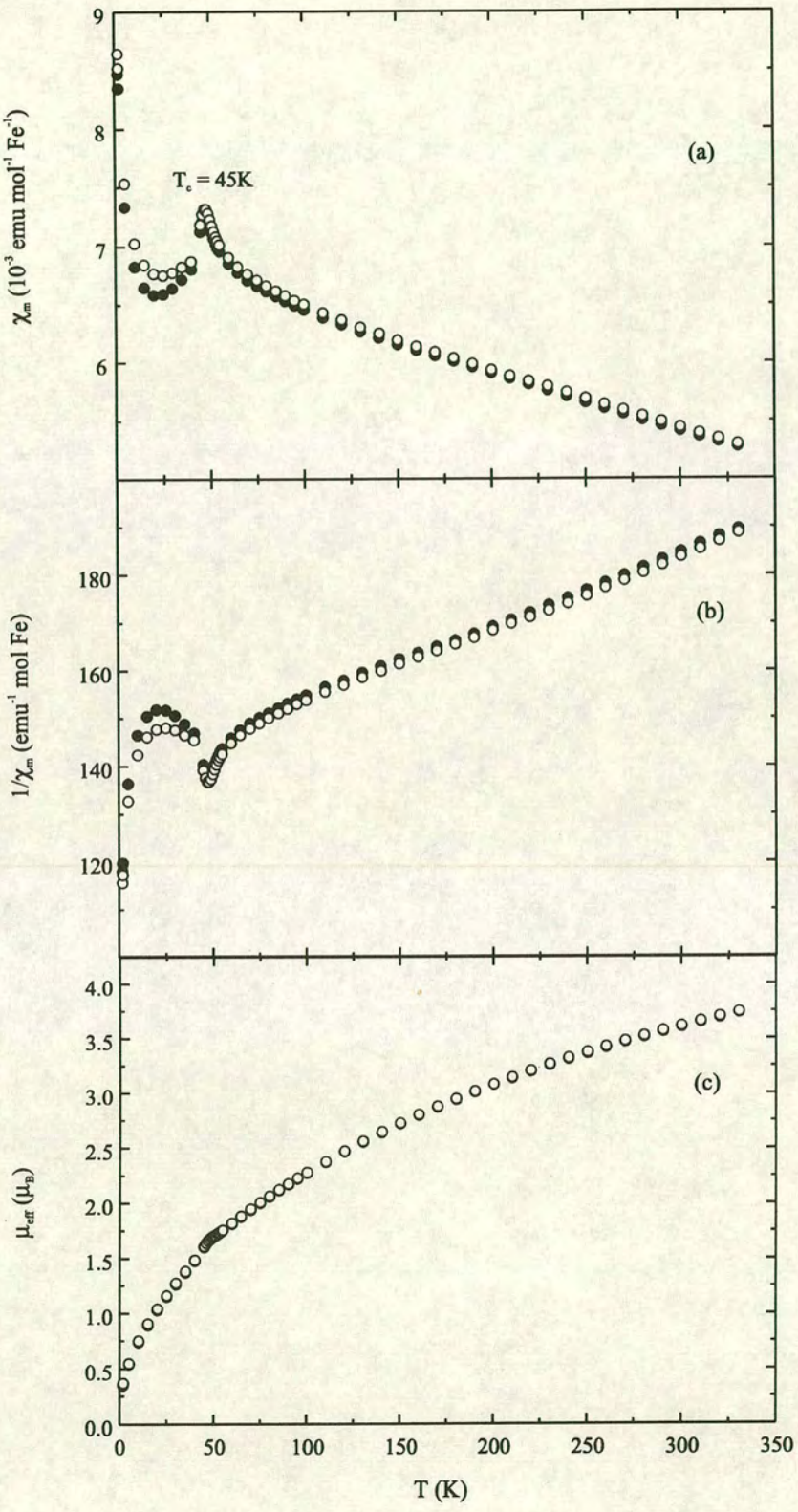

Figure 4.27. (●) Zero-field-cooled and (○) field-cooled dc susceptibility measurements as a function of temperature for $RbFe_3(SO_4)_2(OD)_6$: (a) molar susceptibility, χ_m, shows spin-glass-like separation at T_f = 45K; (b) inverse susceptibility, $1/\chi_m$; (c) effective moment, μ_{eff}.

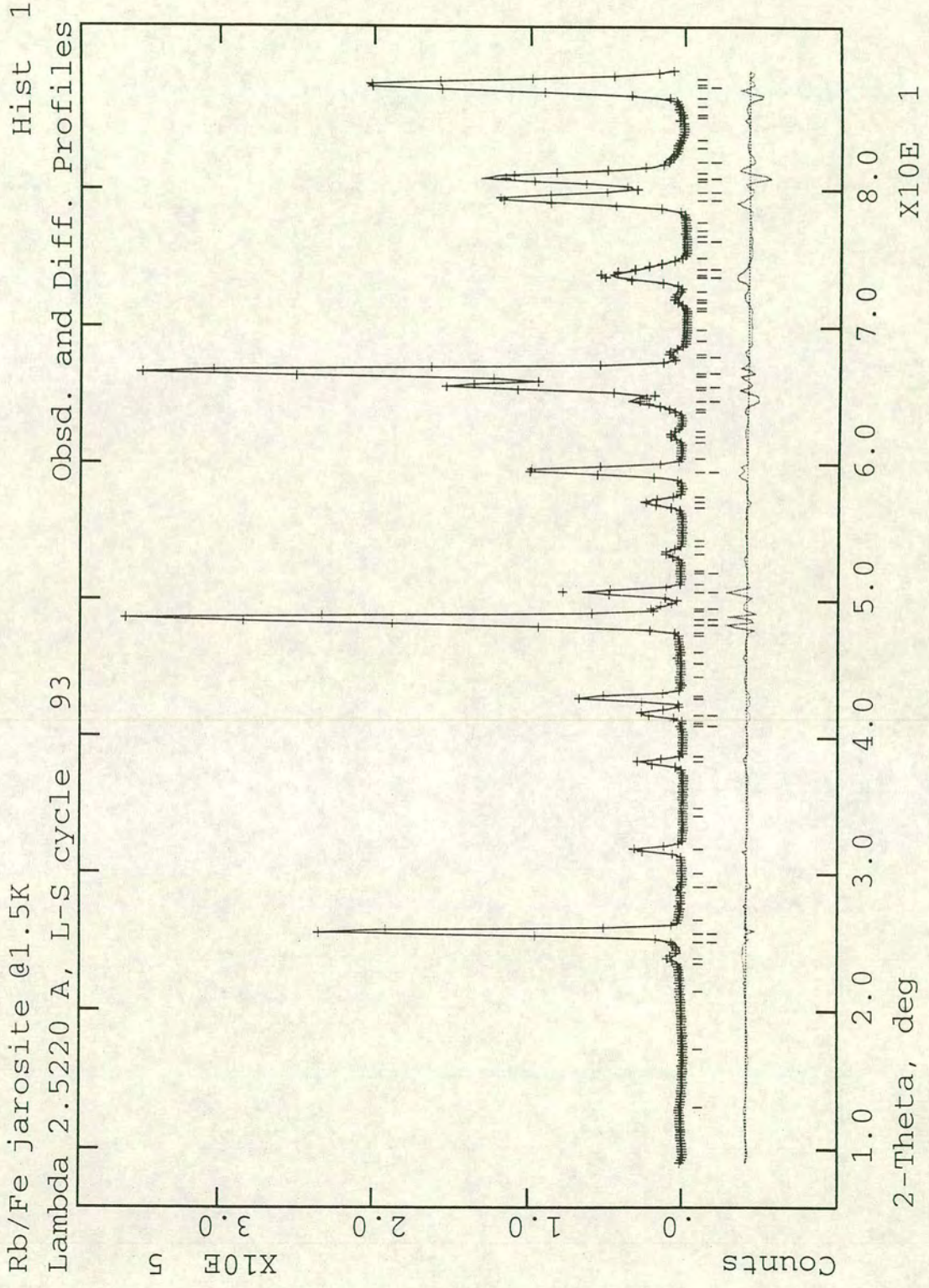

Figure 4.1 Fit of refined profile to neutron scattering data for $RbFe_3(SO_4)_2(OD)_6$ using the $R\bar{3}m$ nuclear and $P\bar{3}$ magnetic unit cells.

4.14 References

1. D.C. Armstrong, Miner.Mag. **59**, 429 (1995).

2. I. Oborn and D. Berggren, GEDMAB **66**, 213 (1995).

3. '*Dana's System of Mineralogy*', C. Palache, H. Berman, and C. Frondel (John Wiley and Sons, London, 1951).

4. J.E. Dutrizac, J.L. Jambor, and J.B. O'Reilly, Cim. Bulletin **76**, 78 (1983).

5. W.T. Schaller, Am.Miner. **8**, 230 (1923).

6. J.E. Dutrizac, *NATO Conf. Ser. (Hydrometall. Process. Fund.)* (1984).

7. J.E. Dutrizac and S. Kaiman, Hydrometall. **1**, 51 (1975).

8. J.E. Dutrizac and S. Kaiman, Can.Miner. **14**, 151 (1976).

9. J. Kubisz, Mineral.Pol. **1**, 47 (1970).

10. C.J. Haigh, Proc.Aust.Inst.Min.Met. **Sept**, 49 (1967).

11. J.G. Fairchild, Am.Miner. **18**, 543 (1933).

12. G.P. Brophy, E.S. Scott, and R.A. Snellgrove, Am.Miner. **47**, 112 (1962).

13. J.B. Brown, Can.Miner. , 696 (1970).

14. E. Matijevic, R.S. Sapieszko, and J.B. Melville, J.Colloid Interface Sci. **50**, 567 (1975).

15. S.B. Hendricks, Am.Miner. **22**, 773 (1937).

16. J.T. Szymanski, Can.Miner. **23**, 659 (1985).

17. T. Kato and Y. Miura, Miner.Mag. **8**, 419 (1977).

18. J.E. Dutrizac, Metall.T.-B **14B**, 531 (1983).

19. C. Härtig, P. Brand, and K. Bohmhammel, Neue Hutte **35**, 205 (1990).

20. A. Martin and A. Feltz, Z.Anorg.Allg.Chem. **575**, 115 (1989).

21. R.S. Sapieszko, R.C. Patel, and E. Matijevic, J.Phys.Chem. **81**, 1061 (1977).

22. C. Hartig, P. Brand, and K. Bohmhammel, Neue Hutte **35**, 205 (1990).

23. A.M. Afanasev, V.D. Gorobchenko, D.S. Kulgawczuk, and I.I. Lukashevich, Phys.Stat.Sol.A **26**, 697 (1974).

24. A.S. Wills and A. Harrison, J.Chem.Soc.,Faraday Trans. **92**, 2161 (1996).

25. '*The Rietveld Method*', ed. R.A. Young (Oxford University Press, Oxford, 1995).

26. F.S. Lee and G.B. Carpenter, J.Phys.Chem. **63**, 279 (1959).

27. Y.K. Yoon and G.B. Carpenter, Acta Cryst. **12**, 17 (1959).

28. C.E. Nordman, Acta Cryst. **15**, 18 (1962).

29. M.H. Begemann and R.J. Saykally, J.Chem.Phys. **82**, 3570 (1985).

30. '*Hydrogen Bonding in Solids*', W.C. Hamilton and J.A. Ibers (Benjamin, New York, 1968).

31. Y.J. Uemura, A. Keren, L.P. Le, G.M. Luke, B.J. Sternlieb, and W.D. Wu, Hyperfine Interact. **85**, 133 (1994).

32. I.A. Campbell, A. Amato, F.N. Gygax, D. Herlach, A. Schenck, R. Cywinski, and S.H. Kilcoyne, Phys.Rev.Lett. **72**, 1291 (1994).

33. A. Keren, P. Mendels, I.A. Campbell, and J. Lord, Phys.Rev.Lett. **77**, 1386 (1996).

34. Y.J. Uemura, A. Keren, K. Kojima, L.P. Le, G.M. Luke, W.D. Wu, Y. Ajiro, T. Asano, Y. Kuriyama, M. Mekata, H. Kikuchi, and K. Kakurai, Phys.Rev.Lett. **73**, 3306 (1994).

35. A. Keren, K. Kojima, L.P. Le, G.M. Luke, W.D. Wu, Y.J. Uemura, M. Takano, H. Dabkowska, and M.J.P. Gingras, Phys.Rev.B Condens.Matter **53**, 6451 (1996).

36. '*Solid State Physics*', N.W. Ashcroft and N.D. Mermin (Saunders College Publishing, Fort Worth, 1976).

37. '*Specific Heats at Low Temperatures*', E.S.R. Gopal (Heywood Books, London, 1966).

38) A.S. Wills, A. Harrison, S.A.M. Mentink, T.E. Mason, and Z. Tun, Phys. Rev. Lett. *in press* (1996).

39. '*Spin glasses: an experimental introduction*', J.A. Mydosh (Taylor & Francis, London, 1993).

40. A.P. Ramirez, G.P. Espinosa, and A.S. Cooper, Phys.Rev.Lett. **64**, 2070 (1990).

41. E.F. Shender and P.C.W. Holdsworth, J.Phys.-Cond. **7**, 3295 (1995).

42. P.C.W. Holdsworth, *personal communication* (1996).

43. A.P. Ramirez, Annu.Rev.Mater.Sci. **24**, 453 (1994).

44. B.E. Warren, Phys.Rev. **59**, 693 (1941).

45. J.E. Greedan, M. Bieringer, J. Britten, D.M. Giaquinta, and H.-C. zur Loye, J.Solid State Chem. **116**, 118 (1995).

46. L.J. de Jongh and A.R. Miedema, Adv.Phys. **23**, 1 (1974).

47. M.G. Townsend, G. Longworth, and E. Roudaut, Phys.Rev.B Condens.Matter **33**, 4919 (1986).

48. C. Broholm, S.H. Lee, M.F. Collins, L. Heller, A.P. Ramirez, C. Kloc, and E. Bucher, *unpublished work* (1992).

49. '*Magnetochemistry*', R.L. Carlin (Springer Verlag, Berlin, 1986)

50. G.J. Long, G. Longworth, P. Battle, A.K. Cheetham, R.V. Thundathil, and D. Beveridge, Inorg.Chem. **18**, 624 (1979).

5 Experimental Kagomé Antiferromagnets: $S = 3/2$

5.1 Introduction

SCGO(x) used to be regarded as presenting an excellent example of a $S = 3/2$ Kagomé antiferromagnet.[1-10] This view is clearly in error as SCGO(x) is in fact a highly frustrated system with a structure derived from slabs of magnetic ions which have the pyrochlore geometry.[11] To date the only example $S = 3/2$ Kagomé antiferromagnets are based on the jarosite series. Previous workers have shown that Cr^{3+} is able to replace Al^{3+} in the alunite structure to create $KCr_3(SO_4)_2(OH)_6$, a $S = 3/2$ analogue of $KFe_3(SO_4)_2(OH)_6$.[12,13] Coverage of the magnetic sites appears to be 75 - 100%, depending on the analysis method and the sample, which is compatible with our previous understanding of jarosite stoichiometry. This range of magnetic occupation complicates any discussion of previous literature as the stoichiometry is often undetermined, and the properties may be those of a high or a low coverage sample. Comparisons with the literature will be made where appropriate but this limitation should always be held in mind.

This work has focused on the magnetic properties of the new material $(H_3O)Cr_3(SO_4)_2(OH)_6$, which has a magnetic occupation of ~ 98%.

5.2 Synthesis

5.2.1 $KCr_3(SO_4)_2(OH)_6$: synthesis 1

A sample of $KCr_3(SO_4)_2(OH)_6$ was prepared by dissolving 3.000g of $KCr(SO_4)_2.12H_2O$ (Aldrich 98%) in H_2O. The solution was made up to 15ml and heated at 210°C in a PTFE-lined stainless-steel bomb (Parr Instrument Company) for 16 hours.[14] The dark green precipitate was then scraped from the walls of the PTFE-liner and washed three times with H_2O before being dried at 120°C for 3 hours. The product was finely ground and is not air-sensitive. The mass of the product was 0.20g.

5.2.2 $KCr_3(SO_4)_2(OH)_6$: synthesis 2

The conditions used in the preparation of $KCr_3(SO_4)_2(OH)_6$ were changed in order to use K_2SO_4 and $Cr_2(SO_4)_3.15H_2O$ (Alfa 99.999%) as soluble sources of K^+, Cr^{3+}, and SO_4^{2-}. 1.820g of $Cr_2(SO_4)_3.15H_2O$ and 0.523g K_2SO_4 were dissolved in H_2O and the solution made up to 15ml. The reaction mixture was heated in a PTFE-lined stainless-steel bomb at 210°C for 16 hours. The precipitate was scraped from the liner, washed, and dried as above. The mass of the product was 0.26g.

The magnetic responses of the samples prepared by the two syntheses were investigated by SQUID magnetometry and found to be identical.

Elemental composition was analysed as (wt.%): 2.1 H, 28.3 Cr, 14.4 S (theoretical composition: 8.0 K, 1.2 H, 31.9 Cr, 13.1 S, and 45.8 O). S and H contents were determined by elemental combustion, while Cr content was determined by atomic absorption spectroscopy using a solution prepared from the digestion of a sample ashed in a silica boat at 700°C over 16 hours, in a solution of manganese sulfate, phosphoric acid, and potassium bromate.[15] The presence of potassium in the digestion mixture prevented analysis of the potassium content. However, as the stoichiometry is determined with respect to the sulfur, this does not prevent calculation of the occupancy of the magnetic sites with the assumption that the S content is stoichiometric. The determined chemical stoichiometry is $Cr_{2.42}H_{9.33}S_{2.00}O_xK_y$. The principal error arises from the metal analysis ± 1.0wt.% and these were worked through to give the error in the coverage of the Cr sites. This gives an occupancy of the magnetic sites of ~ 81 ± 3%.

5.2.3 $(D_3O)Cr_3(SO_4)_2(OD)_6$

Comparison of the syntheses of $KCr_3(SO_4)_2(OH)_6$, $KFe_3(SO_4)_2(OH)_6$, and $(H_3O)Fe_3(SO_4)_2(OH)_6$ gave the initial reaction conditions used for $(H_3O)Cr_3(SO_4)_2(OH)_6$ preparation. These conditions were optimised to give the phase pure jarosite-type product. The temperature gradients within a large reaction bomb were found to be unfavourable and resulted in a marked reduction in the amount of product with respect to that expected. For this reason, preparations of a sample suitable for neutron scattering were carried out in 15ml PTFE-lined stainless-steel bombs.

A partially deuterated sample of $(D_3O)Cr_3(SO_4)(OD)_6$ was prepared by dissolving 45.000g of $Cr_2(SO_4)_3.15H_2O$ in 150ml D_2O. Most of the water was then removed by rotary evaporation before the viscous fluid that remained was redissolved in D_2O and made up to a volume of 75ml. The solution was separated into 5 x 15ml amounts and each was heated in a PTFE-lined stainless-steel bomb at 265°C for 48 hours. The product was washed twice with D_2O and dried at 120°C for 3 hours. Each sample was examined by SQUID magnetometry and three samples, with identical responses, were combined to give the ~ 1.22g sample that was used for neutron diffraction and MuSR experiments.

The elemental composition, of a protonated sample prepared by the same method, that had identical magnetic responses in the χ_m, was analysed as (wt.%): 2.1 H, 34.8 Cr, 14.5 S (theoretical composition: 2 H, 33.2 Cr, 13.7 S, and 51.1 O). S and D contents were determined by elemental combustion, while Cr content was determined by atomic absorption spectroscopy using a solution prepared as for $KCr_3(SO_4)_2(OH)_6$. The O content was then deduced by subtraction, and the overall stoichiometry determined on the assumption that the S content is stoichiometric as $Cr_{2.93}S_{9.33}H_{2.00}O_{13.51}$. This gives an occupancy of the magnetic sites of 98 ± 3%.

5.3 $KCr_3(SO_4)_2(OH)_6$

5.3.1 D.c. susceptibility

The zfc and fc magnetisation of a sample of $KCr_3(SO_4)_2(OH)_6$ measured in an applied field of 100G shows no separation down to 1.8K [*Figure 5.1(a)*]. As the inverse susceptibility is well behaved down to ~ 40K the value of θ_w can be estimated from a fit of χ_m, in this linear region, to the Curie-Weiss law:

$$\chi_m = \frac{C}{T - \theta_w} \qquad (5.1)$$

where C is the Curie constant. To take into account any errors in the corrections for the diamagnetic response of the sample or the gelatine capsule, an additional temperature independent term, χ_{TIP}, can be added to give the extended form of the Curie-Weiss law, known as the Langevin-Debye equation:[16]

$$\chi_m = \frac{C}{T - \theta_w} + \chi_{TIP} \qquad (5.2)$$

χ_{TIP} is a minor correction term. The zfc susceptibility data were fitted to *Equation 5.2* over the temperature range 10 - 330K to give a fitted values of $C = 2.05 \pm 0.03$ emu K mol^{-1} Cr^{-1}, $\theta_w = -78 \pm 10$K, and $\chi_{TIP} = -2.3 \times 10^{-4} \pm 6 \times 10^{-4}$ emu mol^{-1} Cr^{-1} (which is < 1% of the measured chi at 300K). The value of the Curie-Weiss constant, $\theta_w = -78 \pm 10$K agrees well with the previously reported value of -67K.[12,13,17] The temperature range of the magnetometer is insufficient to probe the reported spin-glass transition at $T_f = 1.8$K.

The low value of the spin quantum number will lead to a large degree of quantum fluctuations, this will in turn reduce the tendency of the system to be trapped in a metastable configuration above T_f, and so reduce the tendency towards spin-glass freezing. The absence of a zfc-fc separation above 1.8K is likely to be a result of the low value of θ_w and the large quantum fluctuations present in a $S = 3/2$ sample. These will respectively reduce the size of the energy barriers which separate the metastable configurations, and decrease the tendency towards the system being trapped in any one of these metastable configurations. This will reduce the amount of 2-D short-range order present in the system above T_f with respect to that present in the jarosites (e.g. $AgFe_3(SO_4)_2(OD)_6$ with $\theta_w = -2000 \pm 250$K and $S = 5/2$) and so reduce the magnitude of any field dependent irreversibility in this temperature range. Although $\mu_{eff}(T)$ still has not reached its asymptotic limit within this temperature range, its value at 300K, $\mu_{eff} = 3.55\mu_B$, is ~ 90% of the spin-only value and is compatible with the analysed stoichiometry.

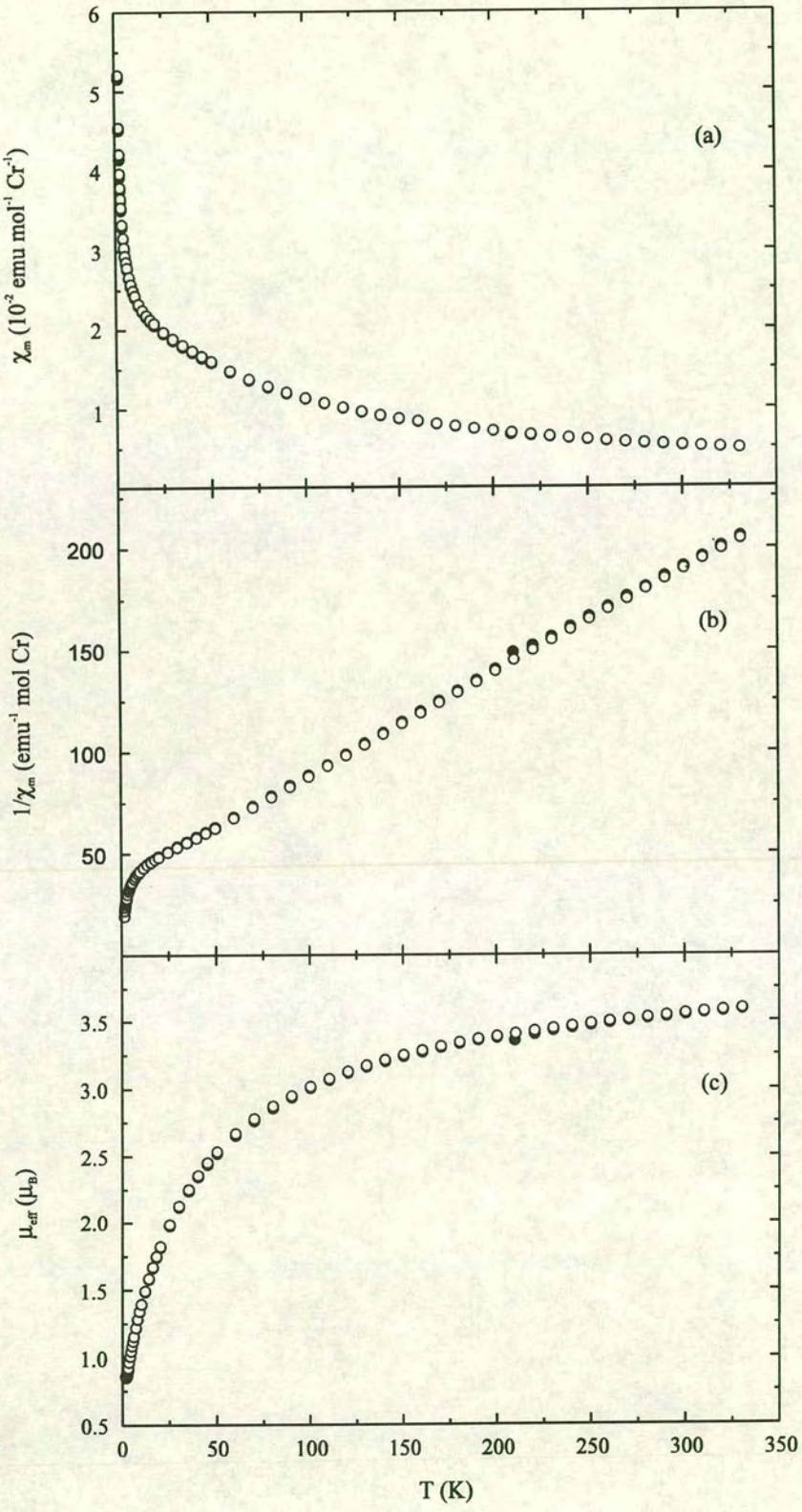

Figure 5.1. (●) Zero-field-cooled and (○) field-cooled dc susceptibility measurements as a function of temperature for $KCr_3(SO_4)_2(OD)_6$: (a) susceptibility, χ_m; (b) inverse susceptibility, $1/\chi_m$; (c) effective moment, μ_{eff}.

5.4 $(D_3O)Cr_3(SO_4)_2(OD)_6$

5.4.1 D.c susceptibility

The dc susceptibility data for $(D_3O)Fe_3(SO_4)_2(OD)_6$ were taken in a measuring field of 100G and are shown in *Figure 5.3*. The behaviour is very different to that observed in $KCr_3(SO_4)_2(OH)_6$. The inverse susceptibility shows linear, Curie-Weiss-type, behaviour down to 50K. Below this temperature there is a broad hump in χ_m with an inflexion at 33K, followed by a sharp ferromagnetic-like increase from ~ 16K which saturates at ~ 2K. In order to investigate data the derivative, $d\chi_m/dT$ was taken [*Figure 5.4*]. This shows a minimum at 2.2K corresponding to the steepest part of the χ_m *vs.* T slope, and so to the ferromagnetic critical temperature T_c. The feature at T = 2.8K is not observed in the specific heat and is therefore likely to be an experimental artefact.

Weak "parasitic" ferromagnetism of this form is typically a consequence of canting of the spins so that the antiferromagnetic alignment of spins on two equivalent sublattices is not exactly antiparallel [*Figure 5.2*]. This gives rise to a small net moment, m_{DM}, and weak ferromagnetism. The effect is termed Dzyaloshimsky-Moriya (D-M) ferromagnetism[18-21] and is responsible for the weak ferromagnetism observed in a number of materials, e.g. NiF_2 and La_2CuO_4.[22,23] If more sublattices are involved there may be no net moment and so no net ferromagnetism. In order that the sublattices may exist in a spontaneously canted state, the magnetic atoms of the unit cell cannot be related by a centre of symmetry. The total symmetry must also be the same as in the uncanted state, i.e. the magnetic and nuclear unit cells must be identical.

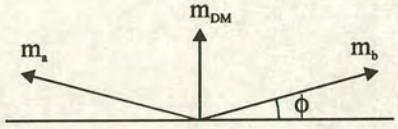

Figure 5.2. Canting of two sublattices, m_a and m_b, to produce a net total magnetic moment m_{DM} and weak ferromagnetism

The interaction is an anisotropic exchange interaction and is caused by spin-orbit coupling. Its general form for a pair of spins s_i and s_j at sites i and j is given by the Hamiltonian:

$$\mathcal{H}_{DM} = \boldsymbol{D}_{ij} \cdot \left[\mathbf{s}_i \times \mathbf{s}_j \right] \qquad (5.3)$$

where $\boldsymbol{D}_{ij}$ is a constant called the Dzyaloshinsky vector and $\boldsymbol{D}_{ij} = -\boldsymbol{D}_{ji}$. This term favours the perpendicular arrangement of spins rather than the antiparallel one and so leads to the canted compromise configuration when it competes with conventional superexchange.

Below T_c the behaviour of D-M ferromagnets is quite different to that seen in usual antiferromagnets or ferromagnets. This is exemplified by the low frequency of the spin waves which leads to a much larger contribution to the specific heat, and a weaker temperature dependence than that normally observed.

Hysteresis measurements, where data are taken as the field is increased and then decreased, show no significant separation at 2K. This is within the ferromagnetic regime of the material and is a most unusual response. Normal ferromagnets and those created by the canting of antiferromagnetic moments display hysteresis effects due to their domain structure.[24,25]. That this behaviour is not observed in this material strongly suggests that static domain walls are not present; the domains may instead be separated by mobile boundaries.

The effective moment $\mu_{eff} = 3.88\mu_B$ at 300K is in agreement with the spin-only value of $3.87\mu_B$ and the chemically determined stoichiometry. A curve fit to the χ_m (zfc) between 70 - 330K to *Equation 5.2* gives $C = 2.43 \pm 0.03$ emu K mol^{-1} Cr^{-1}, $\theta_w = -66 \pm 12$K, $\chi_{TIP} = 4\text{x}10^{-4} \pm 4\text{x}10^{-4}$ emu mol^{-1} Cr^{-1} which is ~ 1% of the measured susceptibility at 300K. This value of the Weiss constant is similar to that observed in $KCr_3(SO_4)_2(OH)_6$ and to a first approximation this indicates that the strength of magnetic exchange between the chromium atoms is similar in the two materials. The difference in behaviour observed is therefore likely to be a consequence of changes to the occupation of the chromium sublattice, as the exchange pathways are largely unchanged [*Section 4.8.4*].

5.4.2 Specific heat

Specific heat data were collected between 0.36 and 40K in zero field and in 10,000G. The phonon contribution was subtracted using the analytical fit to the response of $(H_3O)Ga_3(SO_4)_2(OH)_6$. The magnetic contribution C_m was fitted to a fifth order polynomial and integrated to give the magnetic entropy released [*Figure 5.5(a)*]. C_m displays a hump centred at 2.2K, so a maximum is also observed in C/T at this temperature. There is also a broad hump in C/T centred at ~ 29K. *Figure 5.6* shows the effect of the application of a large magnetic field on the form of the C/T plot. That the 28K broad hump is unchanged by the application of a large magnetic field is strange. Neutron scattering measurements [*Section 5.4*] show that in this region there is only short-ranged magnetic order. As the ordering influence is therefore expected to be weak this order is normally expected to be easily disrupted by the application of a magnetic field. The inability of the field to do this is reminiscent of the undecouplable muon response observed in $(H_3O)Fe_3(SO_4)_2(OH)_6$ and is suggestive of some strongly-correlated short-ranged magnetic ground state. The form of the 2.2K peak is, however,

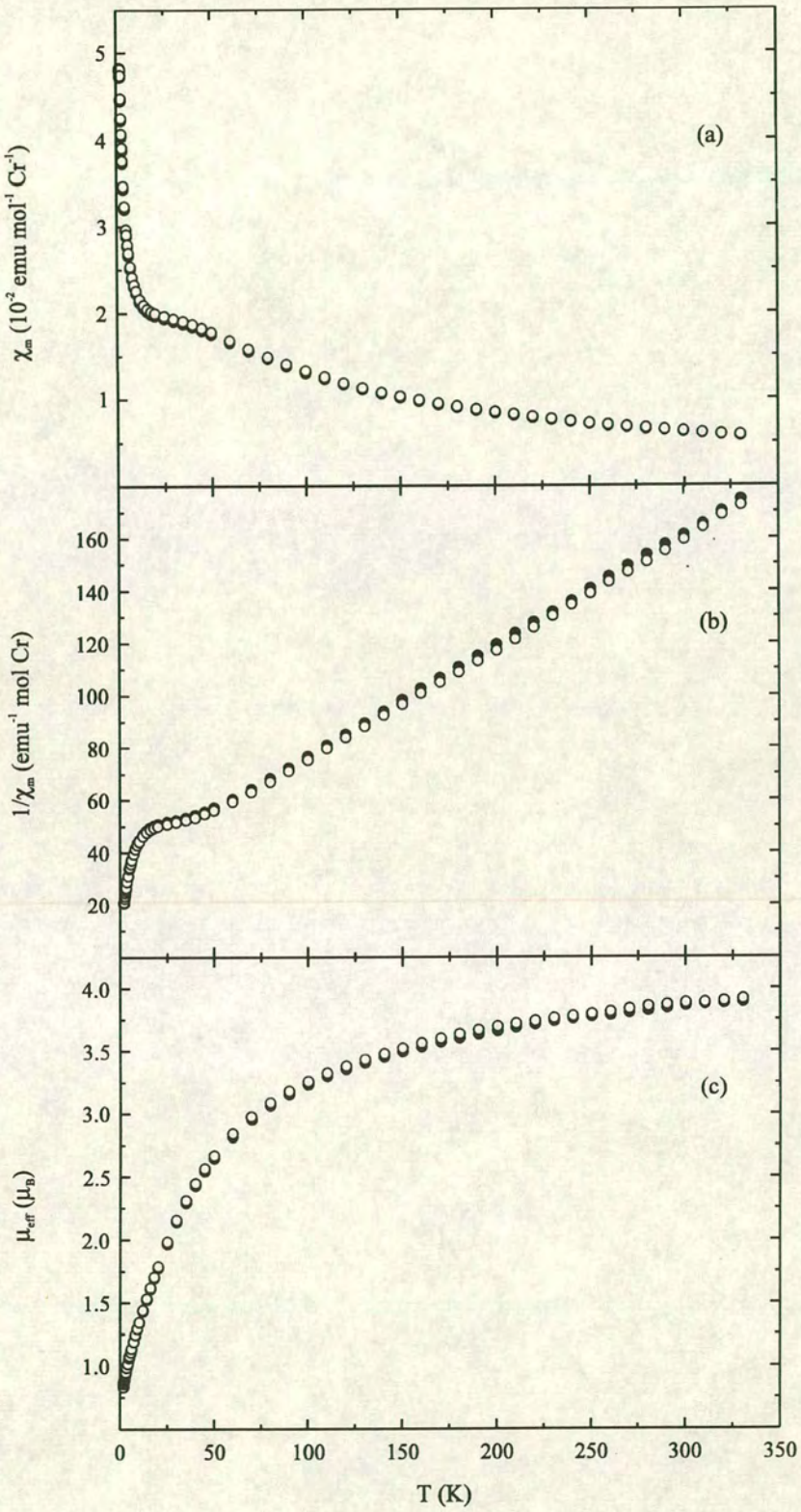

Figure 5.3. (●) Zero-field-cooled and (○) field-cooled dc susceptibility measurements as a function of temperature for $(D_3O)Cr_3(SO_4)_2(OD)_6$: (a) susceptibility, χ_m; (b) inverse susceptibility, $1/\chi_m$; (c) effective moment, μ_{eff}.

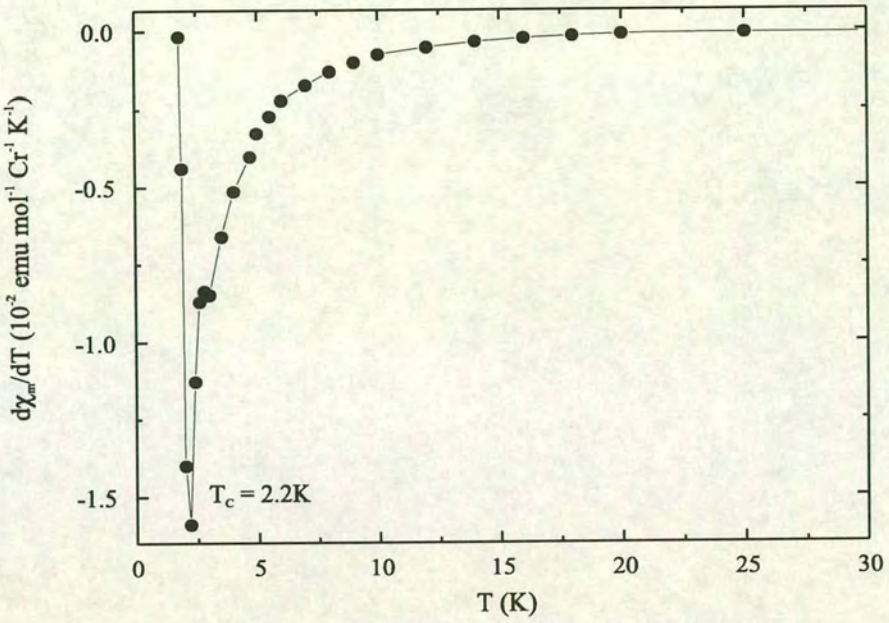

Figure 5.4. The derivative $d\chi_m/dT$ for $(D_3O)Cr_3(SO_4)_2(OD)_6$ indicating the presence of a ferromagnetic transition at T_c = 2.2K. The anomaly at T = 2.8K is believed to be an artefact of the experiment.

changed markedly by the application of the field which indicates that the tendency towards ferromagnetic order is weak in comparison to the interaction with the external field, as a result the transition disrupted and there is correspondingly less magnetic entropy released by 2.6K. In 10,000G only 3.7%, as opposed to 5.4% in zero-field, of the *Rln(2S+1)* magnetic entropy is released by 2.5K. Thus the degree of order is small and comparable with that seen in $(H_3O)Fe_3(SO_4)_2(OH)_6$ at T_f. By 36K, 95% has been released. Comparison with $(H_3O)Fe_3(SO_4)_2(OH)_6$ suggests this large fraction rather than being due to the magnetic response is actually a consequence of the poor modelling of the phonon contribution over this wide temperature range. This comparison is limited as $(H_3O)Fe_3(SO_4)_2(OH)_6$ is a spin-glass and the system is therefore trapped in metastable configurations that will restrict the magnetic ordering. $(D_3O)Cr_3(SO_4)_2(OD)_6$ has no observed spin-glass properties and it is therefore possible that the short-range order is actually highly correlated. The canting of moments to create the ferromagnetic response at 2.2K is only weak in comparison.

In an applied field of 10,000G there is 3.7% of the magnetic entropy released at 2.57K and 95% at 37K, i.e. again the effect of the large applied field is only to disrupt the weak ordering transition at 2.2K.

When plotted on logarithmic axes [*Figure 5.7*], C_m *vs.* T has a gradient below T_c of 1.66 for the zero-field case and 1.96 for the 10,000G data. This again indicated that the application of a large magnetic field has caused an appreciable change in the thermodynamics of the ferromagnetic phase.

5.4.3 Muon Spin Relaxation

MuSR measurements were taken using the EMU spectrometer at the ISIS, facility. Due to the small size of the sample, the remainder of the sample recess in the aluminium plate was filled with an unreactive filler, plasticine. This was blocked from the muon beam using a silver mask. The data were collected at a number of temperatures between 2.2 and 70 K in a decoupling field of 30G. The counting time was ~ 2 hours (1E7 events) at each temperature with ~ 15 minutes equilibration time.

The form of the data is very similar to that observed in $(H_3O)Fe_3(SO_4)_2(OH)_6$, with the longitudinal relaxation function $G_z(t)$ decaying more rapidly as the sample is cooled [*Figure 5.8*]. $G_z(t)$ was fitted to the stretched exponential decay. The muon depolarisation rate, λ, increases slowly with decreasing temperature as the moments slow *[Figure 5.9*]. The value of the exponent β falls as T_c is approached in a manner similar to $(H_3O)Fe_3(SO_4)_2(OH)_6$. Again the limiting value at T_c is ~ 1/3. The poor statistics above 20K make it difficult to determine the temperature at which the spins begin to slow. However, a slowing down is definitely observed below 8K. Unfortunately, the temperature range of the cryostat prevented the acquisition of data below 2.2K so the form of the ferromagnetic correlations below this temperature could not be investigated. At 2.2K $G_z(t)$ [*Figure 5.8*] shows no evidence of muon precession or the recovery of $G_z(t)$ to 1/3 associated with static or ordered moments, which indicates that the moments are still dynamic at this temperature. Detailed analysis of the data at this temperature is again limited as the muon depolarisation rate is very rapid and close to the instrumental limit of EMU.

MuSR measurements made on $KCr_3(SO)_4(OH)_6$ show no evidence of static moments at 25mK.[26] The properties of the longitudinal relaxation function, $G_z(t)$, were found to be very similar to those we have observed in $(H_3O)Fe_3(SO_4)(OH)_6$, i.e. there is no precession, and the decay is initially Gaussian and cannot be decoupled by the application of a 2,000G longitudinal field. The apparent conflict between these data with the long-range ordering transition observed by neutron scattering[13] can be resolved if we look at the variable stoichiometry of $KCr_3(SO_4)_2(OH)_6$. Using previous arguments [*Section 4.2*], the long-range order observed may have been a consequence of a low chromium content. If the sample used for MuSR had a higher coverage, long-range order may not have been present and the magnetic properties would then more closely resemble those of $(H_3O)Cr_3(SO_4)_2(OH)_6$. Therefore, we may again expect $(H_3O)Cr_3(SO_4)_2(OH)6$, below T_c, to show no precession in $G_z(t)$ and an undecouplable Gaussian decay.

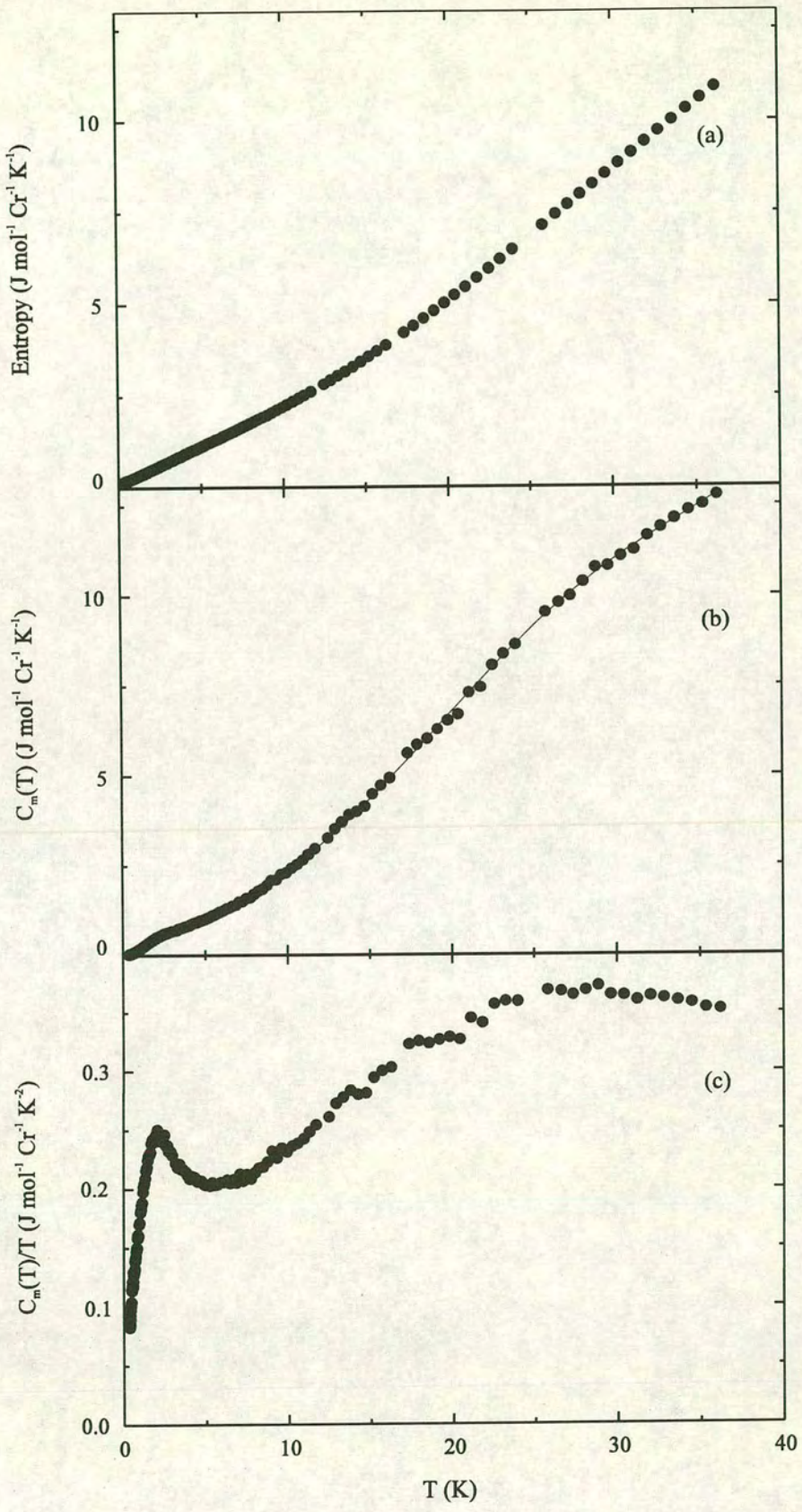

Figure 5.5. Specific heat data for $(D_3O)Cr_3(SO_4)_2(OD)_6$: (a) Entropy; (b) C_m, magnetic contribution to the specific heat and the polynomial function used to calculate the entropy; (c) C_m/T.

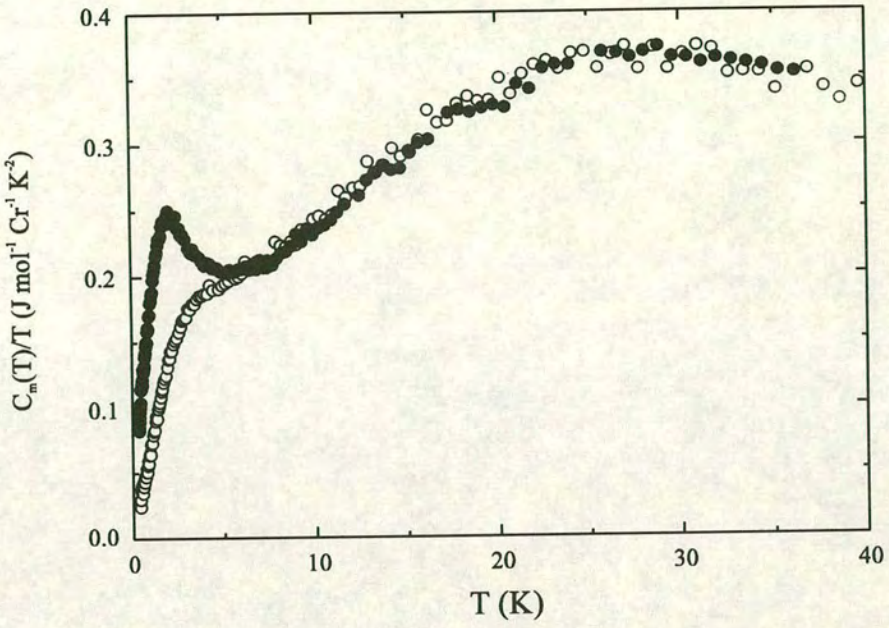

Figure 5.6. Specific heat measurements as a function of temperature for $(D_3O)Cr_3(SO_4)_2(OD)_6$ in zero-field(●) and in an applied magnetic field of (○) 10,000G.

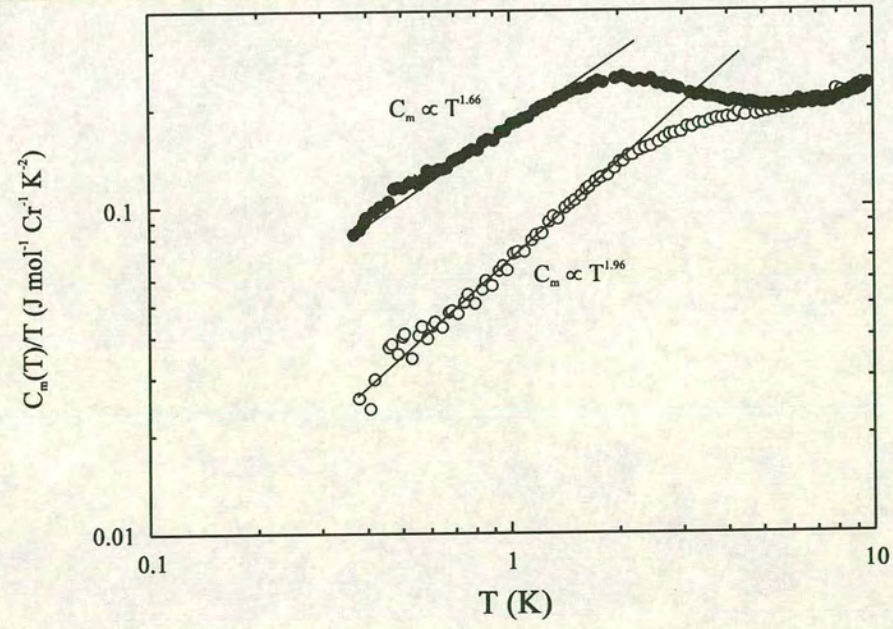

Figure 5.7. C_m/T for $(D_3O)Cr_3(SO_4)_2(OD)_6$ plotted on logarithmic axes in (●)zero-field and in an applied magnetic field of (○) 10,000G.

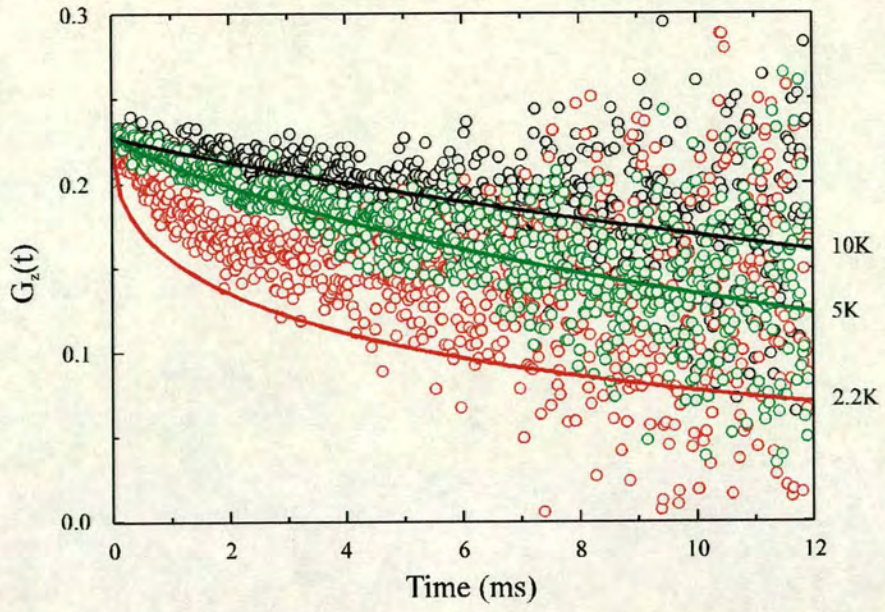

Figure 5.8. The muon spin relaxation function $G_z(t)$ for $(D_3O)Cr_3(SO_4)_2(OD)_6$ and fits to the stretched exponential decay at (-) 2.2, (-) 5, and (-) 10K. The poor fit at 2.2 K, and hence unreliable value of λ and β, is a consequence of the very rapid decay of λ at this temperature, and instrumental limitations.

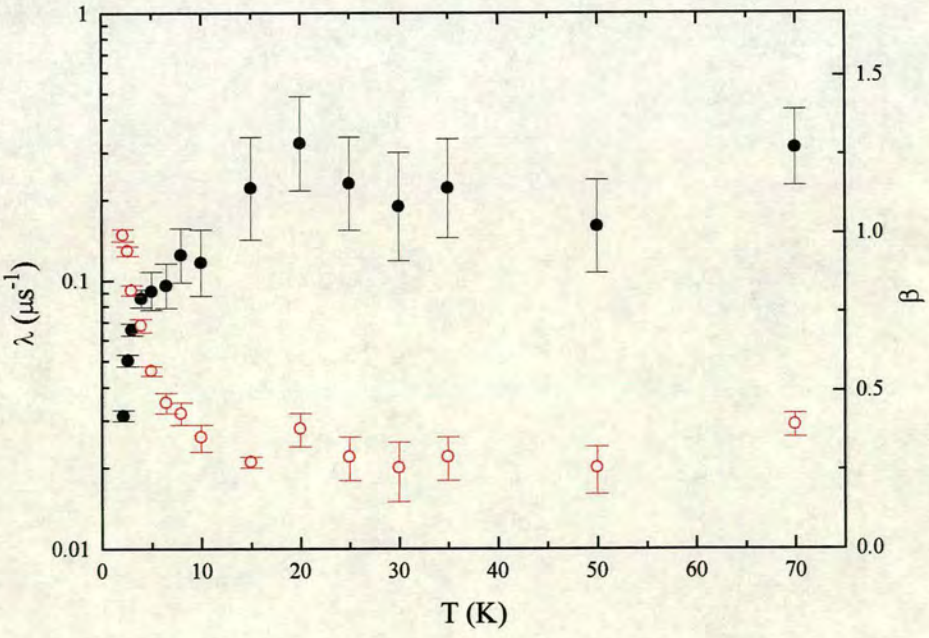

Figure 5.9. (○) Muon depolarisation rate, λ, and exponent (●) β as a function of temperature for $(D_3O)Cr_3(SO_4)_2(OD)_6$.

5.4.4 Neutron diffraction: magnetic structure

Neutron powder diffraction patterns were collected from ~ 1.2g of sample using the D1B diffractometer at a number of temperatures between 1.2 and 141K. The 130K pattern showed no evidence of long-range order and was used as a high temperature comparison in order to examine the magnetic order observed at low temperatures.

Data collected at 1.2 and 5K, counting for 1.75 hours (9E6 events) at each temperature, show the presence of a diffuse Warren-type peak centred at 1.09Å^{-1}, which was fitted to a spin-spin correlation length L = 13 ± 1Å. In addition to a slight increase in the intensity of the Warren peak, comparison with 5K data also revealed the presence of very weak magnetic Bragg peaks superposed on top of some of the nuclear Bragg peaks at 1.2K. The dataset made by the subtraction of the 5K data from 1.2K data is shown in *Figure 5.10(a)*. For comparison, the magnetic peaks of $AgFe_3(SO_4)_2(OD)_6$ [*Section 4.11*] that correspond to the in-plane q = 0 spin configuration and a doubled c-axis, are also displayed [*Figure 5.10(b)*]. Clearly the magnetic peaks of $(D_3O)Cr_3(SO_4)_2(OD)_6$ do not correspond to the same spin configuration as that observed in the jarosites. As the peaks are superposed on top of some of the nuclear peaks, the magnetic unit cell is the same size as the nuclear unit cell and the magnetic order is ferromagnetic. The intensity of the 2θ = 49.3° peak was integrated at 1.2 and at 5K, and was normalised with respect to the monitor count. The magnetic contribution at 1.2K was then calculated to be ~ 0.4% of the total peak intensity, and so corresponds to very weak ferromagnetism.

The weakness of the reflections prevents any attempt at refining the magnetic Bragg peaks observed at 1.2K.

5.4.5 Neutron diffraction: $R\bar{3}m$ crystal structure

The crystal structure of $(D_3O)Cr_3(SO_4)_2(OD)_6$ was examined by powder neutron diffraction at a wavelength of 1.5943Å using the D2B diffractometer at the Institut Laue-Langevin. A powder pattern from ~ 1.2g of sample held in a vanadium can was collected at 65K over 5 hours (4.5E4 events). At this temperature there was no evidence of any long-range or short-range magnetic order. The initial refinement was carried out using the $R\bar{3}m$ structure. The refined parameters are displayed in *Table 5.1* and the fit itself in *Figure 5.11*. The poor value of R_{wp} reflects the inability to model the peak profile function over the entire 2θ range of the data. This could either be caused by the inability of GSAS to model the profile function of D2B, or by a small structural distortion away from the idealised alunite $R\bar{3}m$ structure. The different structural distortions examined are detailed below. They produced no significant improvement in the quality of the model, suggesting that if the structure does indeed possess one of these distortions, then it is very small and cannot be refined using data of this

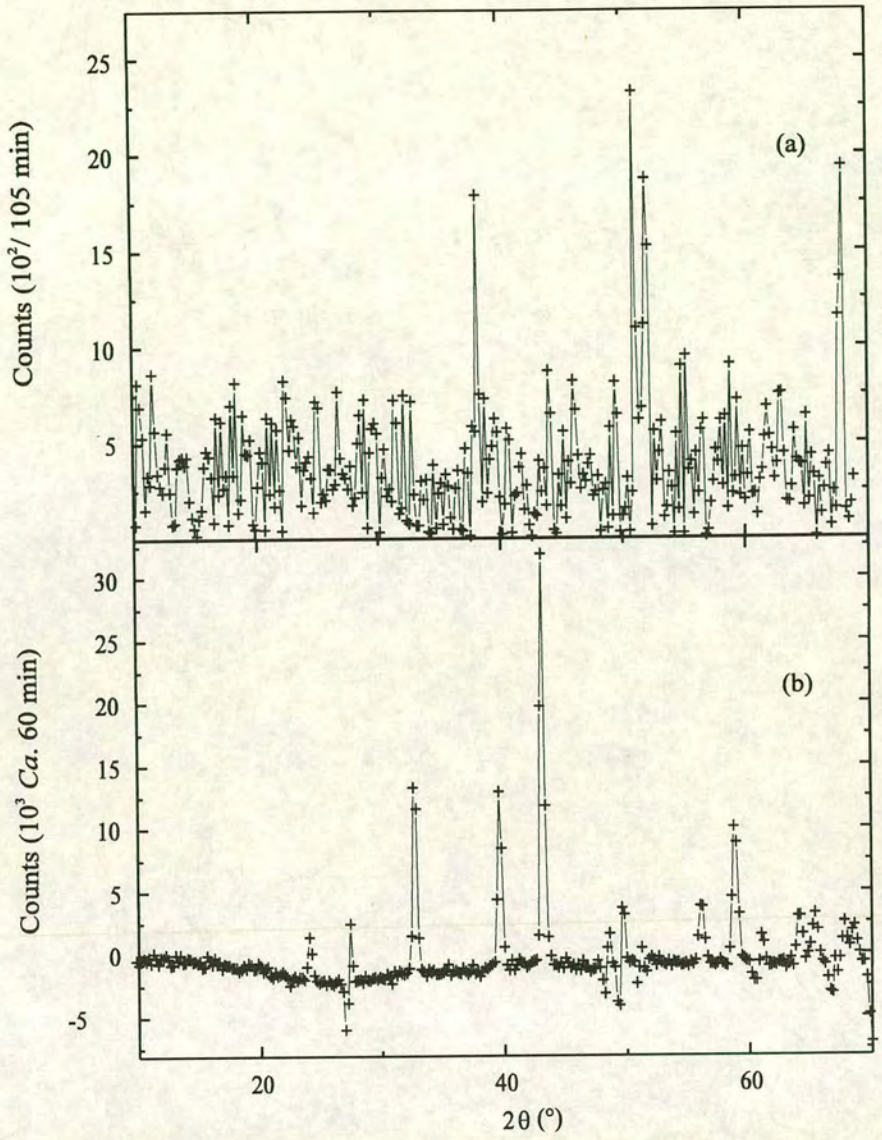

Figure 5.10. Neutron diffraction patterns taken using the D1B diffractometer; a) the result of the subtraction 1.2 - 5K for $(D_3O)Cr_3(SO_4)_2(OD)_6$*; b) the result of the subtraction 1.5 - 65K for* $AgFe_3(SO_4)_2(OD)_6$.

resolution. The similarity of this problem with the peak profile to that seen in $(ND_4)Fe_3(SO_4)_2(OD)_6$ [*Section 4.10.1*] suggests that this distortion is also present in the remaining member of the jarosite series. The presence of the D_3O^+ unit as a rigid body did not improve the refinement and this constraint was relaxed in the other space groups.

The possibility of a second jarosite-type phase was investigated during the initial refinement by the introduction of a second $R\bar{3}m$ phase. This did not lead to any change in the refinement and the second phase was subsequently removed.

No constraints were placed on the values of the thermal parameters and they were allowed to vary independently. As the neutron scattering lengths of deuterium and oxygen atoms dominate the nuclear structure factor, the Cr fractional occupancy could not be refined and was set at unity.

atom (Wyckoff site)	*x*	*y*	*z*	U_{iso}/Å^2	*site symmetry*	*fractional occupancy*
Cr (9d)	0.16667	-0.16667	-0.16667	0.0084 (13)	2/M(110)	1.000
S (6c)	0.00000	0.00000	0.3051 (7)	0.0156 (22)	3M(100)	1.000
O1 (6c)	0.00000	0.00000	0.39137 (30)	0.0024 (9)	3M(100)	1.000
O2 (18h)	0.22116 (20)	-0.22116 (20)	-0.05713 (15)	0.0076 (7)	M(110)	1.000
O3 (18h)	0.12741 (24)	-0.12741 (24)	0.13482 (23)	0.0121 (7)	M(110)	1.000
O4 (6c)	0.00000	0.00000	-0.00975 (67)	0.0061 (19)	3M(100)	0.500
D1 (18h)	-0.06470 (*)	0.06470 (*)	-0.02411 (67)	0.1332 (79)	M(110)	0.500
D4 (18h)	0.19452 (22)	-0.19452 (22)	0.10809 (18)	0.0150 (7)	M(110)	1.000

Table 5.1. Structural parameters for $(D_3O)Cr_3(SO_4)_2(OD)_6$ at 65K in the space group $R\bar{3}m$ with Z = 3. Figures with asterisks are reported without errors because they were subject to rigid body constraints in the refinement that did not allow variation in that parameter. Cell parameters: a = 7.23737 (16)Å and c = 17.0550 (5)Å. χ^2 = 4.66%. R_{wp} = 8.11%.

5.4.6 Neutron diffraction: *R3m* crystal structure

This space group results from the removal of the centre of inversion and the 2-fold axis perpendicular to the mirror plane from the $R\bar{3}m$ space group. The high pseudo-symmetry in the structure led to an unstable refinement if the atomic parameters were unconstrained. For this reason, atoms that were related by the centre of inversion in the $R\bar{3}m$ structure were constrained to have the same thermal parameters and shifts in the x, y, or z co-ordinates were linked so as to retain the centre of inversion. Even with these constraints, a stable refinement only resulted when the oxygen atoms of the D_3O^+ unit were not allowed to move, and the thermal parameters on O1 and O2 were not refined. Refined atomic parameters are displayed in *Table 5.2* and the refinement fit is shown in *Figure 5.12*.

5.4.7 Neutron diffraction: $P\bar{3}m1$ crystal structure

Relaxing the constraint that the crystal structure is rhombohedral converts the $R\bar{3}m$ space group to the $P\bar{3}m1$ space group where the centre of inversion and the 2-fold axis are retained. The thermal parameters of all atoms that were related by the symmetry operations of the $R\bar{3}m$ structure were constrained to be identical with the added constraint that the thermal parameters of all sulfate oxygen atoms were constrained to be the same. Position parameters were individually refined in the early stages of the refinement but were not allowed to vary in the last iterations in order to stabilise the refinement. Refined crystallographic parameters are shown in *Table 5.3* and the refinement profile in *Figure 5.13*.

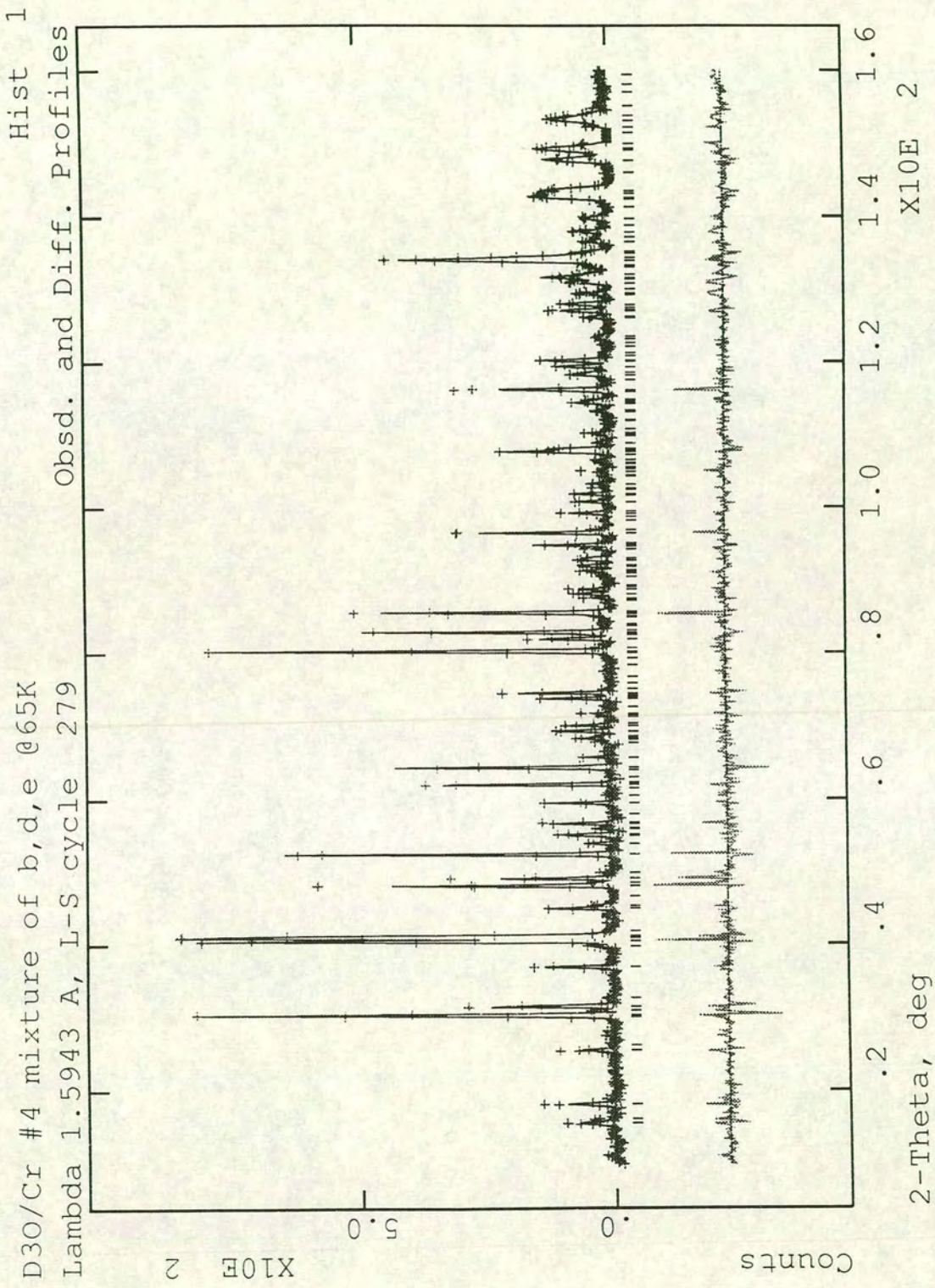

Figure 5.11. Fit of refined profile to neutron scattering data for $(D_3O)Cr_3(SO_4)_2(OD)_6$ using the $R\bar{3}m$ space group.

atom (Wyckoff site)	*x*	*y*	*z*	$U_{iso}/Å^2$	*site symmetry*	*fractional occupancy*
Cr (9b)	0.1646 (10)	-0.1646 (10)	-0.1742 (7)	0.0031 (12)	M(110)	1.000
S1 (3a)	0.00000	0.00000	0.3060 (6)	0.0135 (18)	3M(100)	1.000
S2 (3a)	0.00000	0.00000	-0.3060 (6)	0.0135 (18)	3M(100)	1.000
O1 (3a)	0.00000	0.00000	0.39255 (30)	0.0082 (*)	3M(100)	1.000
O2 (a3)	0.00000	0.00000	-0.39255 (30)	0.0082 (*)	3M(100)	1.000
O3 (9b)	0.22167 (18)	-0.22167 (18)	-0.05679 (14)	0.0084 (6)	M(110)	1.000
O4 (9b)	-0.22167 (18)	0.22167 (18)	0.05679 (14)	0.0084 (6)	M(110)	1.000
O5 (9b)	0.12756 (20)	-0.12756 (20)	0.13614 (18)	0.0103 (5)	M(110)	1.000
O6 (9b)	-0.12756 (20)	0.12756 (20)	-0.13614 (18)	0.0103 (5)	M(110)	1.000
O7 (3a)	0.00000	0.00000	-0.000325 (*)	0.0129 (14)	3M(100)	0.500
O8 (3a)	0.00000	0.00000	0.000325 (*)	0.0129 (14)	3M(100)	0.500
D1 (9b)	-0.05951 (64)	0.05951 (64)	-0.04373 (62)	0.0703 (30)	M(110)	0.500
D2 (9b)	0.05951 (64)	-0.05951 (64)	0.04373 (62)	0.0703 (30)	M(110)	0.500
D3 (9b)	0.19477 (21)	-0.19477 (21)	0.10792 (18)	0.0207 (7)	M(110)	1.000
D4 (9b)	-0.19477 (21)	0.19477 (21)	-0.10792 (18)	0.0207 (7)	M(110)	1.000

Table 5.2. Structural parameters for $(D_3O)Cr_3(SO_4)_2(OD)_6$ at 65K in the space group R3m with Z = 3. Figures with asterisks are reported without errors because they were subject to rigid body constraints in the refinement that did not allow variation in that parameter. Cell parameters: a = 7.23805 (9)Å and c = 17.0561 (33)Å. χ^2 = 4.112%. R_{wp} = 7.6%.

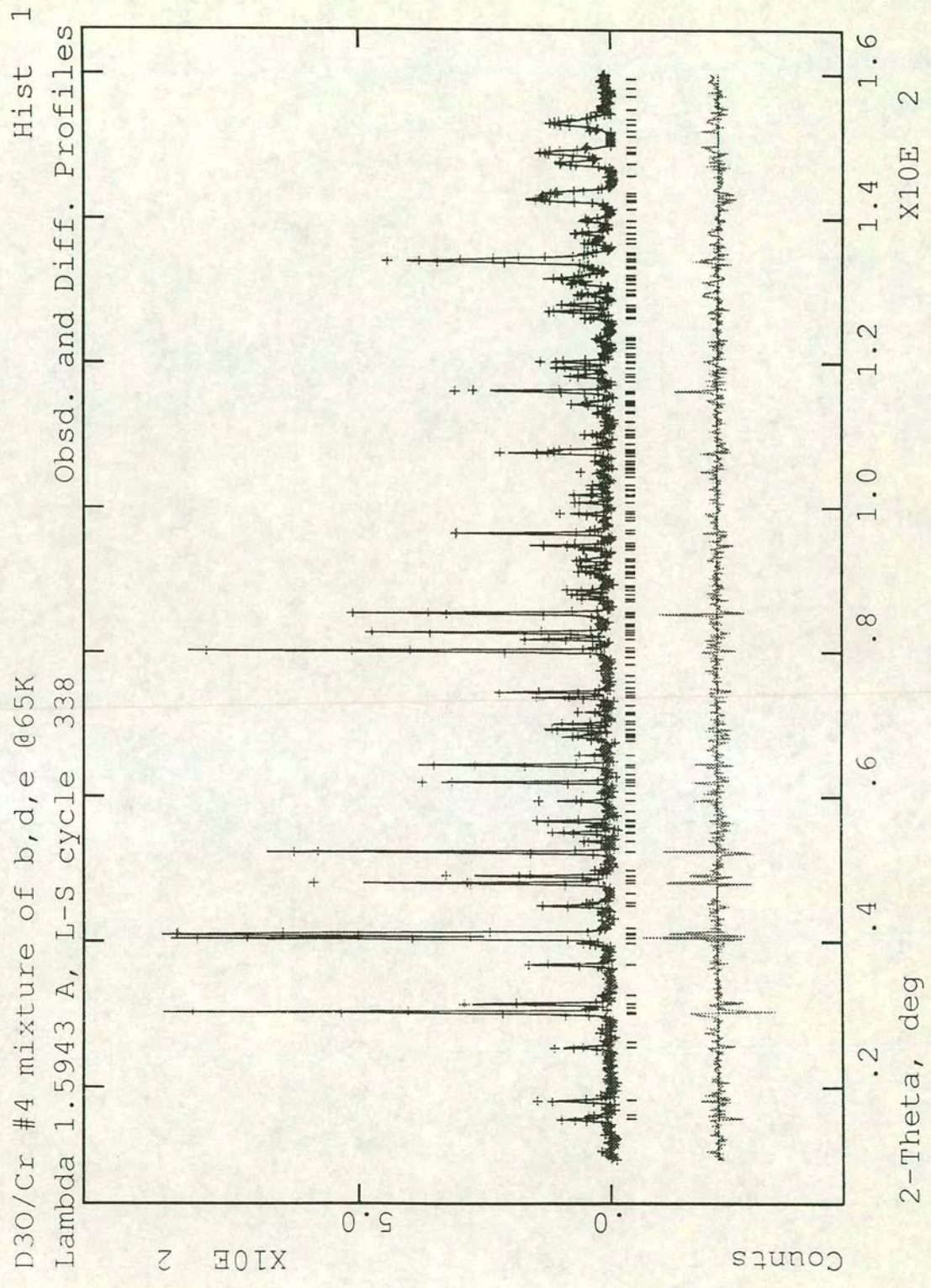

Figure 5.12. Fit of refined profile to neutron scattering data for $(D_3O)Cr_3(SO_4)_2(OD)_6$ using the R3m space group.

atom (Wyckoff site)	*x*	*y*	*z*	$U_{iso}/Å^2$	*site symmetry*	*fractional occupancy*
Cr1 (6i)	0.168309 (*)	-0.168309 (*)	-0.173516 (*)	0.0027 (10)	M(110)	1.000
Cr2 (3f)	0.50000 (*)	0.50000 (*)	0.50000 (*)	0.0027 (10)	2/M(110)	1.000
S1 (2c)	0.00000	0.00000	0.385966 (6)	0.040 (5)	3M(100)	1.000
S2 (2d)	0.33334	0.66667	0.913242 (*)	0.040 (5)	3M(100)	1.000
S3 (2d)	0.66667	0.33334	0.602913 (*)	0.040 (5)	3M(100)	1.000
O1 (2c)	0.00000	0.00000	0.39300 (*)	0.0063 (5)	3M(100)	1.000
O2 (2d)	0.33334	0.66667	0.056145 (*)	0.0063 (5)	3M(100)	1.000
O3 (2d)	0.66667	0.33334	0.725885 (*)	0.0063 (5)	3M(100)	1.000
O4 (6i)	0.222682 (*)	0.777318 (*)	0.942012 (*)	0.0063 (5)	M(110)	1.000
O5 (6i)	0.554349 (*)	0.445651 (*)	0.609508 (*)	0.0063 (5)	M(110)	1.000
O6 (6i)	0.887707 (*)	0.112293 (*)	0.277910 (*)	0.0063 (5)	M(110)	1.000
O7 (6i)	0.121333 (*)	-0.121333 (*)	0.127266 (*)	0.0074 (6)	M(110)	1.000
O8 (6i)	0.463182 (*)	0.536818 (*)	0.804843 (*)	0.0074 (6)	M(110)	1.000
O9 (6i)	0.797201 (*)	0.202799 (*)	0.471297 (*)	0.0074 (6)	M(110)	1.000
O10 (1a)	0.00000	0.00000	0.00000	-0.0053 (13)	-3M(100)	1.000
O11 (2d)	0.33334	0.66667	0.361272 (*)	-0.0053 (13)	3M(100)	1.000
D1 (6i)	-0.058069 (*)	0.058069 (*)	0.954593 (*)	0.0386 (20)	M(110)	0.500
D2 (6i)	0.315829 (*)	0.684171 (*)	0.662210 (*)	0.0386 (20)	M(110)	0.500
D3 (6i)	0.604960 (*)	0.395040 (*)	0.286470 (*)	0.0386 (20)	M(110)	0.500
D4 (6i)	0.189725 (*)	-0.189725 (*)	0.102624 (*)	0.0160 (6)	M(110)	1.000
D5 (6i)	0.534118 (*)	0.465882 (*)	0.774948 (*)	0.0160 (6)	M(110)	1.000
D6 (6i)	0.857959 (*)	0.142041 (*)	0.446150 (*)	0.0160 (6)	M(110)	1.000

Table 5.3. Structural parameters for $(D_3O)Cr_3(SO_4)_2(OD)_6$ at 65K in the space group $P\bar{3}m1$ with Z = 3. Figures with asterisks are reported without errors because they were not allowed to vary in the last cycles of the refinement. Cell parameters: a = 7.23820 (14)Å and c = 17.0567 (4)Å. χ^2 = 3.97%. R_{wp} = 7.50%.

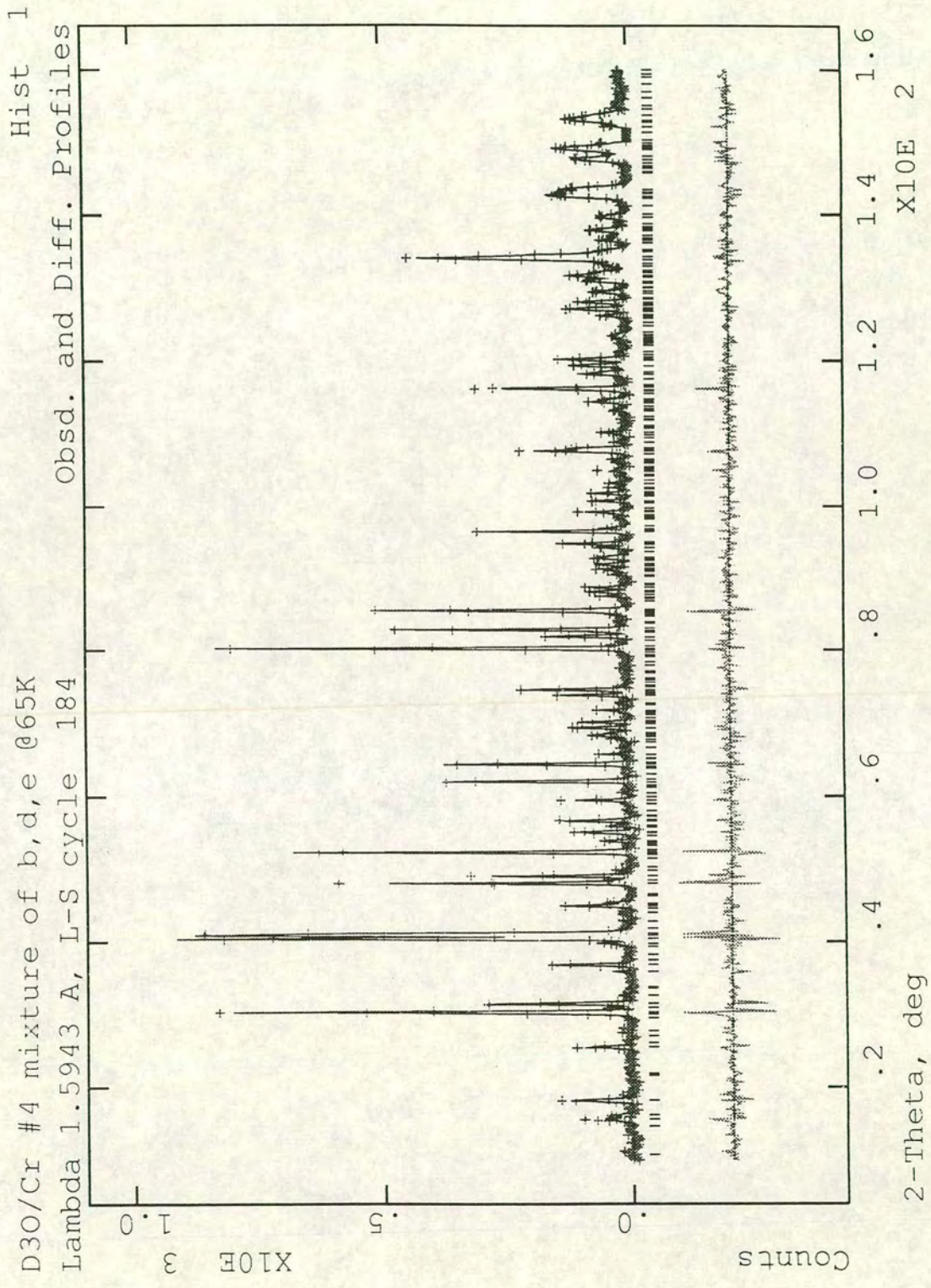

Figure 5.13. Fit of refined profile to neutron scattering data for $(D_3O)Cr_3(SO_4)_2(OD)_6$ using the $P\bar{3}m1$ space group.

5.4.8 Neutron diffraction: Cm crystal structure

Previous X-ray analysis of the mineral gorceixite, $BaAl_3(PO_4)_2(OH)_5.H_2O$, have shown it to be distorted away from the alunite structure, and to have a unit cell with the Cm space group.[27,28] The 3-fold axis present in the previous space groups is now absent and the only symmetry operator that the monoclinic unit cell possesses is a mirror plane. The structural parameters of gorceixite are too distorted away from the $R\bar{3}m$ structure to be used as starting values, so the starting co-ordinates were derived from the $R\bar{3}m$ structural parameters.

The Cm unit cell and its relation to the $R\bar{3}m$ rhombohedral unit cell are shown in *Figure 5.14.* The conversion of the rhombohedral to the monoclinic unit cell was carried out using Matrix A [*Equation 5.3*]. CLLCHG was then used to convert the $R\bar{3}m$ atom locations into those of the Cm unit cell. This process involves using the transpose of A^{-1} [*Equation 5.4*]; the large number of redundant atoms generated by the programme were manually removed. The Cm lattice parameters (*a'*, *b'*, *c'* and β') are related to the hexagonal (*a*, *b* and *c*) according to *Equations 5.5 - 5.8.*

$$A = \begin{bmatrix} 0.33333 & 0.66667 & 0.66667 \\ 1 & 0 & 0 \\ 0.33333 & 0.66667 & -0.33333 \end{bmatrix} \qquad (5.3)$$

$$\text{Transpose of } A^{-1} = \begin{bmatrix} 0 & 0.5 & 1 \\ 1 & -0.5 & 0 \\ 0 & 1 & -1 \end{bmatrix} \qquad (5.4)$$

$$a'^2 = \frac{a^2}{3} + \frac{4c^2}{9} \qquad (5.5)$$

$$b' = a \qquad (5.6)$$

$$c'^2 = \frac{a^2}{3} + \frac{c^2}{9} \qquad (5.7)$$

$$\tan\beta' = \frac{3ac\sqrt{3}}{3a^2 - 2c^2} \qquad (5.8)$$

Thermal parameter constraints were the same as for the $P\bar{3}m1$ structure. The high degree of pseudo-symmetry present in the unit cell made the refinement difficult. The refined values of the atomic parameters are displayed in *Table 5.4*; the refinement profile is shown in *Figure 5.15.*

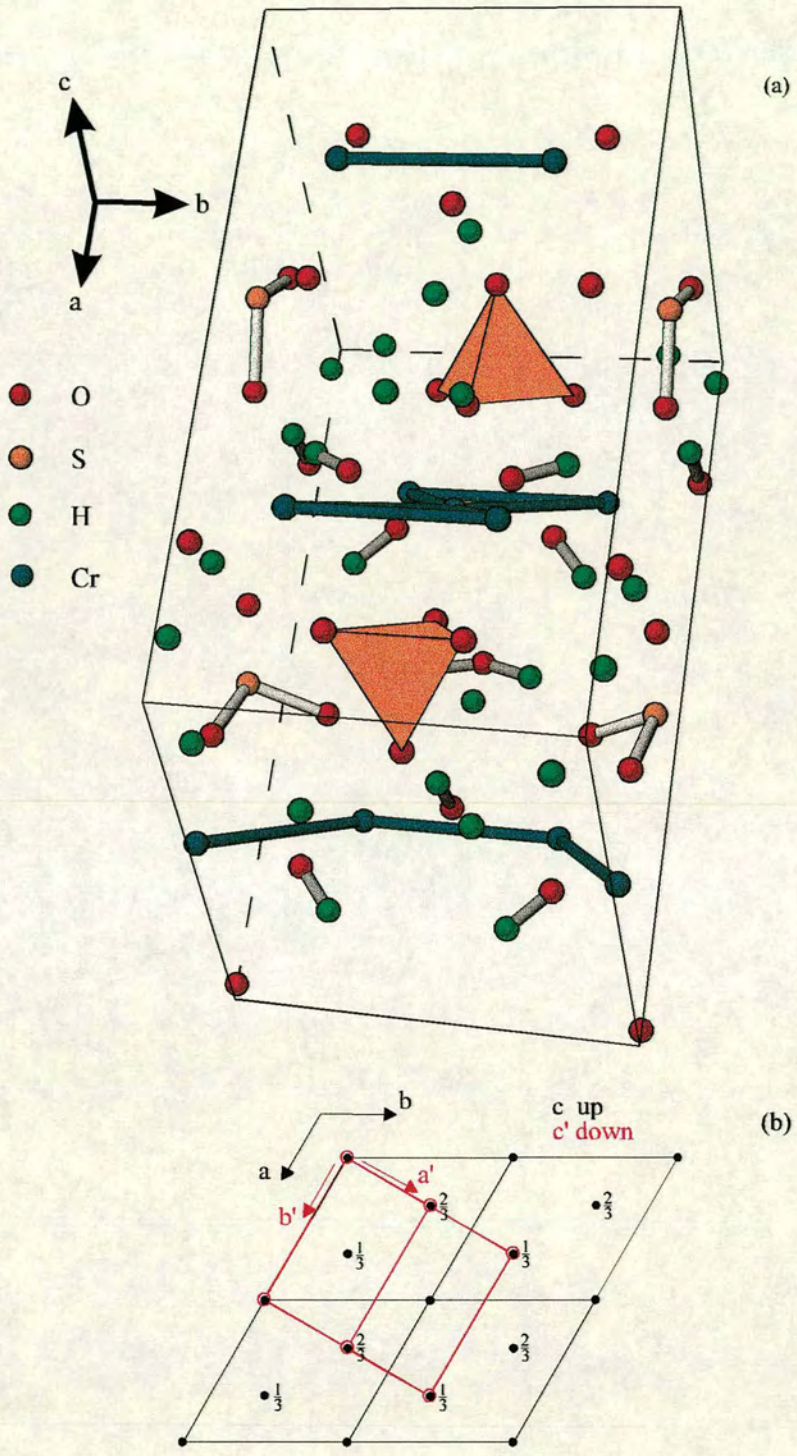

Figure 5.14. (a) The unit cell of $(D_3O)Cr_3(SO_4)_2(OD)_6$ in the Cm space group; (b) the relation between the monoclinic and hexagonal unit cells.

atom (Wyckoff site)	*x*	*y*	*z*	U_{iso}/Å^2	*site symmetry*	*fractional occupancy*
Cr1 (2a)	0.9767 (37)	0.00000	-0.506 (7)	0.0050 (16)	M(010)	1.000
Cr2 (4b)	0.2222 (20)	0.2540 (29)	0.009 (4)	0.0050 (16)	1	1.000
S1 (2a)	0.278 (4)	0.00000	-0.326 (9)	0.111 (33)	M(010)	1.000
S2 (2a)	0.171 (5)	0.50000	0.287 (8)	0.111 (33)	M(010)	1.000
O1 (2a)	-0.0266 (27)	0.00000	0.0037 (44)	0.0068 (6)	M(010)	1.000
O2 (2a)	0.3655	0.00000	0.6090 (39)	0.0068 (6)	M(010)	1.000
O3 (2a)	0.5859 (20)	0.00000	0.3991 (36)	0.0068 (6)	M(010)	1.000
O4 (4b)	0.3092 (16)	0.8330 (23)	-0.1654 (29)	0.0068 (6)	1	1.000
O5 (2a)	0.6456 (22)	0.50000	0.4979 (38)	0.0068 (6)	M(010)	1.000
O6 (2a)	0.8190 (22)	0.00000	0.4986 (38)	0.0068 (6)	M(010)	1.000
O7 (4b)	0.1456 (16)	0.3262 (23)	0.1725 (27)	0.0068(6)	1	1.000
O8 (2a)	0.2438 (22)	0.00000	0.1037 (38)	0.0064 (8)	M(010)	1.000
O9 (4b)	0.5519 (15)	0.3060 (23)	0.7470 (28)	0.0064 (8)	1	1.000
O10 (4b)	0.4060 (16)	0.3025 (20)	0.2667 (27)	0.0064 (8)	1	1.000
O11 (2a)	0.7251 (20)	0.00000	-0.1294 (37)	0.0064 (8)	M(010)	1.000
D1 (4b)	0.5170 (30)	0.3757 (37)	0.0399 (57)	0.00321 (31)	1	0.500
D2 (2a)	0.3698 (52)	0.50000	-0.0703 (80)	0.00321 (31)	M(010)	0.500
D3 (2a)	0.5550 (35)	0.50000	0.0391 (60)	0.00321 (31)	M(010)	0.500
D4 (4b)	0.4949 (36)	0.4092 (46)	0.8831 (64)	0.0321 (31)	1	0.500
D5 (2a)	0.2747 (25)	0.00000	0.2847 (50)	0.0137 (10)	M(010)	1.000
D6 (4b)	0.4904 (16)	0.2025 (24)	0.6685 (32)	0.0137 (10)	1	1.000
D7 (4b)	0.4639 (16)	0.2239 (20)	0.2802 (30)	0.0137 (10)	1	1.000
D8 (2a)	0.6696 (24)	0.00000	0.6917 (40)	0.0137 (10)	M(010)	1.000

Table 5.4. Structural parameters for $(D_3O)Cr_3(SO_4)_2(OD)_6$ at 65K in the space group Cm with Z = 2. Cell parameters: a = 12.1098 (4)Å, b = 7.23885 (31), c = 7.05996 (29)Å, and β = 123.5249° (21). χ^2 = 5.04%. R_{wp} = 7.50%.

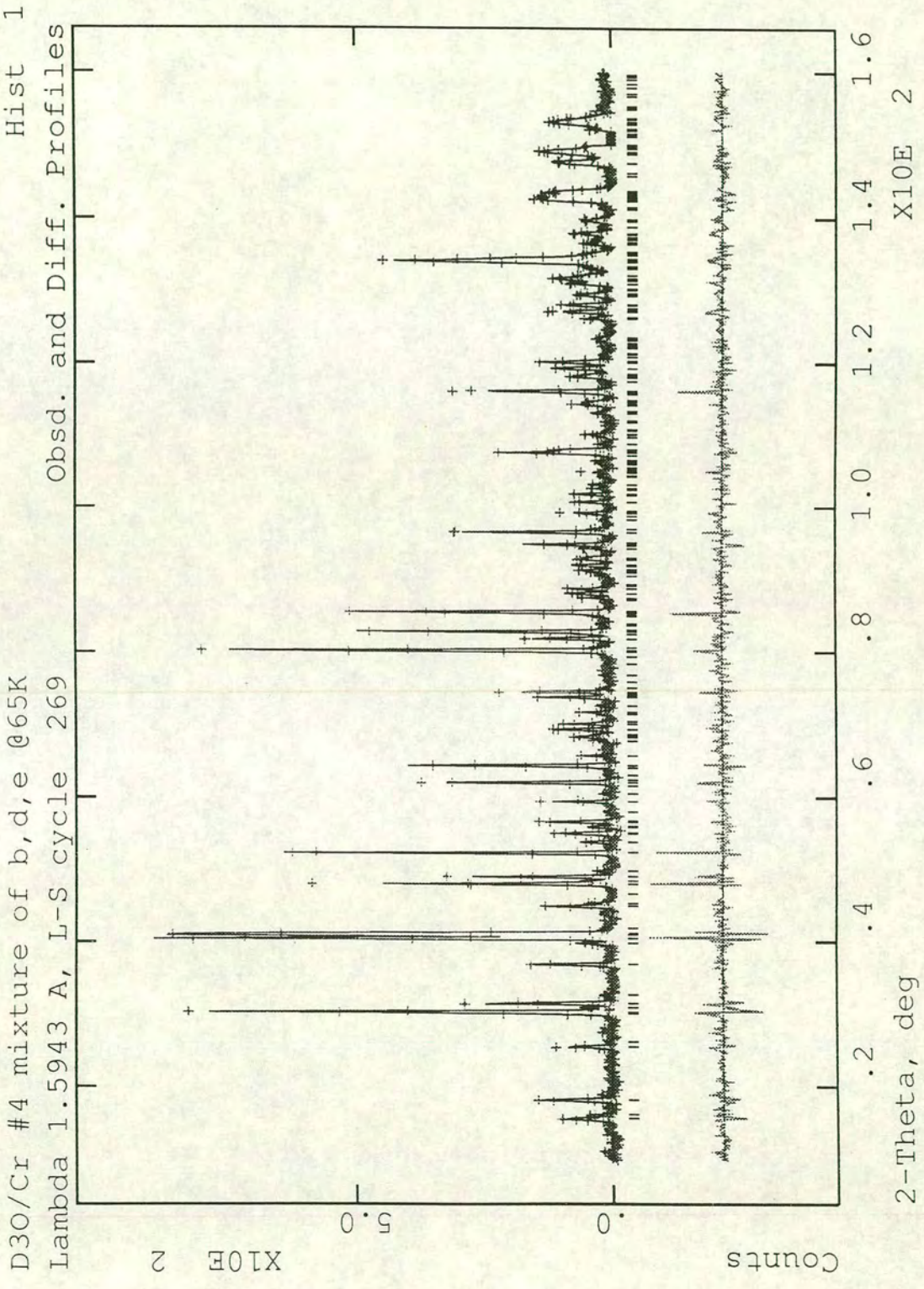

Figure 5.15. Fit of refined profile to neutron scattering data for $(D_3O)Cr_3(SO_4)_2(OD)_6$ using the Cm space group.

5.5 Conclusion

$(H_3O)Cr_3(SO_4)_2(OH)_6$ has been shown to be the highest occupied S = 3/2 Kagomé antiferromagnet studied to date. Its magnetic behaviour is clearly unlike that of $KCr_3(SO_4)_2(OH)_6$, which has a magnetic occupation of ~ 80 - 90%, in that rather than just possessing a simple spin-glass-like transition at low temperature, there is a broad hump in $\chi_m(T)$ at ~ 30K and then a sharp ferromagnetic increase at T_c = 2.2K. Neutron diffraction shows short-range order of the type seen in $(H_3O)Fe_3(SO_4)_2(OH)_6$ below 30K, and very weak ferromagnetic peaks at 1.2K. The lack of hysteresis below 2K is compatible with dynamic domain boundaries and also with the MuSR data which indicates that the moments are still dynamic at 2.5K; freezing of moments below this temperature is unlikely as the specific heat shows very little entropy change by 2.5K. The specific heat data also show that an applied magnetic field has no effect on the form of the 30K transition. This situation is reminiscent of the undecouplable Gaussian decay seen in the MuSR measurements of $(H_3O)Fe_3(SO_4)_2(OH)_6$, and suggests that below 30K the magnetic system has condensed into a spin liquid phase. Unlike $(H_3O)Fe_3(SO_4)_2(OH)_6$ and SCGO(x) this spin liquid features no spin-glass-like behaviour and so represents a new form of magnetic ground state. The ferromagnetic response seen below T_c = 2.2K is compatible with a D-M-type of ferromagnetism created by the canting of antiferromagnetically aligned moments. This effect is weak and the transition is disrupted by the application of an external magnetic field.

An examination of the dynamics of this system both above and below the 2.2K critical temperature by MuSR and inelastic neutron scattering will give important information about the properties of this form of magnetic order.

5.6 References

1. Y.J. Uemura, A. Keren, K. Kojima, L.P. Le, G.M. Luke, W.D. Wu, Y. Ajiro, T. Asano, Y. Kuriyama, M. Mekata, H. Kikuchi, and K. Kakurai, Phys.Rev.Lett. **73**, 3306 (1994).

2. A.P. Ramirez, G.P. Espinosa, and A.S. Cooper, Phys.Rev.B Condens.Matter **45**, 2505 (1992).

3. B. Martinez, A. Labarta, R. Rodriguezsola, and X. Obradors, Phys.Rev.B Condens.Matter **50**, 15779 (1994).

4. A. Keren, L.P. Le, G.M. Luke, W.D. Wu, Y.J. Uemura, Y. Ajiro, T. Asano, H. Kuriyama, M. Mekata, and H. Kikuchi, Hyperfine Interact. **85**, 181 (1994).

5. G. Aeppli, S. Lee, C. Broholm, T.G. Perring, M. Adams, C. Carlile, A.D. Taylor, A.P. Ramirez, and B. Hessen, Physica B **213**, 142 (1995).

6. M. Sumikawa, H. Ohta, M. Motokawa, H. Kikuchi, and H. Nagasawa, Physica B **201**, 123 (1994).

7. A.P. Ramirez, G.P. Espinosa, and A.S. Cooper, Phys.Rev.Lett. **64**, 2070 (1990).

8. B. Martinez, F. Sandiumenge, A. Rouco, A. Labarta, J. Rodriguezcarvajal, M. Tovar, M.T. Causa, S. Gali, and X. Obradors, Phys.Rev.B Condens.Matter **46**, 10786 (1992).

9. C. Broholm, G. Aeppli, G.P. Espinosa, and A.S. Cooper, Phys.Rev.Lett. **65**, 3173 (1990).

10. P. Schiffer, A.P. Ramirez, K.N. Franklin, and S.W. Cheong, Phys.Rev.Lett. **77**, 2085 (1996).

11. S.H. Lee, C. Broholm, G. Aeppli, T.G. Perring, B. Hessen, and A. Taylor, Phys.Rev.Lett. **76**, 4424 (1996).

12. M.G. Townsend, G. Longworth, and E. Roudaut, Phys.Rev.B Condens.Matter **33**, 4919 (1986).

13. C. Broholm, S.H. Lee, M.F. Collins, L. Heller, A.P. Ramirez, C. Kloc, and E. Bucher, *unpublished work* (1992).

14. H.A. Dabkowska, *personal communication* (1995).

15. C.H. Williams, D.J. David, and O. Iismaa, J.Agric.Sci. **59**, 381 (1962).

16. '*Introduction to Ligand Fields*', B.N. Figgis (Interscience Publishers, New York, 1966).

17. A.P. Ramirez, C. Broholm, S.H. Lee, M.F. Collins, L. Heller, C. Kloc, and E. Bucher, J.Appl.Phys. **73**, 5658 (1993).

18. '*Magnetochemistry*', R.L. Carlin (Springer Verlag, Berlin, 1986).

19. T. Moriya, Phys.Rev. **120**, 91 (1960).

20. L. Shekhtman, O. Entin-Wohlman, and A. Aharony, Phys.Rev.Lett. **69**, 836 (1992).

21. L. Klein and A. Aharony, Phys.Rev.B Condens.Matter **44**, 856 (1991).

22. T. Moriya, Phys.Rev. **117**, 635 (1960).

23. W. Koshibae, Y. Ohta, and S. Maekawa, Phys.Rev.Lett. **71**, 467 (1993).

24. '*Solid State Magnetism*', J. Crangle (Edward Arnold, London, 1996).

25. '*Introduction to Magnetism and Magnetic Materials*', D. Jiles (Chapman and Hall, London, 1994).

26. A. Keren, K. Kojima, L.P. Le, G.M. Luke, W.D. Wu, Y.J. Uemura, M. Takano, H. Dabkowska, and M.J.P. Gingras, Phys.Rev.B Condens.Matter **53**, 6451 (1996).

27. E.W. Radoslovich and P.G. Slade, Neues.Jahrb.Mineralogie.Monatsh. 157 (1980).

28. E.W. Radoslovich, Chem. Neues.Jahrb.Mineralogie.Monatsh. 446 (1982).

6 Experimental Kagomé Antiferromagnets: $S = 1$

6.1 Introduction

Previous studies of the organic radical system (*m*-N-methylpyridinium α-nitronyl nitroxide)•X^- have shown that the magnetic centres make up a $S = 1$ Kagomé lattice.[1] There has been no further investigation into the properties of this Kagomé system because of the poor understanding of the complex exchange pathways; the crystal structure is not yet fully refined. Thus, $(H_3O)V_3(SO_4)_2(OH)_6$ provides, what is at present, the best opportunity to examine the properties of a $S = 1$ Kagomé antiferromagnet. No inelastic neutron scattering experiments have yet been done so nothing can be said at this point with regard to the presence or not of a gap in the spin-wave excitation spectrum [*Section 2. 9.4*]. A consequence of the small moment is that the magnetic neutron scattering from long-range and short-range order will be weak. For this reason, MuSR may provide the best experimental probe of the dynamic properties of the antiferromagnetic transition. As theory again predicts a disordered ground state, it is interesting to compare how much entropy is released at T_f, with the other $S = 5/2$ and 3/2 jarosite-type compounds. (Note: T_f will be used to refer to the maximum in the dc susceptibility, as there is currently no evidence that this is a true critical phase transition.)

6.2 $(D_3O)V_3(SO_4)_2(OD)_6$

6.2.1 Synthesis

As no vanadium analogues of jarosite were known, initial synthetic attempts were based on the preparation of $(H_3O)Cr_3(SO_4)_2(OH)_6$. The basic oxide V_2O_3 was used as a soluble source of V^{3+} ions and the SO_4^{2-} introduced in the form of sulfuric acid. The amount of acid and the reaction temperature were then adjusted to optimise the formation of the jarosite-type precipitate and also to minimise the formation of amorphous products.

The thermal gradients in the PTFE lined stainless-steel bombs were such that they hindered the reaction, and markedly reduced the product yield. For this reason all syntheses were carried out in Pyrex ampoules with 15ml of reaction solution. 2.03g of V_2O_3 were added to ~ 5ml of D_2O and 3ml of D_2SO_4 (96%) were slowly added. In order to minimise unwanted oxidative reactions during the addition of the D_2SO_4, this procedure was carried out with the ampoule standing in a cold water bath. The reaction volume was then made up to 15ml and the ampoule sealed. To solubilise the V_2O_3, the ampoule was preheated at 90°C for 1 hour (to give a blue solution) before being heated to 140°C for 16 hours. The black precipitate was washed three times with D_2O and dried in a furnace at 120°C for 3

hours. This process was repeated three times in order to make a sample with a size suitable for neutron scattering. Total product mass ~ 2.3g.

Elemental composition was analysed as (wt.%): 1.7 D, 34.4 V, 13.0 S, and 50.9 O (theoretical composition: 3.8 D, 32.2 V, 13.5 S, and 50.5 O). S and D contents were determined by elemental combustion, while V content was determined by atomic absorption spectroscopy using a solution prepared from boiling the sample in concentrated HCl. The O content was then deduced by subtraction, and the overall stoichiometry determined on the assumption that the S content is stoichiometric as $V_{3.33}D_{4.20}S_{2.00}O_{15.70}$. The higher than stoichiometric level of vanadium indicates the presence of some vanadium rich impurity phases. While X-ray and neutron diffraction shows the presence of impurity Bragg peaks, the presence of amorphous phases is also likely. These impurity species could contain vanadium in the oxidation states III, IV, or V. This last possibility would of course be diamagnetic and would not contribute to any temperature dependent magnetic response. Dc susceptibility measurements show no evidence of contamination from unreacted V_2O_3 (T_c = 170K). Reaction of V_2O_3, prior to use, with water in the air would result in isotopic substitution and the low D content observed.

6.2.2 X-ray diffraction

A powder X-ray diffraction pattern was collected using a Philips X'pert diffractometer with CuKα radiation at the University of Edinburgh. The sample was held in an air-tight holder filled with argon gas to prevent oxidation of the sample. The refinement was carried out as for $(H_3O)Ga_3(SO_4)_2(OH)_6$. The quality of the data is insufficient to determine thermal parameters so they were arbitrarily set at 0.01Å^2. The fit is shown in *Figure 6.1* and the refined structural parameters in *Table 6.1*. The high R_{wp} is largely a reflection of the data quality.

The diffraction pattern did show the presence of a number of low-intensity impurity peaks. These did not correspond to unreacted V_2O_3. The large number of possible non-stoichiometric vanadium oxides and hydroxy sulfates complicates their analysis and the impurity has not yet been identified.

atom (Wyckoff site)	*x*	*y*	*z*	U_{iso}/Å^2	*site symmetry*	*fractional occupancy*
V (9d)	0.16667	-0.16667	-0.16667	0.01 (*)	2/M(110)	1.000
S (6c)	0.00000	0.00000	0.3075 (5)	0.01 (*)	3M(100)	1.000
O1 (6c)	0.00000	0.00000	0.3975 (9)	0.01 (*)	3M(100)	1.000
O2 (18h)	0.2192 (6)	-0.2192 (6)	-0.0512 (5)	0.01 (*)	M(110)	1.000
O3 (18h)	0.1351 (6)	-0.1351 (6)	0.1294 (5)	0.01 (*)	M(110)	1.000
O4 (6c)	0.00000	0.00000	0.00000	0.01 (*)	3M(100)	0.500

Table 6.1. Structural parameters for $(D_3O)V_3(SO_4)_2(OD)_6$ at room temperature in space group $R\bar{3}m$ with Z=3 refined from X-ray diffraction data. Cell parameters: a = 7.3248 (4)Å and c = 17.2182 (10)Å.. R_{wp} = 28.96% and χ^2 = 1.98.

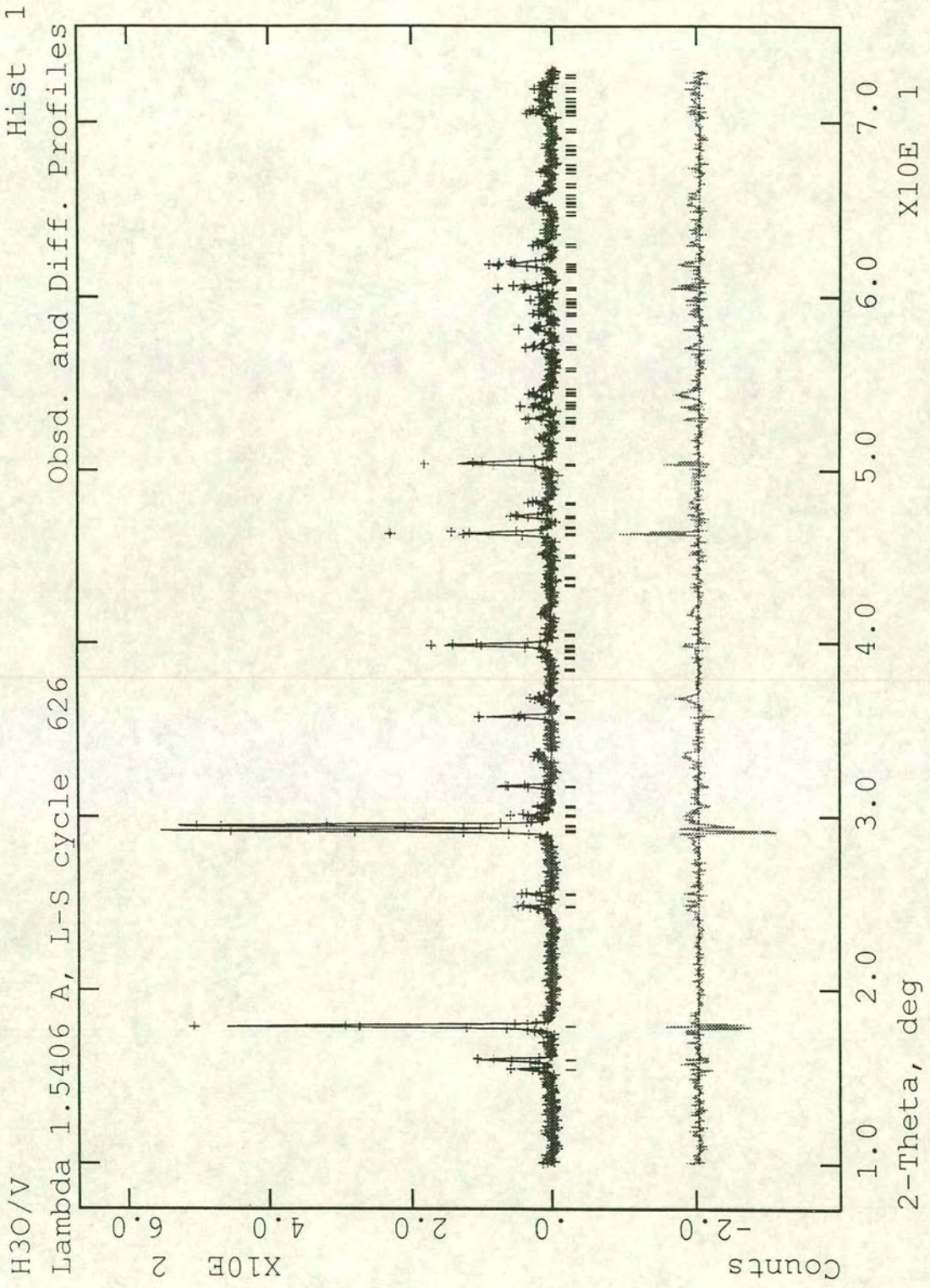

Figure 6.1. Fit of refined profile to X-ray diffraction data for $(D_3O)V_3(SO_4)_2(OD)_6$ using the $R\bar{3}m$ space group.

6.2.3 Dc susceptibility

Dc susceptibility measurements taken in a field of 100G show a cusp at T_f = 21K corresponding to some form of antiferromagnetic transition [*Figure 6.2(a)*]; there is no significant separation of fc and zfc measurements above or below this temperature. The lack of a cusp in χ_m at 170K indicates that the product has no significant contamination from unreacted V_2O_3. The effective moment, μ_{eff}, has a value of $3.1\mu_B$ at 300K which is larger that the spin-only value of $2.83\mu_B$. As vanadium is an early transition metal, the orbital angular momentum of the V(III) $^3T_{1g}$ ground term (in an octahedral co-ordination) opposes the spin angular momentum and leads to a reduction of the effective moment, μ_{eff}, with respect to the spin-only value, μ_{so}. Low symmetry components in the ligand-field created by Jahn-Teller distortions split the degeneracy of the T term into an A and an E term. Commonly, this splitting overwhelms the effect of the spin-orbit coupling and the moment is close to the spin-only value.[2] Contributions from second-order Zeeman terms give rise to a small temperature independent paramagnetism that will again act to reduce μ_{eff}. The curvature of the inverse susceptibility observed in this sample could have a number of causes:

- The presence of a vanadium rich impurity would lead to μ_{eff} greater than μ_{so}. Such a species would introduce an additional paramagnetic term in the Curie-Weiss-type description of the system and cause a curvature in the inverse susceptibility. The temperature range of χ_m is too restricted to allow unambiguous determination of two Curie-Weiss-type paramagnetic terms. Thus, the temperature dependence of the impurity's contribution was assumed to be low, and it was modelled as a temperature independent term. Curve fits of χ_m to *Equation 5.2* over a number of temperature ranges between 150 and 330K allow the Curie-Weiss temperature, θ_w, to be estimated as -45 to -100K. As this temperature is of the order of T_f it corresponds to a low value of the frustration index f [*Section 2.5*] and indicates that the frustration inherent in the Kagomé lattice has been relieved somehow. A simple Jahn-Teller distortion cannot create this effect as it would result in a structure that was topologically identical to the Kagomé lattice, and therefore still very frustrated. The distortion could relieve the frustration by an increase in the interlayer exchange; however this would result in an increased tendency to form 3-D long-range order, which is not observed in neutron scattering experiments [*Section 6.2.5*].
- The effect of the impurity on the inverse susceptibility could be small and the curvature is a property of the Kagomé phase, perhaps caused by a small amount of parasitic ferromagnetism in addition to the underlying antiferromagnetism. This would lead to an apparent reduction of θ_w with cooling and correspond to a value of θ_w > 100K, and so a larger value of f.

In addition to these possibilities there is still the question of the nature of the 21K transition itself: the large quantum effects in this low and integer spin system could result in a new form of ground state, and so transition, where the normal arguments of frustration and of a frustration index do not apply.

6.2.4 Specific heat

A protonated sample of $(H_3O)V_3(SO_4)_2(OH)_6$ was synthesised using the preparation given [Section 6.2.1]. Specific heat data taken over the temperature range 2 - 36K were corrected for the phonon background measured with the gallium compound (which contributes ~ 7% of the signal at these temperatures) to give the magnetic contribution C_m. The presence of a peak at $T_f = 21$K indicates that a substantial number of moments are freezing at this temperature, and that therefore this response, and that observed at this temperature in χ_m, cannot be a property of a small amount of impurity. Below T_f there is no simple linear or quadratic dependence of C_m [*Figure 6.3(c)*] which contrasts with the behaviour observed in the other Kagomé systems. The magnetic specific heat, C_m, was fitted to a fifth order polynomial equation and C_m/T integrated to give the magnetic entropy [*Figure 6.3(a)*]. Approximately 43% of the magnetic entropy is released at T_f, again indicating that this corresponds to a substantial amount of ordering. This value is far larger that that observed in SCGO(x), $(D_3O)Fe_3(SO_4)_2(OD)_6$ or $(D_3O)Cr_3(SO_4)_2(OD)_6$, and indicates that the ground state has a different type of order to these materials. It is difficult to comment on whether this entropy release is compatible with the amount of magnetic order in a spin-fluid ground state, as this will obviously depend on the precise model used and on the restrictions that it places on the allowed spin configurations.

6.2.5 Neutron scattering

Neutron powder patterns were taken using the POLARIS diffractometer at 4.2 and 30K. At 4.2K there was no evidence of long-range magnetic order within the noise level of the data. This cannot be taken as proof that there is no magnetic long-range order, as the strength of magnetic scattering from a spin S is proportional to S^2, and will be therefore weak for a $S = 1$ system. There was no change in the diffuse scattering between the two temperatures which indicates that any short-range order in the system does not change significantly at T_f.

In order to prevent the vanadium (0 1 1) peak from hindering analysis of the impurity Bragg peaks the region around d = 2.13Å was excluded. The refinement of the nuclear structure was performed simultaneously using A and C bank data collected at 4.2K over 10 hours (1344μA) from ~ 2g of sample, as for $(H_3O)Fe_3(SO_4)_2(OH)_6$. The fits are shown in *Figure 6.4.* In addition to the $R\bar{3}m$ structure there was evidence of a crystalline impurity phase; additional amorphous impurities could also be present, but it is impossible to gauge their amount due to the increase in the respective backgrounds towards low d-spacing. The poor quality of the data resulted in the thermal parameters of the V and D1 being refined to unphysical values. The small neutron scattering length of vanadium

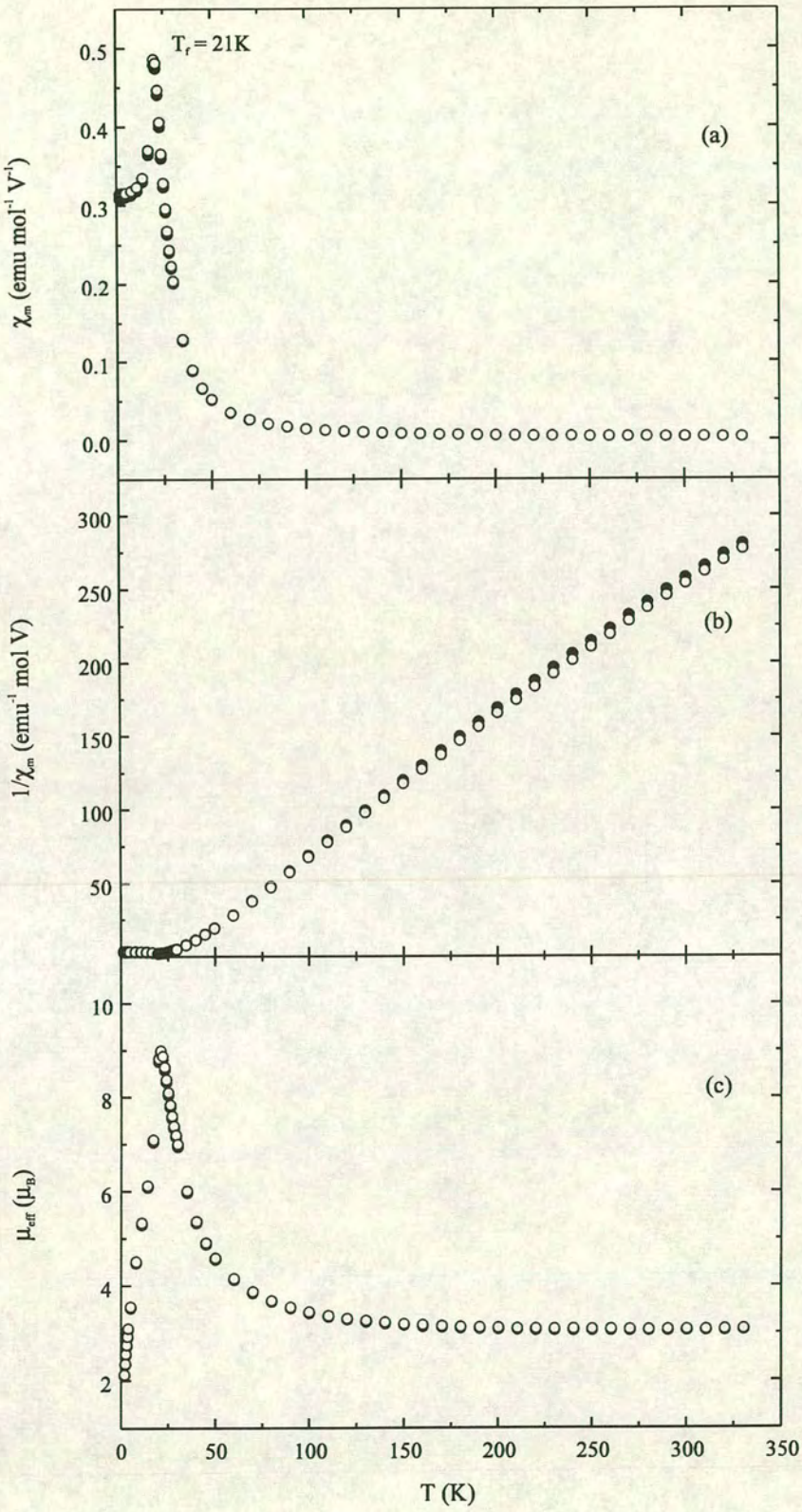

Figure 6.2. (●) Zero-field-cooled and (○) field-cooled dc susceptibility measurements as a function of temperature for $(D_3O)V_3(SO_4)_2(OD)_6$: (a) susceptibility, χ_m, T_f = 21K; (b) inverse susceptibility, $1/\chi_m$; (c) effective moment, μ_{eff}.

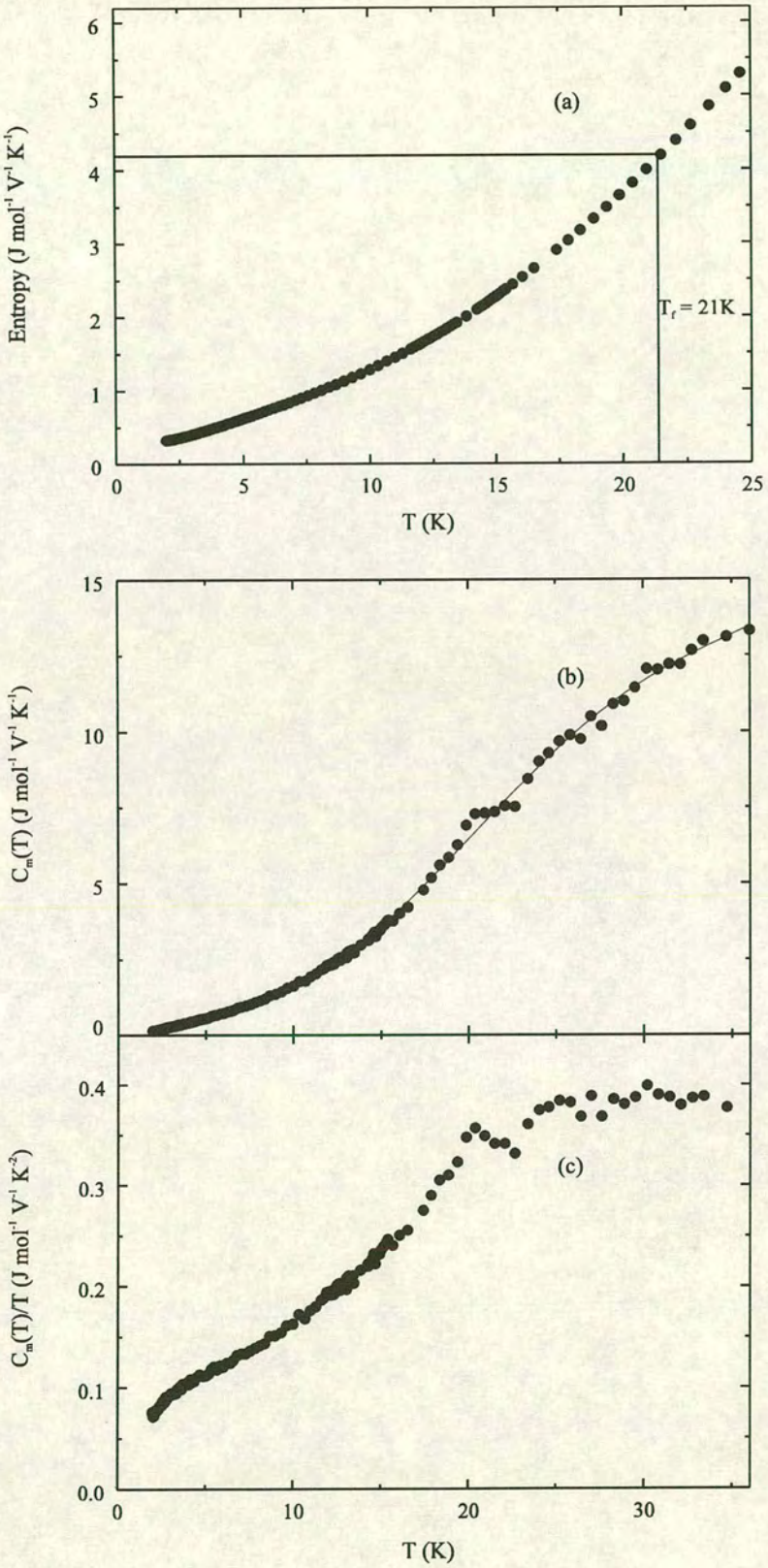

Figure 6.3. Specific heat data for $(H_3O)V_3(SO_4)_2(OH)_6$: (a) Entropy; (b) C_m, magnetic contribution to the specific heat; (c) C_m/T.

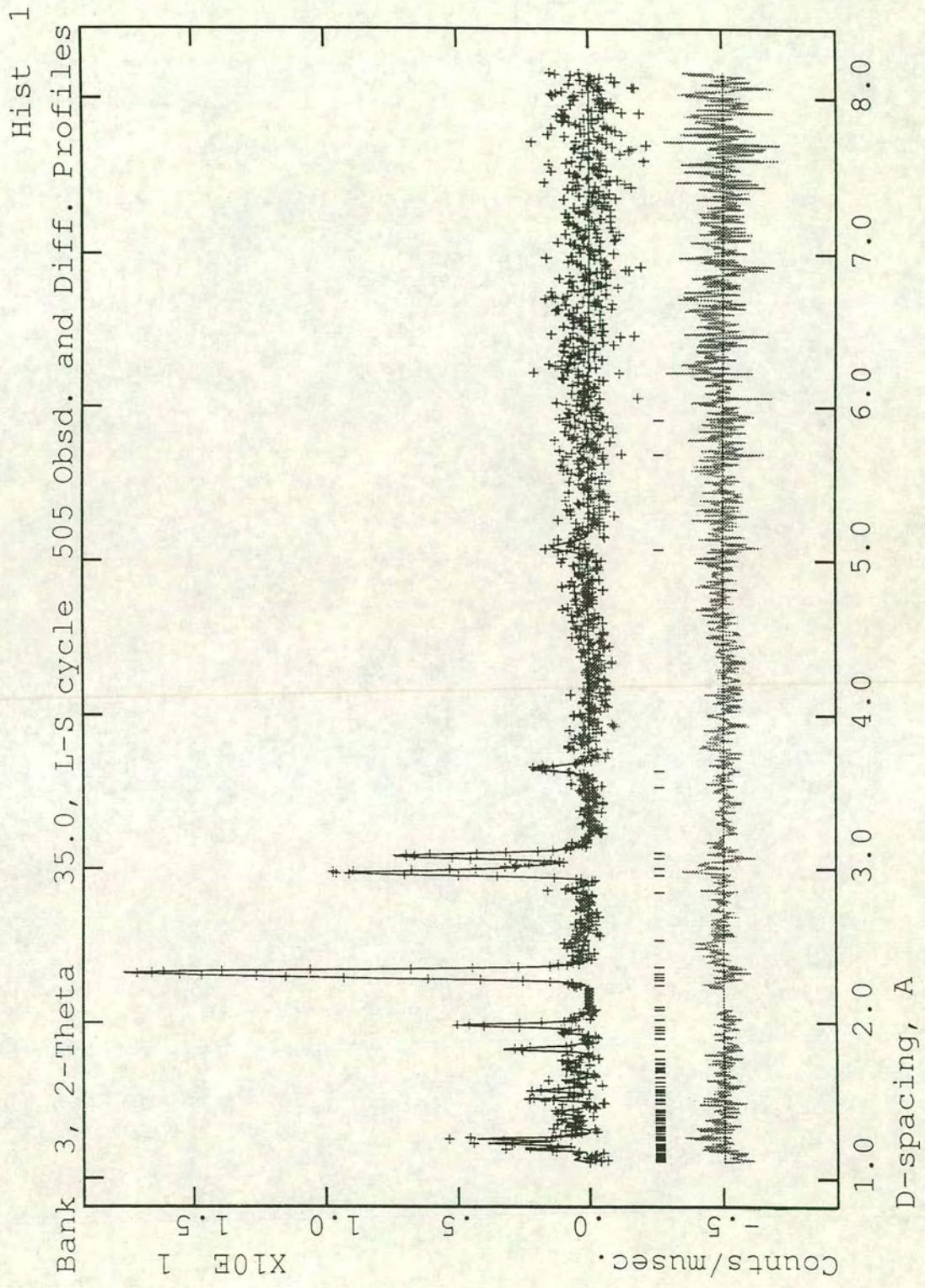

Figure 6.4(a). Fit of refined profile to A bank neutron diffraction data for $(D_3O)V_3(SO_4)_2(OD)_6$ using the $R\bar{3}m$ space group.

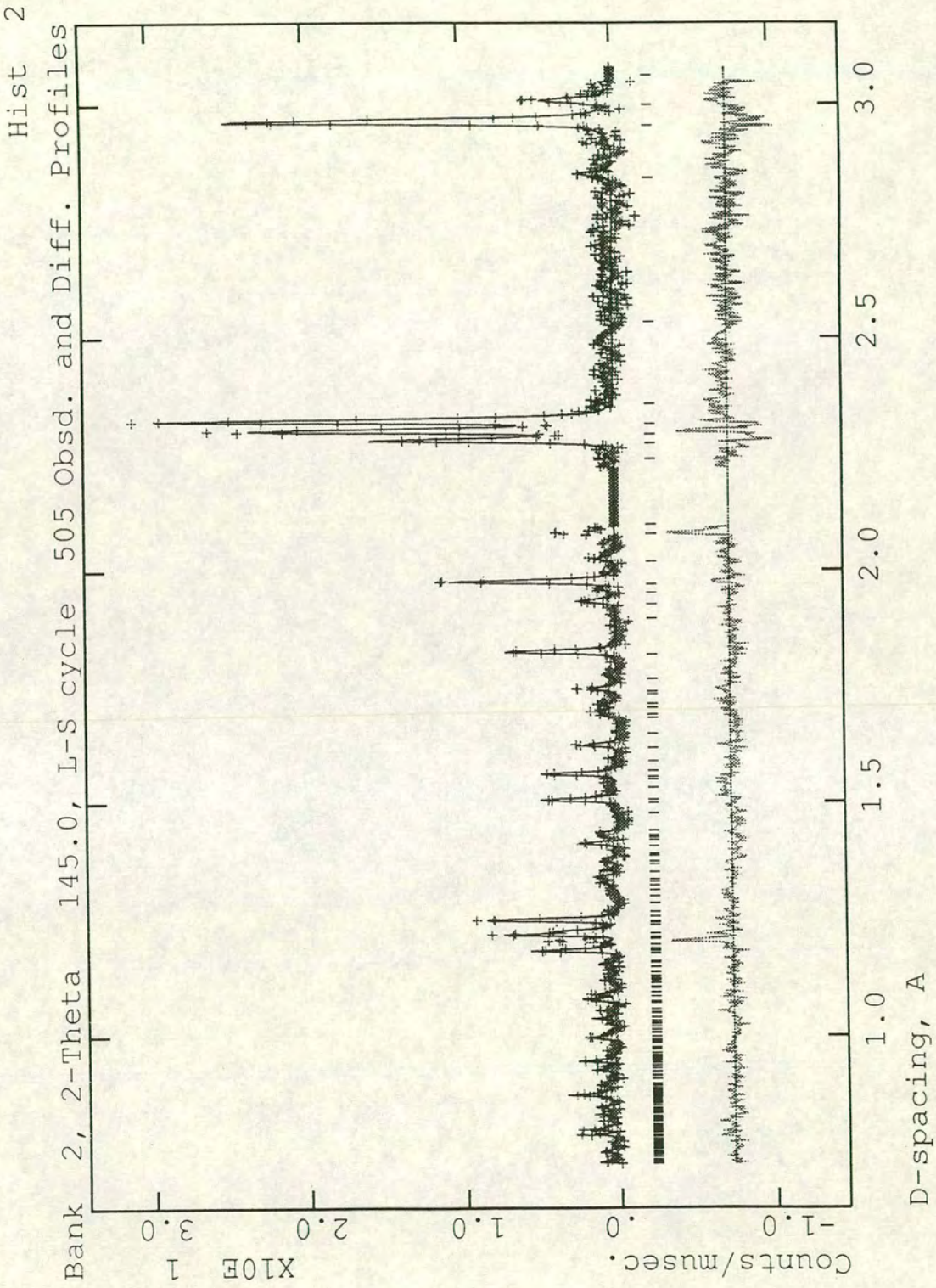

Figure 6.4(b).Fit of refined profile to C bank neutron diffraction data for $(D_3O)V_3(SO_4)_2(OD)_6$ using the $R\bar{3}m$ space group.

6.4 References

1. K. Awaga, T. Okuno, A. Yamaguchi, M. Hasegawa, T. Inabe, Y. Maruyama, and N. Wada, Phys.Rev.B Condens.Matter **49**, 3975 (1994).

2. '*Introduction to Ligand Fields*', B.N. Figgis (Interscience Publishers, New York, 1966).

7 Conclusions

7.1 Kagomé antiferromagnets: S = 1, 3/2 and 5/2

A combination of techniques: ac and dc magnetometry, specific heat, neutron diffraction, and MuSR, were used to study the magnetic properties and crystal structures of members of the series $AB_3(SO_4)_2(OH)_6$ ($A^+ = Na^+$, K^+, Rb^+, Ag^+, NH_4^+, and H_3O^+; $B^{3+} = V^{3+}$, Cr^{3+}, and Fe^{3+}). The hydronium compounds ($A^+ = H_3O^+$; $B^{3+} = V^{3+}$, Cr^{3+}, and Fe^{3+}) have been shown to provide the best model S = 1, 3/2 and 5/2 Kagomé antiferromagnets yet known; the Kagomé sites have a coverage of ~ 98% in the case of $B^{3+} = Cr^{3+}$ and Fe^{3+}.

Neutron diffraction measurements on $(H_3O)Fe_3(SO_4)_2(OH)_6$ have shown it to possess only short-range magnetic order based on the $\sqrt{3}$ x $\sqrt{3}$ spin configuration below a spin-glass transition temperature, T_f ~ 17K. The dynamics of this spin-glass-like phase are similar to those of SCGO(x), in that muon spin relaxation measurements show no evidence of a static component. Instead, the observed response indicates that the moments are dynamic, in opposition to conventional spin-glass theory. $(H_3O)Fe_3(SO_4)_2(OH)_6$ and SCGO(x) both deviate further from expected spin-glass behaviour in that their specific heats have a T^2 dependence below T_f, rather than the linear dependence normally observed. Although such a quadratic behaviour is reminiscent of a gapless excitation spectrum of the type seen in long-range ordered 2-D antiferromagnets, and suggests that the ground state does indeed have some long-range character, it could also be a signature of a 2-D spin nematic phase. In contrast to SCGO(x), where deliberate reduction of the occupation of the magnetic sites causes only a decrease in T_f as the mean-field experienced by each moment is reduced, dilution in hydronium jarosite *stabilises* long-range order with the in-plane q = 0 spin configuration; $(H_3O)Fe_3(SO_4)_2(OH)_6$ is the first example of a system in which dilution of the magnetic sites actually causes the system to order classically, rather then reducing the tendency towards long-range order. We have found the same magnetic structure, below T_c ~ 50K, in the other members of the series: $A^+ = Na^+$, Rb^+, Ag^+ and NH_4^+, and $B^{3+} = Fe^{3+}$. These materials have a lower occupation of magnetic sites, commonly of 80-95%. Neutron scattering measurements, below T_c, show that the moments in these less magnetically concentrated materials contribute to both a long-range ordered phase, and to a short-range ordered phase of the type observed in $(H_3O)Fe_3(SO_4)_2(OH)_6$. This is compatible with a non-uniform distribution of defects stabilising long-range order only in the areas with a high defect concentration; areas with relatively few defects will possess only short-range order.

Preliminary characterisation of the new material $(H_3O)Cr_3(SO_4)_2(OH)_6$ by dc susceptibility and neutron diffraction shows that on cooling below ~30K there is a gradual formation of short-range order of the type observed in $(H_3O)Fe_3(SO_4)_2(OH)_6$, but at 2.2K there is a transition to a state with very weak ferromagnetic ordering, ascribed to a canting of moments out of the Kagomé plane. Such

behaviour has been predicted by Monte-Carlo calculations for a Kagomé system with weak Ising anisotropy. Muon spin relaxation measurements taken at 2.5K show the moments again to be dynamic. The specific heat data show very little release of the magnetic entropy between 0.36 and 2.5K which suggests that the spins do not freeze below this temperature. A dynamic system of moments could not give rise to conventional domain ferromagnetism with the associated irreversibilities. The lack of any observed hysteresis effects is therefore an expected consequence of a dynamic system. While the D-M interaction that creates this weak canted ferromagnetism is overpowered by the application of a large magnetic field, specific heat data show that the broader ~ 30K transition is unaffected. This response is very similar to the undecouplable decay observed in the MuSR measurements of $(H_3O)Fe_3(SO_4)_2(OH)_6$ and so may be indicative of spin-fluid phase. The lack of any observed spin-glass-like behaviour is most likely a consequence of the increased quantum fluctuations present in this S = 3/2 system with respect to the S = 5/2 Fe(III) analogue. This magnetic behaviour is clearly unlike that of $KCr_3(SO_4)_2(OH)_6$, which has a magnetic occupation of 80 - 90%, and possesses long-range and spin-glass-like order at low temperature.

Of all the Kagomé antiferromagnets yet studied, the new material $(H_3O)V_3(SO_4)_2(OH)_6$ is perhaps the most perplexing. χ_m displays a sharp magnetic transition at 25K. Specific heat data show that a substantial amount of magnetic entropy is released by this temperature, ~ 43% of $Rln(2S+1)$, which indicates a transition to a highly ordered ground state. However, no evidence of magnetic long-range order is observed in powder neutron diffraction. While there are at present no MuSR data available for this material, it is tempting to conclude that the ground state is another form of spin-fluid, *a highly correlated spin-fluid.*

To date, $(H_3O)V_3(SO_4)_2(OH)_6$, $(H_3O)Cr_3(SO_4)_2(OH)_6$, and $(H_3O)Fe_3(SO_4)_2(OH)_6$ offer the best examples of S = 1, 3/2, and 5/2 Kagomé antiferromagnets respectively. Detailed characterisation of the elastic, inelastic and dynamic responses of these materials offers a unique opportunity to investigate the effect of the spin quantum number on the competition between the different possible ground states in the Kagomé antiferromagnet, and on the spin-fluid itself. In addition to the pure materials, this competition can be investigated in detail by studying the effects of dilution on the inelastic response, and on the forms of the long-range and short-range order.

Detailed theoretical work is now required to further explain the unique magnetic properties displayed by these materials.

Appendix A

Tables of bond lengths and angles

Atom labels are defined by *Figure 4.5.*

S—O(1)	1.492 (5)	O(2)—S—O(2′)	110.83 (23)
S—O(2)	1.4495 (26)	O(2)—S—O(1)	108.08 (24)
O(1)—O(2)	2.381 (4)		
O(2)—O(2′)	2.3868 (27)		
		S—O(2)—Fe	129.265 (8)
Fe—Fe	3.66228 (6)	Fe—O(3)—Fe′	133.625 (12)
Fe—O(2)	2.0374 (19)	O(2)—Fe—O(3)	88.968 (13)
Fe—O(3)	1.9921 (8)	O(2″)—Fe—O(3)	91.035 (15)
O(2)—O(3)	2.8236 (15)	O(3)—Fe—O(3′)	89.721 (13)
O(2″)—O(3)	2.8750 (27)	O(3′)—Fe—O(3″)	90.279 (19)
O(3)—O(3′)	2.8103 (33)		
O(3′)—O(3″)	2.8240 (20)		

Table 4.5. Selected bond lengths (Å) and angles (degrees) in $(H_3O)Fe_3(SO_4)_2(OH)_6$ at 1.5K with estimated standard deviations in brackets.

S—O(1)	1.490 (6)	O(2)—S—O(2′)	109.68 (32)
S—O(2)	1.5222 (33)	O(2)—S—O(1)	109.27 (18)
O(1)—O(2)	2.457 (5)		
O(2)—O(2′)	2.489 (6)		
		S—O(2)—Ga	127.63 (24)
Ga—Ga	3.58769 (12)	Ga—O(3)—Ga′	132.13 (15)
Ga—O(2)	2.01421 (17)	O(2)—Ga—O(3)	86.04 (12)
Ga—O(3)	1.96259 (15)	O(2″)—Ga—O(3)	93.96 (15)
O(2)—O(3)	2.2134 (31)	O(3)—Ga—O(3′)	89.55 (15)
O(2″)—O(3)	2.908 (31)	O(3′)—Ga—O(3″)	90.45 (16)

O(3)—O(3′)	2.765 (5)
O(3′)—O(3″)	2.7863 (34)

Table 4.6b. Selected bond lengths (Å) and angles (degrees) in $(H_3O)Ga_3(SO_4)_2(OH)_6$ at room temperature with estimated standard deviations in brackets.

S—O(1)	1.475 (13)	O(2)—S—O(2′)	108.7 (5)
S—O(2)	1.490 (6)	O(2)—S—O(1)	110.3 (5)
O(1)—O(2)	2.43288 (26)		
O(2)—O(2′)	2.42154 (22)		
		S—O(2)—Fe	131.3 (5)
Fe—Fe	3.6722 (4)	Fe—O(3)—Fe′	134.53 (27)
Fe—O(2)	2.013 (4)	O(2)—Fe—O(3)	89.68 (15)
Fe—O(3)	1.9908 (20)	O(2″)—Fe—O(3)	90.32 (15)
O(2)—O(3)	2.82291 (19)	O(3)—Fe—O(3′)	90.56 (21)
O(2″)—O(3)	2.83951 (19)	O(3′)—Fe—O(3″)	89.44 (21)
O(3)—O(3′)	2.8291 (8)		
O(3′)—O(3″)	2.80168 (15)		

Table 4.7b. Selected bond lengths (Å) and angles (degrees) in $(D_3O)Fe_3(SO_4)_2(OD)_6$ at 2K with estimated standard deviations in brackets.

S—O(1)	1.501 (4)	O(2)—S—O(2′)	111.45 (16)
S—O(2)	1.4595 (17)	O(2)—S—O(1)	107.41 (17)
O(1)—O(2)	2.3880 (20)		
O(2)—O(2′)	2.4122 (20)		
		S—O(2)—Fe	128.015 (8)
Fe—Fe	3.6629 (6)	Fe—O(3)—Fe′	134.248 (12)
Fe—O(2)	2.02242 (17)	O(2)—Fe—O(3)	88.678 (15)
Fe—O(3)	1.98779 (18)	O(2″)—Fe—O(3)	91.323 (17)
O(2)—O(3)	2.8049 (11)	O(3)—Fe—O(3′)	88.524 (17)

O(2″)—O(3)	2.4711 (16)	O(3′)—Fe—O(3″)	91.4796 (19)
O(3)—O(3′)	2.7747 (27)		
O(3′)—O(3″)	2.8471 (16)		

Table 4.9b. Selected bond lengths (Å) and angles (degrees) in $NaFe_3(SO_4)_2(OD)_6$ at 40K with estimated standard deviations in brackets.

S—O(1)	1.448 (22)	O(2)—S—O(2′)	109.2 (9)
S—O(2)	1.480 (8)	O(2)—S—O(1)	109.8 (8)
O(1)—O(2)	2.3951 (6)		
O(2)—O(2′)	2.41199 (22)		
		S—O(2)—Fe	130.5427 (17)
Fe—Fe	3.66415 (19)	Fe—O(3)—Fe′	133.51 (20)
Fe—O(2)	2.036 (4)	O(2)—Fe—O(3)	89.19 (14)
Fe—O(3)	1.9939 (15)	O(2″)—Fe—O(3)	90.81 (14)
O(2)—O(3)	2.82977 (15)	O(3)—Fe—O(3′)	91.41 (19)
O(2″)—O(3)	2.86997 (19)	O(3′)—Fe—O(3″)	88.59 (19)
O(3)—O(3′)	2.8542 (5)		
O(3′)—O(3″)	2.78490 (5)		

Table 4.11b. Selected bond lengths (Å) and angles (degrees) in $(ND_4)Fe_3(SO_4)_2(OD)_6$ at 1.5K with estimated standard deviations in brackets.

S—O(1)	1.471 (12)	O(2)—S—O(2′)	109.627 (17)
S—O(2)	1.490 (5)	O(2)—S—O(1)	109.3148 (22)
O(1)—O(2)	2.416 (5)		
O(2)—O(2′)	2.4355 (15)		
		S—O(2)—Cr	129.402 (15)
Cr—Cr	3.6187 (12)	Cr—O(3)—Cr′	133.638 (15)
Cr—O(2)	1.9891 (26)	O(2)—Cr—O(3)	88.05 (12)
Cr—O(3)	1.9682 (14)	O(2″)—Cr—O(3)	91.95 (12)

O(2)—O(3)	2.750 (8)	O(3)—Cr—O(3′)	89.29 (17)
O(2″)—O(3)	2.845 (4)	O(3′)—Cr—O(3″)	90.71 (15)
O(3)—O(3′)	2.766 (5)		
O(3′)—O(3″)	2.800 (4)		

Table 5.1b. Selected bond lengths (Å) and angles (degrees) for $(D_3O)Cr_3(SO_4)_2(OD)_6$ in the space group $R\bar{3}m$ at 65K with estimated standard deviations in brackets.

S—O(1)	1.448 (10)	O(2)—S—O(2′)	109.3 (4)
S—O(2)	1.493 (5)	O(2)—S—O(1)	109.6 (4)
O(1)—O(2)	2.404 (6)		
O(2)—O(2′)	2.435 (6)		
		S—O(2)—V	129.981 (19)
V—V	3.644 (6)	V—O(3)—V′	133.310 (17)
V—O(2)	2.0163 (31)	O(2)—V—O(3)	85.57 (13)
V—O(3)	1.9848 (16)	O(2″)—V—O(3)	92.43 (15)
O(2)—O(3)	2.769 (4)	O(3)—V—O(3′)	87.57 (20)
O(2″)—O(3)	2.889 (5)	O(3′)—V—O(3″)	92.07 (20)
O(3)—O(3′)	2.769 (4)		
O(3′)—O(3″)	2.857 (5)		

Table 6.2b. Selected bond lengths (Å) and angles (degrees) in $(D_3O)V_3(SO_4)_2(OD)_6$ at 4.2K with estimated standard deviations in brackets.

Appendix B

Published papers

Structure and magnetism of hydronium jarosite, a model Kagomé antiferromagnet

Andrew S. Wills and Andrew Harrison*
Department of Chemistry, University of Edinburgh, The King's Buildings, West Mains Road, Edinburgh, UK EH9 3JJ

We have determined the structure of a synthetic sample of the mineral hydronium jarosite by powder neutron diffraction, locating all the hydrogen atoms. Octahedrally coordinated Fe^{3+} ions are linked through their vertices to produce Kagomé layers of moments with a coverage of *ca.* 95 ± 4%, depending on the synthesis conditions. Magnetic susceptibility measurements indicate strong coupling of these moments, with a Curie–Weiss constant of −1200 K, but there is no evidence for long-range magnetic order in neutron powder diffraction patterns taken down to 1.5 K. Instead, we observe an anomaly in the magnetic susceptibility at 17.2 K which is a characteristic of spin-glass freezing and similar to experimental work and theory for other Kagomé antiferromagnets.

A common theme that runs through many of the most significant episodes in solid-state magnetism in the past two decades is frustration.[1–4] From spin-glasses through high-T_c superconductors to magnets with spin-fluid ground states, frustration provides a necessary ingredient for the different unusual magnetic properties. The concept is illustrated in Fig. 1 for the case of a triangular array of magnetic moments which are coupled antiferromagnetically and free to rotate in the plane of the paper. Any two moments, taken in isolation, may be coupled antiferromagnetically, but the topology of the lattice prevents a third moment from coupling antiferromagnetically to this pair of moments [Fig. 1(a)]; the compromise arrangement, with the lowest exchange energy, is the 120° array depicted in Fig. 1(b).

This form of frustration arises in any lattice containing odd-numbered loops of moments coupled antiferromagnetically to their nearest neighbours. The ordered ground state depends on a balance of competing spin interactions, and is very sensitive to magnetic or non-magnetic impurities, which may induce canted local states and spin-glass behaviour.[1,5,6] The ground-state spin array of the pure magnet may also be unconventional: although the spin arrangement of the elementary triangle of Fig. 1(b) may be extended infinitely in two dimensions to produce the triangular lattice shown in Fig. 2(a),[2,3] there are other frustrated lattices in which the magnetic ground state is not a simple spin array extended throughout the lattice. The Kagomé lattice (named after a form of Japanese basket weaving) [Fig. 2(b)] is the most celebrated example of this.[3,4] Not only are the individual plaquettes triangular, but they are also connected in a manner that prevents the 120° antiferromagnetic array from propagating coherently. Instead, the ground state is highly degenerate, fluctuating between different forms to produce a new form of magnetic ground state with no conventional long-range correlations.

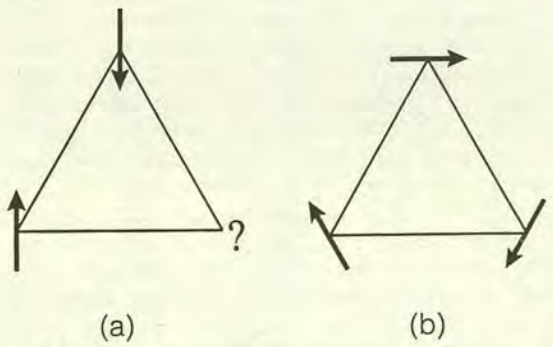

Fig. 1 Spin configurations in a triangular lattice of antiferromagnetically coupled XY moments: (a) depicts the impossibility of arranging a third moment so that it is antiparallel to both its antiferromagnetically coupled neighbours; (b) depicts a compromise spin configuration of minimum energy

Despite the interest in this new form of magnetic ground state, there has been little experimental work on materials with this form of lattice owing to the lack of suitable model compounds. The only material that has been studied in any depth is the layered garnet $SrGa_{12-x}Cr_xO_{19}$ [SCGO(x)][3] for which experiments show that the $S = 3/2$ moments on Cr^{3+} are arranged on a Kagomé lattice with strong antiferromagnetic coupling (the Curie–Weiss constant θ is *ca.* −500 K[7]) yet there is no long-range magnetic order down to at least 1.5 K; instead, hysteretic behaviour is observed at 3.5 K, which is indicative of a spin-glass transition[8] and neutron scattering measurements reveal short-range antiferromagnetic correlations with a length of 7 ± 2 Å.[9] However, SCGO(x) suffers from a severe disadvantage as a model material in that the coverage of the Kagomé lattice sites is significantly less than 100% and, depending on the preparative method, ranges from 88–95%; further, a significant proportion of moments reside on a triangular lattice interspersed between the Kagomé layers. Clearly there is a need for other model systems, with higher lattice coverage and a cleaner separation between Kagomé layers.

The jarosite family of minerals, with general formula $AFe_3(SO_4)_2(OH)_6$ (where A = Na^+, K^+, Rb^+, Ag^+, Tl^+,

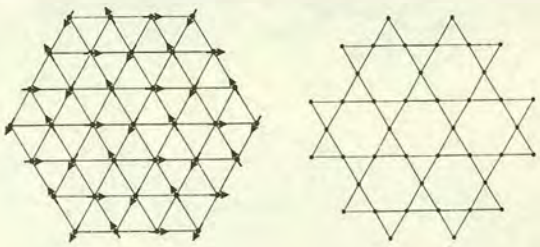

Fig. 2 Extended lattices of (a) triangular and (b) Kagomé symmetry showing the 120° antiferromagnetic spin array in the former

NH_4^+, H_3O^+, $\frac{1}{2}Pb^{2+}$ or $\frac{1}{2}Hg^{2+}$),[10–14] appears to supply such a model. We will discuss the structure in detail below (Fig. 3), but the essential feature for the magnetic properties is the layers of octahedrally coordinated Fe^{3+} ions (Fig. 4) that lie on the vertices of a Kagomé network (Fig. 5). These planes are well separated by further layers of sulfate, hydroxide and A cations. Jarosites, together with the parent minerals, the alunites (in which Fe^{3+} is replaced by Al^{3+}), are also of great interest to mineralogists as common minerals found in diverse environments: considerable effort has been devoted to reproducing the synthetic conditions for natural jarosite formation[15–17] and in studying the incorporation of impurity ions. Interest is further fuelled by their importance as metal ores, particularly of silver,[18] and in metallurgic industries, providing highly efficient methods of precipitating iron from hydrometallurgic processing solutions with low loss of Zn^{2+} or Cu^{2+}.[19] The jarosite family may be extended by synthesis of compounds in which Fe^{3+} is replaced by In^{3+} or Ga^{3+},[19] or the sulfate group is replaced by SeO_4^{2-} or CrO_4^{2-}.[13,19]

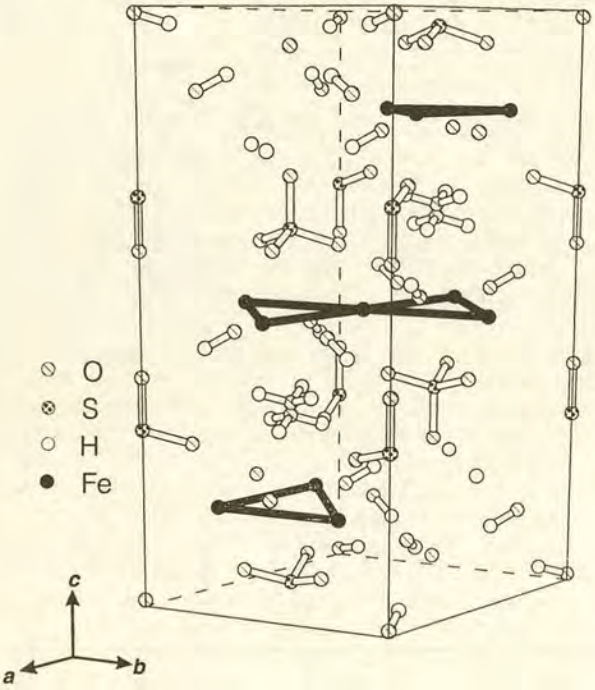

Fig. 3 Unit cell of hydronium jarosite in a hexagonal setting

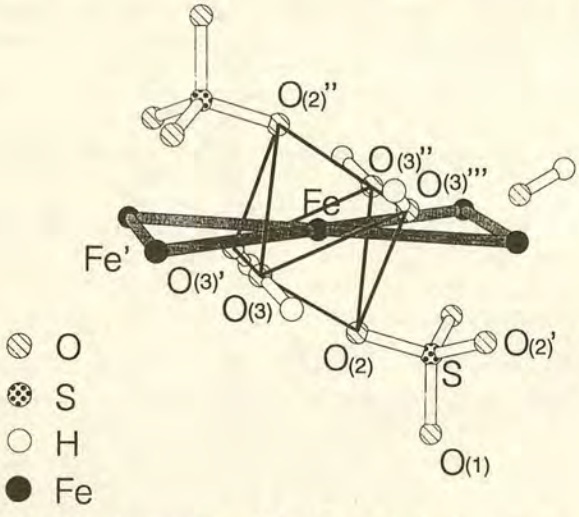

Fig. 4 Local coordination of Fe^{3+} ions in hydronium jarosite, showing the distorted octahedral coordination by OH^- and SO_4^{2-} and defining the atom labels used in Table 2

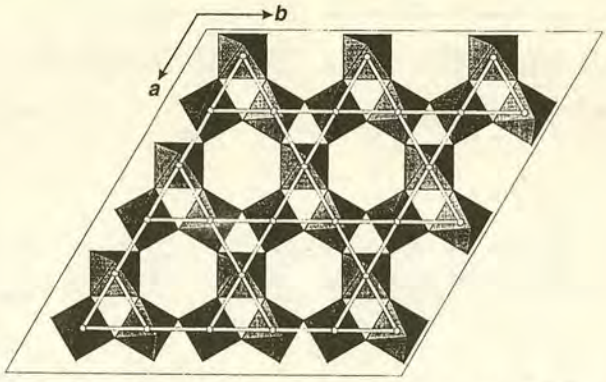

Fig. 5 Network of interlinked Fe–O octahedra that form a Kagomé network of Fe^{3+} ions in hydronium jarosite

There is still uncertainty about the precise location of hydrogen atoms, and the structural role of water as H_3O^+, H_2O or OH^- in jarosites;[20] remarkably, there have been no neutron scattering studies to resolve this. It is known that there is a tendency for H_3O^+ to replace up to 80% of the A cations and also for Fe^{3+} sites to be vacated while charge balance is maintained by protonation of OH^- to form H_2O.[21] This leads to an occupation of Fe^{3+} sites that is generally significantly less than 100%, and typically in the range 83–94%. An exception is the hydronium salt $H_3O \cdot Fe_3(SO_4)_2(OH)_6$ which can be prepared with an iron content of *ca.* 98%.[21] We report the first full structural determination of this mineral, locating the position of all the hydrogen atoms, as well as the results of powder neutron diffraction and magnetic susceptibility measurements designed to probe the nature of any magnetic phase transitions or long-range order down to 1.5 K.

Experimental

Synthesis

The preparation was based on an established hydrothermal route.[21] 40 g of $Fe_2(SO_4)_3 \cdot nH_2O$ (Aldrich Chemical Co., 97%) was dissolved in deionised water and made up to 300 ml. The reaction solution was heated in a PTFE-lined stainless-steel bomb at 140 °C for 4 h. The jarosite precipitate was washed three times with deionised water and dried well at 120 °C for 2 h. The resulting ochre-coloured powder was finely ground. Attempts were also made to grow crystals of hydronium jarosite by slow hydrolysis at a low pH (< 1.0) produced by the addition of concentrated sulfuric acid. Crystals grown in this manner had a truncated cubic form and ranged in size from 5 to 20 μm.

Analysis

Natural jarosites and the parent minerals alunites occur as solid solutions of various members of the family.[16,22] Even when potential impurity ions are excluded, alkali-metal ions tend to be replaced by hydronium ions to give a maximum alkali-metal ion content of 67–75%.[21] The degree of this substitution increases as the reaction temperature is raised[23] and with the degree of dilution of the alkali-metal sulfate,[18] though not with the acidity of the reaction mixture. We have noted that Fe^{3+} may also leave the lattice, accompanied by protonation of OH^- to H_2O to maintain charge balance. It is therefore important to analyse for all component species in synthetic products to determine the coverage of the magnetic lattice.

The identity and crystallinity of samples were checked by powder X-ray diffraction, and elemental composition analysed as (wt.%): 2.1 H, 34.2 Fe, 13.7 S and 50 O (theoretical composition: 1.9 H, 34.9 Fe, 13.3 S and 49.9 O). S and H contents were determined by elemental combustion analysis, while the

Fe content was determined by atomic absorption spectroscopy using a solution prepared by boiling the sample in concentrated HCl. The O content was then deduced by subtraction, and the overall stoichiometry determined using the assumption that the S content is stoichiometric as $Fe_{2.84}H_{9.77}S_{2.00}O_{14.56}$. The principal error arises in the Fe analysis, leading to an estimate of (34.2 ± 1.0) wt.%, or a coverage of Fe sites of 95 ± 4%. We found that the magnetic properties of our product were extremely sensitive to stoichiometry; samples whose composition appeared identical within the experimental error in our analysis had magnetic transitions at temperatures that ranged from 12 to 18 K and this was used as the most sensitive test of composition. We comment on this point below and will report on it in greater detail in a future paper.

Structural studies

Neutron powder diffraction patterns were taken at 1.5, 4.5, 20, 300 and 330 K using an 'Orange' cryostat on the POLARIS diffractometer at the ISIS Facility of the CLRC Rutherford Appleton Laboratory, UK. The data collection from *ca.* 2 g of sample held in a vanadium can took 3 h. Simultaneous refinement was performed on data collected from the low angle (A) and back scattering (C) banks for which the range of *d*-spacing is 0.5–8.15 Å and 0.2–3.2 Å, respectively. Refinement of the crystal structure was carried out using version 6 of the personal computer translation of GSAS.[24] The region of the C bank profile near the (0 1 1) reflection of vanadium ($d = 2.14$ Å) was excluded from the refinement.

Magnetic susceptibility

Magnetic susceptibility data were recorded between 1.8 and 330 K using a Quantum Design $MPMS_2$ SQUID magnetometer. The magnetisation of a 40 mg sample was measured as a function of temperature in an applied field of 10 G, first after cooling the sample in zero applied field and applying the field at 1.8 K, then after cooling the sample from 330 to 1.8 K in 10 G and measuring in the same field. We call these zero-field cooled and field-cooled measurements, respectively. This procedure is designed to reveal spin-glass transitions, manifested by a divergence between zero-field cooled and field-cooled measurements at the freezing transition.

Results

Structure

The jarosite family and the parent alunite mineral family belong to the rhombohedral space group $R\bar{3}m$. The crystal structure is displayed in a hexagonal setting of this space group in Fig. 3 with $a \approx 7.32$ Å and $c \approx 16.92$ Å. The crystal structure of potassium jarosite, including approximate configurations of the hydrogen atoms of the hydroxide groups, had already been determined by single-crystal X-ray diffraction from a natural sample.[11,25] This was used as the starting point for our refinement, with H_3O^+ substituted for K^+ and the oxygen atom O(4) moved to the more general position (6c) (0 0 *z*). The atoms of the H_3O^+ ion were given a 50% fractional occupation at each of the six symmetry-generated sites to represent statistical disorder.

Data taken at 1.5 K were first refined with the H_3O^+ molecular unit entirely free to be distorted, resulting in a profile fit that appeared to be excellent and yielded weighted pattern *R* values, R_{wp}, of 0.97%, 0.86% and 0.89% for the A bank data, the C bank data and combined data set, respectively, and a value for χ^2 of 2.05. These unusually low values of R_{wp} reflect the high incoherent background contribution to the scattering. This refinement resulted in an O—H bond length of 0.846 (10) Å and an H—O—H bond angle of 95.0 (8)°, which is clearly at odds with values determined for these parameters in the few materials containing H_3O^+ that have been studied to date; more typical values are 0.96 ± 0.08 Å for the O—H bond length and 111–120° for the H—O—H angle.[26–30] In this coordination geometry, hydrogen bonding is expected to cause a decrease in the H—O—H bond angle and also an increase in the O—H bond length. For this reason, the H_3O^+ unit was arbitrarily defined as a rigid body with a 112° bond angle and a 0.96 Å bond length, based on the hydronium structure in hydronium perchlorate.[28] Some deviation from this idealised geometry is expected but it does, however, give a physically more reasonable structure than that resulting from free refinement.

Two orientations of the H_3O^+ unit were examined: the first involved the O(4)—H(1) bond pointing towards the basal oxygen atoms O(2) of the sulfate group; the second was derived from this by rotating the H_3O^+ unit by 60° so that the O(4)—H(1) bond points between the oxygen atoms O(2) of the sulfate group and towards the hydroxy oxygen atoms O(3). We were unable to obtain a stable refinement with the first orientation of H_3O^+ while the second gave values of R_{wp} for the A and C bank refinements and also of the combined data of 1.29%, 0.89% and 1.02%, respectively and $\chi^2 = 2.67$, an increase relative to the values obtained when H_3O^+ was free to be distorted. The atomic coordinates of the other atoms in the unit cell and the fractional occupancy of the Fe sites did not change significantly. The final fitted profile is displayed in Fig. 6(a) and (b) for the A and C bank data respectively. The refined positions of atoms and their thermal parameters, together with cell constants, are given in Table 1.

Magnetic structure and susceptibility

There was no indication of long-range magnetic order in any of the powder neutron diffraction patterns: no new Bragg peaks appeared at any temperature even after careful scrutiny at the positions where magnetic Bragg scattering is observed

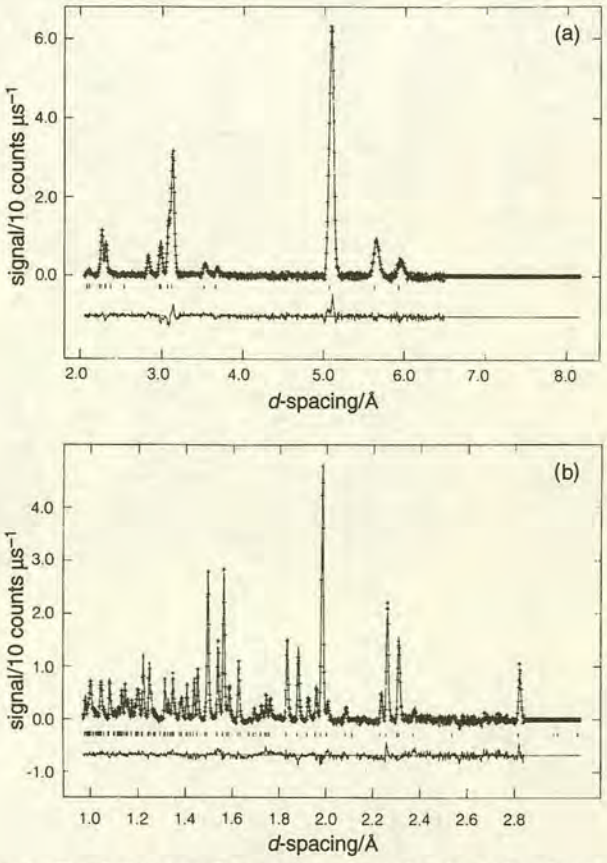

Fig. 6 Fit of refined profile to neutron scattering data taken from (a) the A bank and (b) the C bank of POLARIS

Table 1 Refined atomic and cell parameters for hydronium jarosite at 1.5 K

atom (Wyckoff site)	x	y	z	U_{iso}/Å^2	site symmetry	fractional occupancy
Fe (9d)	0.16667	−0.16667	−0.16667	0.0105 (6)	2/M (110)	0.973 (6)
S (6c)	0.00000	0.00000	0.30555 (34)	0.091 (12)	3M (100)	1.000
O1 (6c)	0.00000	0.00000	0.39374 (20)	0.0162 (5)	3M (100)	1.000
O2 (18h)	0.22471 (12)	−0.22471 (12)	−0.05437 (11)	0.0162 (5)	M (110)	1.000
O3 (18h)	0.12789 (15)	−0.12789 (15)	0.13452 (11)	0.0171 (5)	M (110)	1.000
O4 (6c)	0.00000	0.00000	−0.01076 (46)	0.0047 (14)	3M (100)	0.500
H1 (18h)	−0.07244 (*)	0.07244 (*)	−0.02716 (46)	0.1691 (75)	M (110)	0.500
H4 (18h)	0.19342 (27)	−0.19342 (27)	0.10751 (18)	0.0322 (9)	M (110)	1.000

Cell parameters: $a = 7.32457$ (12) Å and $c = 16.9153$ (4) Å in space group $R\bar{3}m$ with $Z = 3$. Figures with asterisks are reported without errors because they were subject to rigid constraints in the refinement that did not allow variation in that parameter.

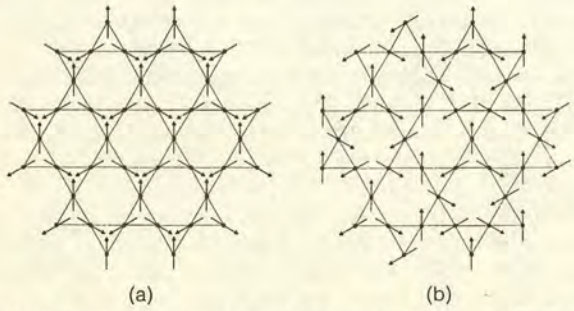

Fig. 7 Spin arrangements for a Kagomé antiferromagnet with second and third neighbour interactions: (a) is the $q = 0$ structure and (b) the $\sqrt{3} \times \sqrt{3}$ structure

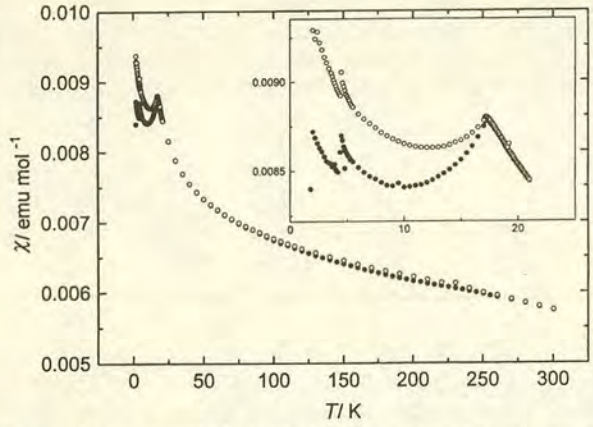

Fig. 8 Molar susceptibility for hydronium jarosite measured in 10 G after cooling the sample in zero field (●) then after cooling in 10 G (○). The inset shows the susceptibility in the region of the spin-glass-like transition.

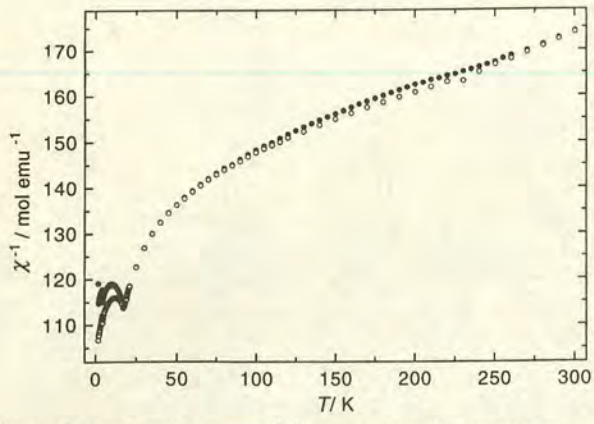

Fig. 9 Inverse molar susceptibility corresponding to the measurements depicted in Fig. 8

in other jarosites.[13,14] Although the Kagomé lattice with nearest-neighbour antiferromagnetic exchange is not expected to show long-range magnetic correlations, further-neighbour exchange may stabilise particular spin structures. If the ratio of 2nd to 3rd neighbour exchange is greater than 1, we expect the so-called $q = 0$ structure depicted in Fig. 7(a) to be stabilised, while a value for this ratio that is less than 1 stabilises the so-called $\sqrt{3} \times \sqrt{3}$ structure depicted in Fig. 7(b). There was no additional scattering corresponding to ferro- or antiferromagnetic interplane exchange combined with either of these intraplane spin structures. The diffuse scattering background rose as the sample temperature was lowered from 330 to 1.5 K, but we were unable to analyse the form it took due to poor signal to noise ratio: the background for this highly hydrogenated sample is high, and POLARIS is not an ideal instrument for the study of such effects.

Magnetic susceptibility

Dc susceptibility data are summarised in Fig. 8 and 9. The dependence of the susceptibility, χ, for a conventional two-dimensional antiferromagnet reflects the effect of strong in-plane correlations at high temperatures which is manifested by a broad maximum. Real, layered antiferromagnets show three-dimensional long-range magnetic order on cooling further owing to the influence of interplane interactions and single-ion anisotropy.[31,32] The susceptibility curve depicted in Fig. 8 shows a broad inflection centred at *ca.* 250 K, which reflects in-plane correlations, and it is likely that deviations from a Curie–Weiss behaviour will extend beyond this temperature. Fig. 9, depicting the inverse molar susceptibility as a function of temperature, confirms this, showing some curvature even at 300 K. In the absence of susceptibility data taken at higher temperature we can only determine a very approximate value of Curie–Weiss constant, θ. Extrapolation of $1/\chi$ against T to $T = 0$ will underestimate $|\theta|$ for T above the broad inflection, while data taken just below the inflection will overestimate $|\theta|$. The range of values deduced from these two extreme cases provides an estimate of θ of -1200 ± 200 K. The effective magnetic moment was found to be *ca.* 3.7 μ_B at 300 K.

At lower temperatures there is a clear divergence between field-cooled and zero-field-cooled measurements at 17.2 K, indicating some form of spin-glass transition. This is consistent with a previous report of spin-freezing in hydronium jarosite at 17.5 K determined by Mössbauer spectroscopy.[12] No other features are observed down to 1.8 K, apart from anomalies at 4.2 and 2.2 K which we believe arise from instabilities in the temperature of the sample near the boiling point and the lambda point of liquid helium, respectively. When the sample is warmed from 1.8 K, it overshoots at these temperatures then equilibrates, and the attendant irreversibility in the magnetic response of the sample is consistent with spin-glass behaviour below $T_g = 17.2$ K.

Discussion

Synthesis

The yield and stoichiometry of jarosite precipitation depends markedly on the reaction temperature; equilibration times range from several months at room temperature[33] to several hours at higher temperatures. The bulk crystal structure is found to be preserved with these substitutions and there is no discernible change in composition, but the magnetic ordering temperature changes, leading to a range of values for T_g for any particular jarosite. In the case of hydronium jarosite we found that T_g varied from 12 to 18 K in samples whose composition was the same according to elemental analysis.

The microscopic mechanism for jarosite precipitation has been studied by spectrophotometry and potentiometric titrations to give equilibrium constants of various complex species present in the solution.[34] At low temperatures, the dominant reaction species were found to be $FeSO_4^+$ and $FeOH^{2+}$. With increasing temperature the relative concentration of $Fe(OH)_2^+$ rises and at 80 °C this species exceeds the concentration of the primary hydrolysis product $FeOH^{2+}$ suggesting that the dominant reaction species under our reaction conditions are $Fe(OH)_2^+$ and $FeSO_4^+$. Further work[35] suggested that the primary building block in these reactions is $Fe(OH)_2^+$ and that the chemical formula of the product is best described as $H_3O[Fe(OH)_2]_3(SO_4)_2$. Protons are released in these reactions, causing the pH of the solution to fall thus retarding the formation of further product. The sulfate concentration also influences the hydrolysis reactions of the Fe^{3+} ion, altering the concentration of the $Fe(OH)_2^+$ and again affecting the rate of precipitation. One consequence of this reaction pathway is that the size of crystallites in the product is commonly very small and we anticipate that it will be very difficult to grow crystals of a size suitable for oriented magnetic susceptibility work, let alone for single-crystal neutron scattering.

Structure

Our neutron refinement defines the character and dispositions of a number of molecular units in the structure. Selected bond lengths and angles are given in Table 2. The Fe^{3+} ions have a distorted octahedral coordination, lying at the centre of a distorted square plane of four hydroxy O(3) atoms, [Fe—O(3) is 1.992 Å], with two basal sulfate O(2) atoms above and below [Fe—O(2) is 2.037 Å] (Fig. 4). These octahedra are linked by their corners to form the Kagomé lattice (Fig. 5). The distance between nearest neighbours within the Kagomé planes is 3.662 Å and the distance between Kagomé planes is 5.639 Å.

The sulfate tetrahedra may be divided into two types, alternately pointing up and down, while H_3O^+ molecules reside in the spaces between the sulfate bilayers. In potassium jarosite the K atom at (0 0 0) is 12-coordinate, with six sulfate oxygen atoms at 2.913 Å and six hydroxy oxygen atoms at 2.816 Å.[25]

Table 2 Selected bond lengths (Å) and angles (degrees) in hydronium jarosite with estimated standard deviations in brackets

S—O(1)	1.492 (5)	O(2)—S—O(2′)	110.83 (23)
S—O(2)	1.4495 (26)	O(2)—S—O(1)	108.08 (24)
O(1)—O(2)	2.381 (4)		
O(2)—O(2′)	2.3868 (27)		
		S—O(2)—Fe	129.265
Fe—Fe	3.66228 (6)	Fe—O(3)—Fe′	133.625
Fe—O(2)	2.0374 (19)	O(2)—Fe—O(3)	88.968
Fe—O(3)	1.9921 (8)	O(2″)—Fe—O(3)	91.035
O(2)—O(3)	2.8236 (15)	O(3)—Fe—O(3′)	89.721
O(2″)—O(3)	2.8750 (27)	O(3′)—Fe—O(3″)	90.279
O(3)—O(3′)	2.8103 (33)		
O(3′)—O(3″)	2.8240 (20)		

Atom labels are defined in Fig. 4.

In hydronium jarosite each proton of the H_3O^+ unit is hydrogen bonded to two sulfate oxygen atoms [H(1)—O(2) is 2.562 Å], and to one hydroxy oxygen atom [H(1)—O(3) is 1.948 Å]. As the shortest hydrogen bonds are to the oxygen atoms of the hydroxy group we conclude that this must be the dominant interaction defining the H_3O^+ orientation. The apical sulfate oxygen atoms are hydrogen bonded to three hydroxy hydrogen atoms, with an H(2)—O(1) separation of 1.946 Å. The inequivalence of the bonding of apical and basal oxygen atoms leads to a slight distortion of the sulfate tetrahedra. The three equivalent bonds from sulfur to the three basal oxygen atoms, S—O(2), have a length of 1.450 Å, while the bond length between the sulfur atom and the apical oxygen atom, S—O(1), is 1.492 Å. The mean S—O bond length is thus 1.461 Å.

Magnetic structure and susceptibility

Hydronium jarosite shows no long-range magnetic order down to 1.5 K, but there is a transition with spin-glass characteristics at 17.2 K. Given that the in-plane magnetic exchange is strongly antiferromagnetic, the absence of long-range magnetic order suggests either that interplane exchange is very weak, or that there is an inherent inability for the Kagomé lattice to show long-range magnetic order. Other jarosites are known to show long-range magnetic order at moderate temperatures,[11,13,14] the sodium, potassium and ammonium salts order at 53, 60 and 55 K, respectively[10] but there is no obvious difference in structure that would suggest that interplane exchange pathways are likely to be worse in the hydronium salt. The difference between the materials that order and the hydronium salt appears to be the degree of coverage of the magnetic lattice: the dilute magnetic lattice shows long-range order while the concentrated lattice does not. The observation of a transition with spin-glass characteristics is compatible with what has been seen in SCGO(x),[8] and also with what has been predicted theoretically.[3,36]

Conclusions

The jarosite structure provides a Kagomé lattice of Fe^{3+} ions, but only the hydronium salt, among the forms studied to date, appears to have a coverage close to 100%. Although we have located all the hydrogen atoms in the structure, there is still uncertainty about the geometry of the H_3O^+ ion. This may be clarified by theoretical work on the expected structure of H_3O^+ in this environment. It is probable that we would also be able to refine the structure to give a more precise set of parameters if the material was fully deuteriated, a process that will greatly reduce the incoherent neutron scattering background. However, it should be noted that the structure and hence the magnetic properties of a deuteriated sample are likely to be different from the hydrogenous material, and therefore also likely to be less relevant to our understanding of the natural material and its geological role.

The absence of magnetic long-range order in the hydronium salt is remarkable: it appears to be the first example of an insulating magnetic material which shows long-range magnetic order when the magnetic sites are diluted, as that appears to be the only important distinction between the hydronium salt, and other jarosites which have lower lattice coverages and also show long-range magnetic order. Further studies are required to reveal the nature of the freezing transition at 17.2 K in detail: heat capacity measurements should reveal whether this is a conventional spin-glass transition with a linear dependence of C_v on T below T_g,[37] or the T^2 form found in SCGO(x);[38] more detailed neutron scattering measurements are required to characterise the static and dynamic character of the short-range magnetic correlations. We also plan to dilute the magnetic lattice deliberately, doping the

hydronium iron salt with the isomorphous aluminium compound to test our hypothesis that it is the high coverage of the magnetic salts that distinguishes this material from other jarosites.

The authors wish to thank Malcolm Collins for drawing their attention to jarosites as Kagomé antiferromagnets. We are grateful to Ron Smith for his assistance with the measurements on POLARIS and Ian Swainson for his help with the GSAS package. We would also like to thank Steve Bramwell, Bob Gould and David Rankin for stimulating and valuable discussions. We thank EPSRC and NATO for financial support, and EPSRC for provision of beam time at the ISIS Facility.

References

1 J. Villain, *Z. Phys.*, 1979, **33**, 31.
2 R. S. Gekht and V. I. Ponomarev, *Phase Transitions*, 1990, **20**, 27.
3 A. P. Ramirez, *Annu. Rev. Mater. Sci.*, 1994, **24**, 453.
4 *Magnetic Systems with Competing Interactions* (*Frustrated Spin Systems*), ed. H. T. Diep, World Scientific, Singapore, 1994.
5 A. Harrison, *J. Phys. C.*, 1987, **20**, 6287.
6 A. Aharony, R. J. Birgeneau, A. Coniglio, M. A. Kastner and H. E. Stanley, *Phys. Rev. Lett.*, 1988, **60**, 1330.
7 X. Obradors, A. Labarta, A. Isalgué, J. Tejada, J. Rodriguez and M. Pernet, *Solid State Commun.*, 1988, **65**, 189.
8 A. P. Ramirez, G. P. Espinosa and A. S. Cooper, *Phys. Rev. Lett.*, 1990, **64**, 2070.
9 C. Broholm, G. Aeppli, G. P. Espinosa and A. S. Cooper, *Phys. Rev. Lett.*, 1990, **65**, 3173.
10 M. Takano, T. Shinjo, M. Kiyama and T. Takada, *J. Phys. Soc. Jpn.*, 1968, **25**, 902.
11 M. Takano, T. Shinjo and T. Takada, *J. Phys. Soc. Jpn.*, 1971, **13**, 1.
12 A. M. Afanasev, V. D. Gorobchenko, D. S. Kulgawczuk and I. I. Lukashevich, *Phys. Stat. Solidi* (*a*), 1974, **26**, 697.
13 M. G. Townsend, G. Longworth and E. Roudaut, *Phys. Rev. B*, 1986, **33**, 4919.
14 C. Broholm, S. H. Lee, M. F. Collins, L. Heller, A. P. Ramirez, C. Kloc and E. Bucher, unpublished work, 1992.
15 J. G. Fairchild, *Am Miner.*, 1933, **18**, 543.
16 G. P. Brophy, E. S. Scott and R. A. Snellgrove, *Am. Miner.*, 1962, **47**, 112.
17 J. E. Dutrizac and S. Kaiman, *Can. Miner.*, 1975, **14**, 151.
18 J. E. Dutrizac and J. L. Jambor, *Hydromet.*, 1987, **17**, 251.
19 J. E. Dutrizac, *NATO Conf. Ser.* (*Hydromet. Process. Fund.*), 1984, **10**, 125.
20 J. A. Ripmeester, C. I. Ratcliffe, J. E. Dutrizac and J. L. Jambor, *Can. Miner.*, 1986, **24**, 435.
21 J. Kubisz, *Miner. Pol.*, 1970, **1**, 45.
22 J. Kubisz, *Bull. Acad. Polon. Sci. Ser. Sci. Geol. Geog.*, 1960, **8**, 95.
23 J. E. Dutrizac, *Metall. Trans. S*, 1983, **14**, 531.
24 Generalised Structural Analysis System, A. C. Larson and R. B. Von Dreele, 1995, obtainable from the authors at LANSCE, MS-H805, Los Alamos National Laboratory, NM 87545, USA.
25 T. Kato and Y. Miura, *Miner. Mag.*, 1977, **8**, 419.
26 F. S. Lee and G. B. Carpenter, *J. Phys. Chem.*, 1959, **63**, 279.
27 Y. K. Yoon and G. B. Carpenter, *Acta Crystallogr.*, 1959, **12**, 17.
28 C. E. Nordman, *Acta Crystallogr.*, 1962, **15**, 18.
29 W. C. Hamilton and J. A. Ibers, *Hydrogen Bonding in Solids*, Benjamin, New York, 1968.
30 M. H. Begemann and R. J. Saykally, *J. Chem. Phys.*, 1985, **82**, 3570.
31 R. L. Carlin, *Magnetochemistry*, Springer-Verlag, Berlin, 1986.
32 L. J. De Jongh, *Magnetic Properties of Layered Transition Metal Compounds*, Kluwer, Dordrecht, 1990.
33 J. B. Brown, *Can. Miner.*, 1970, 696.
34 R. S. Sapieszko, R. C. Patel and E. Matijevic, *J. Phys. Chem.*, 1977, **61**, 1061.
35 C. Härtig, P. Brand and K. Bohmhammel, *Neue Hütte*, 190, **32**, 205.
36 S. T. Bramwell and M. J. P. Gingras, unpublished work, 1994.
37 P. W. Anderson, B. Halperin and C. M. Varma, *Phil. Mag.*, 1972, **25**, 1.
38 A. P. Ramirez, G. P. Espinosa and A. S. Cooper, *Phys. Rev. B*, 1992, **45**, 2505.

Paper 6/01341D; *Received* 26*th February*, 1996

Magnetic Correlations In Deuteronium Jarosite, A Model S = 5/2 Kagomé Antiferromagnet

A. S. Wills and A. Harrison*,

Department of Chemistry, University of Edinburgh, The King's Buildings, West Mains Rd., Edinburgh, EH9 3JJ, UK.

S. A. M. Mentink and T. E. Mason

Department of Physics, University of Toronto, 60 St. George Street, Toronto, Ontario, M5S 1A7, Canada.

Z. Tun

Atomic Energy of Canada Limited, Chalk River, Ontario, Canada, K0J 1JO

* Author to whom correspondence should be addressed

Deuteronium jarosite, $(D_3O)Fe_3(SO_4)_2(OD)_6$, contains a kagomé lattice of Heisenberg spins S=5/2 with a coverage of 97±1%. DC and AC susceptibility measurements show strong in-plane antiferromagnetic exchange ($\theta_{CW} = -1500\pm300$K) and a spin-glass transition at $T_f = 13.8$K, while the magnetic contribution to the specific heat below T_f rises with T as T^2, characteristic of two-dimensional propagating modes. Powder neutron diffraction reveals short-range magnetic correlations ($\xi \approx 19\pm2$ Å) with a wavevector corresponding to the $\sqrt{3} \times \sqrt{3}$ spin structure at 1.9K.

PACS Numbers: (75.10Jm, 75.25.+x, 75.40Gb, 75.50Lk)

The Heisenberg kagomé antiferromagnet presents a fascinating challenge for theorists[1-3] and experimentalists[4-8] alike. The lattice is built from vertex-sharing triangles in which the frustration of nearest-neighbour antiferromagnetic exchange produces a 120° structure within each triangle (Figs 1(a) and 1(b)). For coplanar spin configurations a chirality (handedness) n may be associated with each triangular plaquette, where $n = (2/3\sqrt{3})\sum_{i,j}(S_i \times S_j)$, and S_i, S_j are the spins taken in a clockwise sense around the plaquette. Neither the 120° spin structure nor the chirality is conveyed uniquely between triangles through a shared vertex[9], resulting in a highly degenerate ground state. Thermal and quantum fluctuations lift this degeneracy, selecting spin configurations with softer, more highly entropic excitations. This "order-by-disorder" process selects coplanar configurations in the limit $T \rightarrow 0$, two of which are shown in Figs 1(a) and (b), and referred to as the q = 0 and the $\sqrt{3}$ x $\sqrt{3}$ structure respectively. Both these spin structures can support cooperative fluctuations of blocks of spins and the creation of extended spin defects bounded by spins of one sublattice only [2]. Moments within the blocks may be rotated by an arbitrary angle ϕ about the direction of the peripheral spins at no energy cost, creating open and closed spin folds for the q = 0 and $\sqrt{3}$ x $\sqrt{3}$ structures respectively. Although it takes no energy to create a single open or closed $\phi = \pi$ fold in a coplanar spin state, interactions between such defects give rise to glassy magnetic behaviour. It is still not clear what is the most appropriate description of the spin correlations in the medium that supports these defects. The $\sqrt{3}$ x $\sqrt{3}$ structure is weakly favoured over the q = 0 structure, but Monte Carlo simulations indicate that the appropriate order parameter does not saturate at very low temperatures, and no order is observed in the staggered chirality that would be expected to accompany it, leading to doubt as to whether conventional long-range order can occur as $T \rightarrow 0$.

Theoretical work has been complemented, and in many cases stimulated, by experimental work on the layered garnet $SrGa_{12-x}Cr_xO_{19}$ (SCGO(x)) in which Heisenberg spins S=3/2 sit at the vertices of a kagomé lattice[4] coupled by strong antiferromagnetic exchange (the Curie-Weiss constant θ_{CW} = –500K). DC magnetic susceptibility (χ_{dc}) measurements reveal a spin-glass transition at $T_f = 3-7$K, depending on the composition x; this is accompanied by a progressive

slowing-down of the fluctuations as SCGO(x) is cooled from well above T_f [5] However, this type of spin-glass is most peculiar. Elastic and inelastic neutron scattering data show short-range correlations corresponding to the $\sqrt{3}$ x $\sqrt{3}$ structure with a correlation length of $\approx$ 7Å (approximately twice the Cr-Cr separation)[6], though *ca.* 2/3 of the scattering at $T = 0.5T_f$ is from excitations whose energy is greater than 50GHz, and no static component of the moment could be observed down to 0.01K by muon spin relaxation measurements for which the time-scale of the probe is 170MHz[5]. Specific heat measurements reveal an unusual T^2 dependence below T_f[7] normally associated with long-range two-dimensional magnetic order.

Unfortunately, SCGO(x) has shortcomings as a model kagomé antiferromagnet. The coverage of the kagomé lattice is far from complete, being typically 89 - 92%, though dilution studies indicate that the glassy behaviour is characteristic of the perfectly covered lattice. Further, a significant proportion of the Cr^{3+} ions reside in triangular lattices between the kagomé layers, complicating analysis of the magnetic properties. Recent measurements of the spin excitations in SCGO(x) have shown that this material is best described as a layer of corner sharing tetrahedra (made up of 2 kagomé layers and an intervening triangular layer) separated by triangular layers of spins bound in singlets[8]. Thus, while it is a highly frustrated system, SCGO(x) is far from a faithful representation of the simple kagomé lattice which has been the subject of most theoretical work. In this letter we discuss such a system in the form of a deuterated analogue of the mineral hydronium iron jarosite, $(H_3O)Fe_3(SO_4)_2(OH)_6$, in which the coverage of the kagomé lattice is 97±1%. Measurements of χ_{dc} and the AC susceptibility (χ_{ac}) reveal strong antiferromagnetic exchange (θ_{cw} = −1500±300K) and a spin-glass transition at T_f = 13.8K (from χ_{dc}), while neutron scattering measurements demonstrate that the magnetic correlations remain short-range down to 1.9K, with a wavevector corresponding to the $\sqrt{3}$ x $\sqrt{3}$ structure. Specific heat data show the same T^2 dependence below T_f that has been seen in SCGO(x), suggesting that this behaviour is a universal property for this class of 2D frustrated antiferromagnets.

Jarosites are a family of minerals of general formula $AFe_3(SO_4)_2(OH)_6$ (where A = Na^+, K^+, Rb^+, Ag^+, Tl^+, NH_4^+, H_3O^+, $1/2Pb^{2+}$ or $1/2Hg^{2+}$)[10]. They have already been identified as

kagomé antiferromagnets, in which FeO_6 octahedra are linked through their vertices in layers that are well-separated by hydroxide, sulphate and hydronium groups. The magnetic ion Fe^{3+} has a $^6A_{1g}$ ground term which will approximate very well to a S=5/2 Heisenberg spin. However, until recently[11] it has not been recognised by those studying their magnetic properties that jarosites are prone to nonstoichiometry; a significant proportion of A^+ ions are replaced by H_3O^+, and Fe^{3+} is lost with the accompanying protonation of the hydroxyl groups. This results in a kagomé lattice with a typical coverage of 83 - 95%. An exception to this is the hydronium salt which can be prepared with a coverage of approximately 97%[11].

Partially deuterated hydronium jarosite was prepared by a method based on an established hydrothermal route[12]. 40g of $Fe_2(SO_4)_3.nH_2O$ was dissolved in D_2O and made up to 300ml then heated in a PTFE-lined stainless steel bomb at 140°C for 4 hours. The deuteronium jarosite precipitate was washed with D_2O and dried at 120°C. A new material, $(H_3O)Ga_3(OH)_6(SO_4)_2$, was prepared as a diamagnetic analogue for subtracting the phonon contribution from the specific heat measurements. 2g of $Ga_2(SO_4)_3$ was made up to $5cm^3$ in deionised water and heated at 140°C for 17 hours in a sealed Pyrex tube. The resulting precipitate was washed and dried at 120°C then characterised structurally by powder X-ray diffraction using a Rigaku "Geigerflex" diffractometer with CuKα radiation. The structure was refined from these data using GSAS[13] from the $R\bar{3}m$ jarosite structure[11] with lattice parameters a = 7.1754(23) Å and c = 17.1635(6) Å.

Measurements of χ_{dc} were carried out between 1.8K and 330K using a Quantum Design $MPMS_2$ SQUID Magnetometer. Fig. 2(a) clearly shows the onset of spin glass-like behaviour at T_f = 13.8K as a divergence between zero-field-cooled (ZFC) and field-cooled (FC) measurements, where the cooling and the applied field were both 100G. The anomaly at 4.5K is believed to be an artefact of the temperature control; it is not seen in the measurements of χ_{ac} or specific heat which showed no anomalies other than that at T_f down to 15mK. At higher temperatures the susceptibility conforms approximately to Curie-Weiss behaviour, with some curvature in the dependence of $1/\chi_{dc}$ on T between 150 and 300K as a result of short-range 2D correlations. Extrapolation of this curve to $1/\chi_{dc}$ =0 provides an estimate for θ_{CW} of −1500±300K. Short-range 2D antiferromagnetic

correlations are also believed to be responsible for reducing the effective moment at 300K from the spin-only value of $5.9\mu_B$ to approximately $4.3\mu_B$. Both T_f and θ_{CW} differ slightly for the hydronium and deuterated forms; T_f has also been found to vary between samples of the same material, ranging from 12 to 18K for samples of the hydronium salt of the same nominal composition[11]. Small variations in preparative conditions lead to small changes in lattice coverage, and the limits of the precision of our chemical analysis will encompass a range of values of T_f and θ_{CW}. Jarosites in which hydronium is exchanged for K^+, Tl^+ or NH_4^+ show long-range magnetic ordering transitions at ~ 50K[10]. The structures of all these jarosites are very similar and it is unlikely that the inter- or intraplane exchange pathways differ significantly. What *is* different is the degree of lattice coverage: the salts that order have relatively low coverage (<90%) while the hydronium salts have a coverage greater than 90%. Thus, it appears that *lower* coverage is found to lead to a *lower* value of θ_{CW} but a *higher* value of T_f, consistent with what is observed in SCGO(x). There may also be small differences in single-ion anisotropy and interplane exchange between the hydronium and deuterated salts.

The relative values of T_f and θ_{CW} for a given sample are broadly consistent with theoretical predictions: Monte Carlo simulations on a Heisenberg kagomé antiferromagnet with a small XY exchange anisotropy ($J_x=J_y > J_z$) indicate that the flipping of single stars freezes out at $\approx\theta_{CW}/96$ ($\approx$ 15K for deuteronium iron jarosite), but the simulations were not performed for sufficiently long to study the freezing of longer closed folds[2]. When an Ising anisotropy is present, freezing is expected at $T = 0.058J$ ($\approx$ 4K for deuteronium iron jarosite) accompanied by a parasitic ferromagnetic moment[3].

In-phase and out-of-phase components of the χ_{ac} were measured over the temperature range 5-25K at frequencies of 1.157 - 1157 Hz using a standard mutual inductance technique. The data are presented in Fig. 2(b), showing the fall of T_f with measuring frequency ω in a manner typical of an 'ideal' spin glass: $\Delta T_f/T_f\Delta\log\omega = 0.010$, the value also found for *Au*Fe[14]. These data were fitted to the empirical Vogel-Fulcher law $\omega = \omega_0 \exp[-E_a/(k(T_f-T_0)]$ with the activation energy $E_a = 64K$, the ideal glass temperature $T_0 = 15.6K$ and $\tau_0 = 1/\omega_0 = 1.6 \times 10^{-12}$ sec. Specific

heat data were taken for both $(D_3O)Fe_3(SO_4)_2(OD)_6$ and $(H_3O)Ga_3(SO_4)_2(OH)_6$ over the temperature range 0.4-40K. The data for the iron compound were corrected for the phonon background measured on the gallium compound (which contributes about 10% of the signal at these temperatures) and are displayed as a graph of $C_m(T)/T$ against T in Fig. 2(c) to bring out the T^2 dependence below T_f. This contrasts with conventional spin glasses where localised modes with an energy-independent density of states dominate at low temperatures, giving a linear dependence of $C_m(T)$ on T. A T^2 dependence implies propagating spin-waves based on long-range magnetic order in a conventional 2D antiferromagnet, or from the frozen spin state in a 2D spin-glass[15]; similar behaviour has been observed in SCGO(x). Deuteronium jarosite also ressembles SCGO(x) in the small fraction of the magnetic entropy released at T_f, being 18% of the full value of Rln(2S+1) for free spins S compared with approximately 7% at T_f for SCGO(x). However, in contrast to SCGO(x) and also to 'ideal' spin glasses, no peak is observed in $C_m(T)/T$; instead, $C_m(T)/T$ changes monotonically with T over a wide range of temperature.

Neutron powder diffraction measurements were performed on deuteronium jarosite to probe the magnetic pair correlation function more incisively. Diffraction patterns were taken on the multidetector diffractometer C2 at the NRU Reactor, Chalk River at a wavelength of 1.5041Å. Data taken at 2K were refined successfully from the $R\bar{3}m$ jarosite structure[11] giving a = 7.3445(7)Å and c = 16.9037(16)Å. No additional Bragg peaks were seen at the lowest temperature; instead, we observed a broad asymmetric peak centred at $Q \approx 1.05$Å^{-1} indicative of short-range magnetic correlations (Fig. 3). Nuclear Bragg peaks were excluded from the diffuse scattering, and the data that remained were fitted to a Warren function[16] which gives the scattering power $P_{2\theta}$ of a two-dimensional disordered structure as:

$$P_{2\theta} = Km\frac{F_{hk}^2(1+\cos^2 2\theta)}{2(\sin\theta)^{3/2}}\left(\frac{L}{\sqrt{\pi}\lambda}\right)^{1/2} F(a)$$

where $a = (2\sqrt{\pi}L/\lambda)(\sin\theta - \sin\theta_0)$, K is a constant, m is the multiplicity of the reflection, F_{hk} is the two-dimensional structure factor, λ is the wavelength, L is a two-dimensional correlation

length, θ_0 is the peak position, and the function *F(a)* , which is proportional to an integral of the scattering strength over different sizes and orientations of correlated moments, is calculated self-consistently from *L* and the scattering geometry[16]. This yielded a two-spin correlation length of 19±2Å, the approximate point to point distance across an individual kagomé star. The fitted peak is centred at Q = 1.05Å^{-1}, close to the position (1.09Å^{-1}) of the (2 1) peak of the $\sqrt{3}$ x $\sqrt{3}$ spin structure. Comparison with the pattern obtained at 25K revealed no significant change, indicating that short-range ordering is largely established before the 13.8K transition in χ_{dc}.

The dynamic character of the short-range magnetic correlations was studied in further detail with the triple axis diffractometer N5 at the NRU Reactor, initially configured as a two-axis instrument with an incident energy of 5THz (λ = 1.989Å) and a Si(111) monochromator to reduce contamination of the beam by neutrons of wavelength $\lambda/2$. S(Q) measured at Q = 1.4 Å^{-1}, which is in the region of the strong diffuse scattering but avoids the nearby Bragg peak, rises steadily as the sample is cooled from approximately $4T_f$. The development of short-range magnetic correlations was more marked when the incident neutron energy was reduced to 3THz (λ = 2.568Å) and the instrument was reconfigured as a triple axis spectrometer with an energy resolution of 0.22THz (Fig. 4). After normalisation to the intensity of the (003) reflection, the scattering intensity at this wavevector was found to be reduced by a factor of 4 by the change in spectrometer configuration. Thus, 75% of the neutrons scattered magnetically at 2K are from fluctuations faster than about 0.2THz. The observation that these correlations set in at temperatures higher than the freezing tempetaures observed with DC and AC susceptibility is consistent with the much higher frequency probed in these relatively low resolution measurements.

In conclusion, we have reported measurements of the static and dynamic magnetic correlations in deuteronium jarosite, $(D_3O)Fe_3(SO_4)_2(OD)_6$, which presents a highly covered (97±1%), magnetically isolated, kagomé lattice of antiferromagnetically coupled Heisenberg spins S=5/2. Our results indicate that short-range $\sqrt{3}$ x $\sqrt{3}$ correlations coexist with propagating, spin-wave like modes as well as behaviour more typical of a spin-glass such as FC-ZFC irreversibility in χ_{dc} and a frequency-dependent T_f. Similar behaviour is seen in SCGO(x). This suggests that

this a universal property of this class of 2D frustrated magnets, as well as a feature which should be reproduced in theoretical work. It is interesting to note that these effects are seen in a relatively classical, S=5/2 system, suggesting that quantum effects are not significant. Our observations are consistent with a system of interacting dynamical extended spin defects in a manifold of spin states derived from the $\sqrt{3}$ x $\sqrt{3}$ structure. More theoretical work needs to be done on the energy and dynamics of collections of such defects. In particular, we need a clearer understanding of the energy scale of the defect-defect interactions relative to J, and of the influence of quenched diamagnetic defects on the spin correlations.

The authors would like to thank M.F. Collins for introducing them to jarosites as kagomé magnets, J.E. Greedan for drawing their attention to the Warren function and supplying programs to fit it, and S.T. Bramwell for enlightening conversations. We are also grateful to G.J. Nieuwenhuys for the use of the AC susceptibility and SQUID apparatus at the Kamerlingh Onnes Laboratory, Leiden University. We thank CIAR, EPSRC, NATO and NSERC for financial support, and the technical staff at Chalk River for their expertise in assisting with the neutron scattering measurements.

Figure Captions

1. Spin arrangements and defects for a kagomé antiferromagnet : (a) the q = 0 structure supporting an open defect bounded by the dashed lines and (b) the $\sqrt{3}$ x $\sqrt{3}$ structure supporting a closed defect denoted by the bold hexagon.

2. Changes in (a) χ_{dc} , (b) χ'_{ac} and (c) C_m in the region of T_f for deuteronium jarosite. (a) shows ZFC (closed circles) and FC (open circles) data while the insert depicts ZFC χ_{dc} (circles) and $1/\chi_{dc}$ (triangles) over a wider temperature range. (b) shows the response of the sample with a driving frequency ω of 1.157Hz, while the insert shows how T_f falls with ω in a geometric progression from 1.157 to 1157Hz. The straight line through the low-temperature data in (c) represents a T^2 dependence of C_m on T.

3. Diffuse neutron scattering profile from deuteronium jarosite at 2K with a fit to the Warren lineshape function centred near the (2 1) reflection of the $\sqrt{3}$ x $\sqrt{3}$ spin structure. Breaks in the data and fit indicate regions where nuclear Bragg peaks have been subtracted.

4. Temperature dependence of the diffuse scattering from deuteronium jarosite sampled at Q = 1.4Å^{-1} and $\Delta\omega \leq 0.22$ THz. The line through the data provides a guide to the eye.

References

[1] P. Chandra and P. Coleman, Phys. Rev. Lett. **66**, 100 (1991); A. B. Harris, C. Kallin and A. J. Berlinsky, Phys. Rev. B **45**, 2899 (1992); A. Chubukov, Phys. Rev. Lett. **69**, 832 (1992); J. T. Chalker, P. C. W. Holdsworth and E. F. Shender, Phys. Rev. Lett. **68**, 855 (1992); J. N. Reimers and A. J. Berlinsky, Phys. Rev. B **48**, 9539 (1993); H. Asakawa and M. Suzuki, Int. J. Mod. Phys. B **9**, 933 (1995)

[2] I. Ritchey, P. Chandra and P. Coleman, Phys. Rev. B **47**, 15342 (1993); P. Chandra, P. Coleman and I. Ritchey, J. Phys. I **3**, 591 (1993)

[3] S. T. Bramwell and M. J. P. Gingras, Unpublished work (1994)

[4] X. Obradors *et al*, Solid State Commun. **65**, 189 (1988); A. P. Ramirez, G. P. Espinosa and A. S. Cooper, Phys. Rev. Lett. **64**, 2070 (1990)

[5] S.-H. Lee*et al,* Phys. Rev. Lett. **76**, 4424 (1996)

[6] Y. J. Uemura *et al*, Phys. Rev. Lett. **73**, 3306 (1994)

[7] C. Broholm *et al*, Phys. Rev. Lett. **65**, 3173 (1990)

[8] A. P. Ramirez, G. P. Espinosa and A. S. Cooper, Phys. Rev. B **45**, 2505 (1992)

[9] A. Harrison and T. E. Mason, J. Appl. Phys. **67**, 5424 (1990)

[10] J. E. Dutrizac and S. Kaiman, Can. Miner. **14**, 151 (1975); M. G. Townsend, G. Longworth and E. Roudaut, Phys. Rev. B **33**, 4919 (1986); C. Broholm *et al*, Unpublished work (1992); M. Takano *et al*, J. Phys. Soc. Japan **25**, 902 (1968)

[11] A. S. Wills and A. Harrison, Faraday Trans. **92**, 2161 (1996)

[12] J. Kubisz, Miner. Pol. **1**, 45 (1970)

[13] *Generalised Structure Analysis System*, A. C. Larson and R. B. Von Dreele (1995), Obtainable from the authors at LANSCE, MS-H805, Los Alamos National Laboratory, NM 87454, USA

[14] J. A. Mydosh *Spin Glasses,* , Taylor and Francis, London, 1993.

[15] B. I. Halperin and W. M. Saslow, Phys. Rev. **B 16**, 2154 (1977)

[16] B. E. Warren, Phys. Rev. **59**, 693 (1941); J. E. Greedan *et al*, J. Solid State Chem. **116**, 118 (1995)

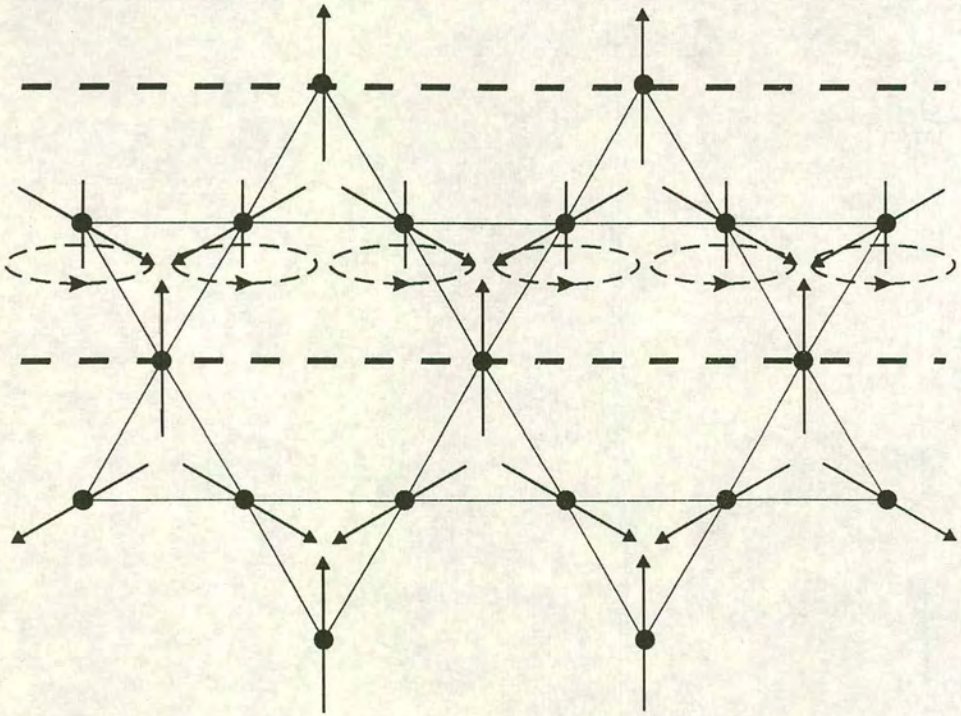

(a)

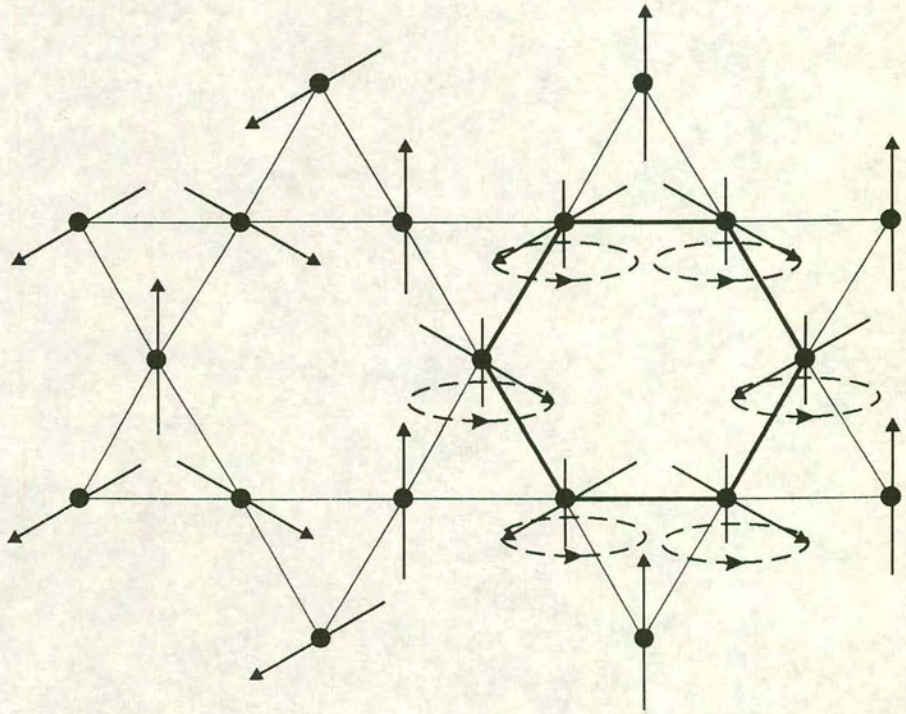

(b)

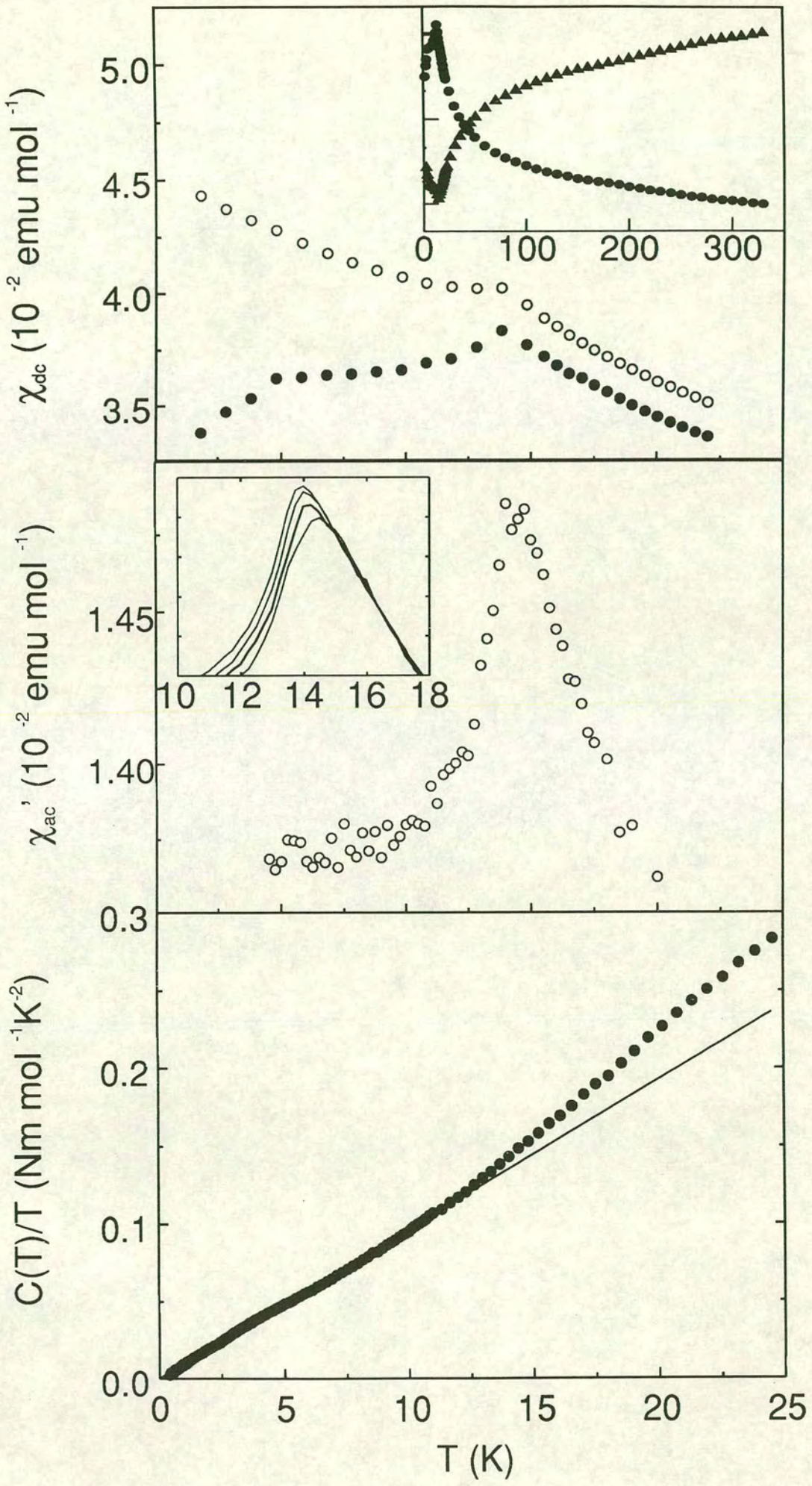
5.0
4.5
4.0
3.5
χ_{dc} (10^{-2} emu mol^{-1})
0
100
200
300
1.45
1.40
χ_{ac}' (10^{-2} emu mol^{-1})
10
12
14
16
18
0.3
0.2
0.1
0.0
C(T)/T (Nm mol^{-1}K^{-2})
0
5
10
15
20
25
T (K)

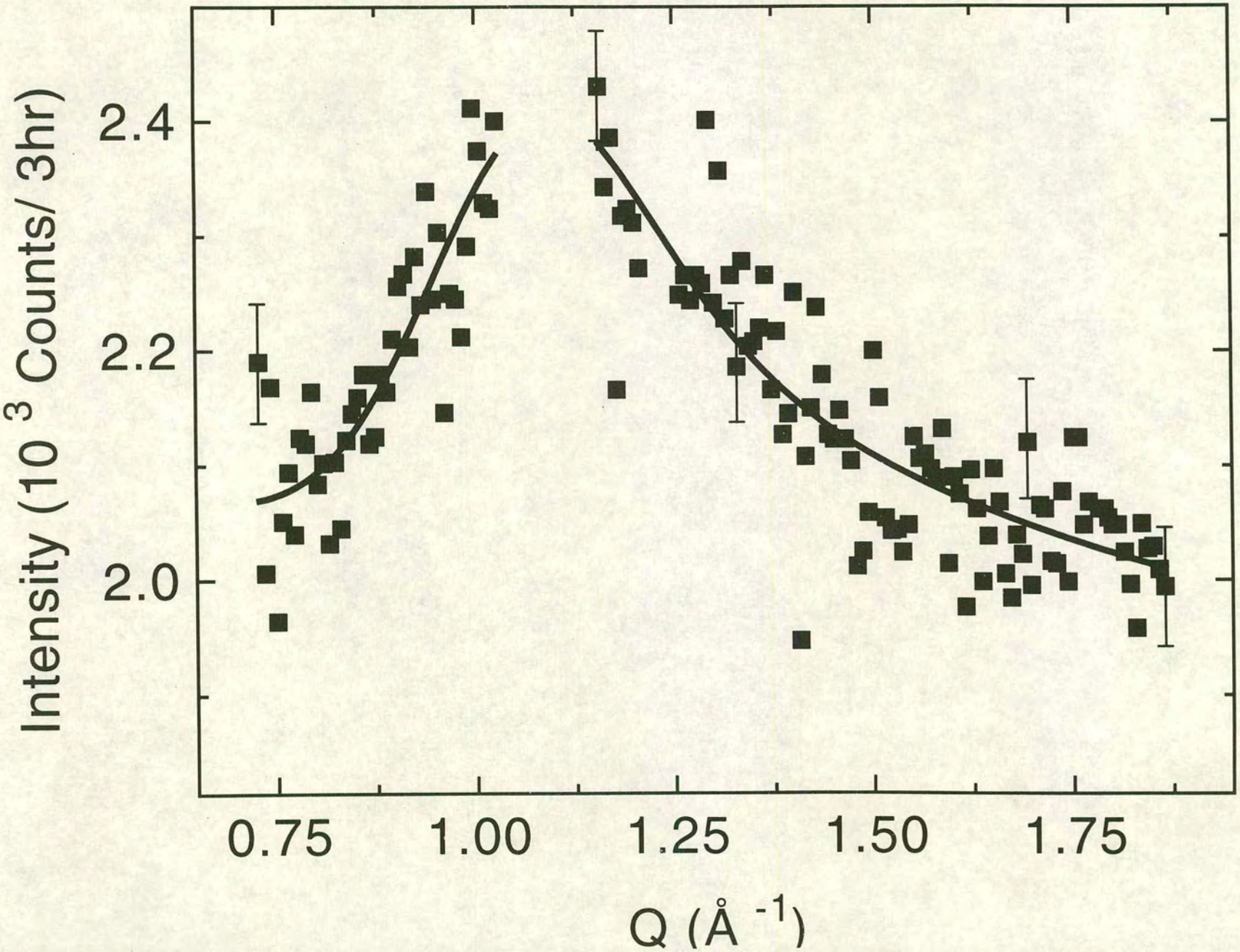
Intensity (10 3 Counts/ 3hr)
2.4
2.2
2.0
0.75
1.00
1.25
1.50
1.75
Q (Å -1)

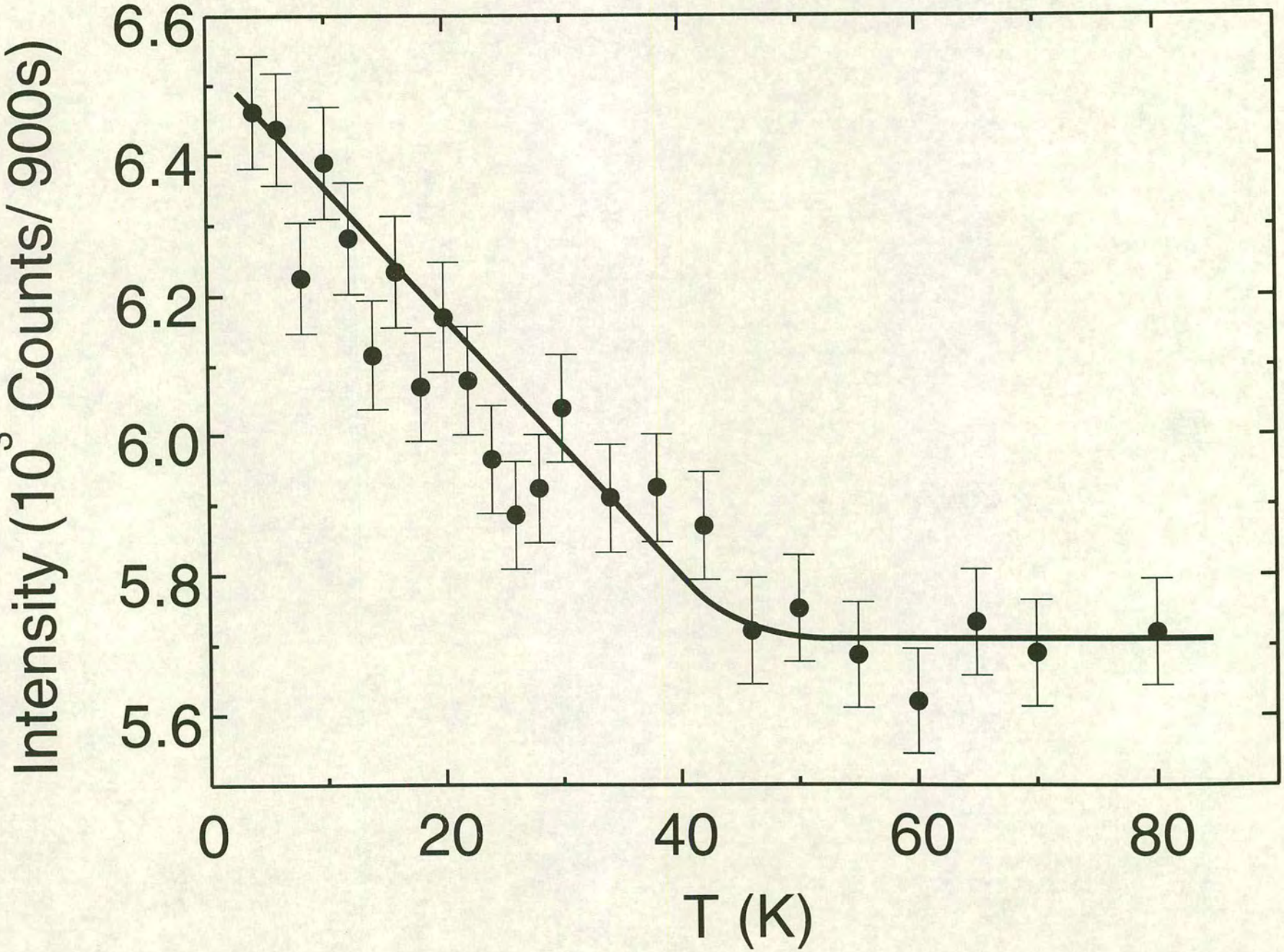
Intensity (10^3 Counts/ 900s)
6.6
6.4
6.2
6.0
5.8
5.6
0
20
40
60
80
T (K)